Proceedings

The Hamlyn Symposium on Medical Robotics

2016

Proceedings

Guang-Zhong Yang and Ara Darzi (Eds.)

Karen Kerr and Valentina Vitiello (Editorial Team)

The Hamlyn Symposium on Medical Robotics

25-28 June 2016
Imperial College London and
the Royal Geographical Society, UK

Proceedings of
The Hamlyn Symposium on Medical Robotics
25-28 June 2016, Imperial College London and
the Royal Geographical Society
London, UK
ISBN: 978-0-9563776-7-8

Preface

The 9th Hamlyn Symposium on Medical Robotics was held at the Royal Geographical Society on 25th to 28th June 2016. The theme for this year's symposium was 'New Challenges and Emerging Platforms' with an impressive line-up of leading scientists and engineers in co-operative, micro and continuum robots, as some of our invited speakers. The keynote lecture was delivered by Professor Peer Fischer, University of Stuttgart, who enlightened us on his experiences in using untethered Micro- and Nano-robots; Professor Darwin Caldwell, Italian Institute of Technology (IIT), spoke on recent developments in augmented, assistive and robotic Technologies in phono-micro surgery; Professor Nabil Simaan shared his expertise and recent advances in continuum robots; Professor Paolo Fiorini, University of Verona, presented an engineering perspective on autonomy in surgical robotics. This year's Storz-Hopkins lecture was delivered by Dr Amir Szold, who provided his insight and vision on bridging the gap between surgeons and engineers.

A total of 89 papers were submitted from 15 countries and 47 institutions, and after systematic peer review, 57 papers were selected for presentation at the Symposium. The topics covered ranged from autonomous and co-operative robots; continuum robots; simulation and training; neurosurgery; orthopaedics; and soft robotics.

For the first time, CAOS UK was run in partnership with the Symposium. CAOS UK is an organisation dedicated to supporting the application and development of modern techniques for orthopaedic surgery. It aims to realise better treatments for patients and hopes to achieve this by encouraging collaboration between surgeons, scientists, engineers and industry. This session involved a series of oral presentations plus interactive workshops with two of the leading companies in this field.

We were delighted to see our workshop programs continue to grow and flourish. Topics focused on some of the following areas: soft robotics; microrobotics and microfabrication; cognitive surgical robotics; image-guided ophthalmology; sewing and suturing; imaging; and robotic assisted neuro- and skull-based surgery.

As with last year, two of the workshops were organised in conjunction with the EPSRC-NIHR Healthcare Technology Co-operatives (HTC) Partnership Award on Devices for Surgery and Rehabilitation. In collaboration with the Trauma HTC at University Hospital Birmingham NHS Foundation Trust, the Rehabilitation and Assistive Technologies workshop had an impressive line-up of international leaders in the field in an area of growing importance. The Surgical Imaging, Guidance and Augmented Reality workshop was supported by the Enteric HTC at Barts Health NHS Trust and Queen Mary University of London.

We were particularly excited to host the second Surgical Robot Challenge following on the open platforms for medical robots in partnership with Intuitive Surgical, Kuka Robotics, and Applied Dexterity. A large number of submissions were received, with 10 teams bringing their kit to London to compete over a 3-day competition, starting in the lab, followed by presentations to an esteemed judging panel and cumulating in the short-listed finalists presenting to the Hamlyn Symposium wider audience.

A lively debate was hosted, based on an opinion piece entitled 'What Has Transformed Robotics?'. This highlighted the progress of robotics technologies over the last two decades and the need to continuously improve surgical robotics through advances in precision medicine, personalised healthcare, and quality-of-life improvements.

We would like to thank the International and Local Programme Committees, the Workshop Organising Committee and the Local Organising Committee for giving up their valuable time to ensure timely review of the submitted papers, to shape an excellent symposium programme.

We are also grateful to the team who have worked behind the scenes and for their continuous effort in managing all aspects of the Symposium organisation. In particular, thanks to Su-Lin Lee, Robert Merrifield, Raphaele Raupp, Daisy Wiley and Charence Wong.

Lastly, special thanks go to Lady Hamlyn. This would not be possible without the generous philanthropic support from both the Helen Hamlyn Trust and Lady Hamlyn herself.

It was our great pleasure to welcome attendees to the 9th Hamlyn Symposium in London.

June 2016, London
Karen Kerr, Valentina Vitiello, Guang-Zhong Yang, Ara Darzi

Organisation

General and Programme Co-Chairs

Guang-Zhong Yang
Ara Darzi

International Programme Committee

Darwin Caldwell	IIT, Italy
Howie Choset	Carnegie Mellon University, USA
Kevin Cleary	The Sheikh Zayed Institute, Washington, USA
Paolo Dario	Scuola Superiore Sant'Anna, Pisa, Italy
Simon DiMaio	Intuitive Surgical Inc, USA
Pierre Dupont	Children's Hospital Boston, USA
Hubertus Feussner	Technical University Munich, Germany
Gabor Fichtinger	Queen's University, Canada
Paolo Fiorini	University of Verona, Italy
Dennis Fowler	Titan Medical Inc., USA
Blake Hannaford	University of Washington, USA
Leo Joskowicz	The Hebrew University of Jerusalem, Israel
Jacques Marescaux	University Hospital Strasbourg, France
Arianna Menciassi	Scuola Superiore Sant'Anna, Pisa, Italy
Bradley Nelson	ETH Zürich, Switzerland
Vipul Patel	Global Robotics Institute, USA
Cameron Riviere	Carnegie Mellon University, USA
Ichiro Sakuma	University of Tokyo, Japan
Rick Satava	University of Washington, USA
Lee Swanstrom	University of Oregon, USA
Mark Talamini	University of California, San Diego, USA
Russ Taylor	Johns Hopkins University, USA
Kirby Vosburgh	Harvard University, USA
Robert Webster III	Vanderbilt University, USA
Steve Wexner	Cleveland Clinic Florida, USA

Local Programme Committee

Kaspar Althoefer	Queen Mary University of London, UK
Thanos Athanasiou	Imperial College London, UK
Colin Bicknell	Imperial College London, UK
Daniel Elson	Imperial College London, UK
Leonard Fass	Imperial College London, UK
Mohamad Hamady	Imperial College London, UK
Daniel Leff	Imperial College London, UK
Erik Mayer	Imperial College London, UK
Andreas Melzer	Dundee University, UK
Azad Najmaldin	St James University Hospital, Leeds, UK
Geoff Pegman	RU Robotics, UK
Ferdinando Rodriguez y Baena	Imperial College London, UK
Julian Teare	Imperial College London, UK
Justin Vale	Imperial College London, UK

Table of Contents

Proof-of-Concept Studies with the da Vinci Robotic System

Surgical Simulation, Training and Skills Assessment

Robotics for Endoscopic Neurosurgery

Robot-Assisted Active Learning for Surgical Technical Skill Acquisition: Early Findings from a Comparative Study

S. S. Vedula[1], B. Gu[2], K. Olds[3], M. Balicki[1], G. L. Gallia[3], G. D. Hager[1], R. H. Taylor[1], M. Ishii[4]

[1]*Department of Computer Science, Johns Hopkins University, USA*

[2]*Department of Biomedical Engineering, Johns Hopkins University, USA*

[3]*Department of Neurology and Neurosurgery, Johns Hopkins University, USA*

[4]*Department of Otolaryngology – Head and Neck Surgery, Johns Hopkins University, USA*
vedula@jhu.edu

INTRODUCTION

Neurological research on robotic assistance for motor recovery following stroke and cerebral palsy suggests that robots can enable automated coaching to facilitate surgical technical skill acquisition [1]. With robotic assistance, trainees may safely learn to perform surgical procedures in the operating room while avoiding harm to patients. Furthermore, operating with a robot yields large amounts of data that can be used to objectively assess surgeons' skill and learning curves.

Several control strategies for robot-assisted motor learning have been studied, mostly in patients recovering from neurologic injury [2]. Haptic guidance is a strategy that involves providing the operator with feedback on the trajectory and velocity profile through proprioception and touch. Simple haptic guidance facilitates observational and use-dependent learning but it may impede error-based learning [2]. Haptic guidance may be beneficial in learning tasks with a high demand on hand-eye coordination [1]. Thus the role of robotic assistance using a haptic guidance strategy in the acquisition of surgical technical skill remains unclear.

Our objective was to determine the effect of robotic assistance on acquiring technical skill and on surgical performance. Sinus surgery, which we used as the prototype in this study, accounts for a large fraction of ambulatory procedures performed in the United States [3]. Trainees are required to become competent at performing several sinus surgical procedures. But teaching sinus surgery in the operating room is extremely challenging because the paranasal sinuses are surrounded by delicate structures such as the eye and the brain. In this study, we compared learning specific tasks in sinus surgery with and without robot assistance.

MATERIALS AND METHODS

We used the Robotic Ear Nose and Throat Microsurgical System (REMS) [4] developed at the Laboratory for Computational Sensing and Robotics at Johns Hopkins. The REMS is a cooperatively controlled robot that relies on admittance control to allow manipulation of rigid surgical tools with five degrees of freedom (DOF), and simultaneously filters hand tremor (Figure 1). The REMS also allows specification of virtual fixtures to constrain the path of the tool-tip with different degrees of rigidity (range=0-1; where 0 is conventional admittance control).

The study tasks involved reaching two targets in the nose – the attachment of the middle turbinate (MTB), which is relatively easy to master, and the sphenoethmoid junction (SEJ), which is somewhat harder to learn because it is situated deep in the nasal cavity. We used an adequately preserved cadaver head for this study, which was approved by the Johns Hopkins University Homewood Institutional Review Board. We tracked tool position and orientation using a 6 DOF electromagnetic sensor attached to the surgical tool and an Aurora tracking system (Northern Digital Inc., Waterloo, Canada).

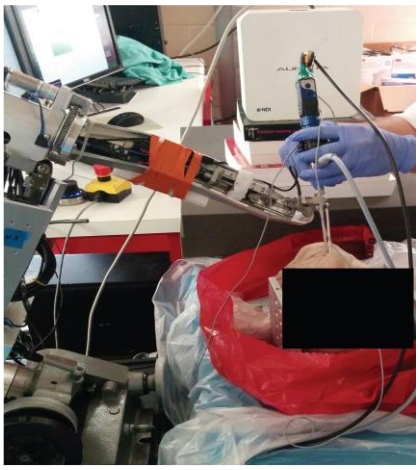

Fig. 1 Setup with REMS, cadaver head, and EM tracker.

We used random numbers to assign four surgically untrained subjects to learn the study tasks either using REMS or freehand. Before beginning to learn in the assigned mode, all subjects practiced operating REMS to replicate pre-specified trajectories on an inanimate bench-top model. In addition, all subjects watched an instructional video showing endoscopic views of the anatomical targets and how to reach them. Finally, all subjects were initially allowed to navigate inside the nose using the surgical tool and the endoscopic camera.

During training, the subjects practiced reaching the MTB and the SEJ on the left side of the head. The subjects repeated each study task eight times. During testing, the subjects performed each study task first

using the same modality as with training followed by the other modalities on the left side of the head. An expert surgeon repeated each study task five times using the robot (no constraints) for the reference standard.

We first analyzed spatial trajectories. We converted each trajectory into a string using descriptive curve coding (DCC; spatial quantization within 3mm windows and a 19-element vocabulary) [5]. We then fitted a trigram language model for each study task using DCC strings of trajectories from expert performances. We computed the negative log probability of a DCC string obtained from a subject's performance of task under this expert model as a measure of its deviation from expert performance. Higher values of this measure indicate greater deviation from the expert model.

We further analyzed speed profiles across task repetitions. For an instance of a study task performance by a subject, we computed the number of movements to execute the task relative to the median number of movements made by an expert to execute the same study task. We considered a movement as a peak in speed [6]. The relative movement score is zero when the subject made the same number of movements as the expert, and larger values indicate greater deviation from the expert. Due to the small sample size, we only conducted a descriptive analysis of the data. We plan to recruit more subjects to allow formal hypothesis tests.

RESULTS

Robot-assisted active learning appears to have enabled subjects to replicate trajectories that are similar to expert performances both spatially and in their speed profile, with the robot and freehand (Figures 2 and 3).

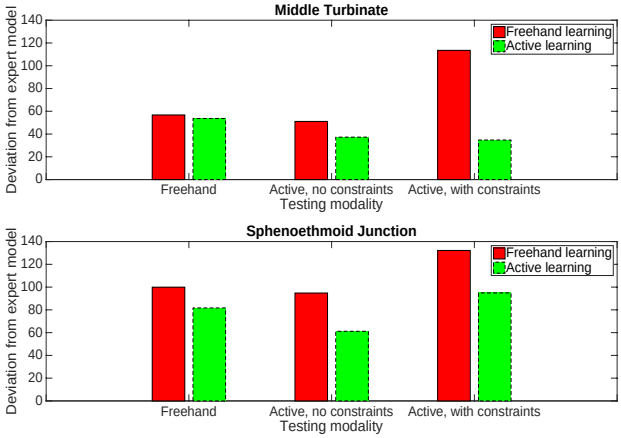

Fig. 2 Trajectory deviation from that of an expert with freehand vs. robot-assisted active learning. Larger values on the Y-axis indicate greater deviation from an expert model.

Subjects who trained freehand replicated similar trajectories with a freehand and robotic assistance without constraints during training (Figure 2), but their speed profile appeared to be worse with the robot (Figure 3). Furthermore, subjects who trained freehand had consistently greater deviation from expert trajectories and speed profiles when testing with robotic assistance and constraints, compared with testing freehand or with robotic assistance and no constraints.

Active learning appeared to have led to subjects performing the easier task of reaching the MTB like an expert with both freehand and with robotic assistance. But its effect on learning the more difficult task of reaching the SEJ remains unclear from available data.

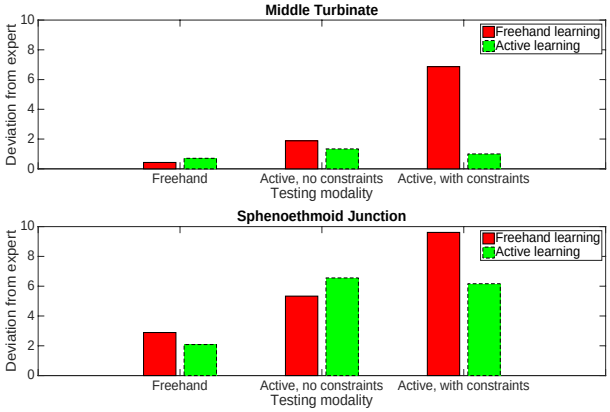

Fig. 3 Speed profile relative to that of an expert with freehand vs. robot-assisted active learning. Larger values on the Y-axis indicate greater deviation from expert speed profile.

DISCUSSION

These preliminary results from our ongoing study demonstrate feasibility and provide insights into the effects of robotic assistance on learning technical skill and on surgical performance. Our finding that subjects learning the tasks freehand appeared to perform poorly with constraints on the robot suggests that simply introducing virtual fixtures without prior training on the robot may have an adverse impact on surgeons' performance. Additional data are needed to verify this observation, which has implications for patient safety in the operating room. Our study provides the basis for further research on the effect of robotic assistance on technical skill acquisition in surgeons.

ACKNOWLEDGMENTS

This work was supported in part by NIH grant #1R01DE025265-01 and by JHU internal funds.

REFERENCES

[1] Reinkensmeyer DJ, Patton JL. Can robots help the learning of skilled actions? Exerc Sport Sci Rev. 2009;37(1):43-51.

[2] Reinkensmeyer DJ, Emken JL, Cramer SC. Robotics, motor learning, and neurologic recovery. Annu Rev Biomed Eng. 2004;6:497-525.

[3] Bhattacharyya N. Ambulatory sinus and nasal surgery in the United States: demographics and perioperative outcomes. Laryngoscope. 2010;120(3):635-38.

[4] Olds KC, et al. Preliminary evaluation of a new microsurgical robotic system for head and neck surgery. IEEE/RSJ IROS 2014, pp. 1276-81.

[5] Ahmidi N, et al. String motif-based description of tool motion for detecting skill and gestures in robotic surgery. Med Image Comput Comput Assist Interv. 2013;16(Pt 1):26-33.

[6] Datta V, Chang A, Mackay S, Darzi A. The relationship between motion analysis and surgical technical assessments. Am J Surg. 2002;184(1):70-73.

Surgical Pre-Planning for Robot-Assisted Fracture Surgery

G. Dagnino[1], I. Georgilas[1], F. Girault[1], P. Tarassoli[2], R. Atkins[2], S. Dogramadzi[1]

[1]*Bristol Robotics Laboratory, University of the West of England, Bristol, UK*

[2]*University Hospitals Bristol, Bristol, UK*

giulio.dagnino@uwe.ac.uk

INTRODUCTION

The treatment of lower limb joint fractures consists in anatomical surgical reduction followed by rigid fixation of the bone fragments using plates and screws or intramedullary nails [1]. The anatomical reduction of the fracture consists in repositioning and aligning the broken fragments to reconstruct the bone as close as possible to its original form, ensuring the correct functionality again. The anatomical reduction can be achieved through an open procedure (involving an open incision into the limb) or minimally invasive techniques (involving orthopaedic manipulation of pins inserted into the fragments through small incisions). Open procedures can be effective but are associated with major damage to the soft tissues, slower bone healing with increased risk of infection, and consequently, prolonged hospitalisation and health-related costs [2]. Minimally invasive techniques are associated with a faster recovery and a lower risk of infection [3], but, the current surgical setup which relies on multiple intra-operative fluoroscopic images of the fracture, can not always achieve the required accuracy of anatomical reduction of the fracture. The 2D nature of these images, and the localised and limited field of view do not provide enough information to the surgeon with respect to the fracture alignment and rotation, which is essentially a 3D problem, resulting often in a sub-optimal fracture reduction [2].

All of these issues lead us to investigate some form of computer and robotic assistance that could support the surgeons in treating fractures that involve joints in terms of efficiency, surgical outcomes, and patient's safety. In this direction, the Bristol Robotics Laboratory (BRL) has developed a robotic system for percutaneous manipulation and reduction of fractures using parallel-robots for fracture manipulation and enhanced 3D imaging [4], [5].

The aim of this work is to introduce the system's new graphical user interface (GUI) and test the efficiency of 'virtual' reduction of fractures using three different control devices: Leap Motion, computer mouse, and Xbox 360 controller. The experimental setup is shown in Fig.1.

MATERIALS AND METHODS

The BRL robotic system is shown and described in [4], [5]. The system setup is made up of: a robotic fracture manipulator (RFM, 6-DOF) attached to the bone fragment through an orthopaedic pin; a carrier platform to position the RFM close to the leg at an extended workspace around the joint; a real-time control workstation; a navigation system consisting of a reduction software [5], an optical tracking system, and the GUI. The GUI (Fig.1) (developed in C# for Unity 5.1 engine) allows the surgeon to: load and visualise 3D models of the fractured bones (pre-generated by segmenting CT data of the fracture); interact with the models to virtually reduce the fracture using the three different controllers (Fig.1c); provide the actual pose of the bones intra-operatively (through the optical tracking system [5]); generate and send the motion command for the robotic system which physically reduces the fracture based on the virtual reduction. The GUI provides the surgeon with 2D views of each anatomical plane (i.e. sagittal, axial, coronal, Fig.1a) and a 3D view of the fracture model (Fig.1b), allowing the surgeon to perform the virtual reduction and visually assess its accuracy. We performed 10 virtual reduction experiments with 10 different subjects using the GUI in the pre-operative phase. Each subject had different experience with teleoperation, video-gaming, non-tactile controllers, and 3D virtual environments, i.e. *previous users' experience*. Two orthopaedic pins were inserted into an unbroken femur model (Sawbones): one in the distal part of the femur, and the other one in the femur shaft. Optical tools attached to the pins recorded their pose through the optical tracker. The recorded pose – $\boldsymbol{P_{goal}}$ – served as the ground truth for the reduction assessment, i.e. it was the target pose for the reduction process. The femur was then fractured into two parts

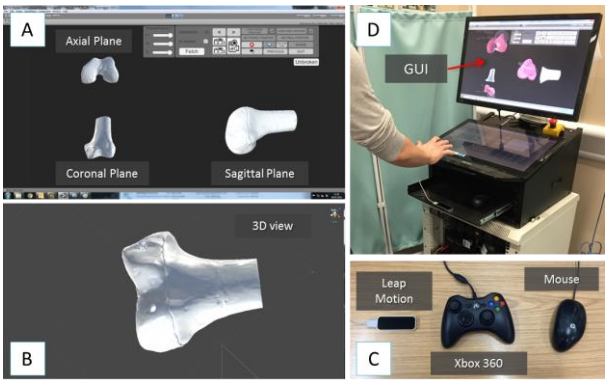

Fig. 1 Experimental setup: Software GUI presenting 2D views (A) and 3D view (B) of the fracture; the three control interfaces (C); a user is virtually reducing a fracture using the Leap Motion (D).

and CT scanned. 3D models of the fragments were generated using commercial software (ImageSim, Volmo, UK), and imported into the reduction software for virtual reduction.

After a short familiarisation phase with the setup (1 minute with each controller), subjects were asked to virtually reduce the fracture (i.e. matching the two fragments) 5 times with each control device. The order of the trials was randomised. During the trials, the final pose of the fragments were stored for subsequent comparison with $\boldsymbol{P_{goal}}$, allowing the objective efficiency evaluation of the control devices in terms of virtual reduction accuracy. The performance metrics chosen for the evaluation were the root-mean-squared-error (RMSE), the maximum absolute error (MAAE) and the minimum absolute error (MIAE) measured during virtual reductions. Also, the execution time was recorded as an additional but rather important performance evaluation parameter.

At the end of the experiment with each controller we submitted a questionnaire to the user in order to collect subjective data about the usability of GUI and the control devices. The System Usability Scale (SUS) questionnaire was utilised as described in [6]. Objective and subjective data from the experiements were used to make a comprehensive evaluation and comparison of the surgeon interfaces.

RESULTS

The experimental results are summarised in Table I, and show the objective evaluation of performances (performance metrics) and the subjective evaluation of usability (SUS score) of using the surgical GUI and three different controllers.

TABLE I. EXPERIMENTAL RESULTS

	Leap Motion	**Mouse**	**Xbox 360**
RMSE*	*2.83 ± 0.8 mm* *1.72 ± 0.6 °*	*2.61 ± 0.8 mm* *1.6 6± 0.6 °*	*2.2 ± 0.7 mm* *1.17 ± 0.5 °*
MAAE	*4.12 mm* *3.5 °*	*4.5 mm* *2.61 °*	*3.35 mm* *2.6 °*
MIAE	*0.94 mm* *0.67 °*	*1.2 mm* *0.36 °*	*0.4 mm* *0.45 °*
Time*	*139 ± 102 s*	*112 ± 80 s*	*113 ± 50 s*
***SUS Score**^*	*63 %*	*83 %*	*80 %*

* Calculated over 50 trials/interface ^ normalised score (0 – minimum; 100 maximum)

DISCUSSION

The experimental results show that the Xbox 360 controller enables the most precise manipulation of the fragments, presenting a residual reduction accuracy error (RMSE) of *2.2 ± 0.7 mm* (position) *1.17 ± 0.5 °* (rotation). Also, both the MAAE (*3.35 mm, 2.6 °*) and MIAE (*0.4 mm*) are lower than the ones obtained with the Leap Motion and the computer mouse. Experiments conducted with the mouse and the Xbox 360 controller resulted in a faster reduction (respectively *112* and *113 s* on average) compared to the Leap Motion (*139 s*). Additional analysis revealed that, the average RMSE and execution time decrease with the number of trials performed by the users with all three controllers. The execution time was reduced by 50% when using the Leap Motion, 20% when using the mouse, and 40% when using the Xbox 360 controller. The average RMSE was reduced by 12% (Leap Motion), 7% (mouse), and 35% (Xbox 360 controller). This means that the usability of the controllers – especially the Xbox 360 controller – could further improve with an extended training time. The *previous users' experience* is directly related to the execution time: experienced users accomplished the reductions faster than less experienced users with all three controllers. Furthermore, *previous users' experience* is correlated with the reduction accuracy when using the Xbox 360 controller: the higher was the experience the lower was the residual average reduction error (RMSE). No similar correlation was observed when the Leap Motion and the mouse were used. Analysis of SUS questionnaires evidenced different levels of usability of each controller. This qualitative evaluation pointed out the superiority of the mouse (score: 83%) and the Xbox 360 controller (80%) over the Leap Motion (63%) in terms of learnability, usability, and user's confidence. In particular, the Leap Motion was classified as not ergonomic and tiring for the arms while both the mouse and the Xbox 360 controller were assessed as easy and comfortable to use. Considering objective and subjective evaluation results, the Xbox 360 controller showed a superior usability and performance capability. These results will be used to guide further development of the surgeon interface. Further studies will be conducted on different types of distal femur factures, and with orthopaedic surgeons as subjects.

ACKNOWLEDGMENT

This is a summary of independent research funded by the National Institute for Health Research's Invention for Innovation (i4i) Programme. The views expressed are those of the author(s) and not necessarily those of the NHS, the NIHR or the Department of Health.

REFERENCES

[1] "Distal Femur Fracture - Reduction and Fixation" *AO Foundation*. 2015.

[2] S. Rammelt, M. Amlang et al., "Percutaneous Treatment of Less Severe Intraarticular Calcaneal Fractures" *Clin. Orthop.*, vol. 468, no. 4, pp. 983–990, Apr. 2010.

[3] Gaston P, Will EM, and Keating JF, "Recovery of knee function following fracture of the tibial plateau" *J Bone Joint Surg Br*, vol. 87, no. 9, pp. 1233–6, 2005.

[4] G. Dagnino, I. Georgilas, P. Tarassoli, R. Atkins, and S. Dogramadzi, "Vision-based real-time position control of a semi-automated system for robot-assisted joint fracture surgery" *Int. J. Comput. Assist. Radiol. Surg.*, Oct. 2015.

[5] G. Dagnino, I. Georgilas, P. Tarassoli, Atkins, R, and S. Dogramadzi, "Intra-Operative 3D Imaging System for Robot-Assisted Fracture Manipulation" *EMBC 2015*.

[6] G. Barresi, N. Deshpande, L. S. Mattos et al., "Comparative usability and performance evaluation of surgeon interfaces in laser phonomicrosurgery" *ICRA 2013.*

Autonomous Ultrasound Scanning for Intraoperative Tumour Localisation and Diagnosis

L. Zhang, M. Ye, C. Chan, G.-Z. Yang

The Hamlyn Centre for Robotic Surgery, IGHI, Imperial College London, UK
lin.zhang11@imperial.ac.uk

INTRODUCTION

Intraoperative ultrasound (iUS) has become a popular tool in robot-assisted laparoscopic surgery to facilitate *in situ* pathology localisation. However, manually controlled ultrasound scanning can cause significant cognitive loads to surgeons, due to the need for maintaining optimal scanning orientation and consistent contact with the tissue, as well as covering a wide area for tumour detection and surveillance. In [1], an iUS probe has been controlled by an auxiliary robotic arm to provide guidance to the surgeon for tumour resection. Although an autonomous tumour dissection framework using the iUS has been proposed in [2] on planar tissue surfaces, a 6-DoF autonomous scanning approach that adapts to arbitrary tissue surfaces has yet to be presented. This paper proposes an automatic iUS scanning framework using the da Vinci® Research Kit (dVRK). Our framework consists of trajectory planning based on 3D surface reconstruction, an automatic scanning via a 6-DoF visual servoing guidance, tumour segmentation and reconstruction using the ultrasound images.

MATERIALS AND METHODS

This paper made use of a da Vinci® Patient Side Manipulator (PSM) via the dVRK [3] that provides kinematic control of the robot. A stereo laparoscope system provides SD (720x576) video streaming for both left and right channels at 25 Hz. A UST-533 linear array ultrasound probe (Aloka Medical, Japan) has been mounted in a custom-made clip that can be picked-up by the robot using Cadiere forceps. A marker (KeyDot®, Key Surgical Inc, USA) was attached on the probe to assist visual tracking and pose estimation. A customised PVA cryogel kidney phantom was utilised with similar elastic and chromatic properties to human tissue.

The tissue surface is recovered from a disparity map using a stereo matching method [4]. The region for scanning is chosen by the user, and the scanning trajectory is planned adaptively to the 3D surface at the beginning of the task. To calculate the local poses (along the trajectory), which place the probe perpendicular to the surface, a local coordinate frame {S} on each surface point is defined using surface gradients and normals. To transform the trajectory from frame {S} to frame {M} (the marker frame), a matrix H_M^S is used and defined based on the calibrated transducer's position. These local poses also enforce that the centre of the transducer is aligned with the surface point.

For every step of visual control, a desired marker pose in frame {C} is calculated as: $H_C^{M*} = H_C^{S*} \cdot H_S^M$, where H_C^{S*} is current desired transformation from frame {C} to {S}. As shown in Fig. 1, a desired robot command H_B^{E*} is calculated based on the current and desired marker pose, H_C^M and H_C^{M*}, in a camera frame {C} via: $H_B^{E*} = H_B^E \cdot H_E^M \cdot H_M^C \cdot H_C^{M*} \cdot H_M^E$. The transformation H_E^M between end-effector frame {E} and marker frame {M} is a constant which can be either measured or calibrated using a standard hand-eye calibration method. For every image in a video sequence, the marker is detected using a circular-grid detection method followed by a pose estimation step [5] that calculates the marker's pose H_C^M in frame {C}. In order to improve the marker detection rate, we have included a tracking component based on pyramidal optical flow [6] to track the circular grid along time.

To segment ultrasound images that contain tumours, speckle noises are removed by applying a Butterworth second order filter followed by an active contour [7] segmentation given a manually chosen seed region. The boundary and holes of the segmented tumour region are smoothed and filled by a set of morphological operations. The boundary is represented as a number of points where each point has correspondence across ultrasound images. In order to reconstruct a 3D model of the tumour using the ultrasound images, we need to transform the segmented boundary points from a 2D image coordinate frame to the 3D camera frame {C}. To this end, an ultrasound coordinate frame {U} is defined in which each pixel of the ultrasound image can be represented as a 3D point p^U. For N segmented boundary points $p^U(i)$ are then transformed to frame {C} via : $p^C(i) = H_C^M \cdot H_M^U \cdot p^U(i), i \in [1, N]$, where H_M^U can be found via calibration and measurement. A 3D model of the tumour can then be created by connecting all the corresponding boundary points.

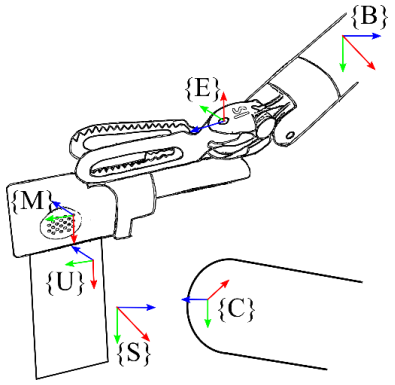

Fig. 1 Coordinate frames defined in this paper: surface frame {S}, marker frame {M}, end-effector frame {E}, robot base frame {B}, ultrasound image frame {U} and camera frame {C}.

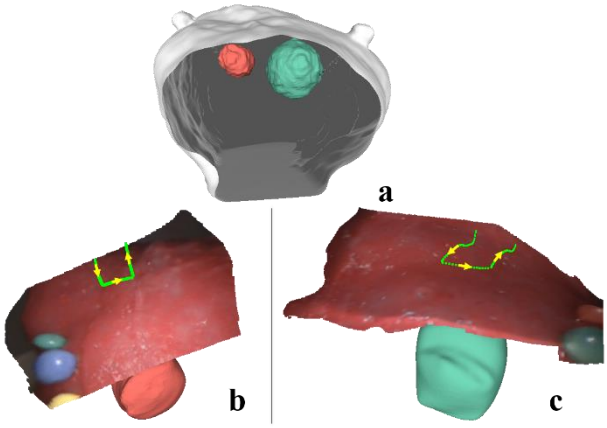

Fig. 2 A 3D visual comparison between the CT ground truth (a) and reconstructed models of proposed framework (b-c). The 10mm and 15mm tumours are coloured in red and green respectively. The green points in b-c show planned trajectory for the ultrasound scanning, where the yellow arrows indicate the scanning direction.

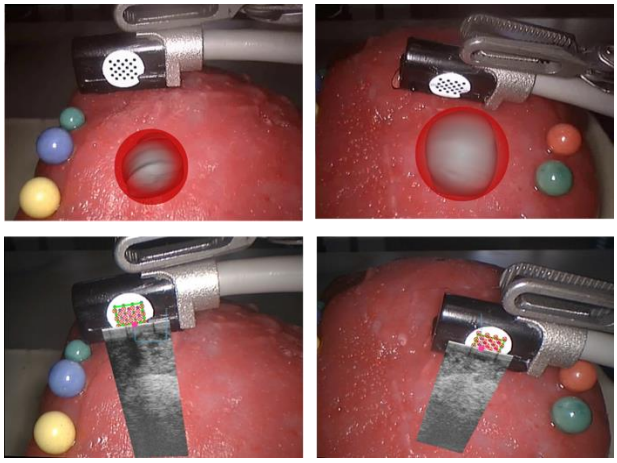

Fig. 3 Top row: the reconstructed tumour is overlaid on laparoscopic images to provide an augmented view for tumour localisation and diagnosis. Bottom row: ultrasound image is overlaid according to current position of the probe. Left and right column show examples of the 10mm and 15mm tumour respectively.

RESULTS

To validate the overall accuracy of the proposed framework, two spherical tumours (diameter: 10mm and 15mm) are implanted in the kidney phantom. The ground truth (position and size) of the tumours is obtained from a CT model of the phantom. Fiducial markers are placed on the phantom in order to assist validation. Each tumour is scanned autonomously while ultrasound images with pose information H_C^U are recorded. As shown in Fig. 2, two tumour models are reconstructed from the ultrasound images using the described method. To compare the reconstructed models with the ground truth, spheres are fit to the CT and reconstructed models, such that the centre position and diameter can be calculated. The errors of centre position are 2.70mm and 2.80mm while the errors of diameter are 0.57mm and 0.43mm for 10mm and 15mm tumours, respectively.

We provide two Augmented Reality (AR) methods of visualisation to assist tumour localisation and diagnosis. As shown in the top row of Fig. 3, reconstructed tumour models are overlaid on the laparoscopic images, displaying the location and size of the tumour relative to the phantom. In order to have better perception of depth and shape of the tumour, inverse realism [8] technique is used. The second visualisation is shown in the bottom row where an ultrasound image is projected and drawn on the laparoscopic image in real-time. The advantage is to provide surgeons both laparoscopic and ultrasound view simultaneously during autonomous scan without distraction. For a 15x10mm region, average scanning time is approximately 90 seconds, which is mainly affected by the scanning path planned at the beginning of the task.

DISCUSSION

This paper proposed a supervised autonomous ultrasound scanning framework for the robot-assisted laparoscopic surgery. It provides smooth scanning motion and maintains optimal orientation using the reconstructed surface. By using stereo vision for motion planning, robust marker detection and tracking, the robot is able to conduct a smooth ultrasound scanning on a non-planar tissue surface autonomously. Different visualisation techniques have been used to present the scanning results of tumours. Both qualitative and quantitative results have demonstrated the feasibility of the framework to detect tumour size and position accurately. Future work will focus on considering tissue deformation and testing the proposed framework in *in vivo* user studies and further improving the surgical AR visualisation.

REFERENCES

[1] Mohareri O, et. al. da Vinci® auxiliary arm as a robotic surgical assistant for semi-autonomous ultrasound guidance during robot-assisted laparoscopic surgery. The Hamlyn Symposium on Medical Robotics. 2014; 45-46.

[2] Pratt P, et. al. Autonomous ultrasound-guided tissue dissection. International Conference on Medical Image Computing and Computer Assisted Intervention. 2015; 249–257.

[3] Kazanzides P, et al. An open-source research kit for the da vinci surgical system. IEEE International Conference on Robotics and Automation. 2014: 6434-6439.

[4] Geiger A, et. al. Efficient large-scale stereo matching. Asian Conference on Computer Vision. 2010; 25-38.

[5] Lepetit V, et. al. Epnp: An accurate o (n) solution to the pnp problem. International Journal of Computer Vision. 2009; Volume 81, Issue 2, 155-166.

[6] Bouguet JY. Pyramidal implementation of the affine lucas kanade feature tracker description of the algorithm. Intel Corporation 2001; 5.1-10: 4.

[7] Chan T, Vese L, Active contours without edges. IEEE Transactions on Image Processing. 2001; Volume 10, Issue 2, 266-277.

[8] Mirna L, et. al. Pq-space based non-photorealistic rendering for augmented reality. MICCAI. 2007; 102-109.

MR-Compatible Robot for Needle-Based Prostate Interventions

P. Moreira[1], S. Misra[1,2]

[1]*Surgical Robotics Laboratory, Department of Biomechanical Engineering, University of Twente, Netherlands*

[2]*Surgical Robotics Laboratory, Department of Biomedical Engineering, University of Groningen and University Medical Center Groningen, Netherlands*

{p.lopesdafrotamoreira,s.misra}@utwente.nl

INTRODUCTION

Prostate cancer is the most common type of cancer worldwide and the second leading cause of death from cancer in men [1]. Early detection and treatment are of significant importance in reducing mortality rate. The common clinical practice for prostate cancer diagnosis is the transrectal ultrasound (TRUS)-guided biopsy. However, an early stage prostate cancer usually cannot be visualized in ultrasound images. On the other hand, an enhanced visualization of an early stage prostate lesion is possible using Magnetic Resonance (MR) imaging. However, MR-guided prostate interventions face several challenges, such as space constraints and electromagnetic compatibility requirement of clinical tools. MR-compatible robotic systems have been proposed to facilitate MR-guided prostate biopsy. These systems can be divided in two groups based on whether the needle is inserted manually [2] or autonomously [3]. In the first group, the robot controls the position of the needle guide and the clinician manually inserts the needle. Whereas in the latter, the guide is robotically positioned and the needle is autonomously inserted. Previous studies using robotic systems for MR-guided prostate interventions were performed in open-loop and needle deflection was not considered.

This work presents a novel robotic system for transperineal prostate biopsy under MRI guidance. The device has 9 degrees-of-freedom (DoF), allowing needle insertions in various directions and a fully autonomous operation (Fig. 1), integrated with a new pre-operative path planning, a steering controller and a needle tracking system.

MATERIALS AND METHODS

The requirements for a robot-assisted transperineal prostate biopsy are defined based on clinical inputs. The workspace is defined by the anthropometric data of a patient in semi-lithotomy position. The robot must be capable of inserting, rotating and firing a biopsy needle (MR-Clear Bio-Cut, Sterylab, Milan, Italy) clinically-approved to be used in the MR scanner. The maximum allowed targeting error is set to be 2.5mm, which is determined based on the smallest clinically significant tumor in pathology (diameter of 5mm) [4].

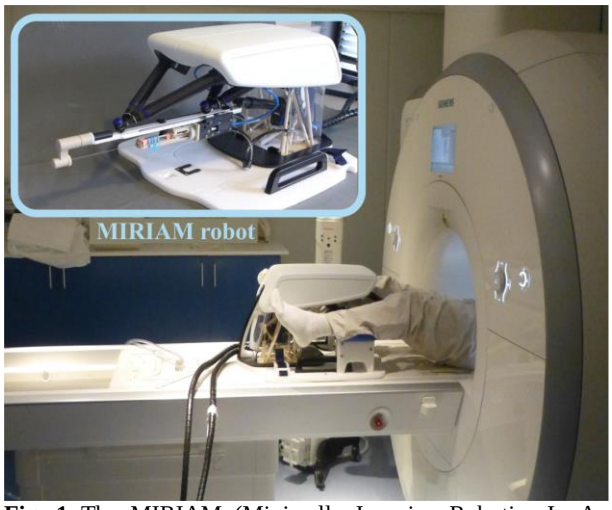

Fig. 1 The MIRIAM (Minimally Invasive Robotics In An MRI environment) robot is a 9 degrees-of-freedom magnetic resonance (MR)-compatible system designed for transperineal prostate biopsy. The system is capable of inserting, rotating and firing a biopsy needle to collect tissue samples.

The MIRIAM (Minimally Invasive Robotics In An MRI environment) system consists of a 5 DoF parallel robot to position and orientate the biopsy needle (Fig. 2) and a 4 DoF needle driver to insert, rotate and fire the biopsy needle. The needle driver inserts and rotates the needle using piezoelectric motors and fires the biopsy needle using pneumatic actuation. The needle driver is primarily designed for prostate biopsy, but it can be modified for other clinical applications, such as brachytherapy or cryotherapy. The 5 DoF parallel robot contains 5 adjustable length rods, which allow for the translation of the needle guided in all three Cartesian axes and also two rotations. Each rod is actuated by a piezoelectric motor (HR2, Nanomotion, Yokneam, Israel). The robot provides maximum translational motion for the needle guide of 24 mm, 70 mm and 130 mm in *x*, *y* and *z* direction, respectively (Fig. 2). The robot also allows rotations of ±15° around the *y*-axis and rotations between 5° and -15° around the *x*-axis. This workspace guarantees that the robot is able to place the needle guide along the perineum and the needle can reach any point within the prostate even considering the variation in its size and location among individuals.

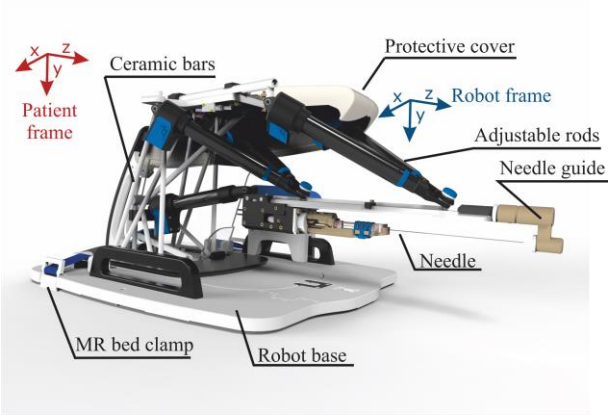

Fig. 2 Magnetic Resonance (MR)-compatible robot for prostate biopsy and its principal components. The x-, y- and z-axis correspond to the Axial, Coronal and Sagittal planes, respectively.

The location of the suspected prostate tumor (target) is selected by the clinician in the pre-operative MR images of the prostate. The pre-operative planner defines the best entry point using a needle deflection model and the information about the insertion environment, such as obstacles and target locations. The pre-planned path is used by the steering controller during the insertion.
The system divides the insertion in iterative steps of fixed insertion depths (typically 10mm). An MR scan is performed at the end of each step. Our tracking system processes MR images and estimates the needle tip position and orientation. A needle steering controller computes thousands of paths from the current needle tip until the target location. The sequence of needle rotations that minimizes targeting error and needle rotations is chosen. This process is repeated until the target is reached. The clinician can also tele-operate the needle insertion depth using a haptic interface located within the control room, while the system autonomously controls the needle rotation.

RESULTS

An MR compatibility analysis is performed by calculating the signal-to-noise (SNR) ratio in different conditions (baseline, robot off, robot on and motors running) [3] and calculating a deterioration factor as defined by Stoianovici [5]. The analysis is performed in an MRI Scanner MAGNETOM Aera (Siemens AG, Erlangen, Germany) using T2 Turbo Spin Echo (TSE) imaging protocol. The SNR drops 16% when the robot is placed inside the scanner and drops 25% when the robot power is turned on. In the last configuration, the SNR reduces 27% when the insertion and rotation motors are running. For the deterioration analysis, the deterioration factors are always lower than the limit of 1%, which means that our system does not induce any interference perceivable by radiologists. The targeting accuracy is evaluated in six needle insertions performed in the same MRI scanner. A clinically-approved 18-gauge is inserted towards physical targets with a radius of 2mm, embedded in a gelatin soft-tissue phantom.

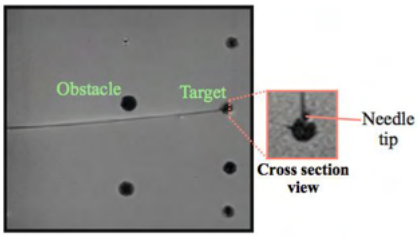

Fig. 3 A coronal magnetic resonance image of one representative insertion. The inset figure shows the cross-sectional view of the final needle tip position.

The targeting error is defined as the Euclidean distance between the final needle tip position and the center of the target. The average targeting error is 1.86mm with a standard deviation of 0.48mm. A representative insertion is presented in Fig. 3.

DISCUSSION

In this study, we present an MR-compatible robotic system for needle-based interventions in the prostate. The image distortion analysis indicates that the robot does not induce any visible deterioration in the image. The needle steering experiments show an average targeting error of 1.86mm, which is 0.64mm less than the desired accuracy defined in the system requirements. Different issues can impact the targeting accuracy, such as target motion and variations of the amount of needle deflection. However, real-time target tracking and online curvature estimation can mitigate these factors and reduce even more the targeting error. Future work will focus on implementing a real-time MR imaging protocol. Additionally, it is planned to perform experiments in biological tissues and cadavers.

ACKNOWLEDGEMENT

This research was supported by funds from the Dutch Ministry of Economic Affairs and the Provinces of Overijssel and Gelderland, within the Pieken in de Delta (PIDON) Initiative, Project MIRIAM.

REFERENCES

[1] R. Siegel, D. Naishadham and A. Jemal, Cancer statistics, 2013, CA Cancer J Clin. 2013;63(1) :11-30.
[2] M. G. Schouten, J. G. Bomers, D. Yakar, H. Huisman, E. Rothgang, D. Bosboom, T. W. Scheenen, S. Misra and J. J. Fütterer, Evaluation of a robotic technique for transrectal MRI-guided prostate biopsies, Eur Radiol. 2012;22(2):476-83.
[3] H. Su, W. Shang, G. Cole, G. Li, K. Harrington, A. Camilo, J. Tokuda, C. Tempany, N. Hata and G. Fischer, Piezoelectrically actuated robotic system for MRI-guided prostate percutaneous therapy, Trans. Mechatronics 2015;20(4):1920-32 .
[4] T. A. Stamey, F. S. Freiha, J. E. McNeal, E. A. Redwine, A. S. Whittemore and h. P. Schmid, Localized prostate cancer. Relationship of tumor volume to clinical significance for treatment of prostate cancer, Cancer 1993;71(S3):933-8.
[5] D. Stoianovici, Multi-imager compatible actuation principles in surgical robotics, The Int J Med Robot. 2005;1(2):86-100.

Toward Transoral Peripheral Lung Access: Steering Bronchoscope-deployed Needles through Porcine Lung Tissue

A. Kuntz[1], P. J. Swaney[2], A. Mahoney[2], R. H. Feins[3], Y. Z. Lee[4], R. J. Webster III[2], R. Alterovitz[1]

[1]*Department of Computer Science, University of North Carolina at Chapel Hill, USA*

[2]*Department of Mechanical Engineering, Vanderbilt University, USA*

[3]*Division of Cardiothoracic Surgery, University of North Carolina School of Medicine, USA*

[4]*Department of Radiology, University of North Carolina School of Medicine, USA*

adkuntz@cs.unc.edu

INTRODUCTION

Lung cancer is the deadliest form of cancer, killing more than 150,000 people each year in the United States alone [1]. It causes more deaths than breast, prostate, colon, and liver cancers combined [1]. To increase the survival rate of lung cancer, diagnosing the cancer early, while the tumor is still a small nodule, is key. Although suspicious nodules can be detected using medical imaging, definitive diagnosis typically requires biopsy. Unfortunately, the lung biopsy approaches currently in use have significant drawbacks, wherein they either cannot reach large portions of the lung, or carry significant safety risks. To bring safe and accurate biopsy to a larger class of patients, our research team recently developed a robotic transoral lung access system [2]. In this paper, we evaluate the system in inflated *ex vivo* porcine lung and visualize the results in a CT scanner (Fig. 1). We demonstrate the robot's ability to reach nodules in the lung which are difficult for current approaches to reach safely.

Currently, lung tumor biopsy is most commonly performed transthoracically, wherein a needle is hand-guided by a physician through the chest wall of the patient into the lung to the nodule. Unfortunately, this process has a diagnostic yield of less than 52% for nodules less than 1.5 cm in diameter [3]. In addition, transthoracic biopsy carries with it significant risk of pneumothorax (collapsed lung), a serious complication. An alternative approach that greatly reduces the risk of pneumothorax is transoral lung biopsy in which biopsy is performed via a bronchoscope. However, this approach is currently limited to nodules close to the bronchial tree or accessible through short straight paths from the airway [4].

Our transoral lung access system leverages the minimally invasive nature and lowered risks of the transoral biopsy approach, while having the potential to reach difficult-to-access lung nodules in the periphery of the lung with high accuracy [2]. The system consists of three stages deployed in sequence: a bronchoscope, a concentric tube channel, and a flexure-tip steerable needle (see Figs. 1 and 2). First, the physician guides the bronchoscope to a feasible location en route to the nodule. From the working channel of the bronchoscope,

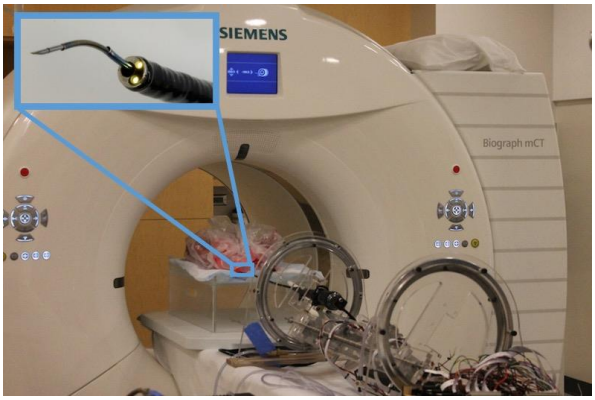

Fig. 1. Our transoral lung access system, consisting of a concentric tube channel and a steerable needle deployed via a bronchoscope, operating in an inflated *ex vivo* porcine lung. CT scans were acquired at each stage of deployment.

the concentric tube channel is deployed, bending toward the wall of the bronchial tree. Using a pneumatic puncture mechanism, the tube then pierces through and enters the parenchyma, orienting its tip toward the lung nodule. The flexure-tip steerable needle then deploys from the tip of the concentric tube and steers through the lung parenchyma, curving around sensitive structures such as large vasculature to reach the nodule. The needle's controller uses an NDI Aurora 6-DOF magnetic tracking probe which is embedded in the tip of the flexure-tip steerable needle. The robot has previously been evaluated only in simulation [5] and in phantom gel [2].

In this paper, we report the first results for the deployment of the robotic lung access system inside an inflated *ex vivo* porcine lung in a CT scanner. We segmented the lung in the CT scan, including bronchial tubes and blood vessels. We steered the needle to avoid obstacles in the parenchyma (i.e., blood vessels and bronchial tubes) and achieved clinically-desirable accuracy in accessing targets near the lung periphery.

MATERIALS AND METHODS

We inflated the *ex vivo* porcine lung using a pressure regulator attached to an endotracheal (ET) tube inserted into the trachea. We connected a T-connector to the ET

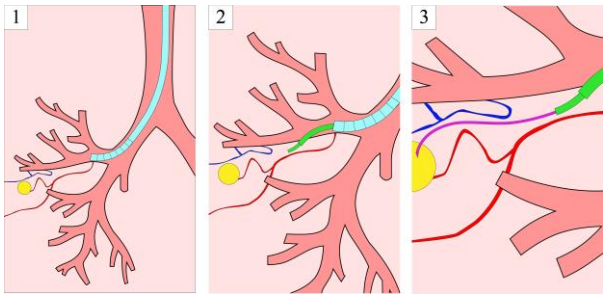

Fig. 2. The robot's three stages: (1) the bronchoscope is inserted into the airway, (2) the concentric tube channel is deployed and exits the bronchial tube, and (3) the steerable needle travels through the parenchyma to the nodule.

tube, capped with a thin membrane to maintain lung inflation, through which we inserted the robot.

We estimated the needle's maximum curvature by inserting the needle without rotation into inflated lung tissue, recording the tip's path using magnetic tracking, and fitting a circle to the path. This curvature value was used in all future experiments.

To conduct the system experiments, we transported the system to the CT scanner, inflated the lung, and acquired a CT scan. We segmented the bronchial tubes and significant vessels in the CT scan using 3D Slicer.

The focus of our experiments was to evaluate the ability of the steerable needle to steer through lung parenchyma and accurately reach targets in the peripheral lung. We evaluated the steerable needle for 6 deployments. For each deployment, we started with the bronchoscope outside the lung and manually guided the bronchoscope into the airway. The concentric tube was then deployed from the bronchoscope's tip to the bronchial tube wall where it pneumatically punctured into the lung parenchyma. Constrained to the reachable workspace of the needle, we chose a point on the surface of the lung as the target by projecting a straight line from the concentric tube and selecting a random offset. Although clinical peripheral targets would be just below the surface, we selected targets on the surface for ease of measurement. We then planned a needle path [5] that avoids the obstacles (i.e., the segmented blood vessels and bronchial tubes) and deployed the steerable needle using closed-loop control [6] to guide the tip of the needle along the planned path. We conducted 3 deployments with obstacle avoidance, and 3 deployments without obstacle avoidance in which we skipped motion planning and applied the automatic controller directly to the target.

RESULTS

We show CT scan slices in Fig. 3 for a deployment of the system. Table 1 shows the accuracy results for the 6 deployments (3 with obstacle avoidance and 3 without). The system used the experimentally determined maximum curvature of 0.498 m^{-1}. The average tip error was 1.97 mm with obstacle avoidance and 1.07 mm without, with average needle insertion length 64.8 mm.

	Tip error (mm)			
	Run 1	Run 2	Run 3	Avg
With obstacle avoidance	0.83	3.27	1.82	1.97
Without obstacle avoidance	0.19	2.47	0.55	1.07

Table 1. Tip error as measured by the magnetic tracker.

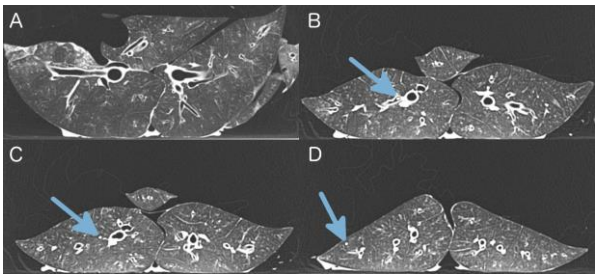

Fig. 3. CT scans of the inflated lung, (A) prior to inserting the robot, (B) prior to the pneumatic puncture, (C) after the pneumatic puncture, and (D) after deployment of the steerable needle to the lung periphery. The blue arrows point to the robot.

DISCUSSION

Our experimental results show that the device is on track to achieve accurate biopsy of clinically-relevant small suspicious nodules, which are defined by the American College of Radiology as being as small as 6 mm in diameter. The results also illustrate the trade-off of obstacle avoidance; the obstacles place constraints on the motion planner and controller that restrict the needle's feasible workspace resulting in slightly larger tip error, but avoiding significant blood vessels is important to reduce the risk of internal bleeding.

The early diagnosis of suspicious lung nodules is integral to combatting lung cancer. To bring definitive diagnosis to a larger percentage of the population earlier in the course of the disease, a new class of medical devices will be required. Our transoral lung access system has the potential to be such a device. While integration into clinical workflows must still be investigated, in this work we showed the ability of the bronchoscope-deployed steerable needle to reach targets with high accuracy in inflated *ex vivo* porcine lungs.

ACKNOWLEDGEMENTS

This work was supported in part by NIH award R21 EB017952 and NSF awards IIS-1149965 and CNS-1305286.

REFERENCES

[1] American Cancer Society. Cancer facts & figure. Technical report, 2016.

[2] P. J. Swaney, et al. Tendons, concentric tubes, and a bevel tip: three steerable robots in one transoral lung access system. In IEEE Int. Conf. Robotics and Automation, pages 5378-5383, May 2015.

[3] N. Kothary, et al. Computed tomography–guided percutaneous needle biopsy of pulmonary nodules: impact of nodule size on diagnostic accuracy. Clinical Lung Cancer, vol. 10, no. 5, pp. 360-363, 2009.

[4] C. Gilbert, et al. Novel bronchoscopic strategies for the diagnosis of peripheral lung lesions: Present techniques and future directions. Respirology, 19(5):636-644, 2014.

[5] A. Kuntz, et al. Motion planning for a three-stage multilumen transoral lung access system. In IEEE/RSJ Int. Conf. Intell. Robot. Syst., pp. 3255-3261, 2015.

[6] D. C. Rucker, et al. Sliding mode control of steerable needles. IEEE Trans. Robotics, 29:1289-1299, 2013.

When will a Robot Outperform a Handheld Instrument? – A Case Study in Beating-Heart Paravalvular Leak Closure

B. Rosa, Z. Machaidze and P. E. Dupont

Pediatric Cardiac Bioengineering, Boston Children's Hospital, Harvard Medical School, Boston, USA

pierre.dupont@childrens.harvard.edu

INTRODUCTION

Paravalvular leaks (PVLs) are a complication of valvular heart surgery, occuring in 5 to 17% of surgically implanted valves [1]. Identifying the leak and deploying a closure device during beating heart surgery is a difficult task that can only be carried out by a highly qualified interdisplinary team of surgeons and imaging experts [2]. Recently, our group introduced a cardioscopic imaging device for beating heart surgery, which was succesfully deployed for septal tissue removal [3]. The tip of the instrument comprises a chip-on-tip digital camera (Awaiba Naneye) and an LED embedded into a silicone optical window. Pressing the optical window against tissue displaces the blood, enabling visualization inside a beating heart. Using this technology, *in situ* high-resolution imaging could be used for precisely locating PVLs for controlled delivery of a closure device.

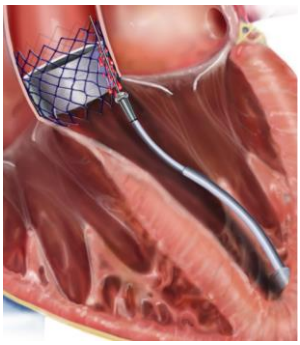

Fig. 1 Aortic PVL repair with a concentric tube robot.

Deploying such a device inside the heart however is complex, and requires a high degree of dexterity for navigating around the valve annulus inside the heart (Fig 1). Moreover, contact with the heart wall should be avoided so as not to cause arrythmias.

While surgical robots, such as those comprised of concentric tubes [4], offer enhanced dexterity with reduced invasiveness, the use of any robot during a surgical procedure can lead to longer set-up times and higher costs compared to similar procedures performed with handheld instruments. Indeed, the question of robot superiority for a specific procedure can often only be addressed after the robot is designed and tested.

This paper attempts to address this question in the context of paravalvular leak closure during the design process by comparing the dexterity and collision avoidance capabilities of three systems: a straight handheld instrument, a manually steerable instrument and a teleoperated robotic instrument. The surgical task and anatomic features are expressed as constraints in an optimization problem, where different robot architectures are optimized and compared. The optimized designs are then fabricated and evaluated in benchtop experiments on a 3D printed heart model.

DESIGN OF CARDIOSCOPIC TOOLS

In order to be able to compare several tool architectures, a constrained optimization framework is developed. Similarly to [4], constrained optimization is used in order to optimize the parameters of each tool in order to carry out the task while respecting anatomy constraints. The anatomical model is segmented from an anonymized patient MRI using the 3D slicer software.

The surgical task is expressed as constraints in the optimization framework. First, a positioning constraint is formulated, which consists of reaching 25 targets evenly spaced on the aortic valve annulus. Second, an orientation constraint is defined as a tip orientation difference being less than 20 degrees with respect to the valve plane normal. Similarly to [4], the structure of the tool/robot is optimized so as to respect the constraints while minimizing contacts with the anatomy.

Three type of architectures are compared. The first one is a simple straight handtool, similar to the one presented in [3] for septal tissue removal. Results show that it is able to reach the points around the valve annulus, but at the cost of significant collisions with the anatomy and of breaking the orientation constraint. The second structure is a steerable handtool. It consists of two concentric tubes, where the innermost tube is fixed and pre-bent, whereas the outer tube is moving over the inner one to straighten it. Optimization results show that a bending radius of 41 mm for the bent section allows it to reach every configuration around the valve annulus with minimal contacts with the anatomy and satisfactory orientations.

Finally, the last architecture is a three-tube concentric tube robot [4]. Optimization results show that the optimal design is with a variable curvature proximal section (minimal bending radius 150 mm, length 72 mm) and a fixed curvature distal section (radius of curvature 41 mm, length 35 mm). Configurations of the steerable handtool and the concentric tube robot reaching towards the targets inside the heart model are shown on Fig.2.

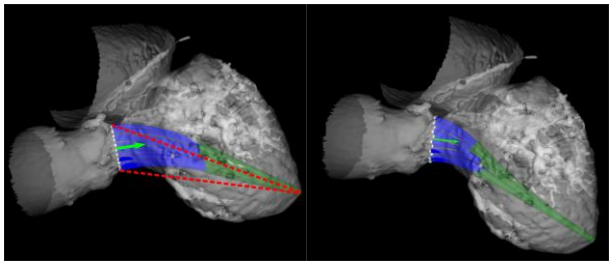

Fig. 2 Access to the valve annulus. Left: handheld instrument with a steerable tip section. Right: concentric tube robot. Green arrow: valve plane normal. Red dotted line: extreme configurations of the straight tool. White points: targets on the valve annulus.

COMPARISON INSIDE A HEART MODEL

In order to validate the proposed designs, a benchtop setup is built. A soft model of the left ventricle of the heart is 3D printed in a soft material (VisiJet CE-NT, 3D systems, USA) and fixed to a support. Through a hole at the apex of the heart devices are inserted and navigated towards the aortic valve. For each experiment, an electromagnetic (EM) tracker (Trakstar, Ascension, USA) is fixed inside the operating channel of the tool to measure the tip position. The experimental setup is depicted on Fig.3.

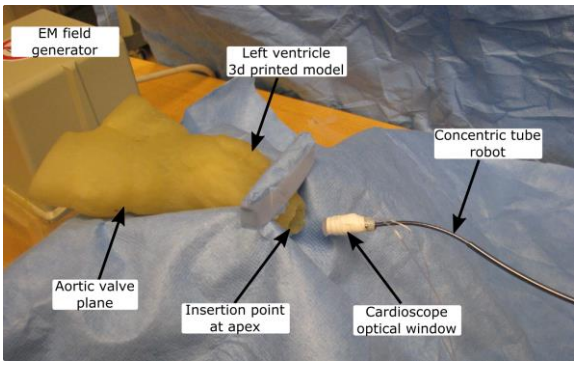

Fig. 3 Experimental setup, with robot about to be inserted.

Fig. 4 shows the results in terms of reachability of the different tools at the annulus. Since the heart model used is not as soft as real heart tissue, it is not possible to reach every point around the annulus with the straight and steerable handtools. This is however representative of the points which would be reached during surgery without touching the anatomy. Moreover, the areas around the annulus that present the highest risk of PVLs [5] can be reached successfully using both devices.

The user is able to steer the robot around the valve annulus satisfactorily, showing good promise for *in vivo* experimentations. However, teleoperating the robot in order to follow the annulus shape is very difficult, mostly because the user has no feedback when touching the anatomy. Therefore in this experiment, points were reached one by one without following a smooth trajectory around the annulus. Smoother navigation is likely to require a large amount of training for the user.

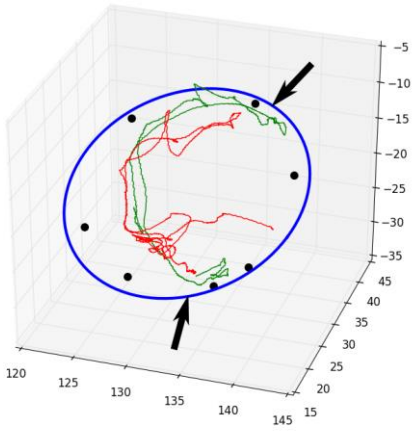

Fig. 4 Comparison of the workspace of the tools at the valve annulus (approximated as the blue ellipse). Red: straight handtool. Green: steerable handtool. Black dots: robot tip positions. Black arrows show zones of highest PVL risk [5].

DISCUSSION

The question of when a robot is truly needed is a recurring question in surgical robotics, mostly because of the costs associated with the introduction of such a device in the operating room. Therefore, identifying the least complex surgical tool able to carry out a given surgical task is a very important question. Through the example of paravalvular leak closure, this paper attempts to address this question, using design optimization before actually building the robot. Though experiments show that the robot is outperforming the handheld devices in terms of reachability, this is also at the cost of loss of haptic feedback, which causes difficulty in steering the robot. *In vivo* experiments are planned in the near future to assess performance of the different devices during a beating heart transapical paravalvular leak closure procedure.

ACKNOWLEDGEMENT

This work was supported by the the NIH under grant R01HL124020.

REFERENCES

[1] K. Maganti, V. H. Rigolin, M. E. Sarano, R. O. Bonow, Valvular Heart Disease: Diagnosis and Management, Mayo Clinic Proc., vol. 85, n. 5, pp: 483-500, 2010.

[2] Kumar, R., Jelnin, V., Kliger, C., *et al.* Percutaneous paravalvular leak closure. Cardiology clinics, 2013, vol. 31, no 3, p. 431-440.

[3] A. Ataollahi, I. Berra, N.V. Vasilyev, Z. Machaidze, P. E. Dupont, Cardioscopic Tool-delivery Instrument for Beating-heart Surgery, IEEE/ASME Trans. Mechatronics, vol. 21, no. 1, pp. 584-590, 2016

[4] C. Bergeles, A.H. Gosline, N.V. Vasilyev, P.J. Codd, P. J. del Nido, P. E. Dupont, "Concentric Tube Robot Design and Optimization Based on Task and Anatomical Constraints", IEEE Trans. Robotics, 33(1):67-84, 2015

[5] Ruiz, C. E., et al. Clinical outcomes in patients undergoing percutaneous closure of periprosthetic paravalvular leaks. J Am Coll Cardiol. 58(21):2210-7, 2011.

A Laparoendoscopic Single-Site Surgery Robot with Stiffness-Controllable Manipulation Arms

J. Wang, S. Wang, X. Ren, Y. Xing

Department of Mechanical Engineering, Tianjin University, China
shuxinw@tju.edu.cn

INTRODUCTION

Laparoendoscopic single-site surgery (LESS) has emerged as an attempt to further enhance cosmetic benefits and reduce morbidity of minimally invasive surgery [1]. Although some articulated manual tools contribute to the operation of LESS, it is still challenging for surgeons to perform LESS due to mirrored hand-eye coordination and "sword fighting" effect among instruments [2]. Several robotic systems [3] were developed to give the surgeons an intuitive way to maneuver the arms and restore triangulation without external instruments clashing. But there are still limitations for the existing platforms, that is, appling continuum segments into the muti-degree of freedom (DoF) manipulation arms could effectively enhance the dexterity of the tool but would loss enough operation force, and using rigid structure could usually provide sufficient operating force but limited flexibility [4].
Therefore, reducing the stiffness of manipulation arm for flexible manauver and supplying sufficient operation force for reliable traction are both necessary for LESS robot. This paper proposes a novel design for LESS robotic system with stiffness-controllable manipulation arms, in which the wrist segment can work under soft status or rigid status depending on the operative need.

MATERIALS AND METHODS

This LESS robotic system is composed of surgeon console part and patient-side cart part. As shown in the Fig. 1, the compact surgeon console consists of a 3D display and two free-motion handles in which the trackSTAR tracking system (NDI Inc., Waterloo, Canada) is employed, the tracker can track the motion of surgeon's hand precisely. The patient-side cart consists of two multi-DoF tendon-driven stiffness-controllable manipulation arms and a 3-DoF stereo vision unit. Each stiffness-controllable arm has a 3-DoF shoulder-elbow segment, a stiffness-controllable wrist segment which is 2-DoF under soft status and 0-DoF rigid bar under rigid status, a 1-DoF self-rotation end tip and a 1-DoF open-close gripper. So, the arm is 7-DoF under soft status while 5-DoF under rigid status. The diameter of the arm is 8.5 mm.
To control the stiffness of the robotic arm, the alloy of several low temperature phase change materials (PCM) is used as the filler material in the continuum wrist segment. In our work, the PCM alloy composed of Ga-In-Bi-Cu, whose melting point is approximately 45 ℃, is firstly prepared and applied as the filler material. The energy exchange system used for heat conduction is designed to convert the PCM alloy between solid phase and liquid phase.

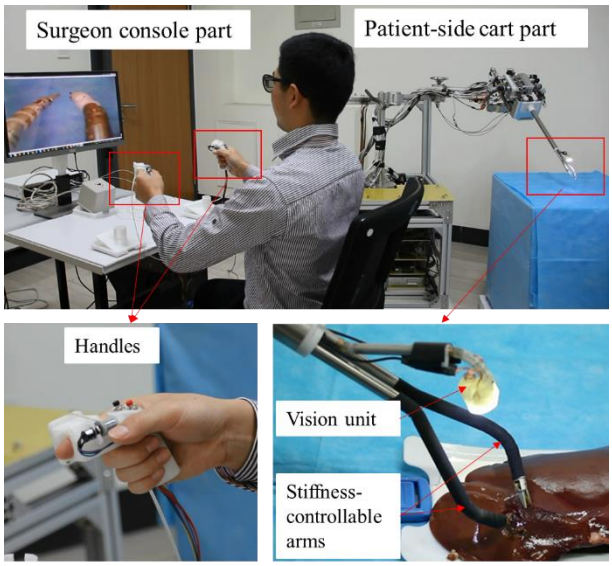

Fig. 1 System overview of the LESS robot.

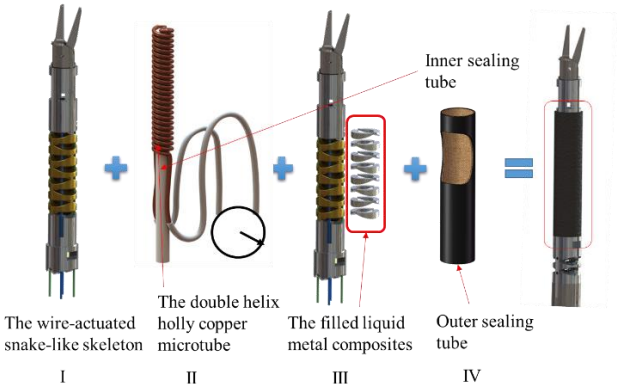

Fig. 2 The construction steps for the stiffness-controllable wrist segment.

The stiffness-controllable wrist is assembled in a layered structure, shown in Fig. 2. The flexible snake-like skeleton is firstly assembled with wire actuation. A double helix holly copper microtube, as the heat conduction part in the energy exchange system, is then added coaxially into the snake-like skeleton, through which high pressure water is circulated via a diaphragm pump. Next, the PCM alloy is filled into the interval of the snake-like skeleton and between it and the copper microtube. Lastly, a thin rubber tube is inserted into the inner of the double helix holly copper microtube and a

thick rubber is coated out the snake-like skeleton to seal this segment. Thus the wrist can be switched between soft status and rigid status when hot or cold water is circulated in the energy exchange system.

RESULTS

To examine the effectiveness of the controllable stiffness of the arm, initial experiments were conducted on a weight-lifting test platform. As shown in Fig. 3 (a), the wrist segment was fixed on the testing platform horizontally as a cantilever beam on the tip of which the payload was applied. A set of weight-lifting experiments in which different weights from 0.2 N to 1.6 N in increments of 0.2N were loaded to the gripper, were then carried out under soft status and rigid status separately. As shown in the Fig. 3 (b), the stiffness of the wrist segment under soft status is about 0.04 N/mm, which shows that the wrist is soft enough for flexible manipulation with wire-actuation, resulting a 2-DoF flexible wrist. The stiffness of the wrist segment under rigid status is about 1.40 N/mm, illustrating that the wrist can be regarded as a rigid bar under rigid status. Furthermore, the payload capability test was performed. Fig. 3 (c) (d) show that the deflection of 155-mm long manipulation arm was less than 20 mm with 8 N payload under rigid status while the deflection of 65-mm long rigid wrist was less than 15 mm with 10 N payload. This results suggest that the manipulation arm could provide enough force during the operation.

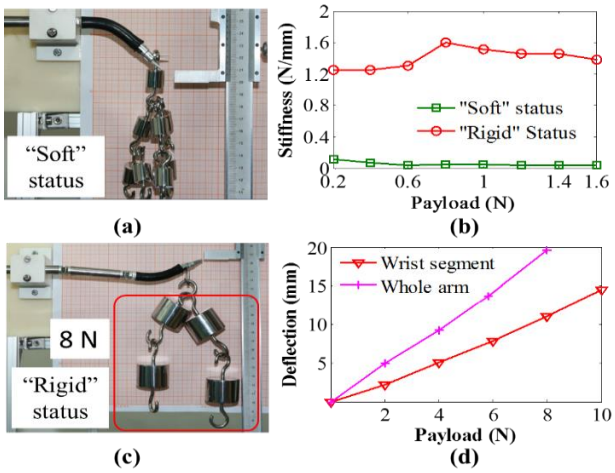

Fig. 3 (a) Stiffness test of the wrist segment; (b) The stiffness results of the wrist; (c) Payload capability test; (d) The payload result of the wrist segment and the whole arm under rigid status.

The switching time between soft status and rigid status was tested as about 16 s under the condition that hot water of 60 ℃ or cold water of 10 ℃ was applied alternately with the circulation rate of 32.23 mL/min.

Then, the ex-vivo surgical experiment of the developed LESS robot was performed on a porcine liver to test the feasibility of clinical application. The goal of this experiment was to remove a small piece of liver tissue from the marked region simulating the surgical resection of diseased tissues from large organ that usually requires large traction force and flexible posture adjustment. In the experiment, the manipulation arms worked under soft status or rigid status during the operation depending on manipulating acquirements. Figure 4 shows different stages of this resection procedure.

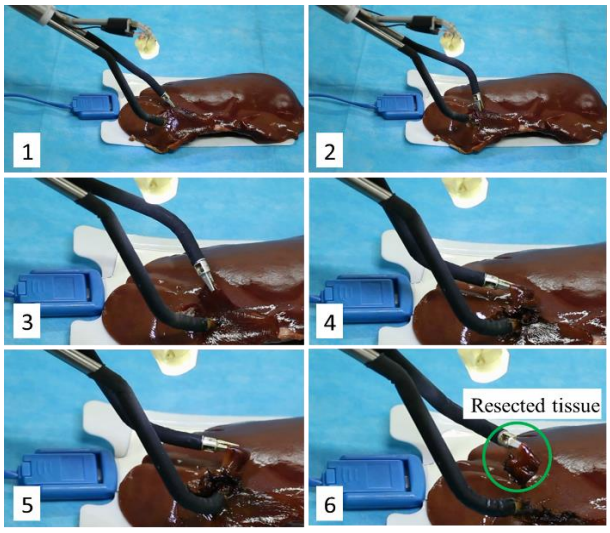

Fig. 4 Capability of performing surgical dissection using the developed LESS robot with stiffness-controllable arms.

DISCUSSION

In this paper, a LESS robotic system with stiffness-controllable manipulator arms was designed and manufactured. The manipulation arms can work under soft status or rigid status by using the PCM alloy of Ga-In-Bi-Cu as the filler material into the sealed wrist. It has been shown that the stiffness of the arm is low enough under soft status for flexible maneuvers to adjust the posture at when it is 7-DoF, and the stiffness of the arm is high enough under rigid status to provide enough strength for reliable traction at when it is 5-DoF.

Future work will focus on reducing the switching time between the two status and conducting more complex ex-vivo and in-vivo experiments to further evaluate the benefits of this LESS robot.

ACKNOWLEDGEMENT

This work is supported by National Natural Science Foundation of China (No. 51290293 and No.51405339) and International S&T Cooperation Program of China (No. 2014DFA70710)

REFERENCES

[1] Canes D, Desai MM, Aron M, Haber GP, Goel RK, Stein RJ, Kaouk JH, Gill IS. Transumbilical single-port surgery: evolution and current status. European urology. 2008 Nov 30;54(5):1020-30.

[2] Xu K, Zhao J, Fu M. Development of the SJTU unfoldable robotic system (SURS) for single port laparoscopy. Mechatronics, IEEE/ASME Transactions on. 2015 Oct;20(5):2133-45.

[3] Vitiello V, Lee SL, Yang GZ. Emerging robotic platforms for minimally invasive surgery. Biomedical Engineering, IEEE Reviews in. 2013;6:111-26.

[4] Autorino R, Kaouk JH. Current status and future directions of robotic single-site surgery: a systematic review. European urology. 2013 Feb 28;63(2):266-80.

Robotic Control of Ultrasound Catheters for Intra-cardiac Visualization

P. M. Loschak[1], A. Degirmenci[1], L. J. Brattain[1,2], C. M. Tschabrunn[3], E. Anter[3], R. D. Howe[1]

[1]*Harvard Paulson School of Engineering and Applied Sciences, USA*

[2]*MIT Lincoln Laboratory, Lexington, USA*

[3]*Harvard-Thorndike Electrophysiology Institute, Beth Israel Deaconess Medical Center, Harvard Medical School, USA*

loschak@seas.harvard.edu

INTRODUCTION

Imaging catheters can provide real time imaging from within the heart, but manual navigation is difficult and requires extensive training. This study focuses on the first examples of automatically pointing ultrasound (US) catheters (frequently referred to as intracardiac echocardiography, or ICE) in *in vivo* animal studies. US catheters feature an US transducer at the tip for imaging cardiac structures. US catheters are manually steered to assist in high-resolution, low-distortion visualization during critical steps of minimally invasive cardiac procedures. Our four degree of freedom (DOF) robotic system automatically aims the imager at target anatomical structures and working instruments (Fig. 1), therefore alleviating the difficulty in manual control [1]. Automatically positioning flexible imaging instruments within the body can improve diagnoses and treatments of medical conditions such as cardiac arrhythmias (atrial fibrillation) while reducing the need for burdensome manual manipulation.

MATERIALS AND METHODS

AcuNav US catheters (Biosense Webster, USA) are the most commonly used clinical ICE catheters. They are manipulated by adjusting the two bending knobs (pitch and yaw), rotating the catheter handle (roll), and inserting/retracting the catheter handle (translation) (Fig. 2). A 4-DOF robot (Fig. 3) was designed to actuate the 4-DOF US catheter [2]. All four joints are actuated by DC motors and controllers (EPOS2, Maxon Motors, Switzerland). The tip position and orientation of the catheter are tracked using electromagnetic (EM) trackers (Ascension Technology Corp., USA).

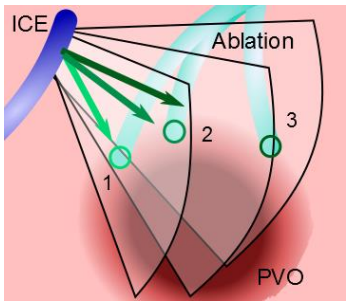

Fig. 1 US imager tracks instrument tooltip.

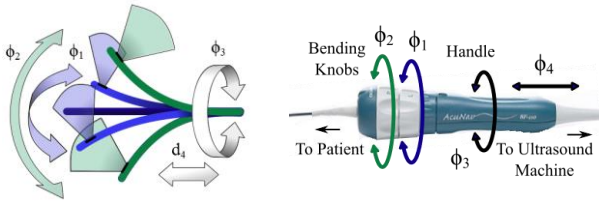

Fig. 2 (*left*) US catheter tip motions resulting from (*right*) US catheter handle joint controls.

The novelty in this work specifically relates to the robust closed-loop control strategy (Fig. 4) [3]. This new strategy rejects disturbances to the body of the catheter. This is important during *in vivo* procedures in which the catheter navigates through tortuous vasculature. Respiratory motion causes disturbances to the catheter body and the base of the bending section, which then disturb the catheter tip pose. The robot must be able to maintain the catheter tip at the desired pose despite these disturbances.

The system measures the catheter bending section tip and base poses to calculate the existing catheter bending section rotation, γ_{curr}. The target pose can be either a relative pose adjustment or based on EM tracking measurements of the angle between the US imaging plane and the target. Achieving the automated motions described in Fig. 1 requires two control goals: (1) maintaining the fixed position, and (2) aligning the US image plane with the target. Inverse kinematic calculations convert the tip space current and target

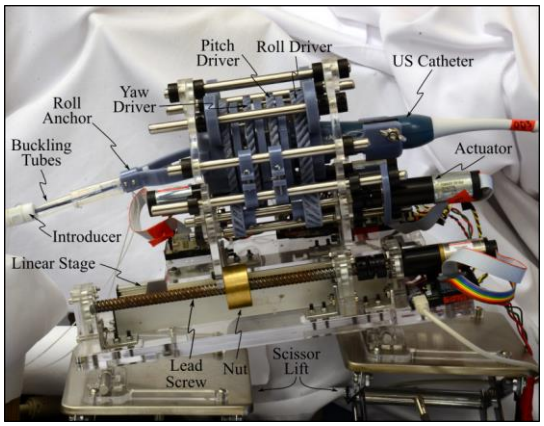

Fig. 3 US catheter mounted in robot.

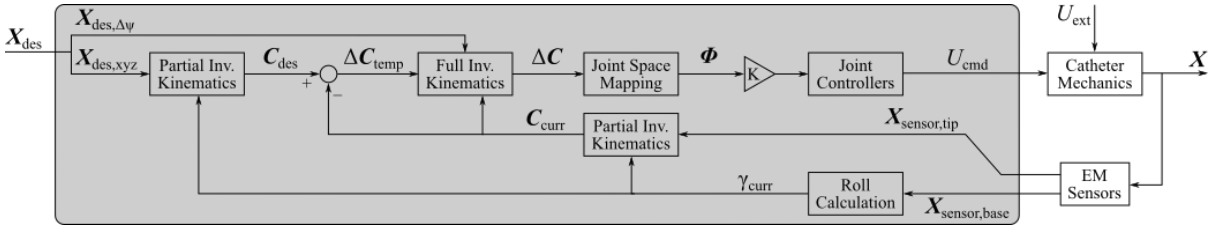

Fig. 4 Position and imager angle control diagram.

poses, X_{des} and X_{sensor}, to configuration space variables, C_{des} and C_{curr}, which describe the bending section curvature and orientation. The difference between the current and target configurations, ΔC, is converted to joint space, Φ. The robot actuates each joint by sending commands to the motor controllers, which run onboard servo loops at 1 kHz. The controller navigates the catheter to the target pose. US images are collected when the tip pose converges to allowable error thresholds.

RESULTS

The robotic catheter navigation system was tested through *in vivo* porcine experiments to demonstrate tip positioning, US imager orientation, and disturbance rejection. The clinician manually introduced the US catheter through the femoral vein to a safe location within the right atrium of the heart. The US catheter handle was then attached to the robot and switched to autonomous motion mode. The US imager was rotated about the catheter axis while maintaining the same safe position in the right atrium. This required active manipulation of all four DOF. During 4D volume reconstruction tests a sequence of 80 2° US imager adjustments was given as target step inputs. The resulting motions had mean absolute errors 2.0 mm (σ = 1.1 mm) and 0.65° (σ = 0.51°). Ramp disturbances

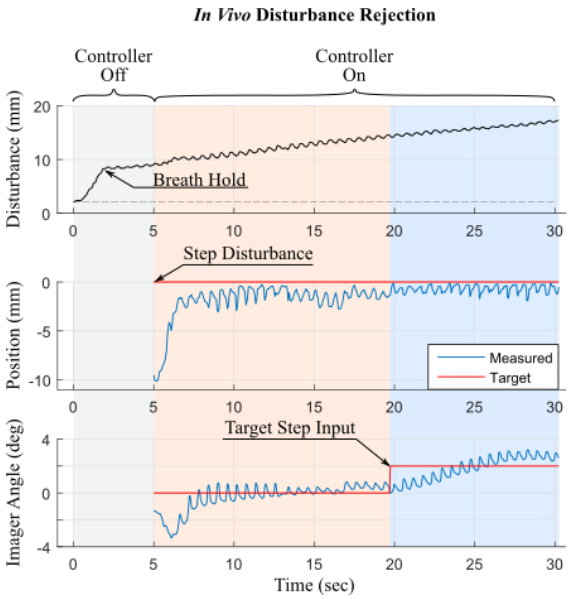

Fig. 5 *In vivo* tests: (*Top*) Ramp input disturbances to the catheter body are rejected. (*Middle*) The catheter tip remains at the fixed point. (*Bottom*) Step input angles command the US imager to rotate towards the target.

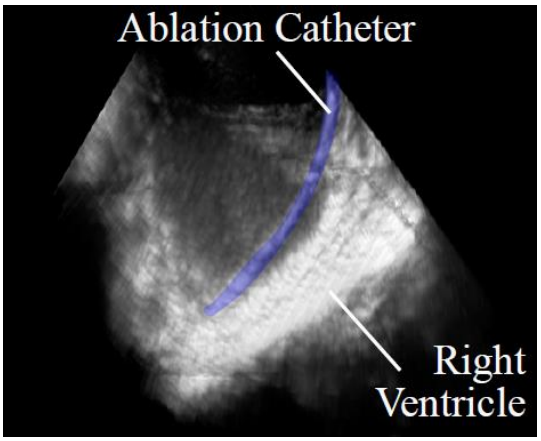

Fig. 6 *In vivo* instrument tracking (false color applied).

(Fig. 5) due to respiratory motion on breath-hold were rejected by the controller. The system was able to maintain its pose with mean absolute errors 1.1 mm (σ = 0.7 mm) and 0.44° (σ = 0.31°). An ablation catheter (Fig. 6, highlighted in blue false color) in the right ventricle was imaged by the US catheter system. The sequence of 2D US images was reconstructed into 3D and 4D volumes using the method described in [4].

DISCUSSION

Experimental results from *in vivo* studies demonstrate a system for automatically steering US imaging catheters to provide better clinical visualization during procedures. Future work includes actively steering to compensate for respiratory motion disturbance. The robot system for controlling US imaging catheters has the potential to improve workflow, enhance situational awareness, and improve outcomes in a range of minimally invasive procedures.

REFERENCES

[1] Loschak PM, Brattain LJ, Howe RD. Automated pointing of cardiac imaging catheters. ICRA 2013; 5774-5779.

[2] Loschak PM, Degirmenci A, Tenzer Y, Tschabrunn CM, Anter E, Howe RD. A 4-DOF robot for positioning ultrasound imaging catheters. JMR 2015.

[3] Degirmenci A, Loschak PM, Tschabrunn CM, Anter E, Howe RD. Compensation for unconstrained catheter shaft motion in cardiac catheters. ICRA 2016.

[4] Brattain LJ, Loschak PM, Tschabrunn CM, Anter E, Howe RD. Instrument tracking and visualization for ultrasound catheter guided procedures. MICCAI workshop AECAI 2014.

This material is based upon work supported by the Assistant Secretary of Defense for Research and Engineering under Air Force Contract No. FA8721-05-C-0002 and/or FA8702-15-D-0001. Any opinions, findings, conclusions or recommendations expressed in this material are those of the author(s) and do not necessarily reflect the views of the Assistant Secretary of Defense for Research and Engineering.

Robot-Assisted Approach with Insufflation for Minimally Invasive Multilevel Posterior Vertebral Exposure: A Proof-of-Concept Study with Applicability to Scoliosis Correction

J. J Howard[1], J. Abinahed[2], N. Navkar[2], A. Al-Ansari[3], D. L. Sigalet[1], A. E. Zarroug[1]

[1]Department of Surgery, Sidra Medical and Research Center, Qatar

[2]Qatar Robotic Surgery Centre, Qatar Science and Technology Park, Qatar

[3]Urology Department, Hamad Medical Corporation, Qatar
jhoward@sidra.org nnavkar@qstp.org.qa

INTRODUCTION

Standard surgical techniques for multilevel posterior spinal procedures involve extensive soft tissue disruption leading to pain, increased length of stay, and disfiguring scars. There is a need for a minimally invasive technique that provides unobstructed access to the posterolateral spine while minimizing soft tissue injury. Minimally invasive access to deep tissues has been successfully achieved using laparoscopic techniques and, more recently, robot assistance. For posterior spinal procedures, only one previous study [1] has investigated the use of robot assistance and none have explored its use for minimally invasive access over multiple levels.

In this work, using an ovine model, a proof-of-concept study investigating the use of the da Vinci surgical robot to perform minimally invasive, multilevel access to the posterolateral spinal elements was performed. To support the maintenance of a submuscular tunnel volume for surgical working room, the exposure was supported with carbon dioxide insufflation according to laparoscopic principles.

MATERIALS AND METHODS

An adult Australian Merino sheep specimen underwent minimally invasive surgical exposures of the posterior spinal elements over multiple vertebral levels. The da Vinci S Surgical system was used for robot assistance during the experimental trials to aid in the development of a submuscular tunnel for posterolateral spinal access. A mid-thoracic, caudally-directed 5 cm paramedian incision was made with subsequent blunt dissection via an intramuscular 'Wiltse' approach to the posterior spinal elements (facet joints, laminae). To support the maintenance of a sub-paraspinal tunnel volume for surgical working room, a single port 'laparoscopic' technique was utilized. To facilitate the development of the volume, carbon dioxide insufflation (20 mmHg) was used with seal maintained via a subfascial Alexis Wound Retractor [2] and glove port as shown in Figure-1. Electrocautery facilitated the dissection and volume expansion. The length of submuscular tunnel, number of vertebrae exposed, and associated technical challenges were recorded.

RESULTS

From the initial surgical incision, we were able to develop a submuscular tunnel of 12.5 cm for a total distance of 17.5 cm (Figure-2). Through this tunnel, subperiosteal dissection of five vertebrae was easily achieved with successful integration of carbon dioxide insufflation to support the surgical working room. Ready vertebral anatomic landmark exposure (facet joints, laminae) was achieved for all 5 levels. When attempting the second (lumbar-based, cranially-directed) tunnel meant to be contiguous with the first, an increased frequency of robotic arm collisions secondary to spinous process blocking, in this lordotic segment of the spine, made it difficult to connect the distal to proximal tunnel.

CONCLUSION

This study demonstrated the feasibility of achieving robotic-assisted minimally invasive access to the posterolateral spine over multiple vertebral levels - as is required for scoliosis correction - using carbon dioxide insufflation to facilitate the exposure. Difficulties encountered with respect to robotic arm collisions will likely be mitigated with newer single port robots that are better suited for different types of spinal alignments (e.g. kyphosis).

REFERENCES

[1] Ponnusamy K, Chewning S, Mohr C. Robotic approaches to the posterior spine. Spine.2009;34(19):2104 –2109.

[2] Greenberg JA. Alexis® OTM C-Section Retractor. Reviews in Obstetrics and Gynecology.2008;1(3):142-143.

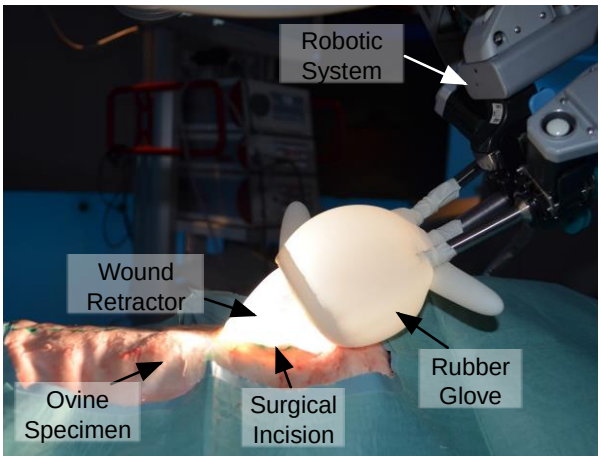

Fig. 1 Robotic setup showing effective seal with insufflator.

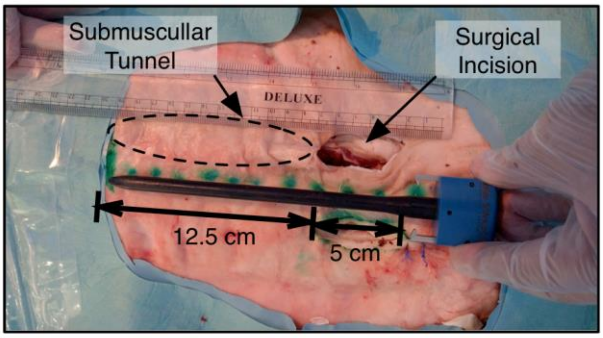

(a)

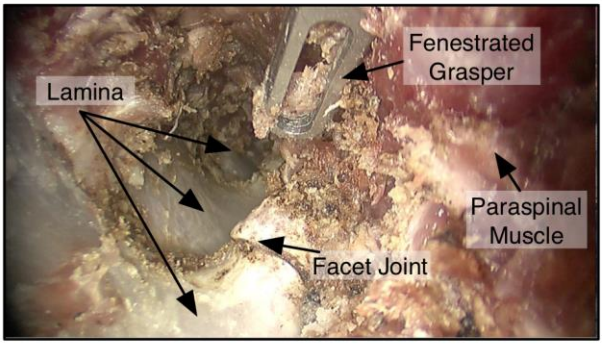

(b)

Fig. 2 (a) Submuscular tunnel development was achieved to a distance of 12.5 cm from the 5 cm surgical incision; 17.5 cm distance in total. (b) View of submuscular tunnel from da Vinci console.

Expanding Image Guidance into New Surgical Specialties – Initial Experience in Gynaecology Oncology

J. Dilley[1], P. Pratt[1], E. Mayer[1], A. Rockall[2], J. Yazbek[3], M. Kyrgiou[3], A. Darzi[1]

[1]Department of Surgery and Cancer, Imperial College, London, UK

[2]Department of Radiology, Hammersmith Hospital, London, UK

[3]Department of Gynaecology Oncology, Hammersmith Hospital, London, UK

j.dilley@imperial.ac.uk

ABSTRACT

Minimal access surgery has become the established approach in gynaecological surgery providing many benefits compared with the open route. However one disadvantage is a reduction in haptic feedback, which is reduced in laparoscopic surgery and currently entirely absent in robotic surgery. Image guidance is one technique that can compensate for this deficit by increasing the visual information provided to the surgeon as well as revealing subsurface anatomy. This has been developed and used clinically in the field of urology (Hughes-Hallett et al. [1]). We report on our initial experience using this surgical tool in the specialty of gynaecology.

Under an existing ethical protocol (REC reference 07/Q0703/24), informed and written consent was obtained from a 26 year old female patient diagnosed with presumed Stage 1b1 cervical cancer who required laparoscopic excision of three suspicious lymph nodes lymph nodes to complete staging.

The patient underwent standard segmental imaging as well as diffusion weighted MRI and PET CT. A preoperative MRI sequence was segmented manually using ITK-SNAP to combine the relevant information derived from the different imaging modalities. This allowed the spatial relationship of the three nodes in relation to surrounding anatomy to be displayed. These mesh-based models were complemented by real-time volumetric renderings of the raw DICOM data, provided by the Fovia HDVR® engine.

Fig. 1 Photo of 3D display and surgeons in theatre wearing 3D glasses (left); and intuitive iPad user interface (right).

The surgeon viewed the 3D images on a monitor whilst wearing 3D glasses prior to and during the procedure. The view was manipulated using an iPad. Image guidance depicting important anatomy and stages of the operation could be saved and immediately shown when needed (Figure 1).

All three nodes were taken with no intraoperative or postoperative complications (Figure 2). Surgeons' feedback was positive; it increased both their confidence in targeting the abnormality and their awareness of the anatomical location of surrounding structures. Histology confirmed lymph nodes that were all negative.

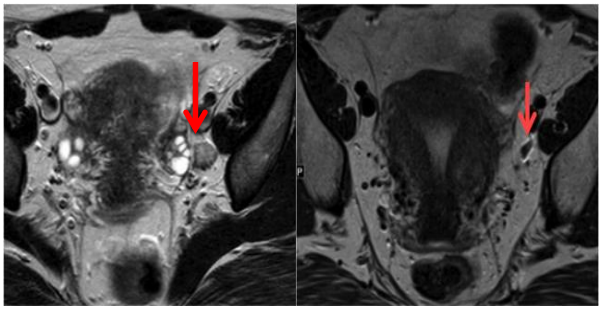

Fig. 2 MRI showing presence of node before surgery (left) and absence after surgery (right).

This report highlights that image guidance can be and has the potential to be applied to multiple surgical specialties. Future studies will need to explore the potential barriers preventing ongoing uptake and integration of this exciting surgical tool.

ACKNOWLEDGMENTS

The authors are grateful for support from the Hamlyn Centre, Fovia Inc., and the NIHR Biomedical Research Centre funding scheme.

REFERENCES

[1] Hughes-Hallett, A. et al., 2014. Image guidance for all - TilePro display of 3-dimensionally reconstructed images in robotic partial nephrectomy. Urology, 84(1), pp.237–242. Available at: http://dx.doi.org/10.1016/j.urology.2014.02.051.

The Feasibility of the da Vinci® System and Development of a Pin Jointed Wrist for Infant Cleft Palate Surgery

D. Podolsky[1,2], D. Fisher[2], K. Wong[2], T. Looi[1], J. Drake[1], C. Forrest[2]

[1]Center for Image Guided Innovation and Therapeutic Intervention, The Hospital for Sick Children, Canada

[2]Department of Plastic and Reconstructive Surgery, The Hospital for Sick Children, Canada

dale.podolsky@mail.utoronto.ca

INTRODUCTION

Cleft palate is the most common congenital anomaly requiring surgical repair at 6-12 months of age [1]. The procedure is challenging due to the delicate tissue as well as the limited access and visualization posed by the small confined infant oral cavity. A surgical robot offers the advantage of improved access, visualization and precision. Therefore, cleft palate repair is the ideal environment for robotic application.

Cleft palate surgery requires six degrees-of-freedom (DOF) to perform the majority of the surgical steps. Recently, the da Vinci® (6 DOF and gripping) was used to perform a limited muscular dissection in a series of 10 patients for cleft palate repair in infants [2].

We performed an assessment of the latest da Vinci® systems for cleft palate repair to assess feasibility and to guide development of a more optimal instrument wrist for cleft palate surgery using a high-fidelity cleft palate phantom as a test bed.

MATERIALS AND METHODS

A robotic cleft palate repair was completed with the da Vinci® Si with 5 mm instruments and Xi with 8 mm instruments. For each step of the procedure, the number of collisions and ease of instrument excursion was compared by visual assessment at the time of the procedure and endoscopic video recordings.

Performance limitations from the da Vinci® testing guided development of a novel wrist mechanism with the following requirements: (1) minimize total link length for compact articulation within the infant oral cavity, (2) minimize the number of components to facilitate miniaturization, (3) three DOF (pitch, yaw, roll) with gripping, (4) couple to the da Vinci® platform to provide the remaining DOF, and (5) 5 mm diameter or less. The novel wrist kinematics were developed and utilized to simulate its workspace. The simulated workspace was placed within the cleft palate phantom oral cavity computer model and compared to the 8 mm EndoWrist® instruments for size comparison.

A prototype was 3D printed using Nanotool material and manually actuated to assess range of motion using an NDI Aurora tip tracker. The new wrist was positioned and oriented for the muscle release of a repair and the proximity to the oral aperture compared to the current EndoWrist® instruments.

RESULTS

The smaller total link lengths (19 mm) of the 8 mm EndoWrist® instruments facilitates more compact articulation than the 5 mm instruments (23.5-26 mm). This results in less frequent collisions and smoother instrument excursion. However, collisions still occur with the 8 mm instruments especially during close up visualization and manipulation due to their larger size.

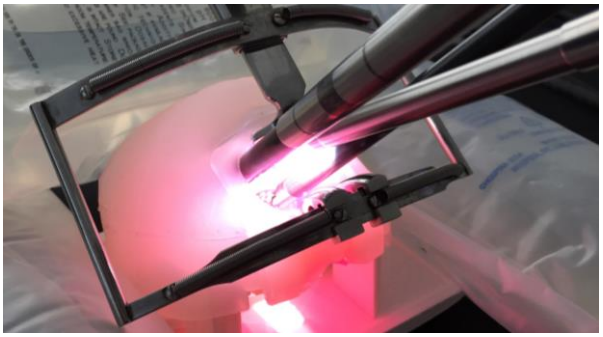

Fig. 1: da Vinci® Xi with 8 mm instruments performing a cleft palate repair on the cleft palate phantom.

Building on the 8 mm EndoWrist® design, the novel wrist presented is 5 mm in diameter and has a 13 mm total link length (Fig. 2 and Table 1). Guide channels in the first link (Fig. 2) reduce the number of overall main components to four while ensuring a maximum cable bending radius during wrist pitch.

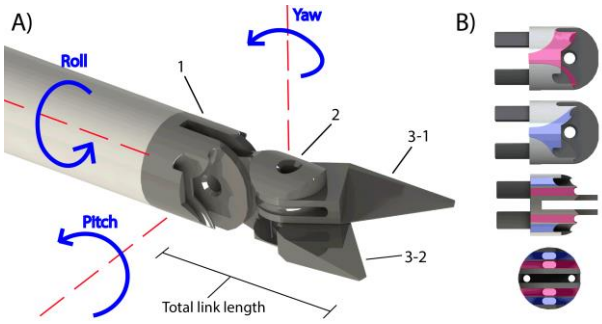

Fig. 2: A) Wrist mechanism illustrating four main components with roll, pitch, yaw and grip motion. B) Link 1 with channels that guide cables for each of Link 3-1 (pink highlights) and Link 3-2 (blue highlights).

Fig. 3 illustrates the workspace of the new wrist in comparison to the current da Vinci® 8 mm instruments and within the cleft palate phantom computer model. As

can be seen, the workspace of the new wrist is smaller in size and better matched for the infant oral cavity. When operating at the hard-soft palate junction, the new wrist workspace fits entirely within the oral cavity (Fig. 3 C and D).

Table 1. Wrist Joint Range of Motion

Joint Limits	
Roll	$[-\pi, \pi]$
Pitch	$[-\frac{\pi}{2}, \frac{\pi}{2}]$
Yaw	$[-\frac{\pi}{2}, \frac{\pi}{2}]$

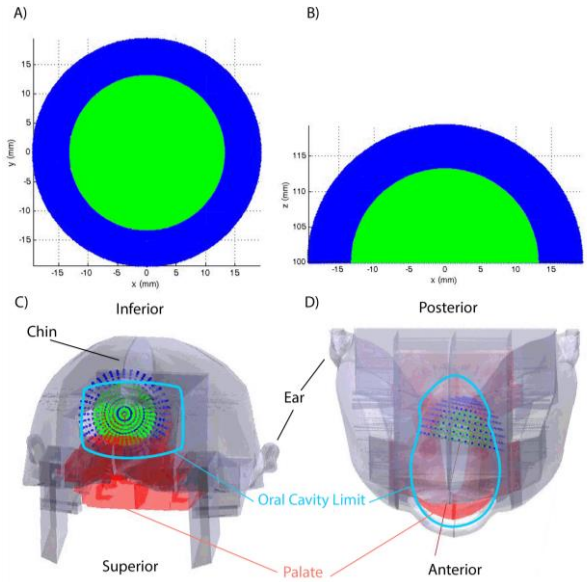

Fig 3. A) X-Y and B) X-Z view comparing the new wrist (green) to the 8 mm EndoWrist® (blue) workspace outer limit through roll $(-\pi, \pi)$, pitch $(-\frac{\pi}{2}, \frac{\pi}{2})$ and yaw fixed. C) Perspective view of cleft palate simulator (similar to Fig. 1) and D) planar view showing the new wrist workspace compared to the 8 mm EndoWrist® within the oral cavity (blue outline). The new wrist workspace (green) fits within the cavity at a specific point (left hard-soft palate junction).

The first prototype can be seen in Fig. 4 A), B) and C), illustrating the cable routing. The performance of the wrist was assessed by manually pulling the cables to move the wrist through its full range of motion. Fig. 4 D) shows a three-dimensional representation of the outer limits of the workspace with yaw fixed. The first link channels guide the cables as the wrist is pitched. Fig. 5 compares the clearance of the instrument shaft to oral aperture for a maneuver in cleft palate surgery.

DISCUSSION

Currently available clinical robotic systems are sub-optimal for the infant oral cavity as demonstrated by testing the latest da Vinci® systems for cleft palate repair. Continuum robots such as concentric tube designs are more readily miniaturized. However, they lack the dexterity required to perform complex surgical tasks within tight workspaces. Similarly, multi-backbone designs, such as the 5 mm EndoWrist® have longer total link lengths to achieve acceptable joint range of motion. Classical pin jointed designs provide smaller workspaces at the expense of increased complexity.

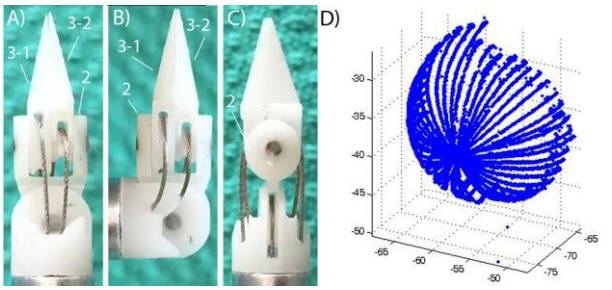

Fig 4. Wrist cable routing illustrating cables running through channels in first link to components 3-1 and 3-2 with pitch at 0° and B) 90° and C) cables routing to link 2. Experimental workspace through roll $(-\pi, \pi)$, pitch $(-\frac{\pi}{2}, \frac{\pi}{2})$ with yaw fixed.

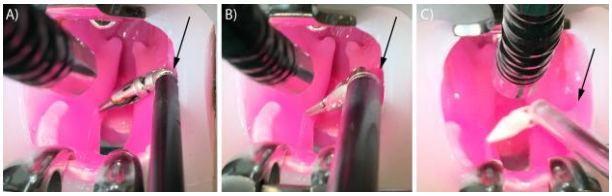

Fig 5. Comparison of clearance between instrument shaft and oral aperture of the A) 5 mm and B) 8 mm EndoWrist® instruments and C) the new wrist design when touching the left palate with an orientation typical for muscular release.

The new wrist presented is less complex, has the required degrees of freedom, is more readily miniaturized and minimizes total link length to accommodate complex tasks within confined surgical environments. The primary reason for this is the design of a single component (link 1) to guide the cables. The first prototype at 5 mm in diameter has a total link length of 13 mm with an outer limit workspace that is optimized for the infant oral cavity. A review [3] demonstrates that at 5 mm, this is amongst the smallest diameter pin jointed wrists that contains the presented range of motion and small total link length. The use of guide channels has previously been described, but in a different configuration [4].

The main limitation of this design is the introduction of additional friction forces within the channels that likely increases the tension requirements of the cables to achieve a given tip force. Future work will further miniaturize this design to 4 and 3 mm diameter fabricated in metal. This will allow characterization of cable tension and the wrist force capability.

REFERENCES

[1] Losee JE, Kirschner RE. Comprehensive Cleft Care: The McGraw-Hill Companies; 2009.

[2] Nadjmi N. Trans Oral Robotic Cleft Surgery. Cleft Palate Craniofacial J. 2015 June.

[3] Catherine J, Rotinat-Libersa C, Micaelli A. Comparative Review of Endoscopic Devices Articulations Technologies Developed for Minimally Invasive Medical Procedures. Applied Bionics and Biomechanics 2011:8:151-171.

[4] Burbank W. Four-cable wrist with solid surface cable channels. Intuitive Surgical Operations, Inc. U.S. Patent 8,821,480. 2008 July.

A Method for Installing FBG Sensors inside Surgical Robotic Instruments

R. Xu[1], A. Escoto[2], K. S. Shahzada[1], C. Ward[2], R. V. Patel[1,2,3]

[1]Dept. of Elec. and Comp. Eng., Western University, Canada

[2]Canadian Surgical Technologies and Advanced Robotics (CSTAR), Lawson Health Research Institute, Canada

[3]Dept. of Surgery, Western University, Canada

rxu25@uwo.ca

INTRODUCTION

Metallic foil strain gauges are widely used in sensorizing robotic surgical instruments for research applications, due to their small size with respect to commercially available force/torque sensors [1], [2]. However, these gauges offer poor signal-to-noise ratio, require constant calibration and cannot survive sterilization procedures without specialized protective coating.

Fiber Bragg Grating (FBG) sensors overcome these problems and have become a good alternative to metallic foil strain gauges in surgical robotic applications [3], [4]. The authors have previously sensorized a da Vinci® surgical instrument with FBG sensors [5] that provides force measurements at 1 kHz rate with high resolution. A drawback of this design is that the sensors are prone to damage. In [6], it is suggested to embed the FBG sensors into engraved slots on the instrument shaft. This method provides better protection to the sensors; however, it modifies the mechanical design of the instrument, reduces its structural rigidity, and adds machining costs. Furthermore, the interaction between the trocar and the instrument shaft may scrape off the adhesive or protective coating used in installing the FBG sensors.

In this paper, a novel method for installing FBG sensors on the interior of a da Vinci® surgical instrument (Intuitive Surgical, Inc., Sunnyvale, CA, USA) is proposed and validated. Four FBG sensors (Technica S.A, Beijing, China) were installed on the inner surface of the instrument using a custom template. These sensors are well protected, capable of providing accurate force sensing and do not interfere with the functioning of the instrument. Fig. 1 illustrates the sensorized instrument mounted on the da Vinci® surgical system. The proposed technique does not require expensive components or special manufacturing facilities, and it therefore ideal for use in research labs in order to sensorize existing instruments for projects related to robot control, surgical training and skills assessment.

MATERIALS AND METHODS

This section describes the method for sensorizing a da Vinci® instrument without major modifications to the tool. A Large Needle Driver da Vinci® instrument was disassembled as shown in Fig. 2(a). The grasper and the pull rods were removed from the tool shaft to allow the installation of the sensors. Two cross-sections of the tool shaft were sensorized with optical fibers that both contained two FBGs. Previous work demonstrated that

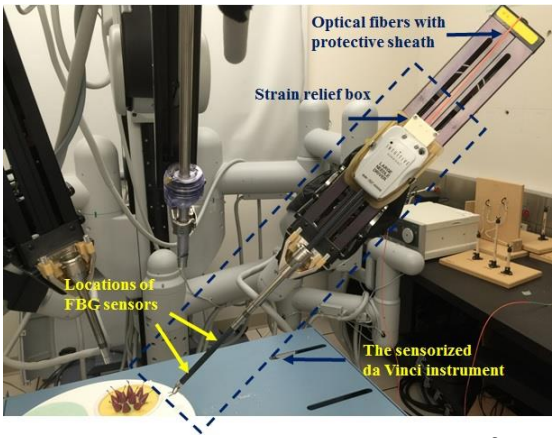

Fig. 1 Sensorized instrument mounted on a da Vinci® robot.

this sensor layout was able to provide accurate measurement of lateral forces, independent of the location of the forces and orientations of the instrument tip. Disturbances caused by axial force, bending and torsional moment were mostly eliminated [5]. If the two-cross sections experience temperature changes, then the thermal effects on FBGs can be compensated as well.

A template was designed as a key component to facilitate the installation process (Fig. 2(b)). This template has three main functionalities: *1) A sensor alignment guide*: to measure forces in orthogonal directions, the optical fibers should be installed 90° apart around the instrument shaft. This template aligns the FBGs and separates the

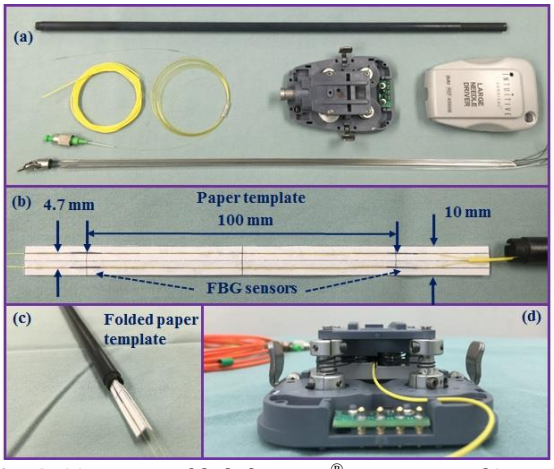

Fig. 2 (a) Disassembled da Vinci® instrument; (b) paper template; (c) folded paper template (d) rear view of the sensorized instrument after reassembly.

fibers for a certain distance in order to place the sensors at the desired locations on the inner surface (Fig. 2(b)); *2) An adhesive carrier*: to ensure proper bonding of the fibers to the inner surface, an adequate amount of adhesive (10810, Elmers Products Inc., Westerville, OH, USA) needs to be applied. The template provides a flat and wide area allowing for insertion of the fibers in the shaft while keeping the adhesive in place (Fig. 2(c)). Once the fibers are in the desired location, a rigid rod is used to push the paper against the inner surface, ensuring the fibers are in full contact with the shaft. *3) Protective layer*: the template permanently covers the FBG sensors inside the tool shaft, preventing damage from the pull rods during instrument reassembly and robotic manipulation.

Calibration of the parameters for force sensing uses the same procedure as that described in [5]. Two experiments were conducted to assess the performance of the sensorized instrument. The first experiment assessed the effectiveness of the sensors to measure force. A force/torque sensor (Nano17, ATI Industrial Automation, Apex, NC, USA) was mounted on the tip of the instrument (Fig. 3). Time varying forces were manually applied on the handle and the readings from both sensing modalities were recorded. The second experiment determined the resolution of the sensor. A set of weights were hung at the tip of the instrument to determine the smallest distinguishable increment that can be measured.

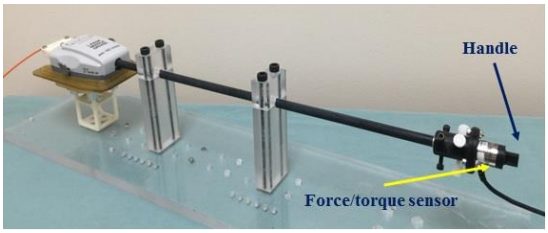

Fig. 3 Experimental setup for evaluating the performane of force sensing.

RESULTS

Fig. 4 shows the force measurements from the force/torque sensor and the FBG sensors. For the *x* and *y* directions (in the frame of the force/torque sensor), both sensing modalities presented very similar measurements at low and high frequencies. The RMS errors were 0.09 N in the *x* direction and 0.08 N in the *y* direction. The resolution of this sensing technology is shown in Fig. 5. The minimal distinguishable increment is 10 gf (0.098N) at 1 kHz sampling rate (Fig. 5(a)). This resolution can be improved to 5 gf (0.049N) using the built-in averaging filter (10 times) of the interrogator (SM130, Micron Optics, Atlanta, GA, USA) as shown in Fig. 5(b).

DISCUSSION AND CONCLUSION

In this work, a novel technique for integrating FBG sensors on the interior of robotic surgical instruments was presented. A custom template allows accurate placement of the FBG sensors and protects them from damage during re-assembly of the instrument and also during

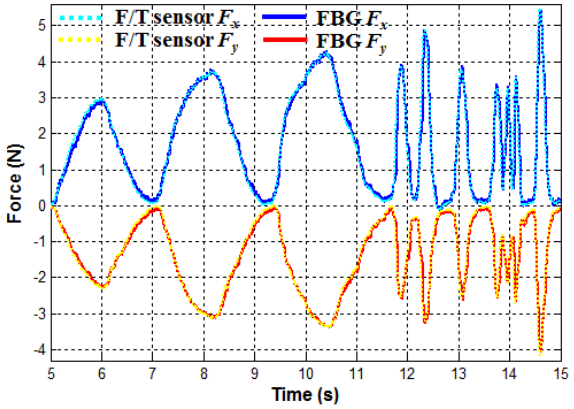

Fig. 4 Comparision of the force measurements from the force/torque sensor (dot) and the sensorized instrument (solid).

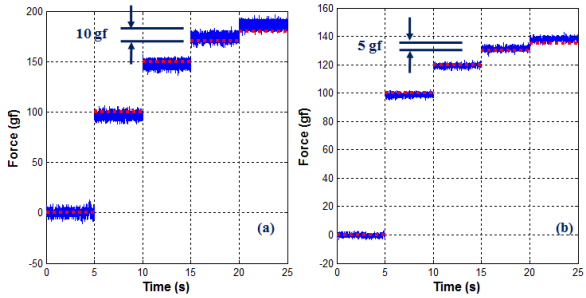

Fig. 5 Comparision of the theoretical force values (red) and the measured values from the sensorized instrument (blue).

normal instrument use. The proposed technique was demonstrated on a standard da Vinci® instrument, showing that only minor modifications are necessary that do not affect how the instrument is interfaced with and controlled by a da Vinci® robot. Furthermore, validation experiments with this instrument show that accurate force measurements can be achieved at a sampling rate of 1 kHz.

Our ongoing research focuses on using this force sensing technology for hybrid position and force control, impedance control, haptics-enabled tele-operation and approaches for surgical skills assessment.

REFERENCE

[1] C.E. Reiley, et al., "Effects of visual force feedback on robot-assisted surgical task performance." *J. Thorac. Cardiovasc. Surg.*, vol. 135 no. 1, pp.196-202, 2008.

[2] A. Talasaz, A.L. Trejos, S. Perreault, H. Bassan, and R.V. Patel, "A Dual-Arm 7-Degrees-of-Freedom Haptics-Enabled Teleoperation Test-Bed for Minimally Invasive Surgery", *ASME J. Med. Devices*, 8(4), 041004 (2014).

[3] R. Xu, et al., "Curvature, torsion and force sensing in continuum robots using helically-wrapped FBG sensors," *IEEE Robot. Autom. Letters*, 1(2):1052-1059, 2016.

[4] X. He, et al., "A submillimetric 3-dof force sensing instrument with integrated fiber Bragg grating for retinal microsurgery," *IEEE Trans. Biomed. Eng.*, 61(2):522–534, 2014.

[5] K.S. Shahzada, A. Yurkewich, R. Xu, and R.V. Patel. "Sensorization of a surgical robotic instrument for force sensing." *SPIE BiOS*, 2016, pp. 97020U.

[6] S.J. Blumenkranz, D.Q. Larkin, "Force and Torque Sensing for Surgical Instruments", 20070151390, US (2007)

Comparison of Soft Tissue, Bony, and Conservative Procedures used to Improve Patellar Kinematics and Contact Pressures: A Finite Element Study

M. Ingels[1], R. Summers[1], A. Amerinatanzi[1], A. Gupta[1], A. Agarwal[1], V. Goel[1], T.E. Hewett[2], K. Deep[3]

[1]Engineering Center for Orthopaedic Research Excellence (E-CORE), University of Toledo, USA

[2]Mayo Clinic, Rochester, USA

[3]Golden Jubilee National Hospital Glasgow, UK

mrkdeep@gmail.com

INTRODUCTION

Maltracking of the patella can cause anterior knee pain and patellar instability. It is widely accepted that maltracking causes elevated patellofemoral contact pressures resulting in anterior knee pain and subsequent arthrosis [1, 2]. Although most patients with patellofemoral symptoms experience improvement with conservative treatment, a subset of patients fail to respond to such interventions and ultimately require surgery. Surgeons can perform a variety of soft tissue releases and bony procedures to address patellofemoral tracking pathology in conjunction with conservative treatments such as strengthening of the vastus medialis. Specifically, lateral retinacular release and tibial tuberosity osteotomies (TTO) are commonly used to correct abnormal patellar tracking. However, there is little experimental evidence regarding patellar kinematics and contact mechanics after these realignment procedures. As some TTO procedures are difficult, such as anteriorization, experimental insights may benefit clinicians to help in understanding the potential outcomes of using a combination of TTO, soft tissue release and conservative intervention. The objective of this study was to use finite element analysis to evaluate the effects of tibial tuberosity osteotomies on patellar kinematics and patellofemoral joint (PFJ) contact pressure. Finite element analysis provides a more robust way to approach various procedures used to treat certain pathologies due to the reusability of the models (i.e., one model can be used in hundreds of simulations). Through proper validation, these models are powerful predictive tools for in-vivo surgical methodologies.

METHODS

A lower extremity finite element (FE) model was developed from magnetic resonance imaging (MRI) and computed tomography (CT) images of a female subject with no history of knee injury. 3D geometries of hard and soft tissues were digitized using Mimics v15.0 (Materialise, Leuven, Belgium). Geometries were converted into solid 8-node hexahedral elements for the patella, ligaments (ACL, MCL, LCL, and PCL), and menisci. The geometries of the femur, fibula, and tibia were constructed with an outer layer of wedge C3D6 elements for cortical bone and tetrahedral C3D4 elements for cancellous bone, while cartilage utilized tetrahedral C3D4 elements. Completed meshes were imported into ABAQUS 6.14 (SIMULIA, Providence, RI, USA) wherein capsules, muscles, tendons, and remaining ligaments were simulated using uniaxial truss elements. The material properties of the ACL, PCL, and MCL were modeled with hyperelastic properties following the Holzapfel-Gasser-Ogden model. Material properties of all other tissues were modeled as linear elastic with different moduli assigned to the corresponding tissue. The shafts of the femur, fibula, and tibia were defined as non-deformable rigid bodies. The resultant model was validated against cadaveric testing with respect to passive flexion patellar kinematics [4] and to ligament strain in quasi static motion [5]. The resultant model was initially subjected to various TTO procedures including medialization, anteromedialization, and anteriorization under passive flexion. Currently, the intact model and TTO models are being simulated with and without lateral release and quadriceps imbalance.

RESULTS

Medialization reduced patellar lateral translation (i.e. 6.26 mm in normal vs. 0.12 mm in medialization, Figure 1 left) and decreased medial side patellar rotation in the coronal plane. Anteriorization had no discernible effect on rotation

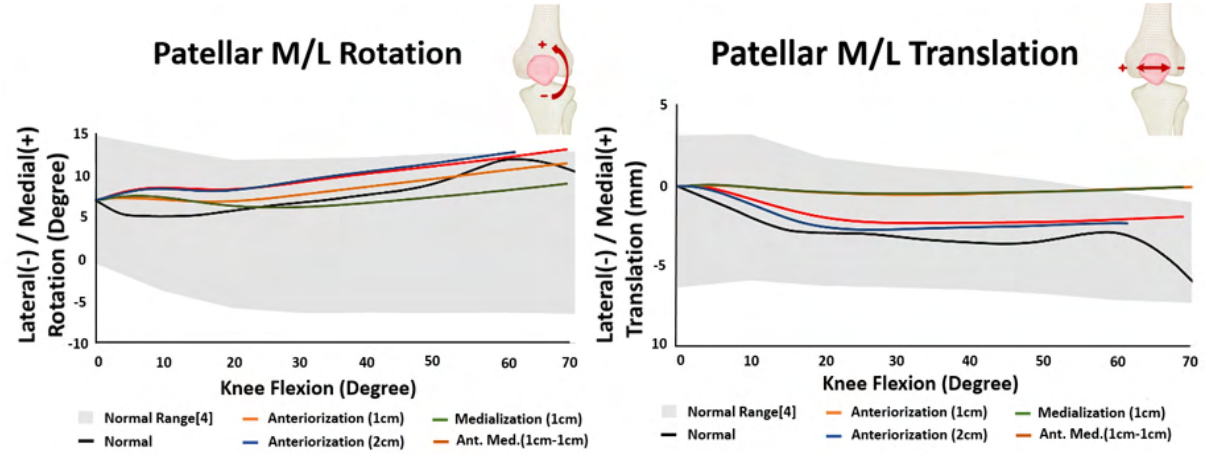

Fig. 1 (Left) Patellar Medial/Lateral Rotation Comparison; (Right) Patellar Medial/Lateral Translation Comparison.

Table 1: Maximum Contact Pressure on Patellofemoral Joint.

	Normal	Anteriorization	Medialization	Anteromedialization
Max. Contact Pressure on Patella Cartilage (MPa)	4.52	4.36	4.38	4.14
Max. Contact Pressure on Femoral Cartilage (MPa)	3.83	3.65	3.69	3.37

(Figure 1 right). Patellofemoral contact pressure decreased for all cases, as compared to a normal (no simulated surgical intervention) case (Table 1). Anteromedialisation performed the best for reducing the contact pressures at the same time reducing the lateral translation.

DISCUSSION

The preliminary kinematic data agreed with experimental data [1] and clinical statistics [3] for the normal knee, and supports surgical antero medialization to correct for significant patellar lateralization associated with patellar instability. Anteromedialization resulted in 8% and 11% reductions of contact pressure on patellar and femoral cartilage components, respectively. Our results support the findings of previous experimental work on the role of high contact pressures in incidence of osteoarthritis [6]. Current efforts are underway to include quadriceps imbalance and lateral rentinacular release data to better understand patient outcome.

ACKNOWLEDGEMENT

Work supported in part by the NSF Industry/University Cooperative Research Center at the University of California at San Francisco and University of Toledo, Toledo (www.nsfcdmi.org), National Institutes of Health (R01 AR056259-06-THE), and by an allocation from the Ohio Supercomputer Center.

REFERENCES

[1] Ramappa A, Wilson DR, Apreleva M, Harrold F, Fitzgibbons P, Gill T. The effects of medialization and anteromedialization of the tibial tubercle on patellofemoral mechanics and kinematics in knees with patellofemoral malalignment. In Transactions of the 47th Annual Meeting of the Orthopaedic Research Society, Rosemount, IL 2001 (Vol. 818).

[2] Fulkerson J. P., and K. P. Shea. "Disorders of patellofemoral alignment." J Bone Joint Surg Am 72.9 (1990): 1424-1429.

[3] Bellemans J., et al. "Fracture of the proximal tibia after fulkerson anteromedial tibial tubercle transfer a report of four cases." The American journal of sports medicine 26.2 (1998): 300-302.

[4] Belvedere C., et al. "Tibio-femoral and patello-femoral joint kinematics during navigated total knee arthroplasty with patellar resurfacing." Knee Surgery, Sports Traumatology, Arthroscopy 22.8 (2014): 1719-1727.

[5] Kiapour A., et al. "Finite element model of the knee for investigation of injury mechanisms: development and validation." Journal of biomechanical engineering 136.1 (2014): 011002.

[6] Zhang Y, Jordan JM. Epidemiology of osteoarthritis. Clinics in geriatric medicine. 2010 Aug 31;26(3):355-69.

High-fidelity Kidney Phantom for Multi-purpose Surgical Training

T. Qiu[1], F. Adams[1,2], B. Fritz[3], L. Kramer[4], U. Wetterauer[2], A. Miernik[2], P. Fischer[1,5]

[1]Max Planck Institute for Intelligent Systems, Stuttgart, Germany

[2]Department of Urology, University Medical Centre Freiburg, Germany

[3]Department of Radiology, University Medical Centre Freiburg, Germany

[4]Institute of Forensic Medicine, University Medical Centre Freiburg, Germany

[5]Institute of Physical Chemistry, University of Stuttgart, Germany

fischer@is.mpg.de

INTRODUCTION

An organ phantom system is important not only for the development of new surgical instruments, but also for medical training, especially in the case of minimally invasive and robotic urological surgeries. Animal models do not satisfactorily represent key structures of human organs and their preparation is labor intensive and they cannot be used repeatedly. Some commercial surgical simulation systems for urologic surgery training are available, *e.g.* Cook ureterorenoscopy model (Cook Medical, US) [1] and Uro-Scopic Trainer (Limbs & Things, UK) [2]. However, there is still a need for models that are made from soft materials rather than hard plastics and that reproduce fine anatomical details.

Recently developed 3D (three-dimensional) printing technologies provide unique opportunities for constructing organ phantoms. Bernhard *et al.* reported the direct 3D printing of kidney models with tumors to facilitate the understanding of a patient's medical condition. [3] Although important anatomies were labelled by different colors, the direct printed material is too rigid to mimic tissues and the inner cavity is not realized, making it unsuitable for surgical simulations. Cheung *et al.* reported a simulator made by molding of a 3D printed negative mold to perform pyleoplasty in ureteropelvic junction stenosis of children. [4] Although the model was made of silicone to mimic tissues, it lacked an inner cavity structure. Turney *et al.* 3D printed the shape of a collecting system using polyvinyl alcohol (PVA), which was embedded in silicone and dissolved in water to leave a hollow collecting system. [5] However, only the shape of the collecting system was simulated, but the surrounding tissue was only resembled by a block of silicone. Thus, the model can only be used for training of percutaneous procedures [5], but is unsuitable for other purposes. Moreover, only limited resolution was achieved using the polymer extrusion 3D printer [5], and a quantitative analysis of the spatial error was not presented.

To our knowledge, a realistic kidney phantom that is capable of simulating multiple surgical procedures has not been reported previously. Here, we establish a high-fidelity model of the human kidney based on computer tomography (CT) data. The phantom consists of three characteristic parts: a hollow collecting system, the surrounding kidney tissue (parenchyma) and a tumor. Not only the detailed anatomical morphology, but also certain physical properties of the tissues are mimicked and validated in the phantom. Two kinds of surgical procedures, *i.e.* ureterorenoscopy and renal tumor removal are performed on the phantom.

MATERIALS AND METHODS

The data was obtained by CT scans of a human cadaveric kidney (experimental plan approved by the ethics committee of the Albert-Ludwigs-University of Freiburg). Iodinated contrast agent was injected into the collecting system. The collecting system and the surrounding tissue were selected and reconstructed respectively to generate two 3D models, which were used to design the negative molds. The molds were 3D printed and molded in silicone materials. Finally, the constructed phantom was scanned by CT and quantitatively compared with the original CT data to evaluate its accuracy. Two surgical training procedures were carried out on the phantom: The collecting system was intubated and examined by a flexible 10 Fr. ureterorenoscope (Richard Wolf, Knittlingen, Germany) and a renal tumor removal procedure was performed.

RESULTS

Different polymeric materials can be applied for the phantom according to its intended use. For example, as shown in Fig. 1, a transparent phantom was built for the training of ureterorenoscopic procedures. The movement of the endoscope inside the collecting system can be clearly observed (Fig. 3(a)), which helps junior medics to quickly capture the spatial orientation of the instrument. For tumor removal operations, a tissue-like elastomer material mixed with red pigment was used. The elastomer has an elastic modulus of 60 kPa, very close to that of the real kidney tissue of 48.56±7.32 kPa [6]. According to experienced surgeons, the cutting and suturing of the material feel similar to real tissues (Fig. 4). Moreover, the molding scheme reported herein also allows the simultaneous usage of multiple materials. A

14 mm-diameter sphere made of a harder polymer (the green part in Fig. 1(b)) was embedded in the red phantom to simulate a renal tumor.

The anatomy of the phantom was validated by a CT scan. The comparison of the phantom with the real organ (Fig. 2(b) and 2(a)) suggests that the phantom successfully reproduces the shapes of both the collecting system and the surrounding tissues. A quantitative analysis of the collecting system suggests the spatial mean error is as low as 0.7 mm (Fig. 2(c)). From the endoscopic examination, the internal structure of the upper calyx in the phantom also appears to be identical to that of a real kidney (Fig. 3(c) and 3(b)). Five kidney phantoms were prepared with different polymeric materials respectively, and the endoscopic and CT examinations verified a good reproducibility of the anatomical structures in all phantoms.

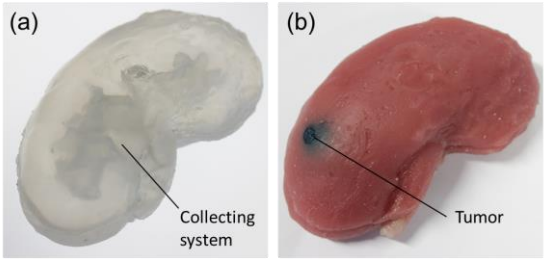

Fig. 1 Perspective view of the kidney phantoms made of different materials. (a) A transparent phantom for observing the endoscope movement, (b) A tissue-colored phantom with an embedded tumor (in green) for surgical simulation.

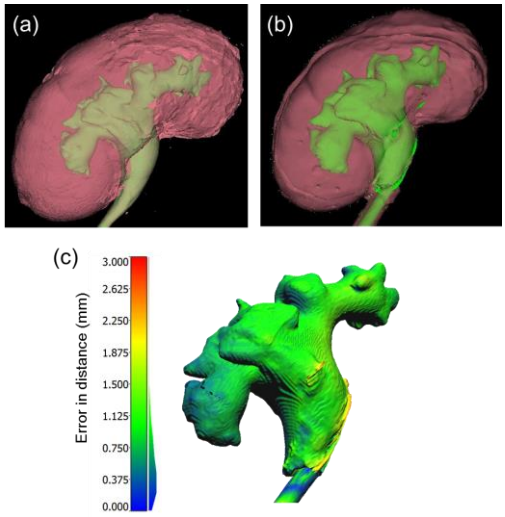

Fig. 2 Comparison of 3D reconstructed CT data of (a) the real human kidney, (b) the constructed kidney phantom. The collecting system and the surrounding tissue are labelled in green and red, respectively. (c) Quantitative comparison between the collecting system in (a) and (b) and the surface colors correspond to the error (in mm).

DISCUSSION

We report a general method to obtain realistic human organ phantoms. A kidney phantom is demonstrated that reproduces the human organ anatomy, especially the inner cavity structure with sub-millimeter resolution. A wide range of materials can be implemented. The phantom is durable and can be produced at low-cost. Therefore, the kidney phantom developed herein can be used as a realistic model in a variety of applications including surgical instruments testing, operation simulation and medical training.

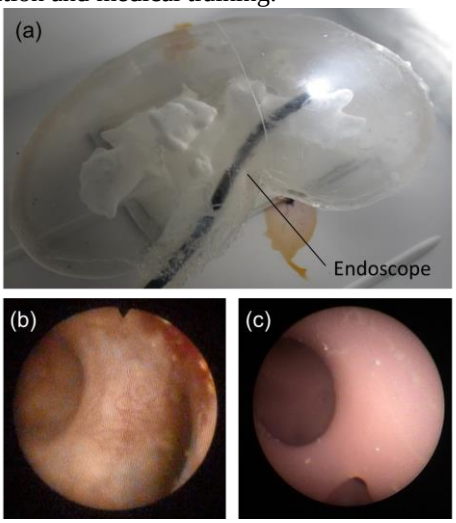

Fig. 3 Endoscopic surgery training on the kidney phantom. (a) View of an endoscope positioned inside the transparent phantom. The endoscopic views of an upper calyx in (b) the human kidney and (c) the phantom.

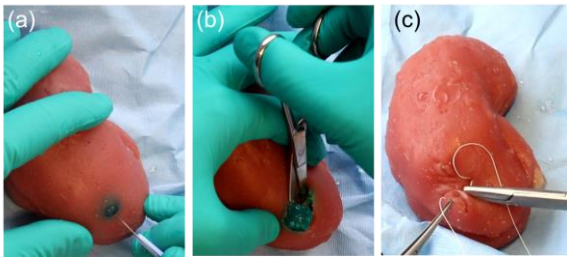

Fig. 4 Renal tumor removal (open surgery) performed on the soft kidney phantom. (a) Tissue cutting and exposition of the tumor, (b) tumor removal, (c) suturing.

REFERENCES

[1] U. Blankstein, A.G. Lantz, R.J. Honey *et al.* Simulation-based flexible ureteroscopy training using a novel ureteroscopy part-task trainer. Can. Urol. Assoc. J. 2015; 9(9-10): 331-5.

[2] Uro-Scopic Trainer. http://assets.limbsandthings.com/documents/Urology_REV_2.pdf .

[3] J.-C. Bernhard, S. Isotani, T. Matsugasumi *et al.* Personalized 3D printed model of kidney and tumor anatomy: a useful tool for patient education. World J. Urol. 2016; 34(3): 337-45.

[4] C.L. Cheung, T. Looi, T.S. Lendvay, *et al.* Use of 3-D Printing Technology and Silicone Modeling in Surgical Simulation: Development and Face Validation in Pediatric Laparoscopic Pyeloplasty. J. Surgical Education. 2014; 71(5): 762-7.

[5] B.W. Turney. A New Model with an Anatomically Accurate Human Renal Collecting System for Training in Fluoroscopy-Guided Percutaneous Nephrolithotomy Access. J. Endourology. 2014; 28(3): 360-3.

[6] R. Opik, A. Hunt, A. Ristolainen, *et al.* Development of high fidelity liver and kidney phantom organs for use with robotic surgical systems, 4th IEEE Inter. Conf. on Biomed. Robotics and Biomechatronics (BioRob). 2012; 425-30.

"Coping or Choking": Sustained Prefrontal Activation and Improved Laparoscopic Performance under Time Pressure

H. N. Modi, H. Singh, G.-Z. Yang, A. Darzi, D. R. Leff

Hamlyn Centre for Robotic Surgery, IGHI, Imperial College London,UK

hemel.modi12@imperial.ac.uk

INTRODUCTION

Unexpected intra-operative bleeding that occurs during an operation requires the surgeon to perform haemostatic manoeuvres swiftly yet accurately. However, temporal demands in the operating theatre can increase mental effort or *'cognitive workload'* resulting in physiological and psychological stress that may impair surgical performance[1-3].

Neuroimaging technology may provide the means by which cognitive workload can be measured directly. Investigators are now exploiting techniques such functional near-infrared spectroscopy to assess operator brain function during realistic surgical tasks[4-7] These studies highlight the importance of the pre-frontal cortex (PFC), an area known to be important for executive control, attention and concentration, and performance monitoring[8]. However, these studies have failed to shed light on expertise-related disparity in attention and concentration changes in and around times of temporal operative stress.

Aim: To assess the prefrontal cortical haemodynamic response in surgical trainees with varying operative experience performing a laparoscopic suturing task under time-pressured conditions.

METHODS

28 surgical trainees [15 junior trainees (ST3-4), 8 intermediate trainees (ST5-6), and 5 senior trainees (ST7+)] performed a laparoscopic suturing task under two conditions: (1) "self-paced", in which trainees were permitted to take as long as required to tie each knot, and (2) "time pressure", in which a maximum of 2 minutes were allowed. Subjective workload was quantified using the Surgical Task Load Index (SURG-TLX). A 24-channel optical topography system (ETG-4000, Hitachi Medical Corp., Japan) which measures changes in cortical haemodynamic parameters was used to infer PFC activation responses. Technical skill was assessed using task progression scores (au), error scores (mm), leak volumes (ml), and knot tensile strengths (N).

RESULTS

Subjective Workload and Motor Performance

Among junior and intermediate trainees, time pressure led to an increase in subjective workload and significant deterioration in performance. In contrast, no such change in subjective workload was observed amongst senior trainees who demonstrated less performance deterioration under time pressure (Figure 1).

Cortical Brain Function

Diminished prefrontal activation was observed among junior and intermediate trainees in the time pressure condition, relative to the self-paced condition [junior trainees: ΔHbO_2 (μM) median ± IQR (self-paced vs time pressure): 0.485 ± 1.952 vs 0.229 ± 1.846, Wilcoxon Signed Ranks $p<0.001$]; intermediate trainees [ΔHbO_2 (μM) median ± IQR (self-paced vs time pressure): 0.443 ± 2.298 vs 0.127 ± 2.192, Wilcoxon Signed Ranks $p=0.002$]. Conversely, sustained PFC activation was evident amongst senior trainees [ΔHbO_2 (μM) median ± IQR (self-paced vs time pressire): 0.918 ± 2.177 vs 0.726 ± 2.363, Wilcoxon Signed Ranks $p=0.129$] (Figure 2). Furthermore, time pressure led a reduction in size of the spatially distributed network of activated channels among junior and intermediate trainees, but not in senior trainees in whom an equally sized network of channels remained activated. (Figure 2).

DISCUSSION

Senior trainees are better able to cope with intra-operative cognitive demands and stabilise their performance under pressure, perhaps due to enhanced PFC recruitment and task engagement. Future work will seek to develop cognitive training strategies that will maintain task engagement among more junior trainees, allowing them to improve performance under pressure.

REFERENCES

[1] Arora S, Sevdalis N, Nestel D, et al. The impact of stress on surgical performance: a systematic review of the literature. *Surgery* 2010; 147(3):318-30, 330 e1-6.

[2] Moorthy K, Munz Y, Dosis A, et al. The effect of stress-inducing conditions on the performance of a laparoscopic task. *Surg Endosc* 2003; 17(9):1481-4.

[3] Arora S, Sevdalis N, Aggarwal R, et al. Stress impairs psychomotor performance in novice laparoscopic surgeons. *Surg Endosc* 2010; 24(10):2588-93.

[4] Leff DR, Elwell CE, Orihuela-Espina F, et al. Changes in prefrontal cortical behaviour depend upon familiarity on a bimanual co-ordination task: an fNIRS study. *Neuroimage* 2008; 39(2):805-13.

[5] Ohuchida K, Kenmotsu H, Yamamoto A, et al. The frontal cortex is activated during learning of endoscopic procedures. *Surg Endosc* 2009; 23(10):2296-301.

[6] Leff DR, Yongue G, Vlaev I, et al. "Contemplating the Next Maneuver": Functional Neuroimaging Reveals Intraoperative Decision-making Strategies. *Ann Surg* 2016.

[7] Leff DR, Orihuela-Espina F, Athanasiou T, et al. "Circadian cortical compensation": a longitudinal study of brain function during technical and cognitive skills in

acutely sleep-deprived surgical residents. *Ann Surg* 2010; 252(6):1082-90.

[8] Roberts AC, Robbins TW, Weiskrantz LE. The prefrontal cortex: Executive and cognitive functions: Oxford University Press, 1998.

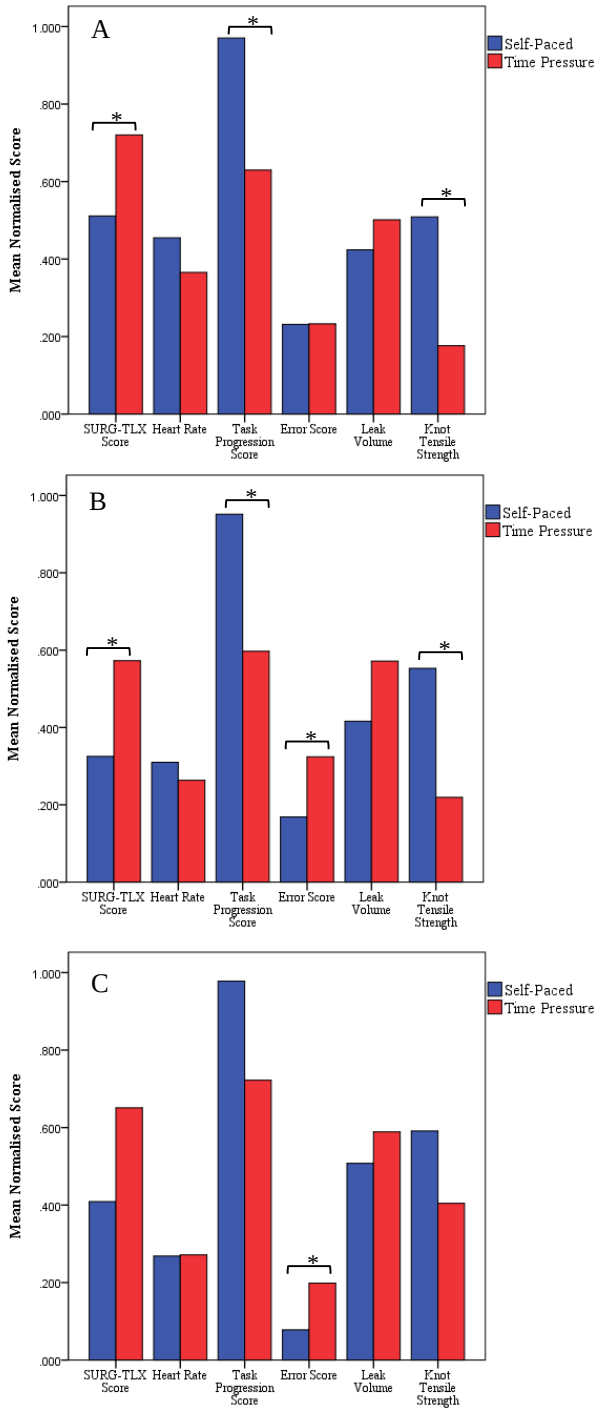

Fig. 1 Normalised subjective workload and performance scores in self-paced (blue bars) and time pressure (red bars) conditions in junior trainees (A), intermediate trainees (B) and senior trainees (C). SURG-TLX: Surgical Task Load Index. *p<0.05.

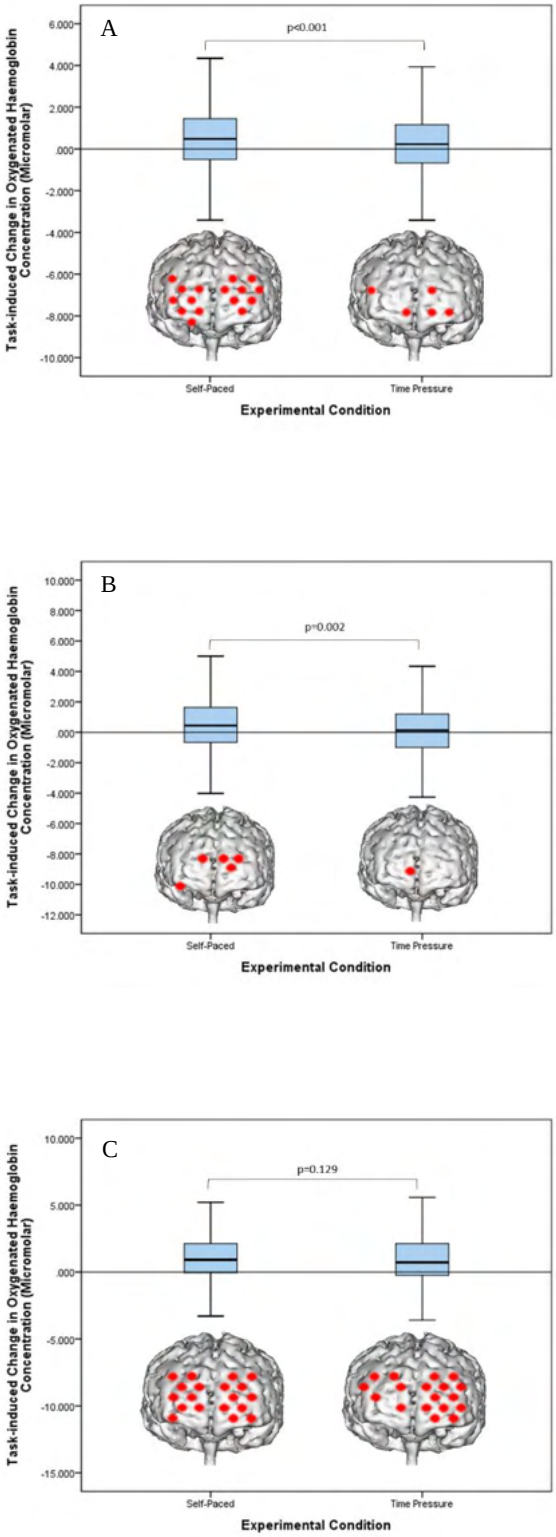

Fig. 2 Boxplots demonstrate median task-induced change in oxygenated haemoglobin concentration averaged across channels in each conditions in junior trainees (A), intermediate trainees (B) and senior trainees (C). The 3D MRI reconstructions demonstrate activated channels in each condition based on a statistically significant increase in task-induced HbO_2 concentration.

Surgical Workflow Integration of the Robotic ENT Microsurgical System

Y. Sevimli[1], P. Wilkening[1], L. Feng[1], M. Balicki[1],
K. C. Olds[1], T. Keady[1], R. H. Taylor[1]

[1]Laboratory for Computational Sensing and Robotics, Johns Hopkins University, USA
[yunus, pwilken3, lfeng8, mbalick1, kolds1, thomas.keady, rht]@jhu.edu

INTRODUCTION

The Robotic ENT Microsurgical System (REMS) is a versatile, low-cost, small-footprint platform with capabilities that surpass similar commercially available surgical robots [1]. The system works with the surgeon to eliminate hand tremor and avoids critical anatomical features by enforcing virtual boundaries and by following predefined trajectories [1-2]. A delta stage, coupled with tilt and roll mechanisms is driven by the force and torque input from the user holding the surgical instrument that is attached to the robot. The result is an intuitive and highly precise cooperative system (0.14mm transitional and 0.0011 rad rotational mean error after calibration) within a workspace in the size of an average skull. Other than otolaryngeal cases, the REMS is also appropriate for applications in neurosurgery, hand surgery and similar fields where high precision and accuracy are crucial.

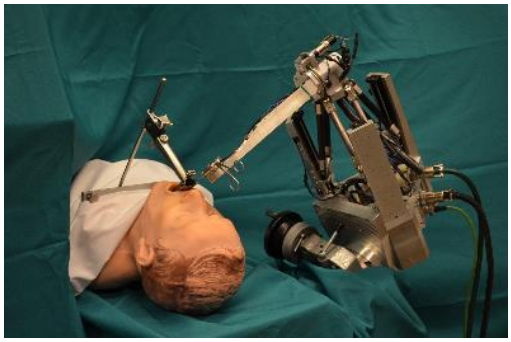

Fig. 1 The REMS, without the Preoperative Positioning System. [1]

This paper focuses on the aspects of the platform that transform it from a bench-top system towards realistic clinical scenarios with minimal interruption to the existing workflows.

SYSTEM OVERVIEW AND EXPERIMENTS

Universal Surgical Tool Exchanger (USTE)

The REMS can accommodate most otolaryngeal tools owing to the USTE, allowing the surgeons to use the robot with the tools they are accustomed to. The robot-side of the adapter comprises a female dovetail joint with a spring loaded locking pin. The tool-side is a simple two-sided part: one end is a standard male dovetail joint and the other end is a custom attachment for surgical tools with different shaft diameters. Any tool containing this attachment can simply be slid and passively locked into the standard female joint. The tool can then be removed with a single-handed operation by pressing in the lever to disengage the locking pin with the thumb and by sliding the tool out of the holder.

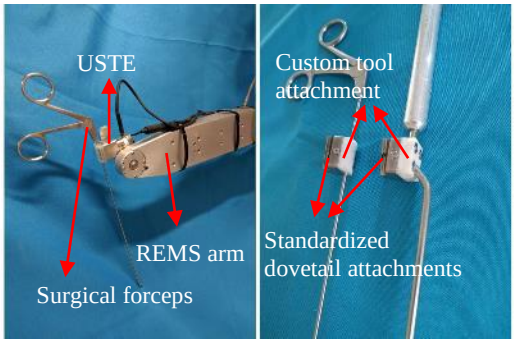

Fig. 2 A laryngeal instrument attached to the REMS via the USTE (left). Different surgical tools with the standardized attachments (right).

Experiment: In order to test the ease of use and the ergonomics of the mechanism, 5 subjects with no prior training were asked to swap 3 tools successively using the USTE. After one training round, each subject was given 2 trials and the times for completion were recorded. **Results:** Each subject was able to swap 3 tools under 5 seconds in total. The average time to put in and take out a tool was under 2 seconds. A previous method for tool switching required manipulation of a thumbscrew and took about three times as long to accomplish a tool swap using both hands.

Laser-guided Alignment System (LAS)

The LAS is used to align the workspace of the REMS with the surgical target. It is comprised of a laser projector tool compatible with the USTE, containing 4 laser projectors all pointing downward. The central projector projects a cross, while the remaining 3 projectors, positioned at 3, 6, and 9 o'clock positions project lines. The slight angles between the projectors allow all the lines to appear collinear with the cross when

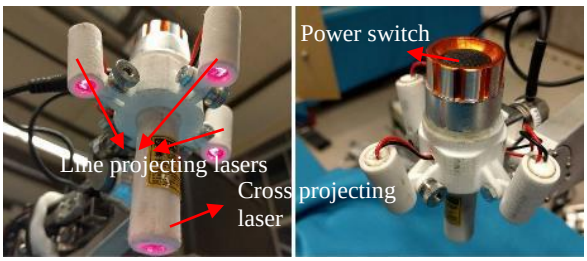

Fig. 3 The laser projector tool.

the beams are focused on a plane orthogonal to the shaft of the tool, at a specific distance.
The alignment procedure requires the laser projector tool to be attached onto the robot and aimed towards the surgical target area. The separation and the angle between the projected laser beams gives the user feedback on how the robot needs to be positioned to achieve alignment in 3D space (see Figure 4). Once all the outer laser lines are focused on the central cross the alignment is complete and the surgical target is centered within the workspace of the REMS. Afterwards, the laser tool can be removed from the USTE and a surgical tool can be attached instead.

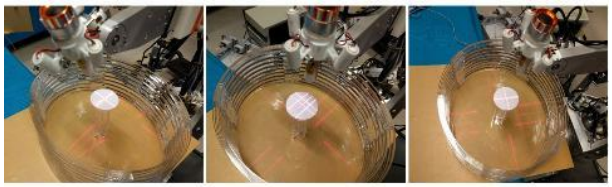

Fig. 4 Alignment demonstrated on a phantom: misalignment due to orientation (left), misalignment due to distance (middle) perfect alignment (right)

Experiment: In order to test the accuracy of the system, 3 subjects who are familiar with the system were asked to align the robot to a phantom first by "eyeballing" and then by using the LAS. Each trial was repeated twice and the time to achieve alignment was recorded. After being aligned on the center of the phantom the robot is expected be able to access the entire inner volume of the phantom as this defines a successful calibration.
Results: The Laser-guided Alignment System is shown to achieve alignment within an average time of 1 min. 36 sec. with 100% success rate compared to "eyeballing" which resulted in an average time of 1 min. 54 sec. with a 43% success rate. The worst case times to achieve alignment were 1 min. 55 sec. and 2 min 28 sec., with and without the LAS, respectively.

Preoperative Positioning System (PPS)
It is crucial that the REMS is properly oriented with respect to the patient before the operation to ensure that the surgical workspace is fully enclosed within the reachability of the robot. To meet this need, the PPS offers a 5-DOF actuated frame that supports and orients the REMS as required.
The aluminum frame rests on spherical rollers, on which the system can be holonomically moved along a surface. Once in the right location, the user commands the rollers to retract, allowing the frame to sit rigidly on its rubber feet. The frame also allows the user to adjust the height of the REMS with a range of 350mm, and adjust the roll angle and tilt angles, each up to 30° bidirectional from the vertical. The roller deployment, height adjustment and tilt rotation are realized by hydraulic cylinders, while the roll joint is driven by a geared stepper motor. All joints are controlled with a 3D joystick, with the corresponding axes of the workspace and the joystick mapped onto each other (up/down for height, forward/backwards for tilt and sideways for roll). This provides the user an intuitive way to control the joints, either individually or in parallel by moving the joystick accordingly. Once in the desired pose, each joint of the PPS is mechanically locked to ensure rigidity during the surgery.

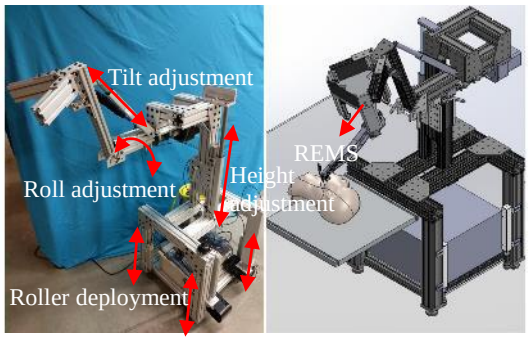

Fig. 5 The Preoperative Positioning System with the actuated joints shown. The CAD image on the right shows the system in an otology case setup with the REMS attached.

Status: The PPS is being developed with the feedback from 4 practicing surgeons. The frame is built and basic functionality is demonstrated. Work is currently being done to achieve coordinated motions by using the joint angle data.

DISCUSSION

The main goal of the three systems discussed in this paper is to transform the REMS from a bench-top device to a surgical robot. Furthermore, through these three key components we aim to increase the versatility of the system by making it compatible with various surgical cases while minimizing the interruption to the conventional surgical workflows.
As demonstrated, the Universal Surgical Tool Exchanger and the Laser-guided Alignment System have performed well in the laboratory tests and are shown to offer significant advantages over alternative methods. The Preoperative Positioning System is still under development but shows promise in meeting the clinical needs for robot positioning.
The next step for the overall system is to repeat the tests in different clinical scenarios with practicing surgeons and to further improve the designs accordingly. With these improvements, our hope is that REMS will be available as a versatile, high precision robotic platform to assist surgeons with their most challenging tasks.

REFERENCES

[1] K. C. Olds, Robotic Assistant Systems for Otolaryngology-Head and Neck Surgery, Ph.D Thesis, The Johns Hopkins University, 2008.
[2] C. He, K. C. Olds, I. Iordachita, and R. H. Taylor, "A new ENT microsurgery robot: error analysis and implementation," in Proc. IEEE Int. Conf. on Robotics and Automation (ICRA), 2013, pp. 1221-1227.

Multi-port Neuroendoscope for Robotic Intraventricular Procedures

M. Mencattelli[1,2], S. Manjila[2], B. Rosa[2], K. Price[2], G. Fagogenis[2], P. E. Dupont[2]

[1]*The Biorobotics Institute, Scuola Superiore Sant'Anna, Pisa, Italy*

[2]*Paediatric Cardiac Bioengineering Lab, Boston Children's Hospital, Harvard Medical School, Boston, USA*
Pierre.Dupont@childrens.harvard.edu

INTRODUCTION

About 20% of brain surgeries are performed to remove lesions located inside or adjacent to the brain's ventricles [**1**]. Using endoscopes, neurosurgeons can navigate their instruments through the ventricles to reach these lesions with less damage to healthy brain tissue than occurs in open surgery. Current endoscopes, however, are restricted by several factors. First, the tools emerge parallel to the endoscope, precluding many of the two-handed surgical techniques of open surgery that are used to dissect tissue and stop bleeding. Second, most neurosurgeons use straight rigid endoscopes that can only image and deploy tools from their tips and so cannot negotiate around corners without causing significant brain retraction injury. While a few neurosurgeons have mastered flexible endoscopes, these instruments typically provide only a single instrument channel. A recently proposed solution to the first problem deploys concentric tube robots from the endoscope working channels to enable dexterous bimanual manipulation (**Fig. 1**) **[2, 3]** The contribution of this paper is to provide a solution to the second problem by introducing the concept of multiple imaging/tool ports on a single endoscope. In this approach, imaging ports can be positioned not only at the instrument tip, but also anywhere and at any angle along the endoscope body. If the imaging and illumination is accomplished using chip cameras and LED's, many imaging ports can be supported in a given diameter instrument while also producing an instrument that is much lighter and easier to manipulate than a standard rigid endoscope.

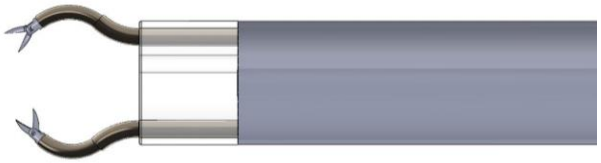

Fig 1. Continuum robots deployed from a neuroendscope.

MATERIALS AND METHODS

As an initial step toward a robotic system, we developed the multi-port concept in the context of an MR-compatible, hand tool for colloid cyst resection combined with septostomy. By developing the device MR-compatible, the benefits of stereoataxy together with a real-time continuous imaging are also provided.

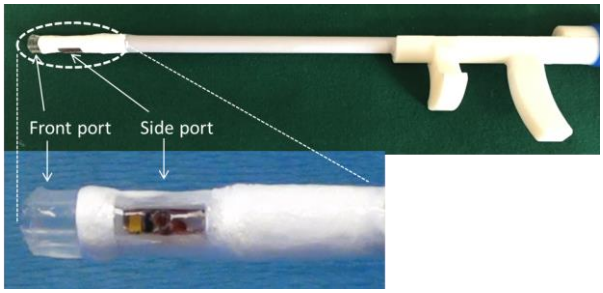

Fig. 2 Novel neuroendoscope prototype.

The neuroendoscope (**Fig. 2**) was designed with two imaging ports enabling tissue resection at the tip port and electrocautery at the lateral port. The device has a total weight of 50 grams, which adds up to less than 150 grams including its camera processor, making it a light-weight neuroendoscope without any torque at the proximal end.

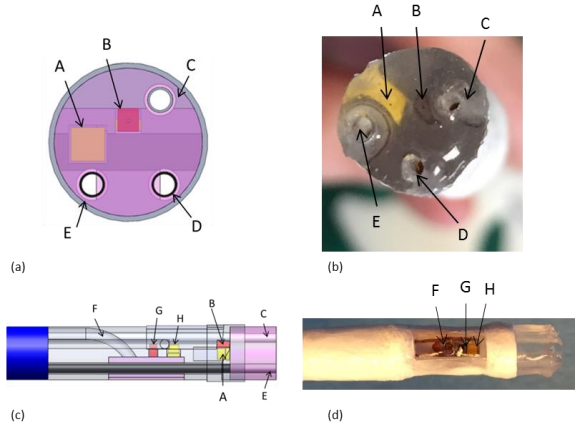

Fig. 3 Imaging ports. (a) CAD model of tip port. (b) Tip port. (c) CAD model of lateral port. (d) Lateral port.
A = Front LED, B = Front camera, C = Front working channel, D = Flush channel, E = Suction channel, F = Side working channel, G = Side camera, H = Side LED.

The novel neuroendoscope has an instrument body (7 mm outer diameter, OD) consisting of a straight 150mm long plastic tube with a proximal ergonomic handle. The tip and lateral imaging ports (**Fig. 3**) each contain a 1x1x1mm CMOS video camera (250x250 pixels, NanEye, Awaiba, Inc.) and an LED for illumination (1.6x1.6x**Q,** Cree Inc, Durham NC). The tip port contains three 1mm channels positioned in the corners of the camera image. These can be used for tools, irrigation and aspiration. The lateral port contains a single 1mm channel with a 7mm radius of curvature,

which is sized to deliver a Bugbee wire to perform monopolar cautery for fenestration of the septum pellucidum. All channels are lined by 1.2mm OD polyimide tubes. Each imaging port is molded from optically clear silicone (QSil 218, Quantum Silicones LLC), which serves to encapsulate the camera and LED. While the optical window of the lateral port is ~2mm thick and molded to be flush with the instrument's cylindrical surface, the window of the tip port has been designed with a thickness of ~6mm.
While a much thinner window can be substituted, this thickness was used to enable (1) visualization of inserted tools before they extend from the tip of the endoscope, and (2) safe tissue contact with concurrent imaging.

RESULTS

MRI compatibilty was evaluated in a 3T scanner by inserting the endoscope into the brain of a freshly sacrificed adult Yorkshire pig. Both video cameras were observed to operate inside the scanner with no change in image quality. Furthermore, MR images using standard brain imaging sequences revealed that the imaging artifact (void) matched the dimensions of the device itself (**Fig. 4**).

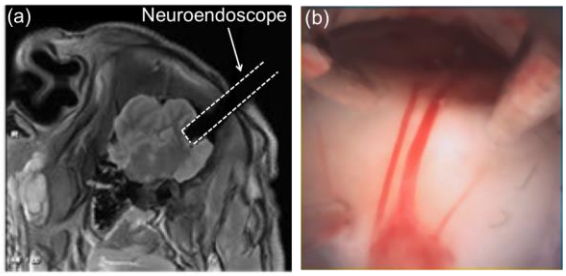

Fig. 4 (a) MR image of porcine brain with endoscope inserted (b) Endoscopic view of porcine ex-vivo ventricle.

Image quality was also evaluated using the USAF 3-bar Resolving Power Test target [**4**]. **Fig. 5** compares images obtained from both imaging ports with that of a clinical rigid endoscope. As shown in Fig. 5a, there are three instrument channels at the tip. As a safety feature, the channels are clear making it is possible to see instruments before they extend from the device. The single instruments channel of the lateral port is visible in Fig. 5b. An image from a clinical endoscope is shown in Fig. 5c for comparison. Image quality is better owing to the use of multiple larger lenses compared to a chip camera. Note that the image from a flexible clinical neuroendoscope, not shown, is likely to be worse than the dual-port prototype owing to fewer image pixels.

DISCUSSION

Despite progress in neuroendoscopy, there are many procedures such as resection of paraventricular lesions, that are still not amenable to a transventricular endoscopic approach. By replacing straight-shafted instruments with needle-sized continuum robots, the dexterity of open microsurgery can be reproduced with an endoscope. The multi-port concept introduced in this paper is a passive, inexpensive alternative to a steerable robotic wrist for enabling reorientation of imaging and tool deployment.

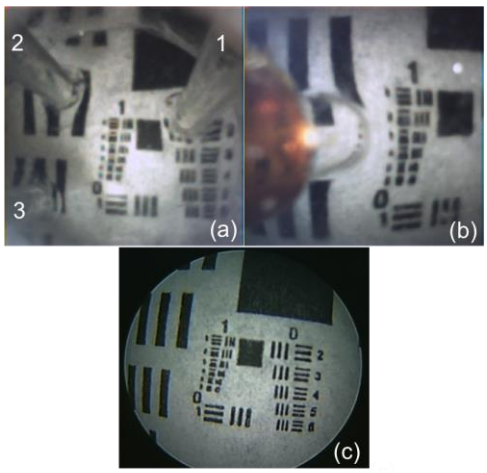

Fig. 5 Endoscope images. (a) Prototype tip port. Instrument channels are numbered, (b) Prototype lateral port. Orange polyamide tube and transparent working channel are visible. (c) Commercial 6mm rigid neuroendoscope. To achieve similar magnification, standoff distance was 10mm for prototype and 15mm for commercial system.

It is made possible by chip camera technology. The CMOS camera used in our prototype, at 1mm on a side, is among the smallest currently available and provides an image size of 250x250=62,500 pixels. For comparison, a fiber bundle of comparable cross section contains only 20,000 fibers / pixels. **[5]** This places the image quality of our endoscope between that of existing rigid and flexible neuroendoscopes.
The prototype shown here was designed for performing colloid cyst resection combined with septostomy with minimal pivoting of the instrument shaft about the center of the burr hole. Pilot ex-vivo tests in human cadaver and phantom brain are underway to achieve further validation.
This particular design choice could also be used in lieu of a steerable endoscope for treating multiloculated hydrocephalus, where the sideport enable the lysis of intraventricular adhesions that could not be fenestrated easily by the tip port alone. Many design variations are possible since the port number, location, orientation and working channels can be tailored to address specific procedures or classes of intraventricular procedures.

REFERENCES

[1] Souweidane M. M., Endoscopic surgery for intraventricular brain tumors in patients without hydrocephalus,. Neurosurgery, 57(4), 2005.
[2] https://www.youtube.com/watch?v=Zs_-G8pD2Jw.
[3] https://www.youtube.com/watch?v=WOIDAc4YtYQ.
[4] Bedard N, Tkaczyk TS. Snapshot spectrally encoded fluorescence imaging through a fiber bundle. J Biomed 17(8), 2012
[5] Friedman G. N., Grannan B. L., Nahed B. V., Codd P. J. Initial Experience with High-Definition Camera-On-a-Chip Flexible Endoscopy for Intraventricular Neurosurgery. World Neurosurg. 84(6), 2015.

A Dual-Arm Robotic Neuroendoscope: Early Results

H. Azimian, T. Looi, J. Drake

Center for Image-Guided Innovation and Therapeutic Intervention, Hospital for Sick Children, Toronto, Canada

hamidreza.azimian@sickkids.ca

INTRODUCTION

Robotic-assisted Minimally Invasive Surgery (MIS) is becoming a standard practice in many therapeutic procedures in hospitals around the world. Adopting robots in many MIS procedures has been proven to be effective in reducing the postoperative trauma, and the length of hospital stay amongst other benefits. However, due to the size of the available surgical robotic tools, application of robotic-assisted MIS has remained limited to adults and procedures with relatively large workspace. At Centre for Image-Guided Innovation and Therapeutic Intervention (CIGITI), along with several other research centers around the world, we have been working on developing miniaturized robotic tools to bring the benefits of robotic surgery to challenging procedures such as neurosurgery. It is expected that these tools will offer superior dexterity over the current manual endoscopic tools while traversing to the surgical site through small ports.

Performing brain intraventricular procedures including endoscopic third ventriculostomy (ETV) and tumor biopsy/excision using standard endoscopic tools is technically challenging or sometimes not possible. An ETV procedure is performed by introducing an endoscope into the brain through a small burr hole in the skull to create a small perforation in the floor of the third ventricle to discharge the cerebrospinal fluid (CSF) that has blocked the ventricle. This is usually followed by choroid plexus cauterization (CPC) to ensure a sufficient reduction in CSF production. In this paper, a bi-manual robotic neuroendoscopic tool is presented that can provide additional dexterity and stiffness over the standard endoscopic tools for performing procedures such as ETV and tumor biopsy or excision.

MATERIALS AND METHODS

The system is composed of a slave device, two haptic master devices and an embedded controller, which consists of Quanser QPID boards, and a PC running Simulink and Quanser QUARC. The slave device is a dual-arm concentric-tube robot equipped with miniaturized end-effectors (Fig. 1). Of all common miniaturized manipulator design concepts, concentric-tube robots (CTRs) [2] have proven to deliver an optimum blend of dexterity and stiffness with a relatively straight-forward fabrication process. The slave device is composed of a trocar, (with dimensions close to a standard trocar), two arms and the actuation unit. The trocar is 120 mm extended beyond the trocar holder and has a diameter of 9 mm. It has five channels including two 2.7-mm channels for the instrument arms, a 5.5-mm channel for the camera, and three 2-mm channels for suction, irrigation and overflow.

Each arm is composed of two NiTi superelastic tubes and an end-effector. The actuation unit houses eight Maxon DC motors for rotation and translation of the tubes, and two Firgelli linear actuators (Firgelli Technologies Inc., BC, Canada) for the end-effectors. The left arm is equipped with a pair of biopsy forceps taken from Olympus Inc., Japan, and the right arm is equipped with a pair of scissors from Hipp Endoskop Service, Germany. The linear motion of the tubes is realized using four lead screws with a pitch of 5 mm. The unit is equipped with 4 linear and 4 rotary potentiometers along with motor encoders, i.e. a total of 16 sensors.

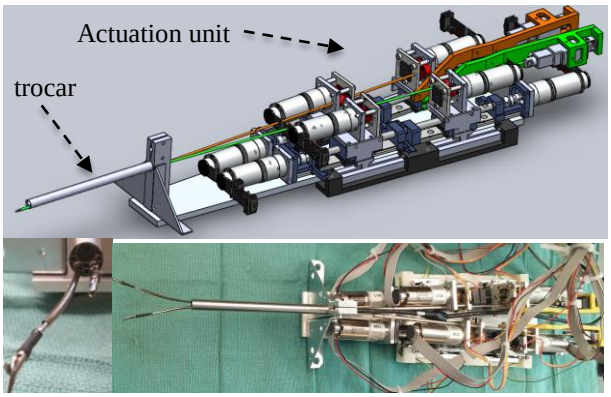

Fig. 1 The slave device is a dual-arm concentric-tube robot that is composed of the trocar, the arms and the actuation unit. The CAD model (top), the actual prototype (bottom right), the trocar (bottom left).

As indicated in Table I, each arm consists of a straight 0.94 mm by 1.37 mm inner tube and a precurved 1.95 mm by 2.41 mm outer tube rendering 4 degrees of freedom that is superior to what can be achieved by standard endoscopes. Theoretically, with this design, torsion in the system will be eliminated and the inverse kinematics can be solved analytically.

Table I. The tubes dimensions

	ID (mm)	OD (mm)	κ (1/mm)
Inner tube	0.94	1.37	0
Outer tube	1.95	2.41	0.012

The arms are operated by means of two Geomagic touch haptic controllers (Geomagic Inc., NC, USA), and a real-time video of the surgical site is captured by a

camera endoscope. This visual feedback enables the operator to intuitively operate the robotic arms to manipulate tissue using the master controllers.

A snapshot of the workspace of the dual-arm system is shown in Fig. 2. (left) This workspace is significantly different from the workspace of the master devices we used. This dissimilarity could potentially make the teleoperation less intuitive. In order to address this issue, a reactive barrier force (aka virtual fixture) is implemented to confine the operator's hand position to a subset of the master workspace with a similar geometry to that of the slave. In order to avoid energy leaks and guarantee stability, the barrier force is modeled as a spring/damper system [1].

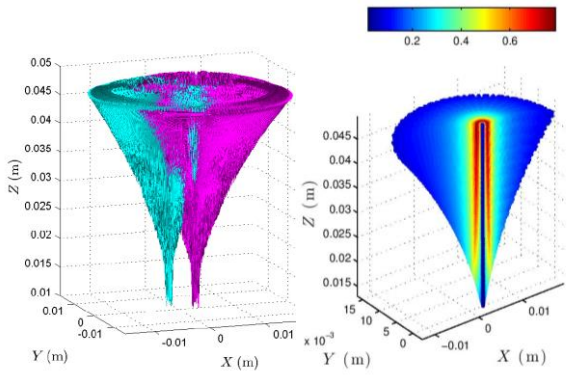

Fig. 2 The dual-arm workspace (left) Dexterity (right).

RESULTS

The system performance is quantitatively evaluated in terms of various measures such as system accuracy, dexterity, and stiffness. Table II outlines the accuracy and stiffness of the arms and Fig. 2 (right) shows the dexterity distribution of the arms over the workspace.

Table II. System Performance

	Accuracy (mean, 95th percentile)	Minimum stiffness
Right Arm	(0.7 mm, 1.3 mm)	6.73E-3 Nm^2
Left Arm	(1.2 mm, 2.2 mm)	6.73E-3 Nm^2

Finally, the system was evaluated qualitatively through two experiments. In the first experiment, a silicon phantom model created from the MR images of the brain of a patient diagnosed with hydrocephalus was used to evaluate the reachability of the slave arms. The brain phantom and the ventricle measured 120 mm x 140 mm and 30 mm x 40 mm respectively. The trocar was inserted through a burr hole into the phantom and the arms were deployed through the trocar. Under direct vision the arms were teleoperated to touch various locations inside the ventricle. As shown in Fig. 3, the experiment demonstrated that the intraventricular extremities were reachable by the arms.

In the second experiment, the system capability was qualitatively tested through a peg transfer task (Fig. 4). On the first attempt, we were able to transfer three pegs on the board within a minute. The speed could have been further improved provided that a stereo camera endoscope had been adopted to improve the depth perception. This result also signifies that this teleoperation system provides an acceptable hand/eye coordination as well as sufficient dexterity for many complex tasks.

Fig. 3 Intraventricular reachability evaluation in a silicon brain phantom.

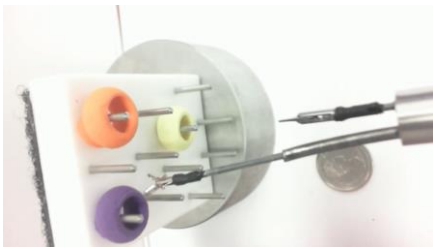

Fig. 4 A snapshot of the peg transfer demonstration[1].

DISCUSSION

In this paper, design and preliminary evaluation of a dual-arm teleoperated robotic neuroendoscope is reported. Through quantitative and qualitative analysis, it was demonstrated that the system is clinically advantageous by enabling miniaturized surgical tools to travel within a small workspace while maintaining a perfect balance of dexterity and stiffness for manipulation. While it is evident that the current system offers a significant advantage over standard neuroendoscopes, the preliminary evaluations suggest that the performance of the system could be drastically improved by incorporating additional degrees of freedom, i.e. more tubes, reducing the friction/backlash, and finally by accurate shape setting of the tubes.

REFERENCES

[1] Colgate J. E., Grafing PE, Stanley MC, Schenkel G. Implementation of stiff virtual walls in force-reflecting interfaces. InVirtual Reality Annual International Symposium, 1993., 1993 IEEE 1993 Sep 18 (pp. 202-208). IEEE.

[2] Webster III RJ, Romano JM, Cowan NJ. Mechanics of precurved-tube continuum robots. Robotics, IEEE Transactions on. 2009 Feb;25(1):67-78.

[1]Watch a demo video at: https://www.youtube.com/watch?v=kCwUAm8hnXE.

NeuroCYCLOPS: A Novel System for Endoscopic Neurosurgery

T. J. C. Oude Vrielink[1], D. Z. Khan[2], H. J. Marcus[1], A. Darzi[1], G. P. Mylonas[1]

[1]Department of Surgery & Cancer, Imperial College London

[2]School of Medicine, Royal College of Surgeons in Ireland

t.oude-vrielink15@imperial.ac.uk

INTRODUCTION

In many minimally invasive surgical (MIS) procedures - including intraparenchymal brain tumour resection, endoscopic laryngeal microsurgery, transanal endoscopic microsurgery (TEM), endoscopic lumbar discectomy and - tubular retraction devices are used to create and maintain a narrow corridor to the area of interest while causing minimal harm to surrounding tissue. In these procedures tissue manipulation is achieved by inserting long rigid instruments into the corridor. However, the geometry of the retraction device, in combination with the length of the instruments, limits the dexterity and control of the instrument.

In previous studies, the CYCLOPS system has shown to be able to overcome these limitations by offering 5 or 6 DOF while maintaining force feedback capabilities in general surgical procedures [1]. The present study applies the same tendon-driven parallel manipulation principle of the CYCLOPS to microsurgical procedures that use tubular retraction devices.

Among the most common microsurgical procedures performed within the brain is the microsurgical resection of intrinsic brain tumours. The 11.5mm diameter Neuro-endoport® (NEP) (UPMC, Pittsburgh, PA) has been used for nearly atraumatic brain tissue retraction to gain transparenchymal access to deep-seated lesions [2]. However, approaches using the NEP are very technically challenging and have not been widely adopted by the neurosurgical community [3]. Here, we report the development and early validation of the neuro-CYCLOPS, a manually controlled parallel-driven manipulator for NEP surgery.

MATERIALS AND METHODS

An early 3D printed neuroCYCLOPS prototype has been developed and tested (Fig. 1). An inexpensive Ultimaker 2+ Desktop 3D printer (Ultimaker Holding B.V., The Netherlands) was used for manufacturing. The design is scaled up 2.2 times, to an inner NEP diameter of 21mm. The Olympus FB-52C-1 (Olympus, Japan) grasper was modified and incorporated into the design. Whereas the original CYCLOPS system is robotic, the current system is developed for manual control, but can be made robotic with the addition of motor units. The essence of the manual controlled CYCLOPS lies in replicating the slave's parallel tendon configuration for the master (Fig. 2a) and applying alterations to offer intuitive manual control. Bowden cables (shown in Fig 1a) are used to guide the 8 tendons from the master to the slave, allowing position and forces to be transferred.

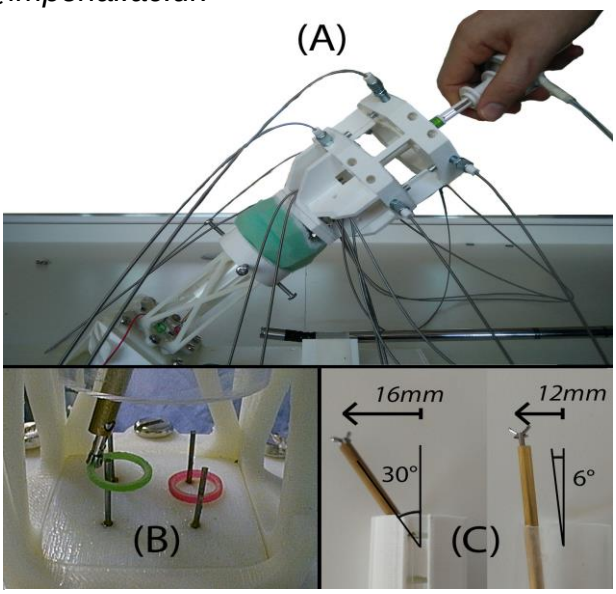

Fig. 1 A) The neuroCYCLOPS being operated during the experiments **B)** View from the scope during the pick and place task **C)** The neuroCYCLOPS can achieve higher angles than rigid instruments inserted in the modified NEP.

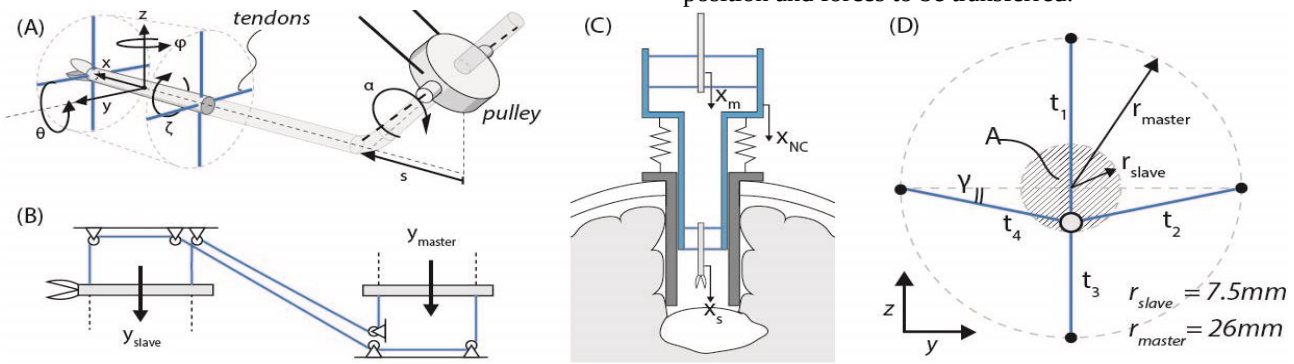

Fig. 2 A) The slave system with 6 DOF. The torsional rigid shaft is used to transmit the rotation of the master to the slave and enable rotation ζ. **B)** The alternative tendon configuration shown schematically in a 2D plane. The configuration is required for the slave to mimic the movement of the master in 4DOF (y,z,θ,φ). **C)** Schematic of the neuroCYCLOPS placed in the NEP. The movement of the end-effector in the x-axis (x_s) is facilitated by allowing the entire system to move with x_{NC}. **D)** Elongation of the tendons is minimized by increasing the size of the master relative to the slave ($r_{master} \gg r_{slave}$).

The first alteration to achieve manual control is the connection between the master and slave, as shown in Fig. 2b, resulting in a direct duplication of movement of the master in 4 DOF (y, z, θ, φ). However, this tendon rearrangement results in movement in the X-axis to be mirrored ($x_m = -x_s$ Fig. 2c). This is compensated by allowing the entire scaffold to move relative to the NEP in the x-direction, denoted as X_{NC}. This is beneficial for neurosurgical applications, as it allows for large movement in the x-direction required for the resection of large lesions. The 6th DOF, rotation around the x-axis (ζ), is achieved by using a torsionally rigid – yet with a low flexural stiffness - tube to transmit this additional degree of freedom to the end-effector. The torsion is transmitted from the master using a pulley mechanism (Fig. 2a). The pulley tendons are guided through Bowden cables, and the pulley is able to rotate at an angle α to accommodate length changes in the *s*-direction. Lastly, the master manipulator is increased in size compared to the slave to be able to compensate for elongation of the tendons ($r_{master} \gg r_{slave}$, Fig. 2d). If the radius would be equal ($r_{master} = r_{slave}$) movement of the master in the Z-direction will result in the lengthening Δt_1 of tendon t_1 and shortening Δt_3 of tendon t_3. As the tendons have been reconfigured (Fig. 2b) the overall lengthening of the tendons is described as $\Delta L_1 = \Delta t_{1,master} - \Delta t_{3,slave} = 0$. Thus, for movement in the z-axis, the tendons aligned with this direction will not lengthen. However, for this same movement the tendons t_2 and t_4 - aligned in the y-axis – will both increase in length: $\Delta L_Y = \Delta t_{2,master} - \Delta t_{4,\mathrm{slave}} > 0$. Energy will be put into the elongation of these lateral tendons, resulting in an increase in stiffness during control and limited of controllability of the device. By increasing the diameter of the master relative to the slave scaffold, $r_{master} \gg r_{slave}$, the maximum angle γ required to manipulate the end-effector within the area A ($A = \pi r_{slave}^2$, Fig. 2d) is reduced. As a result significantly less tendon elongation is required, offering controllable manipulation within this area A.

A simple pick and place task was adopted to compare the performance of the neuroCYCLOPS against rigid instruments, both placed in a tube resembling the scaled up NEP geometry. The task was performed within an 81cm3 box trainer that has previously been validated for keyhole neurosurgery [3]. An Endoeye Flex 3D laparoscope (Olympus, Japan) was used, and set in 2D mode to mimic the more commonly used 2D scopes. Performance was assessed using the MISTELS and NASA-TLX for task working load assessment. The number of collisions between the instruments and the surrounding structures was used as a metric for controllability, and were measured using an Arduino Leonardo (Arduino, Italy) and electrical contact between the instrument (anode) and the environment (cathode).

	neuroCYCLOPS	Conventional
Time [s]	$51.8 \pm 19.7s$	$50.3 \pm 16.4s$
Clashes [#]	11.7 ± 7.3	24.7 ± 12.9
NASA-TLX [-]	50.0 ± 17.7	62.5 ± 16.8

Table 1 – Comparison between the neuroCYCLOPS and conventional rigid instruments (n = 10).

RESULTS

While using the neuroCYCLOPS, novice participants (n = 10, 24-57 years old, 7:3 Male:Female) showed a significant decrease of clashes with surrounding structures (p = 0.0068, one-tailed paired T-test, Table 1), without any difference in time (p = 0.787, two-tailed paired T-test). The NASA-TLX also indicated that the participants perceived a lower workload in favour of the neuroCYCLOPS (p = 0.0025, one-tailed paired T-test).

DISCUSSION

The first tests with the manual controlled neuro-CYCLOPS were positive, showing the pick and place test could be performed successfully and intuitively. Also, the neuroCYCLOPS was more stable to control and was least affected by hand tremor when compared to standard long rigid instruments. This is signified by the reduced amount of clashes with surrounding structures. Additionally, the neuroCYCLOPS has shown to be able to attain a larger instrument angle and have a wider range for the same protrusion compared to the rigid instrument (Fig 1c). Dexterous and accurate control of the end-effector is highly desirable for safety in many microsurgical procedures, and in particular when handling delicate brain tissue. Also, the increased dexterous workspace may allow further reduction of the NEP diameter without loss of surgical efficacy. This initial study with the neuroCYCLOPS has shown that the prototype offers a safe, intuitive, and low-cost platform for neurosurgical procedures.

This abstract demonstrated the early steps in the combination of the CYCLOPS system with existing tubular retraction devices to offer accurate and intuitive control for microsurgical minimally invasive procedures. Further development includes the addition of a second instrument to allow for bimanual control, and the introduction of a small diameter endoscope via the NEP shaft. More accurate manufacturing methods will allow miniaturisation of the device for use in clinical settings. The current system is designed for manual control, which offers significant cost savings and imposes less regulatory hurdles. However, for applications that may benefit from robotic control the system can be easily adapted.

This work is supported by the ERANDA Rothschild Foundation.

REFERENCES

[1] Mylonas GP, Vitiello V, Cundy TP, Darzi A, Yang GZ. CYCLOPS: A versatile robotic tool for bimanual single-access and natural-orifice endoscopic surgery. Proc - IEEE Int Conf Robot Autom. 2014:2436-2442.

[2] Kassam AB, Engh J a, Mintz AH, Prevedello DM. Completely endoscopic resection of intraparenchymal brain tumors. J Neurosurg. 2009;110(1):116-123.

[3] Marcus HJ, et al. Endoscopic and keyhole endoscope-assisted neurosurgical approaches: a qualitative survey on technical challenges and technological solutions. British J Neurosurg. 2014:28(5): 606-610.

[4] Marcus HJ, et al. Comparative Performance in Single-Port Versus Multiport Minimally Invasive Surgery, and Small Versus Large Operative Working Spaces A Preclinical Randomized Crossover Trial. Surg. Innov. 2015, 23(2):148-155.

Direct Permanent Magnet Localisation for Catheter Tracking in Intracranial Navigation

L. Maréchal[1], Z. Sun[2], S. Foong[2], K.L. Wood[2], V. Patil[3], R. Gupta[4]

[1]*Centre for Robotics Research, Department of Informatics, King's College London, UK*

[2]*Magneto-Mechatronics Lab, Singapore University of Technology and Design, Singapore*

[3]*Patient Informatics, Boston, USA*

[4]*Harvard Medical School, MGH, Boston, USA*

luc.marechal@kcl.ac.uk

INTRODUCTION

Magnetic localisation systems based on passive permanent magnets (PM) are of great interest due to their ability to provide non-contact sensing and without any power requirement for the PM. Medical procedures such as ventriculostomy can benefit greatly from real-time feedback of the inserted catheter tip. Motivated by the need to improve the accuracy and precision of localisation of permanent magnet based systems, we propose an adapted method to achieve ventriculostomy tracking. Magnetic sensors usually exhibit non-systematic errors that are difficult to characterise adequately with a parametric function since it occurs in the 3 dimensions with possible non-linear coupling effects. This leads to inevitable tracking errors when using the traditional inverse optimisation method for dipole model (DM) localisation [1-2]. In contrary to a physical model, Artificial Neural Networks (ANNs) are directly used for solving the inverse problem for improved efficiency and precision [3]. Key advantage of this direct approach is that sensor intrinsic characteristics can be incorporated directly with the ANN.

MATERIALS AND METHODS

The sensing device is composed of a cluster of eight MAG3110 3-axis magnetic sensors (Freescale, Austin, TX) mounted onto the fixed reference frame arranged around a hole with a specific pattern to let the catheter go through. As shown in Figure 1, it is positioned normal to the skull surface and its origin coincides with the catheter insertion burr hole in the skull. The digital sensors have a resolution of 0.10 µT within a range of ±1000 µT. The sensors measurements are acquired with an ATmega32U4 microcontroller, running at 8 MHz and sent to a computer via a ZigBee wireless communication. The sensing mechanism, shown in Figure 2, uses the direct approach of mapping magnetic field measurements directly to position of the PM from the sensor assembly with a 20 hidden network layer ANN. For numerical computation, MATLAB's neural network toolbox (Mathworks, Natick, MA) is used to design and train the ANN for direct sensing. The implemented neural networks accepts n magnetic sensors field data as inputs (B_{x1}, B_{y1}, B_{z1}, … , B_{xn}, B_{yn}, B_{zn}) and produce (x, y, z, m, n, p) coordinates and orientation of the tracked location outputs. The main drawback of ANNs is that they are in essence non-parametric functions and should be considered within the framework of the application for which the calibration is thought to be applied. They therefore need a learning process and are only reliable in a beforehand mapped region of interest (ROI). It consisted in multiple uniform magnetic field measurements with random orientation of the magnet (within relevant ranges) at each position. The catheter is inserted through a small hole in the skull for the ventriculostomy procedure. Consequently, we can reasonably define the whole expected tracking positions as a cone. The possible orientations of the magnet can also be limited regarding the physical constrains of the catheter. This one is thus very unlikely to bend of an angle exceeding 45˚ from the axial plane. We used 52800 training points with a 3D spatial resolution of 1 mm in a volume of 90 cm^3.

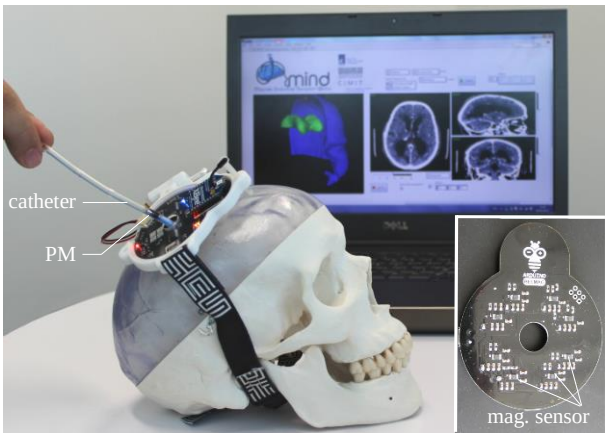

Fig. 1 Magnetic sensor based localisation device.

To quantify and characterise the localisation error, a 6-axis high-precision articulated robotic arm (VS-068, Denso Robotics, Aichi, Japan) is employed. A Grade N52 Neodymium (Nd-Fe-B) magnet from K&J Magnetics (Jamison, PA, USA) with length of 9.5 mm and diameter of 3.2 mm is attached at the end of the end-effector of the arm. The robotic arm has a positional repeatability of ±0.02 mm and was used to accurately manoeuvre the PM to the desired position and orientation. It was then used to replicate four different

representative catheter trajectories of the intervention composed of 120 points. This was performed within and outside of the ROI. The inverse DM-based model and the direct ANN tracking efficiency were concurrently tested on the same sets of data by comparing the actual position of the magnet (through the robot arm) with the estimated position (via magnetic sensor measurements). The setup is presented in Figure 3. We used a pig's head to be as close as possible to the real situation.

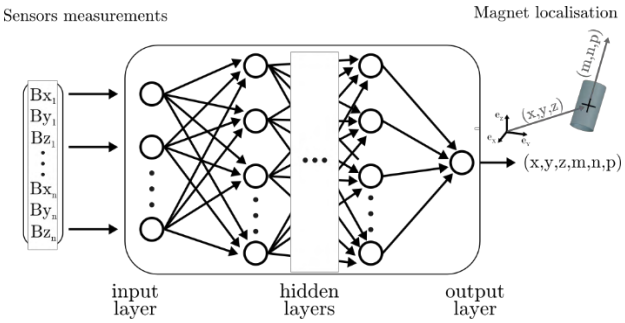

Fig. 2 ANN-based direct magnetic field-based sensing scheme. The sensors data are input in the model and associated to the output (position and orientation estimates of the PM) through the neural network (adapted from [4]).

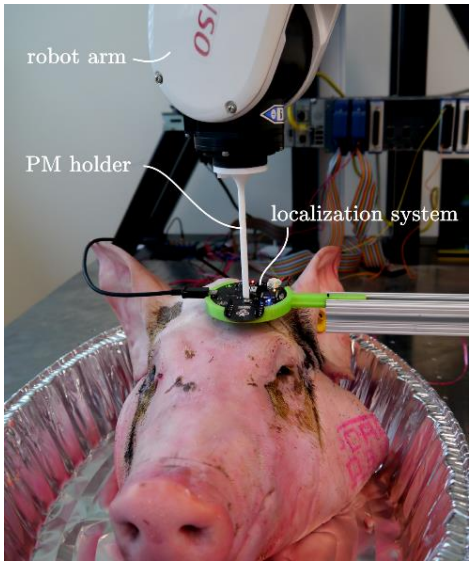

Fig. 3 Experimental setup. The referent catheter insertion into the pig's head are performed by the robotic arm.

RESULTS

Table 1 summarises the RMSE and the maximum tracking error throughout the referent catheter insertion paths tested. Based on the results, also illustrated in Figure 4 which overlays the true and estimated position, the ANN outperforms the DM for the localisation efficiency when the PM remains within the ROI. The trace of the PM was found to deviate by maximum 1.6 mm from the original pathway at distance to sensors up to 62 mm. The average tracking error with the ANN is about 1 mm (greater than 5 mm with DM). In contrary, the inverse method is more able to accurately track the PM outside of the ROI but still with a relative low accuracy and a maximum Euclidean error encountered significantly high.

TABLE I
Localisation Accuracy across the Field Models

Model	DM	ANN
Within the ROI		
RMSE (mm)	5.8	1.1
Euclidean error max.	12.6	1.6
Outside the ROI		
RMSE (mm)	7.1	11.6
Euclidean error max.	11.7	23.2

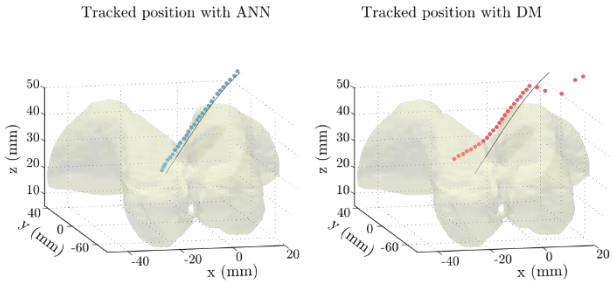

Fig. 4 Representation of the brain ventricle targeted and comparison of the spatial localisation of the inserted catheter path between ANN (in blue) and DM-based model (in red). The dark plain lines represent the true trajectories. The dots stand for the estimated coordinates.

DISCUSSION

Even though the improvements obtained with the proposed model and training technique is significant in comparison to DM-based tracking, the ANN method can only work within the trained ROI completed. For now, the choice of tracking methods depends on the actual requirements in the specific medical interventions. For future work, a hybrid model fusing both the ANN and DM based method will be formulated in order to simultaneously capitalise on the accuracy of the ANN and the wide range of solution space of the DM where points have not been characterised *a priori*.

REFERENCES

[1] L. Maréchal, S. Foong, S. Ding, KL. Wood, V. Patil, R. Gupta, Design Optimization of a Magnetic Field-Based Localization Device for Enhanced Ventriculostomy. ASME. J. Med. Devices. 2016:10(1).

[2] Z. Sun, S. Foong, L. Maréchal, U-X. Tan, T.H. Teo and A. Shabbir. A Non-invasive Real-time Localization System for Enhanced Efficacy in Nasogastric Intubation. Annals of Biomedical Engineering. 2015:43(12): 2941-2952.

[3] F. Wu, S. Foong and Z. Sun. A hybrid magnetic field model for axisymmetric magnets. IEEE/ASME Transactions on Mechatronics. 2015:20(3):1278-1287.

[4] S. Haykin, Neural Networks and Learning Machine. 3rd ed. Pearson, Ed. Prentice Hall. 2009.

Compliant Rolling DOF for a Soft Surgical Module

D. van der Pol, M. Brancadoro, G. Gerboni, M. Cianchetti, A. Menciassi

The BioRobotics Institute, Scuola Superiore Sant'Anna, Italy

d.g.m.vanderpol@student.tudelft.nl, m.brancadoro@sssup.it

INTRODUCTION

Minimally invasive surgical instruments are continuously evolving in order to respect the constraints of the limited size of access ports (small incisions in the skin), to fulfil the need of high dexterity and flexibility in a small workspace, and to identify effective actuation methods able to develop relevant forces using remote power sources [1]. These aspects, combined with the need for safe tissue interaction and manipulation, contributed to the growth of novel soft robotic devices for Minimally Invasive Surgery (MIS) procedures. An example of a soft manipulator is the STIFF-FLOP arm (http://www.stiff-flop.eu/). It is a bioinspired surgical device composed by three silicone modules, which replicates most of the motion capabilities of an octopus arm. Each module is remotely controlled in 3D space by a pneumatic system which manages the pressure supply to all its inner chambers. Thanks to the chamber geometry and combination of supplied pressures, each STIFF-FLOP module is able to either elongate or bend in all the directions [2]. The STIFF-FLOP manipulator contains an inner free lumen to allow the insertion and fixation of different surgical tools (*e.g.* gripper, cauterization and camera) at the end-effector. On the other hand, the full articulation of the soft robot does not allow the end-effector to be rolled around its axis without changing the configuration of the entire soft robot. For this reason, the possibility to add a rolling Degree Of Freedom (DOF) to the end-effector would represent a relevant improvement for the system, as most of the MIS procedure tasks would require such capability for the tool.

The aim of this work is to implement a rolling DOF to the end-effector of the STIFF-FLOP arm. The authors propose a device combining a pneumatic actuator with an origami twisting module [3].

MATERIALS AND METHODS

The proposed device (Fig. 1a) is composed by two main parts: a soft pneumatic actuator and an origami module. The actuator has the same structure as a STIFF-FLOP module, but with reduced length and with all the chambers connected at the same input of pressure (for obtaining elongation along the z axis and not bending). As described in [3], a longitudinal force, which in this case is produced by the soft pneumatic actuator (F_a) can be converted into a rotary motion by means of a twisting origami module. Fig. 1b shows the forces applied to the device where F_l represents the force produced by one origami leg. According to the geometry of the twisting module and screw-like motion, the twisting angle γ of the origami upper plate with respect to the base plate (fixed to the pneumatic actuator) can be described as [3]:

$$\gamma = 2\,sin^{-1}\left(\frac{\sqrt{l^2-(l-d)^2}}{2r}\right) \quad (1)$$

Where d is the actuator elongation along the z-axis and l and r represent the geometrical values relative to the origami legs (Fig. 1c). Note that the equation (1) holds when the initial distance between the upper plate and the origami base is equal to l. The values of l (10.6 mm) and r (7.5 mm) have been selected in order to obtain a maximum twisting angle of about 90° at the maximum actuator elongation. The 2D drawing in Fig. 1c shows the cutting lines (solid lines) and the folding lines (dashed lines) of the origami twisting module. This drawing was used to create different origami twisting modules, in terms of materials, all fabricated by using a laser cutting machine. The 3D structures depicted in Fig. 1d resulted from folding the four laser cut 2D geometries of Fig. 1c. The materials used were the following: (1) inkjet paper (density of 100 g/m^2), (2) transparency film (Polyester with coating), (3) Polypropylene with reinforced legs using a 1 mm layer of Plexiglas and (4) Polyvinylchloride. All the different origami modules were combined with a soft pneumatic actuator and tested. Material (3) showed the most promising performance in terms of rolling reliability and stability. This was mainly due to the low bending stiffness of the propylene which facilitated the folding process.

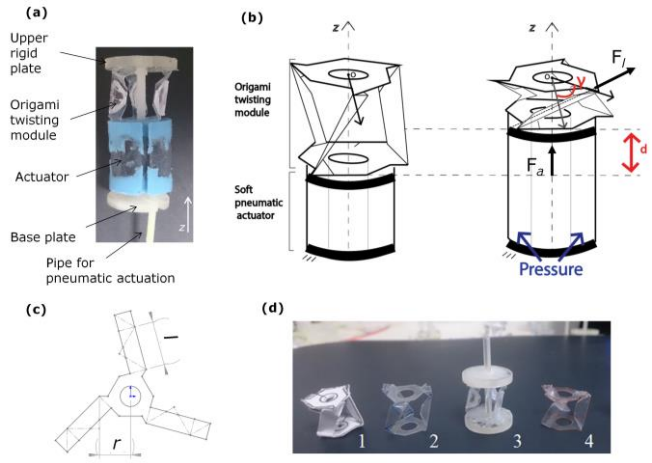

Fig. 1 (a) Picture of the prototype. (b) Scheme showing the working principle of the rolling DOF. (c) Drawing pattern used with the laser cutter to realize the origami module. (d) Four origami modules made out of different laser-cut thin sheet materials.

Furthermore, the legs of origami were reinforced to reduce their deformation during working, which improves the effectiveness of the structure.

The entire structure (*i.e.* soft pneumatic actuator and origami structure) is hollow to allow the passage of eventual pipes/wires used for the activation of the end-effector tool (*e.g.* pneumatic gripper, electro-cauterization tools, etc.). The behaviour of the origami twisting module combined with the soft pneumatic actuator was evaluated with a series of experimental tests (Fig 2). During the tests the base of the actuator was attached to a Mitsubishi MELFA RV-3SB 6DOF robot arm. In all the tests the controlled variable was the air pressure to the pneumatic actuator, while the dependent variables were the twisting angle γ, the actuator elongation d, the actuation force F_a and the twisting module torque T.

The twisting angle γ was obtained from a scale indication on top of the rotating disk (Fig 2a) while the actuated elongation d was measured with a calliper (Fig 2b). The force and torque were measured by an ATI Nano 17 Force & Torque sensor (Fig 2c and Fig 2d).

During the tests, the same pressure range (from 0 to 1.3 bar, with 0.1 steps) was used and four repetitions for each test were performed.

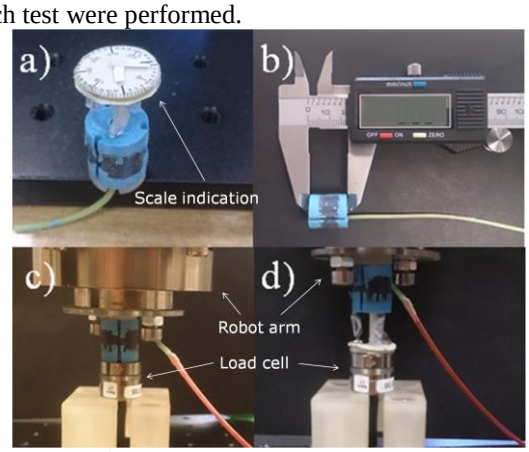

Fig. 2 Setup of the experimental test to evaluate: (a) the twisting angle, (b) the actuator elongation, (c) the force and (d) the torque of the proposed device.

RESULTS

In the final prototype, the soft pneumatic actuator reached a maximum elongation of about 6 mm at a pressure of 1.3 bar, generating a maximum pushing force of 12.7 N (measured at the top of the silicone module, that is where the twisting mechanism should be attached). The relationship between the generated force in isometric condition and air pressure is reported in Fig. 3a. The twisting angle of the origami (γ) versus the actuator elongation (d) is plotted in Fig. 3b, which also shows the comparison between analytical model and experimental results. For the first one, equation (1) was used. The analytical twisting angle corresponding to the maximum actuator elongation is 78°, while the experimental angle reached approximately 54°.

Finally, the torque-pressure relationship is shown in Fig. 3c, where it can be observed that the maximum torque produced by the proposed device was about 2.5 Nmm.

DISCUSSION

The force generated by the soft pneumatic actuator is demonstrated in Fig. 3a, showing the potential of a STIFF-FLOP module-like actuator. The difference between the analytical and the measured twisting angle can be due to the error in starting position, in which the legs should be pointing up and be perfectly straight. The large standard deviation of the experimental data in Fig. 3b is due to the stick-slip behaviour caused by the friction between the rotating upper plate and the sliding bearing, made out of 3D printed material (Acrylonitrile Butadiene Styrene). In Fig. 3c the standard deviation of the measurements is much smaller because the top plate of the mechanism was locked for measuring the torque, so there is no stick-slip behaviour here.

The origami module geometry can be optimized by increasing the leg length and reducing the radius and leg thickness. The stick-slip behaviour can be reduced by using a smoother sliding bearing.

In conclusion, this work presents the development and characterization of a pneumatically activated rolling DOF mechanism which is very lightweight (3.3 g) and is composed of flexible materials. The analytical model and the experimental tests demonstrated that the system is able to perform an acceptable range of twisting angle and to develop relevant values of torque.

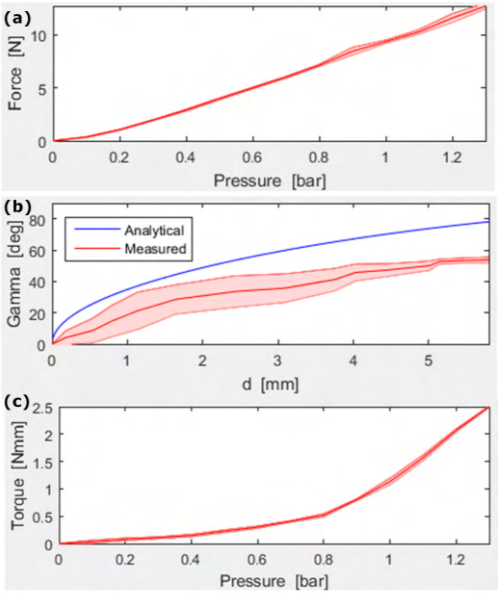

Fig. 3 (a) Actuation force from the soft pneumatic actuator. (b) Twisting angle of the origami top structure (d = 6 mm corresponds to 1.3 bar). (c) Torque produced by the device. All graphs show standard deviation of 4 measurements.

REFERENCES

[1] Antoniou SA, Antoniou GA, Antoniou AI, Granderath FA. Past, present, and future of minimally invasive abdominal surgery. JSLS: Journal of the Society of Laparoendoscopic Surgeons. 2015; 19(3).

[2] Ranzani T, Gerboni G, Cianchetti M, Menciassi A. A bioinspired soft manipulator for minimally invasive surgery. Bioinspiration & Biomimetics. 2015; 10(3): 035008.

[3] Salerno M, Zhang K, Menciassi A, Dai JS. A Novel 4-DOFs Origami Enabled, SMA Actuated, Robotic End-Effector for Minimally Invasive Surgery. In Robotics and Automation (ICRA). 2014; pp. 2844-2849.

A Soft Suction-Based End Effector for Endoluminal Tissue Manipulation

T. Ranzani, S. Russo, C. Walsh, R. Wood

Harvard John A. Paulson School of Engineering and Applied Sciences, USA

Wyss Institute for Biologically Inspired Engineering, USA
tranzani@seas.harvard.edu

INTRODUCTION

The trend towards reducing the invasiveness of surgical procedures has pushed research towards the development of smaller and smarter instrumentation, able to access remote body locations by passing through natural orifices or more convenient access points [1]. Although a variety of flexible instruments have been proposed in literature, the endoscope remains the gold standard for diagnostic and therapeutics procedures in the gastrointestinal (GI) tract. Performing therapeutic procedures, such as removal of early stage cancer, through an endoscope introduces several challenges with current instrumentation in terms of instrument stability and the capability to provide accurate and repeatable dexterous motions at the surgical site [2]. Techniques such as endoscopic submucosal dissection (ESD) have been proposed [3], but they require substantial learning curves. Different strategies have been proposed for augmenting the therapeutic capabilities of endoscopes by introducing manipulation aids or add-ons to the endoscope [4]-[6]. Embedding additional functionalities into a system that can be fixed at the tip of the endoscope represent a promising approach for improving current manipulation capabilities without disrupting the current procedure workflow. However, the design and fabrication of tools at these scales introduces several technical challenges, potentially limiting functionality. Recently, we have proposed a soft pop-up hybrid fabrication method as a promising approach for developing mm-scale mechanisms for minimally invasive surgery (MIS), and in particular in [7] we demonstrate a three degree of freedom (DoFs) arm actuated through embedded soft fluidic micro actuators that can be connected to the tip of an endoscope for manipulating endoluminal tissue (Fig. 1).

In this paper, we address the design of an end effector for manipulation of endoluminal tissue. Millimeter-scale end effectors that provide safe and effective manipulation presents a challenge for design and manufacturing. Previous work has primarily focused on jaw-like cable-actuated [8] or SMA-based grippers [9]. We propose a soft suction-based gripper that can be integrated at the tip of an arm as represented in Fig.1. The use of vacuum grippers in laparoscopy has been successfully investigated in [10][11], showing reduced skill-dependent damage to the tissues. In addition,

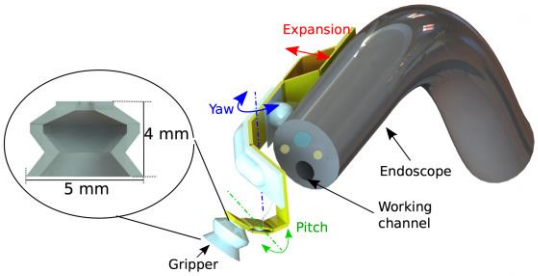

Fig. 1 CAD rendering of the soft pop-up arm proposed in [7] with an integrated suction based soft gripper.

Fig. 2. Left, fabricated prototypes of suction based soft grippers, right, zoomed view of the gripper.

suction has been successfully adopted as safe and painless locomotion strategy in the GI tract [12].

MATERIALS AND METHODS

The soft grippers are fabricated by molding Dragonskin 20 (DS20) and Ecoflex 0030 (Eco0030), (Smooth-On, PA, USA), using 3D printed molds. Four grippers are fabricated for each material (Fig. 2); the relevant dimensions are reported in the inset of Fig.1. A variation on the design includes a 200 μm membrane fabricated by spin coating Ecoflex 0030 on a wafer at 800 rpm for 30 s. The membrane is then bonded on the tip of the gripper to prevent clogging during suction.

The grippers are tested both *in vitro* and *ex vivo*. The *in vitro* characterization involved fixing the gripper on the moving tool of an Instron materials testing machine as shown in Fig.3a. Applying continuous vacuum pressure (-0.9 MPa) results in adhesion to the bottom plate. The maximum force before detachment is measured. In the *ex-vivo* test, pig stomach is selected as a specimen. The same protocol as for the *in vitro* tests is adopted. The gripper is fixed in the same way and the pig stomach is positioned on the bottom plate (Fig. 3b). A final test consisted of exploiting the gripper to tension the tissue specimen and use a scalpel to cut it (Fig. 4).

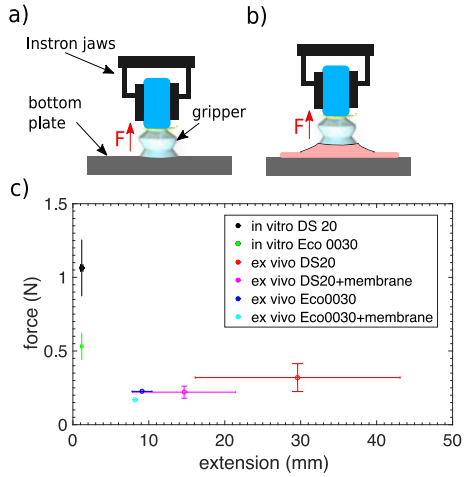

Fig. 3 Suction-based soft gripper characterization. Diagram of the setup used for *in vitro* a) and *ex vivo* b) tests. c) Results from the *in vitro* and *ex vivo* tests on pig stomach in terms of maximum tissue extension versus force required. Scale bars represents one standard deviation (for both maximum force and maximum extension) computed on three prototypes for each material, tested three times each.

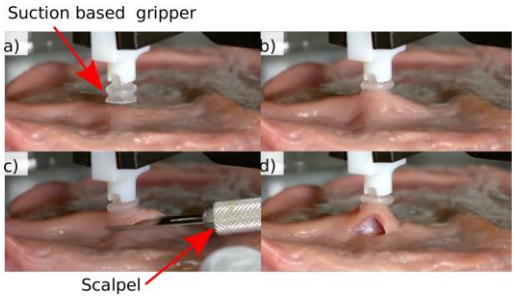

Fig. 4 Demo of the soft suction-based gripper: a) approaching the tissue, b) retraction, c) holding during cutting with a scalpel, d) additional tissue retraction.

RESULTS

Results from the i*n vitro* and *ex vivo* tests are reported in Fig. 3c. The plot shows the maximum extension versus the maximum force needed for three grippers for each material, grasping at three different locations on the tissue analogue. In the *in vitro* tests, the DS20 gripper is able to generate forces ranging from 0.9 to 1.26 N while the Eco0030 provided roughly half this force. In the *ex vivo* tests, the DS20 gripper is able to retract the tissue between 16 to 44 mm above the surface. The integration of the membrane leads to lower performance but still guarantees tissue tensioning and exposure for cutting (between 8 and 22 mm). The Eco0030 gripper resulted in lower retraction both with and without membrane. A demonstration of tissue cutting with a scalpel after pretensioning with a DS20 gripper is shown in Fig. 4.

DISCUSSION

We introduced a soft suction-based gripper for endoluminal manipulation. We tested two different materials, one softer (Eco0030) and one stiffer (DS20), the first one provided low forces and thus lower tissue exposure making it less suitable for effective tissue manipulation. The DS20 showed promising performance, providing newton range forces in *in vitro* conditions and tissue retraction up to 40 mm in *ex vivo*. We also investigate the effect of integrating a membrane on the grippers to prevent clogging during operation. The membrane reduces the performances of the gripper, although in the case of the DS20 gripper, it still provides a retraction of more than 10 mm. In order to better assess the functionality of the proposed gripper we performed a demonstration showing that the tensioning provided is sufficient to enable cutting of the specimen using a scalpel that would reasonably need more force with respect to commonly used electrocautery devices. Since the gripper uses suction, it easily grasps the tissue as soon as it is in contact with it. In addition, due to its soft nature, it passively follows changes in orientation during manipulation without requiring distal DoFs. Future work will focus on integrating the gripper on the arm presented in [7].

ACKNOWLEDGMENT

The authors would like to acknowledge the Wyss Institute for Biologically-Inspired Engineering for their support of this work. The authors would also like to acknowledge DARPA (grant FA8650-15-C-7548).

REFERENCES

[1] Vitiello V, Lee SL, Cundy TP, Yang GZ. Emerging robotic platforms for minimally invasive surgery. IEEE Rev Biomed Eng. 2013;6:111-26.

[2] Loeve A, Breedveld P, Dankelman J. Scopes too flexible... and too stiff. IEEE pulse. 2010 Nov;1(3):26-41.

[3] Maple JT, et al. Endoscopic submucosal dissection. Gastrointest endosc. 2015 Jun 1;81(6):1311-25.

[4] J. Gafford, et al, Snap-On Robotic Wrist Module for Enhanced Dexterity in Endoscopic Surgery, IEEE Int Conf Robot Autom, 2016.

[5] Phee SJ, et al Master and slave transluminal endoscopic robot (MASTER) for natural orifice transluminal endoscopic surgery (NOTES). Conf Proc IEEE Eng Med Biol Soc 2009 Sep 3 (pp. 1192-1195).

[6] Yeung BP, Gourlay T. A technical review of flexible endoscopic multitasking platforms. Int. J. Surg. 2012 Dec 31;10(7):345-54.

[7] S. Russo, et al, Soft pop-up mechanisms for micro surgical tools: design and characterization of compliant millimeter-scale articulates structures, IEEE Int Conf Robot Autom, 2016.

[8] Gafford JB, Kesner SB, Wood RJ, Walsh CJ. Force-Sensing Surgical Grasper Enabled by Pop-Up Book MEMS. IEEE Int Conf Intel Rob Sys, 2013.

[9] Houston K, et al, Polymer sensorised microgrippers using SMA actuation. IEEE Int Conf Robot Autom, 2007.

[10] Horie T, Sawano S, Konishi S. Micro switchable sucker for fixable and mobile mechanism of medical mems. Microelectromech. Syst. 2007 Jan (pp. 691-694).

[11] Vonck D, et al. Vacuum grasping as a manipulation technique for minimally invasive surgery. Surg endosc. 2010 Oct 1;24(10):2418-23.

[12] Dario P, Ciarletta P, Menciassi A, Kim B. Modeling and experimental validation of the locomotion of endoscopic robots in the colon. Int. J. Robot. Res. 2004 Apr 1;23(4-5):549-56.

Computer Assisted Navigation in Total Hip Arthroplasty – A Systematic Review

F. Mohamed[1], R. Shenoy[2], S. Malik[3], I. Ryland[4], E. Davis[5]

[1]Leicester Royal Infirmary, Leicester, UK

[2]Royal National Orthopaedic Hospital, Stanmore, UK

[3]Sandwell and Birmingham Hospital, Birmingham, UK

[4]Edge Hill University, Ormskirk, UK

[5]Russell's Hall Hospital, Dudley, UK

Fahad.Mohamed@uhltr.nhs.uk

INTRODUCTION

The cup position in a total hip replacement (THR) plays a crucial role in achieving stability and reducing wear, thereby improving the longevity of the hip replacement [1,2]. The inaccuracy in component placement using conventional mechanical guides has resulted in the development of tools to aid precise cup positioning. Computer assisted navigation is emerging as one of the tools aiding total hip replacement.

AIM

We conducted a systematic review of randomised control studies (RCT) comparing computer assisted navigation, specifically in cup positioning during THR, with free hand cup positioning.

METHODS

All RCT's published in English from 2008 to August 2014 were included in the review. The Preferred Reporting items for Systematic Reviews and meta-analysis (PRISMA) statement [3] was used in this study. Primary outcomes were cup inclination and anteversion. Secondary outcome measures including surgical time, limb length discrepancy, complications and functional scores were reviewed.

RESULTS

Accuracy of mean anteversion with navigation was significantly better in 2 out of 4 studies [Table 1]. There was no difference in the mean cup inclination in 3 out of 4 studies [Table 2]. Complication rates were similar between the groups. Navigation leads to increased surgical time. Navigation increased the chance of placing the cup within the safe zone by reducing the number of outliers.

DISCUSSION AND CONCLUSION

Navigation improves the precision of cup placement within the target zone compared to conventional methods. Evidence on the functional benefits of navigation are limited and cost implications are a drawback for surgeons aiming to adapt computer navigation into clinical practice. We recommend further studies assessing functional benefits of navigation.

Study	Expected cup anteversion	Mean cup anteversion navigated group	Mean cup anteversion freehand group	P value
Lass 2014	15°	19.5° +/- 4.6°	17.3° +/- 10.4°	0.007
Gurgel 2014	15°	17.4° +/- 6.3°	14.5° +/- 8.3°	0.239
Sendtner 2011	15°- 20°	24.5° (12°- 33.3°)	23.8° (5.6°- 46.9°)	0.739
Lin 2011	22.6°	15.5° +/- 5.6°	20.3° +/- 7.6°	<0.05

Table 1 Mean cup anteversion in the studies reviewed.

Study	Expected cup inclination	Mean cup inclination navigated group	Mean cup inclination freehand group	P value
Lass 2014	40°	38.6° +/- 3.6	37.7° +/- 5.2°	0.29
Gurgel 2014	40°	41.7° +/- 3°	42.2° +/- 3.3°	0.633
Sendtner 2011	40°- 45°	42.3° (32.7°- 50.6°)	37.9° (25.6°- 50.2°)	0.002
Lin 2011	42.3°	39.8° +/-2.2°	42.5° +/- 6.3°	N/A

Table 2 Mean cup inclination in the studies reviewed.

REFERENCES

[1] Lewinnek GE, Lewis JL, Tarr R, Compere CL, Zimmerman JR. (1978) Dislocations after total hip- replacement arthroplasties. J Bone Joint Surg [Am]. 1978;60:217–220.

[2] Wan Z, Boutary M, Dorr LD. (2008) The influence of acetabular component position on wear in total hip arthroplasty. J Arthroplasty. 2008;23:51-6.

[3] Moher, D., Liberati, A., Tetzlaff, J., Altman, D.G. & PRISMA Group 2009, "Preferred reporting items for systematic reviews and meta-analyses: the PRISMA statement", BMJ (Clinical research ed.), vol. 339, pp. b2535.

Computer Navigation Helps Reduce the Incidence of Noise after Ceramic-on-Ceramic Total Hip Arthroplasty

S. Shah, K. Deep, C. Siramanakul, V. Mahajan, A. H. Deakin, F. Picard, D. Allen, J. Baines

Golden Jubilee National Hospital, Clydebank, UK

Siddharth.Shah@gjnh.scot.nhs.uk

ABSTRACT

Background and Aim: Noises like squeaks, clicks, grunts, grinds, etc. are well recognised after ceramic-on- ceramic (CoC) total hip arthroplasty (THA). Computer navigation can help control several factors like cup orientation, global anteversion, centre of rotation, limb lengths, and offsets which may reduce the overall incidence of noise. Our primary aim was to compare the incidence of noise between navigated and conventional CoC THA. Our secondary aim was to determine the factors associated with noise.

Materials and Methods: Between March 2009 and August 2012, all patients undergoing CoC THA with the same type of implant were identified from the hospital database. Data regarding noise was obtained from patients on a pre- written questionnaire over telephone or by post. Demographic variations [age, gender, body mass index (BMI), head size] were assessed for relationship with noise for the entire cohort. Demographics for navigated and conventional groups were compared. Based on these results a subgroup of cohort of <65 years and 32mm head size was used to compare the navigated and conventional groups for noise. Postoperative pelvic x-rays were evaluated for cup anteversion, cup inclination, femoral offset, and hip offset.

Results: A total of 375 CoC THAs (202 navigated and 173 conventional THAs) were evaluated. The overall incidence of noise was 14.7% with 7.7% squeaking THAs and 7% THAs with other noises. Patients <65 years of age had significantly greater incidence of noise (22.4%) as compared to those ≥65 years (6.1%; $p<0.001$). There was no significant difference between silent and noisy THAs with respect to gender ($p=0.47$) and BMI ($p=0.38$). Patients in the conventional group were significantly younger (58.3 ± 9.1 years) as compared to navigated group (67.2 ± 9.4 years; $p<0.0001$). There was significant difference in the head sizes between the two groups ($p=0.0006$). In order to ensure similarity, a subgroup of cohort of <65 years and 32mm head size was used to compare the navigated (68 THAs) and conventional (118 THAs) groups for noise. The overall incidence of noise was significantly greater in the conventional group (28%) as compared to navigated group (10%; $p=0.005$). Odds ratio for noise for conventional vs. navigated group was 3.4 ($p=0.007$) and for squeaking was 2 ($p=0.2$). Squeaking THAs (13.4°± 5.2°) had significantly lower cup anteversion as compared to silent THAs (17.6°± 6.9°; $p=0.01$). There was no significant difference between silent and squeaking THA groups with respect to cup inclination, femoral offset, and hip offset ($p\geq0.15$). There was no significant difference between silent THAs and THAs with noises other than squeak with respect to cup anteversion, cup inclination, femoral offset, and hip offset ($p\geq0.07$). No patient in either conventional or navigated group was revised for noise.

Conclusion: Navigated CoC THAs were 3.4 times less likely to make noise & 2 times less likely to squeak, although the latter was not statistically significant. Squeaking THAs had significantly lower cup anteversion as compared to silent ones. Younger patients (<65 years) were significantly more likely to have noise after CoC THA.

One Hundred Consecutive Computer Navigated Fixed Bearing Unicompartmental Knee Replacements:
A Prospective Study Reporting on Patient Reported Outcome and Radiological Analysis at a Minimum of 5 Years

D. Nathwani, P. Pastides, J. Windley

Department of Trauma and Orthopaedics, Imperial College Healthcare NHS Trust, Charing Cross Hospital, London, UK

ppastides@hotmail.com

BACKGROUND

The use of unicompartmental knee replacements (UKR) to treat isolated degenerative arthritis of the knee is gaining in popularity. Computer navigation utilisation during knee arthroplasty remains somewhat limited within the United Kingdom, however it allows for more accurate component implantation, which in turn may lead to a reduction in revision rates for prosthetic mal-positioning. We suggest that computer navigation plays a vital role, in addition to precise surgical technique, in the successful outcome following UKRs.

METHODS

One-hundred consecutive computer-navigated, fixed bearing UKRs were implanted between April 2007 and December 2010 by the senior author. Patients were assessed prospectively clinically and radiologically in the outpatient clinic. Sequential Oxford Knee Scores (OKS) were collected.

RESULTS

Our cohort included 54 male and 46 female knees; 8 patients having had staged bilateral procedures. Three patients had passed away and 3 were lost to long term follow up; leaving a final cohort of 94 patients. The mean patient age at the time of surgery was 66.7years and the mean follow up period was 69.9 months. There were no cases of prosthetic subsidence or loosening. Table 1 shows the post operative alignment of the components.

Table 1. Post operative assessment of components alignment.

	Coronal Alignment (varus-/valgus+)	Sagittal Alignment (posterior slope)
Pre Op Aim	0	-3
Post Op Assessment		
Mode (degrees)	0	-2
Mean (degrees)	-0.55	-2.1
SD	0.81	0.74
Range	0 to -3	0 to -4

Table 2 shows the patient reported functional OKS. The mean OKS was 38.6 (range 48-9). One overhanging tibial base plate was revised at 10 months for pain, while another was revised to a TKR in another institution.

Table 2. Mean Oxford Knee Scores.

	Mean OKS	Range
All cohort (N=93*)	38.6	48-9
Age < 55 (N=9)	22.9	48-9
Age 55-64 (N=36)	39.8	48-23
Age 65-74 (N=29*)	42.7	48-30
Age > 75 (N=19)	38.5	48-4
Medial UKR (N=88)	39.1	48-4
Lateral UKR (N=5*)	33.8	48-19
* excludes 1 case that was revised to a TKR		

REVISION RATES

The reported revision rate from the UK NJR at 5 years for <55 year olds, 55-64 year olds, 65-74 year olds and > 75 year olds is 10.2%, 6.64%, 5.66% and 3.05% respectively. Our revision rate is 1 case (3.3%) in the 65-74 aged category.

CONCLUSIONS

Our 5 year conversion rate to TKR is 1%. Our patient cohort appear both clinically and radiologically satisfied with the outcome of their surgery.

IMPLICATIONS

We conclude that in experienced hands and with a predictable design, aided by the use of computer navigation, a UKR results in a more accurate, successful and reliable surgical outcome with a very high functional outcome. Our revision rate is lower than the reported NJR rate and we are confident that our longer term results will continue to show favourable outcomes.

Longitudinal Gait Analysis of Orthopaedic Patients using a Single Ear-Worn Sensor: A Potential for Remote Home-Based Assessment of Post-Operative Gait Improvement

D. Jarchi[1], P. Pastides[1], B. Lo[2], C. Wong[2], E. Leong[1], D. Nathwani[1], G.Z. Yang[2]

[1]Department of Trauma and Orthopaedics, Imperial College Healthcare NHS Trust, Charing Cross Hospital, London, UK

[2]The Hamlyn Centre for Robotic Surgery, IGHI, Imperial College London, UK

ppastides@hotmail.com

BACKGROUND

Gait analysis as a tool following orthopaedic surgery is an excellent method of assessing objective functional outcome. Furthermore, pre operative analysis may allow a tailored, patient centred therapy regimen to be formulated. Methods of gait assessment include general observation or a more formal, time consuming and expensive analysis in a gait laboratory. We present data on the use of the ear-worn Activity Recognition (e-AR) sensor for clinical gait analysis in free walking environments to facilitate clinical asesssment of orthopaedic patients after surgery.

METHODS

The e-AR sensor developed by Sensixa shown in Fig. 1 is used for this study. It contains a 3D accelerometer (Analog Devices ADXL335), an 8051 processor with a 2.4-GHz transceiver (Nordic nRF24E1), a 2-MB EEPROM (Atmel AT45DB161), and a 55-mAhr LiPolymer [26]. The sensor is ergonomically designed and proven to be robust for capturing gait related acceleration signals from either the left or right ear. The sensor signal can be either stored on the sensor node or wirelessly interrogated on a tablet. It allows real-time visualisation and processing of detailed gait signals, as well as capturing individual patient information that can be interfaced to electronic medical records. The platform also permits synchronised video recording, which can be used as a reference or ground truth for subsequent data analysis.

Fig. 1 The e-AR sensor developed by Sensixa.

The sensor includes an accelerometer and the major advantages of the sensor are in its bio-inspired design, simplicity in consistent sensor placement, ease of clinical adoption, and good patient compliance, which makes the sensor suitable for large-scale deployment in the clinic.

For analysis of force-related gait asymmetry, a pair of pressure insoles (PAROTEC, Paromed, Germany) was used in 10 patients to provide reference data for validating the e-AR sensor and associated analysis algorithm. Both insoles are connected to the controller using two cables. The PAROTEC system is used in this study to observe left/right gait asymmetry from the e-AR sensor versus the ground reaction forces (GRFs) given by the insoles

Data from 54 patients (23 ACL patients and 31 patients with unicompartmental or total knee replacement) was collected for reliability assessment of the proposed algorithm. In addition, a dataset from 16 patients with lower limb trauma has been used for detecting changes in their gait every three months following surgery.

RESULTS

The sensor and the algorithm utilised was able to assess symmetry of movement, over exerted pressure on either heel or foot, speed of movement and acceleration from each foot. This was validiated against the PAROTEC pressure insoles.

CONCLUSIONS

The e-AR sensor has been shown to be an accurate, easy to use and reproducible method of assessing, mapping, recording, analysing and ultimating forming a patient centred and personalised recovery program in order to improve post operative rehabilitation for orthopaedic patients. Furthermore, it can be use in a free walking environment, during a routine outpatient clinic and provide realtime information to the treating physician.

IMPLICATIONS

The e-AR sensor has the potential to allow easy, reproducible and accessible data to enhance post operative orthopaedic rehabilitation with the prospect if developing to a home-based gait analysis platform.

The Transverse Acetabular Ligament and Acetabular Margin as a Guide to Cup Orientation in Total Hip Arthroplasty

K. Deep

Department of Orthopaedics, Golden Jubilee National Hospital, UK

mrkdeep@gmail.com

INTRODUCTION

In THA many surgeons orientate the cup in the same anteversion and inclination as the inherent anatomy of the acetabulum, using either the acetabular rim or transverse acetabular ligament (TAL) as a reference. The aim of this study was to describe the orientation of acetabular rim and compare it with TAL orientation.

METHODS

Sixty eight hips with osteoarthritis undergoing THA with computer navigation were included. The anterior pelvic plane was registered using anterior superior iliac spines and pubic symphysis, with orientations recorded in the radiological frame of reference. The orientation of the acetabular rim with any osteophytes excised was measured. The orientations of the outer, middle and inner margin of the rectangular band of the TAL were recorded.

RESULTS

All patients were Caucasian, 30 males and 38 females with mean age 67 (SD9.6) and mean BMI 30 (SD5). Mean inclinations were: acetabular rim=55° (SD7.9); outer TAL margin = 53° (SD6.9) middle TAL = 48° (SD6.8); inner TAL margin = 42° (SD6.7). Mean anteversions were 6° (SD8.7), 5° (SD9.9), 10° (SD9.6), 14° (SD9.4) for acetabular rim, outer, middle and inner margins of the TAL respectively. For inclination the TAL outer margin was not significantly different to acetabular rim ($p=0.082$) but the middle and inner borders were (both $p<0.001$). For anteversion the TAL outer margin was not significantly different to acetabular rim (mean $p=0.758$) but the middle and inner borders were (both $p<0.001$). The anteversion of the TAL for males was significantly lower than females for all three margins (5° to 6°, $p<0.05$).

DISCUSSION

The TAL middle and inner margins differ in orientation as compared to acetabular rim and TAL outer border. When using the TAL as an orientation landmark variation across the anatomic structure must be taken into account and the difference between males and females, particularly in terms of anteversion, should be considered.

Knee alignment – dynamicity and issues in normal, arthritic and replaced knees

K. Deep

Department of Orthopaedics, Golden Jubilee National Hospital, Glasgow, UK

mrkdeep@gmail.com

INTRODUCTION

Knee alignment has been a subject of much debate recently. Traditionally the goal of TKR has been to create a neutral mechanical femoro tibial mechanical axis angle (FTMA). Measurement methods have varied, traditionally being mainly radiological are not without flaws and involve radiation exposure. We used a validated method of computer navigation to measure this. We also looked at its variations.

METHODS

We looked at 267 normal knees of which 155 were from male and 112 female subjects. Mean age was 26.2(SD4.4). Mean FTMA was a varus of 1.2 degrees (SD 4.0). The supine FTMA changed by a mean of varus 2.2 (SD 3.6) in bipedal stance and 3.4 varus (SD 3.8) in monopedal stance.

RESULTS

On standing, the knee extension increased by 5.6 degrees (SD 6.8) in bipedal stance and by 5.5(SD 7.7) in monopedal stance.

The mean male FTMA in extension was1.7 varus (SD 4) while in females it was 0.4 varus (SD 3.9). The detailed analysis and results will be shown in the presentation.

DISCUSSION

We found the mechanical axis was not only not neutral but varied with person to person and even in the same person under different posture and loading conditions. It differed between males and females. Hence the goals of alignment in the knee replacement and alignment surgery need to be different for different individual and assessed for postural variations.

CONCLUSION

Arthritic knee changes deformity as it is flexed from extension, a classification system is also proposed for this behavior, which may shed light on mid flexion instability etilology in class 3 and 4C knees. The neutral alignment may not be the best for everyone. It also changes with posture as one stands from a non weight bearing supine position. Different alignment goals may be needed in males and females as well as different individuals.

Novel Design of an MR-safe Pneumatic Stepper Motor for MRI-guided Robotic Interventions

Z. Guo[1], T. T. L. Lun[1], Y. Chen[1], H. Su[2], D. T. M. Chan[3], K.-W. Kwok[1]

[1]*Department of Mechanical Engineering, The University of Hong Kong, Hong Kong*

[2]*John A. Paulson School of Engineering and Applied Sciences, Harvard University, USA*

[3] *Division of Neurosurgery, Prince of Wales Hospital, The Chinese University of Hong Kong, Hong Kong*

guoziyan@hku.hk

INTRODUCTION

Magnetic resonance imaging (MRI) superiority is well-known by providing non-ionizing radiation, non-invasive and high-contrast imaging in particular for soft tissues [1]. These advantages have prompted MRI for the various application in surgical interventions ranging from neurosurgery, cardiac ablation to prostate biopsies. However, MR-safe mechatronics is still confronted by the fundamental challenge, namely to maintain zero interference of its imaging operation during the MRI navigation.

Currently, four types of MRI actuations have been explored at different MR-safety conditions [2]: 1) electric actuators, e.g. piezoelectric motors and ultrasonic motors; 2) fluid-power motors; 3) MR-powered actuators. In terms of adaptability in general hospital setup, image quality and MR-safety, pneumatic actuators are advantageous in both material and energetics considerations. The material of pneumatic actuators could be non-magnetic and non-conducting, minimizing the effects on inhomogeneity of magnetic field. Pressured clean air as power supply is commonly available in MRI scanner rooms. This ensures zero image artifacts caused by the electromagnetic (EM) waves of electricity. Such pneumatic stepper actuators with the capability of generating accurate stepwise motion have been introduced recently. Stoianovici et al. [3] invented the first MR-safe pneumatic stepper motor that comprises three actuated diaphragms driving a hoop gear. Several pneumatic stepper motors [4-6] have been sequentially developed and their performances (e.g. torque-speed) have been demonstrated. However, many technical challenges still have not been addressed in these motors, e.g. typically large in motor size, high cost for the complicated fabrication and sterilization, dissatisfactory signal-to-noise ratio (SNR), as well as image distortion induced by the proximal electronics and valves of motor drivers.

In this paper, we propose a novel MR-safe pneumatic stepper motor, whose design could be relatively compact, flexibly customized for various actuation requirements. Such a motor can be made of a homogeneous material for ease of minimization and reconfiguration. One set of design parameters are selected for the experimental evaluation. Self-locking and high speed (up to 160RPM) is achieved in both rotation directions. Steady torque within a wide range of speed can also be preserved. Low imaging interference has been experimentally demonstrated while operating the motor inside the MRI scanner. Regarding these specifications, this motor is potential to be incorporated into an MRI-compatible robot for needle manipulation during intra-operative procedures, e.g. prostate surgery.

MATERIALS AND METHODS

The presented motor is compactly designed in cylindrical structure within the dimension of Ø35×88mm. It weighs 70g only. **Fig. 1** shows the motor assembly offering flexibility for design of a small-size and light-weight robot for MRI-guided interventions. The assembly can be completed manually and rapidly. The starting point of this mechanism is based on the design of Chen et al. [5], by merging such two uni-directional units together to achieve bi-directional rotation and continuous torque-speed performance.

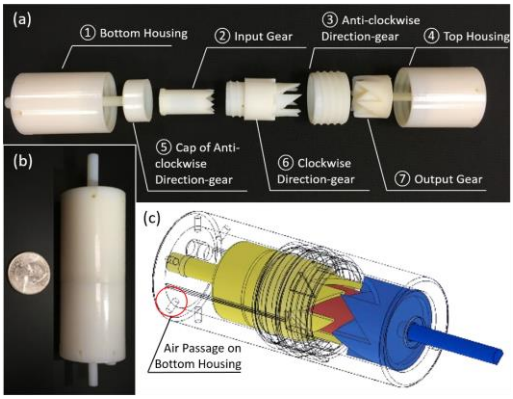

Fig. 1 (a) Exploded component view, (b) dimension and (c) CAD model of the stepper motor.

All the components made of an acrylic compounds material (VeroWhitePlus, Stratasys, USA) are fabricated by a rapid prototyping machine (Objet260 Connex, Stratasys, USA), constructing a rigid structure of the motor. Smooth surface of the 3D printout also ensures rather low friction coefficient (μ=0.157, obtained from pre-experiments). The completion time in printing one prototype is approximately 4 hours. Additionally small amount of semisolid lubricant could satisfactorily further smoothen the motion. Very little

heat is dissipated accredited to the less friction, ensuring its durable uses and reliable performance after long repeatable run.

RESULTS

Output torque and speed are two key metrics to characterize performance of various motors. Apart from design parameters, the maximum output torque is dependent on the exerted pressure and actuation frequency. **Fig. 2** illustrates torque-speed performance curves varied with applied pressure from 0.30 MPa to 0.51 MPa in sampling interval of 0.03 MPa. Under the lower level of pressure <4.2MPa, it is evident that torque can maintain at a stable level within a relatively wide range of speed (0-60 RPM). Stronger correlation is found between torque and speed when speed is over 60 RPM, in which torque is declining gently with the speed rising. This is because the disturbances between pulses become severe. Insufficient time for air diffusion may just provide very limited momentum for pressurized air to drive the gears, thus resulting in the decreasing torque. Overall the maximum power is 46.5 mW achieved at 0.48MPa, 140 RPM.

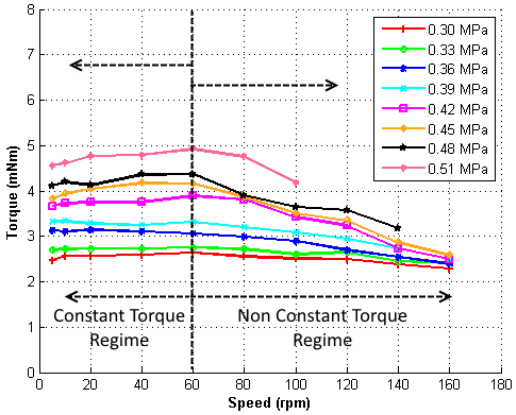

Fig. 2 Output torque varying with motor speed at the eight levels of pressure.

To quantify the MRI-compatibility, experiments with motor running under MRI have been conducted. The motor was placed closely to a commercial MRI phantom cylinder (#452213095955, CadMed+, USA), which was located at the isocenter of the scanner. The experimental setup is as shown in **Fig. 3**. Related electronic is all placed outside the MRI room, thus no extra shielding is required. To measure SNR and the maximum width of image artifacts, two common image sequences, T2-weighted Turbo Spin Echo (TSE) and T1- weighted Fast Field Echo (FFE) were applied to generate images of the phantom under different motor operation settings (as in **Fig. 3**), showing that the proposed stepper motor does not cause significant SNR loss. No image artifact is observable even within the delicate structures inside the phantom.

DISCUSSION

We presented a novel design of an MR-safe pneumatic stepper motor, which comprises only seven components made of homogeneous material. Not only does this significantly simplify the design process, but it also reduces the manufacturing cost. The motor can be disposable for single-use, without having to deal with complicated sterilization. The maximum torque and highest speed of our preliminary design was measured at 4.92 mNm and 160 RPM respectively, under the pressure up to 0.51 MPa. Validation through the operation under MRI has demonstrated its impressive MR-compatibility, thus supporting its practical use in many MRI-guided intervention assisted by robot.

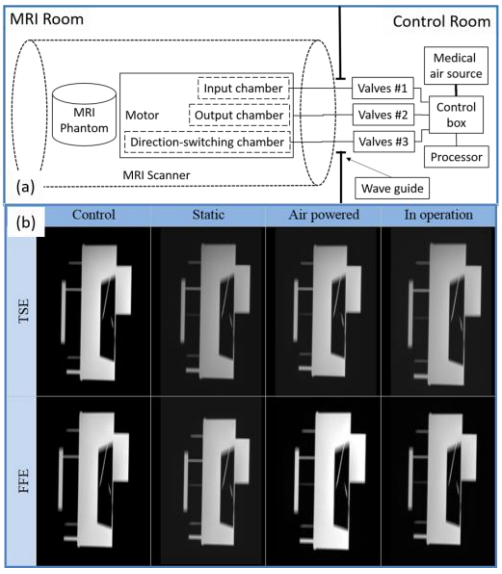

Fig. 3 (a) Motor evaluation setup with pneumatic components for the MRI-compatibility test. (b) MR images of the phantom with two sequences T2-weighted TSE and T1-weighted FFE images under different scenarios.

ACKNOWLEDGMENT

This work is supported in parts by the Croucher Foundation and the Research Grants Council (RGC) of Hong Kong. We sincerely thank to the team in the Department of Imaging and Interventional Radiology, the Prince of Wales Hospital, The Chinese University of Hong Kong (CUHK) for the access to their equipment.

REFERENCES

[1] F. Jolesz, *Intraoperative imaging and image-guided therapy*: Springer Science & Business Media, 2014.

[2] O. Felfoul, A. Becker, C. Bergeles, and P. E. Dupont, "Achieving commutation control of an MRI-powered robot actuator," *Robotics, IEEE Transactions on*, vol. 31, pp. 387-399, 2015.

[3] D. Stoianovici, A. Patriciu, D. Petrisor, D. Mazilu, and L. Kavoussi, "A new type of motor: Pneumatic step motor," *IEEE/ASME Transactions on Mechatronics*, vol. 12, pp. 98-106, 2007.

[4] H. Sajima, H. Kamiuchi, K. Kuwana, T. Dohi, and K. Masamune, "MR-safe pneumatic rotation stepping actuator," *Journal of Robotics and Mechatronics*, vol. 24, pp. 820-826, 2012.

[5] Y. Chen, C. D. Mershon, Z. Tsz, and H. Tse, "A 10-mm MR-Conditional Unidirectional Pneumatic Stepper Motor," *IEEE/ASME Transactions on Mechatronics*, vol. 20, pp. 782-788, 2015.

[6] Y. Chen, K.-W. Kwok, and Z. T. H. Tse, "An MR-conditional high-torque pneumatic stepper motor for MRI-guided and robot-assisted intervention," *Annals of biomedical engineering*, vol. 42, pp. 1823-1833, 2014.

Stormram 2: A MRI-Compatible Robotic System for Breast Biopsy

V. Groenhuis[1], J. Veltman[2], S. Stramigioli[1]

[1]*Department of Robotics and Mechatronics, University of Twente, The Netherlands*
[2]*Ziekenhuis Groep Twente, The Netherlands*

v.groenhuis@utwente.nl , j.veltman@zgt.nl

INTRODUCTION

In breast cancer screening, the doctor looks for lesions using mammography, ultrasound, palpation and/or MRI. A suspicious lesion may need to be biopsied; if the lesion is only visible on MRI, then a MRI-guided biopsy is required which is a long and costly procedure. Also, because manual needle insertion takes place outside the scanner, there is no real-time imaging feedback resulting in insertion accuracies which needs to be compensated by taking away a large amount of tissue material, causing discomfort. For the previous reasons, there is strong request for new systems for MRI-guided biopsy which allow real-time imaging feedback, more or less implying the use of a MRI-compatible robotic device.

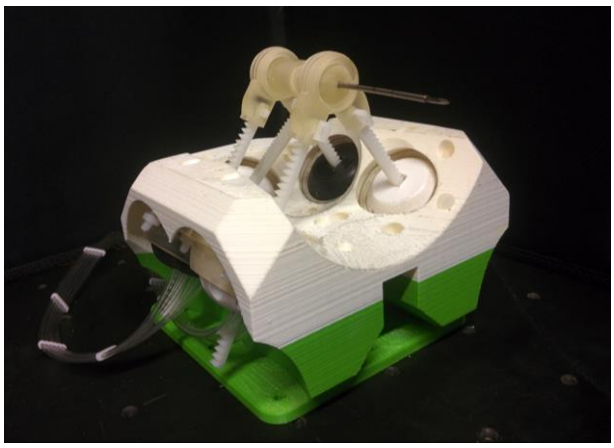

Fig. 1 The Stormram 2 biopsy robot.

In this paper, a novel 5 DOF needle manipulator (Fig. 1) driven by custom pneumatic linear stepper motors is described. Compared to its predecessor described in [1], all dimensions have been roughly cut in half, making the Stormram 2 small enough to easily fit inside the bore of the scanner together with the patient in prone position. It also has sufficient speed, force and dexterity to manipulate the needle towards a chosen target in a soft breast phantom.

MATERIALS AND METHODS

Because of the strong magnetic field in the MRI scanner, the use of metallic materials is severily restricted. Therefore, the whole robot (except for the needle) is made out of plastic materials. For the actuation system, pneumatics was preferred over hydraulics because control is easier and small leakages are acceptable.

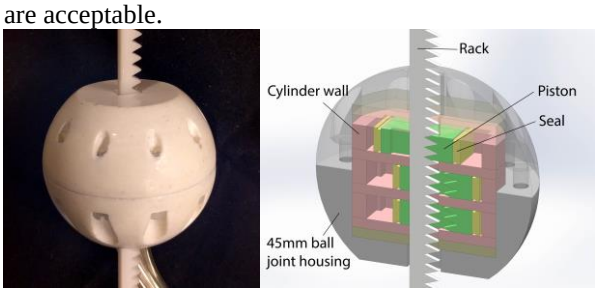

Fig. 2 Left: assembled actuator. Right: cutaway view, exposing three pneumatic cylinders with toothed pistons.

The actuators (Fig. 2) are custom-developed pneumatic linear stepper motors. In each stepper motor, three laser-cut rectangular pneumatic cylinders are embedded which together drive a rack in steps of 1mm. For a more detailed explaination of the mechanism, see [1]. The housing of each actuator also acts as a passive ball joint, with a ball diameter of 45mm.
The robot's frame was fully 3D printed and measures 140x140x100mm. Five actuators are mounted in the frame, driving a needle holder using a five-link parallel platform system, whose kinematic structure is inspired by MrBot [2].
Several different 3D printed needle holders (Figure 3, right) were developed, allowing the mounting of various off-the-shelf (MRI-compatible or MRI-safe) needles and performing different (semi-)automatic needle insertion strategies.

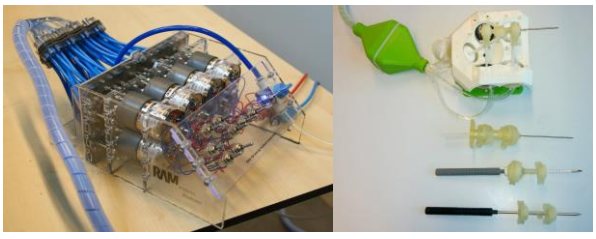

Fig. 3 Left: Pneumatic distributor for manual control of up to eight stepper motors, each controlled by six pneumatic tubes. Right: Four needle holders, for 14 gauge (2.1mm) or 9 gauge (3.8mm) needles, allowing for different biopsy strategies.

The robot is driven by a manually-controlled motorized pneumatic distributor (Figure 3, left) placed outside the MRI room, at a working pressure of 4 bar. It is operated by hand using visual guidance. The maximum actuator and needle insertion forces were measured with spring scales. MRI scans of the robot (with and without needle) were made to check if there is any influence of the robot

on scans of a phantom, or that all artefacts can be attributed to the needle.

RESULTS

With short pneumatic lines, the individual actuators can operate at speeds up to 10 mm/sec, with a maximum force of 15N (±2N) at low speeds. The effective maximum tissue penetration force of the 14 gauge (2.1mm) needle, positioned in the center of the workspace, was found to be around 8N. This value is lower than the individual actuator force, because of the particular kinematic configuration and because of resistance in the passive joints.

The robot's needle tip can reach targets with 1-2mm accuracy within a volume of approximately 90x80x50mm (as determined experimentally), and tilt the needle horizontally and vertically at different angles, up to ±30° in the center of the workspace.

The 45mm ball joints have a clearance in the order of 0.2mm, because the 3D printed ball and socket surfaces are not exactly spherical and friction has to be kept low. Parasitic movements of individual links were found to be in the order of 0.5mm, together resulting in a needle tip backlash of up to 2mm in free motion, depending on the actual position in the workspace.

To connect the robot to the valve manifold, 8 metre long and 2mm thick pneumatic lines were used. As air is compressible and airflow in the pneumatic distributor is limited due to the 0.8mm orifices, relatively much time is needed to pressurize the air in the pneumatic lines, effectively limiting the the maximum operating speed to about 3 mm/sec. Manual tele-operation under visual guidance has shown that it is possible to pierce a target lesion in a phantom made of gelatin or PVC (Figure 4).

Fig. 4 Left: Measurement setup in a 0.25T MRI scanner. Right: 3d rendering of the ex vivo tissue phantom, made out of gelatin (yellow) containing four fish oil capsules (red). The fifth marker is attached to the needle.

MRI tests with a Esaote G-scan Brio 0.25T scanner have shown that the robot without needle is completely invisible on the scans and produces no measurable artefacts in scans of phantom tissue. When equipped with the 14 gauge (2.1mm) titanium needle, significant artefacts are present up to a distance of 4mm around needle (Fig. 5) when it is inserted in a gelatine phantom.

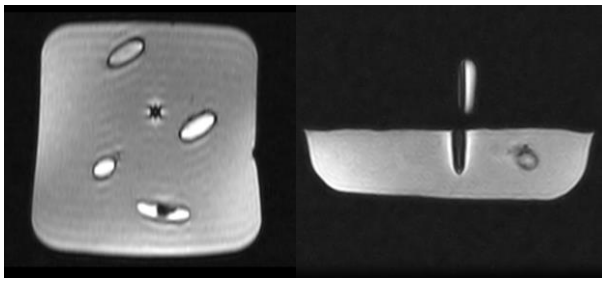

Fig. 5 Slices of a 3D Hyce MRI scan. Left: transversal plane through the phantom, showing four markers (white) and the needle insertion point just above the center. Right: sagittal plane through both the phantom and needle, showing two markers (one attached to the needle) and artefacts around the needle.

DISCUSSION

The developed miniature pneumatic actuators are shown to be strong enough to position and tilt the needle and pierce a soft phantom breast, but to penetrate a real skin a higher force is needed. This could be solved by improving the actuator design, or by driving the needle with a separate, more powerful actuator.

For the needle backlash problem, a possible solution is to change the 45mm ball joints to revolute joints, which can also be manufactured using rapid prototyping techniques with zero clearance and minimal friction. Also, the actuator's step size (1mm) could be reduced, increasing the precision of the system at the cost of lower speed. The operating speed can be increased by using valves with higher airflow and optimizing the pneumatic tubing thickness.

Computerized control of the biopsy robot has to be developed in order to effectively make use of real-time MR imaging, target lesions accurately and assess the robot's performance quantitatively. An electronic valve manifold driven by path planning software needs to be developed for this.

CONCLUSIONS

To conclude, the Stormram 2 has shown that it is possible to develop a fully MRI-compatible needle manipulator actuated by minituature pneumatic linear stepper motors, in which all parts are rapid prototype-able by 3D printing or laser-cutting from commonly available materials.

REFERENCES

[1] V. Groenhuis, S. Stramigioli, "Laser-cutting Pneumatics" in IEEE/ASME Transactions on Mechatronics, vol.PP, no.99, pp.1-1

[2] J. A. Cunha, I. Hsu, J. Pouliot, M. Roach III, K. Shinohara, J. Kurhanewicz, G. Reed, and D Stoianovici, "Toward adaptive stereotactic robotic brachytherapy for prostate cancer: Demonstration of an adaptive work flow incorporating inverse planning and an MR stealth robot" in Minimally Invasive Therapy. 2010;19:189–202

Concentric Tube Instrument for the Da Vinci Platform

P. Francis, K. Eastwood, V. Bodani, H. Azimian, K. Price, K. Upadhyaya, D. Podolsky, T. Looi, J. M. Drake

Center for Image Guided Innovation and Therapeutic Intervention (CIGITI), The Hospital for Sick Children, Toronto, Canada
p.francis@mail.utoronto.ca

INTRODUCTION

The da Vinci® Surgical System is the most prominent commercially available tele-robotic platform in the world, with more than 450,000 surgeries performed annually [1]. This technology enables surgeons to operate with improved dexterity, precision and control, particularly in complex cases within confined body cavities [1]. Presently, gynaecological and urological procedures represent 90% of the cases successfully treated using currently available instruments, which feature simple and rapid tool interchangeability and minimum shaft diameters of 5mm [1]. However, certain surgical procedures, particularly those in the head and neck as well as many paediatric cases, require smaller instrument sizes [2]. There is an unmet need in providing the benefits of the da Vinci platform to treat these patient populations.

Concentric tube robots are compact, dexterous devices capable of relatively high force transmission at small scales. These mechanisms function through the rotation and translation of concentric, curved, super-elastic tubes to achieve a tentacle-like motion [3]. We have applied this technology to create a dexterous, customized da Vinci instrument with a diameter less than 2mm.

This paper describes the design of a novel mechanism developed to create a da Vinci compatible concentric-tube wrist. The instrument's current performance was assessed, under teleoperation, with a pick-and-place task.

MATERIALS AND METHODS

The custom concentric tube instrument (CTI) is designed as a stand-alone, interchangeable tool that is compatible with the da Vinci platform. An early prototype of this device was presented at the 2015 Hamlyn Surgical Robotics Challenge. It uses the same disk-driven adapter that is employed on all standard da Vinci instruments. Each of the four actuation disks on the Patient Side Manipulator (PSM) actuate an independent degree of freedom (DOF) on the CTI. The CTI was developed as a cable driven concentric tube tool in order to minimize its weight and to take advantage of the da Vinci's counterbalancing system. The capstans, which are coupled to the PSM actuation disks and anchor the CTI's actuation cables, were redesigned to enable the necessary range of motion for each DOF. Since all da Vinci instruments are limited to four DOF, the tube configuration was selected as shown in Fig. 1, creating a roll-pitch-roll wrist. Each of these three DOF are individually driven by a single disk and the fourth disk drives the end-effector.

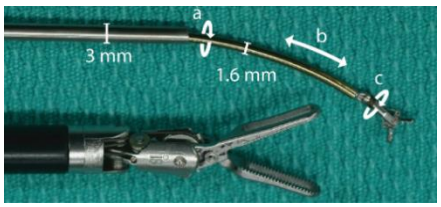

Fig. 1 Tube configuration: *Outer Tube* - straight, steel fixed to tool base. *Middle Tube* - curved, nitinol with rotation (a) and translation (b). *Inner Tube* - straight, nitinol with rotation (c). Included is an 8mm instrument for size comparison.

In order to translate the middle tube, a cart system which extends above the tool's base was implemented as shown in Fig. 2. This prismatic joint has a unique design consisting of a *lead* and *follower* cart. The mechanisms used for the middle tube rotation, the end-effector rotation and the end-effector actuation are positioned on the *lead cart*. To decouple these three DOF from the translation, the *follower cart* is used as illustrated in Fig. 3. With this design, the lead cart can be directly driven while the cable lengths of the other DOF routed onto the *lead cart* remain unchanged.

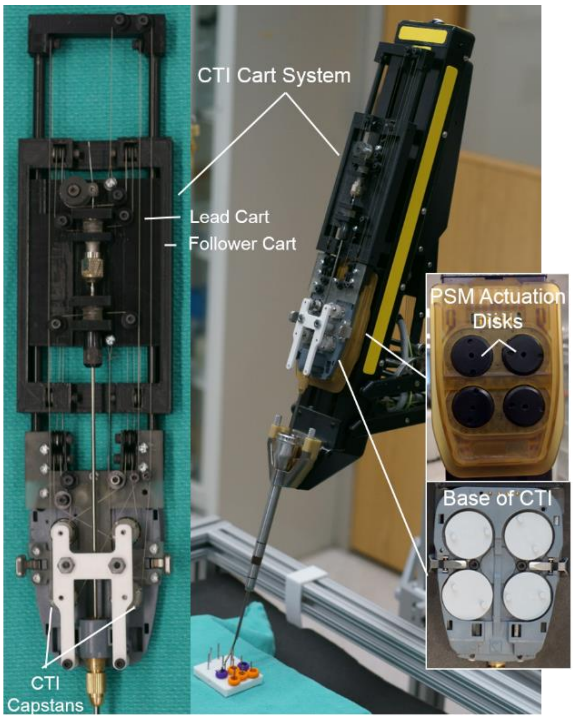

Fig. 2 Concentric tube instrument (CTI) with cart system [Left]. Tool mounted on PSM [Right]. PSM actuation disks that mate to disks on the instrument base [Right Panel].

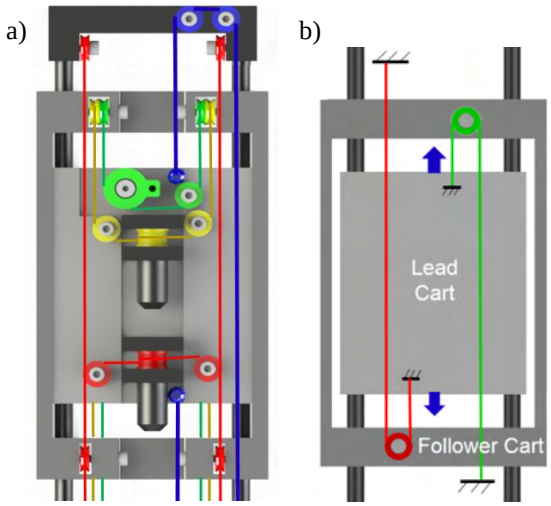

Fig. 3 a) Cart system cable routing diagram: *Blue* lines translate the lead cart, *Red* lines rotate the middle tube, *Yellow* lines rotate the inner tube, and *Green* lines actuate the graspers.
b) Simplified illustration of the cart system's mechanism.

The PSM actuation disks are limited by the manufacturer to ± 170 degrees. Therefore, the CTI capstans were designed to ensure that the necessary range of motion for each degree of freedom can be achieved given these limits. The CTI's joint limits and tube geometries are summarized in Tables 1 and 2.

The CTI is driven and controlled using the da Vinci Research Kit and the *sawIntuitiveResearchKit.* Using a UDP connection, a Simulink® program was developed to run in parallel to handle registration between the master and the slave, the inverse kinematics and the linear mapping from the CTI joint angles to the PSM's disk rotations. The inverse kinematics were solved as follows: First, the translation of the middle tube is solved using a least squares optimization, minimizing the tracking error of the position and orientation of the end effector. This value is used to analytically determine the remaining five joints. The offset from the tip of the PSM to the end of the trocar is 28mm and the range of the PSM's translation of the CTI is 50mm.

RESULTS

The CTI's performance was assessed using a pick-and-place task in which each trial consists of the transfer of 12 rings on a peg board. A novice performed 10 trials using a single tool, with the focus being precision and economy of motion. *Collisions* were defined as any unintentional instrument contact with a peg or the peg-board, and *drops* were defined as a ring being released early from the gripper onto a peg. The results are summarized in Table 3 and an example trial was recorded: https://youtu.be/MB1wVMMXfqg.

Table 1. CTI Joint Limits

Joint Ranges	
Middle (Curved) Tube Translation (mm)	[0, 30]
Middle (Curved) Tube Rotation (Deg)	[-210, 210]
Inner Tube (End-Effector) Rotation (Deg)	[-210, 210]

Table 2. CTI Tube Geometry

Tube	*Material*	*ID(mm)*	*OD(mm)*	*κ (mm^{-1})*
Outer	*Steel*	*2.6*	*3*	*0*
Middle	*Nitinol*	*1.2*	*1.6*	*0.018*
Inner	*Nitinol*	*0.7*	*0.8*	*0*

Table 3. Pick-and-Place Task Results

Assessment	*Mean (Std Dev)*	*Range*
Transfer Time/Trial (s)	213.2 (16.1)	190-231
No. of Drops/Trial	0.1 (0.32)	0-1
No. of Collisions/Trial	0.9 (0.74)	0-2

DISCUSSION

We have successfully developed a concentric tube tool for the da Vinci Surgical System, aimed at applications in the cranial vault or the confined body cavities found within paediatric patients. Leveraging the da Vinci's superior actuation and teleoperation system allowed for the focus to be placed on the size and dexterity of the concentric tube technology. Further, as an add-on for a commercially available robotic platform, this design may aid in the transfer of concentric tube technology into wider clinical use.

The pick-and-place task was performed successfully with the operator able to smoothly and precisely navigate the workspace at the cost of time. These results provide an adequate benchmark of the current performance of the instrument. Observing the tool's behaviour during the pick-and-place task, friction between the innermost tube and the middle, curved tube resulted in a minor snapping motion seen when rolling the end-effector. This effect was minimized by reducing the inner tube's diameter. However, the tube selection for this prototype must be further optimized. Additionally, regarding cable tension, the circuit that translates the cart was subject to small amounts of backlash. This outcome was minimized by ensuring that the cart remains well within its mechanical limits. After addressing these issues, the primary source of error for the pick-and-place task resulted from the controller. Further refinement of the controller will significantly improve performance.

A limitation of the mechanics of concentric tube technology is the challenge of achieving high curvatures while maintaining a required stiffness. Future work will focus on optimizing the tube geometry and conducting a controlled comparison to the EndoWrist® in confined workspaces.

REFERENCES

[1] Brody F, Richards NG. Review of Robotic Versus Conventional Laparoscopic Surgery. Surg Endosc. 2014 May:28(5):1413-24.

[2] Marcus HJ, Hughes-Hallett A, Cundy TP, Yang GZ. da Vinci Robot-Assisted Keyhole Neurosurgery: A Cadaver Study on Feasibility and Safety. Neurosurg. Rev. 2015 Apr:38(2):367-71.

[3] Gilbert HB, Rucker DC, Webster III RJ. Concentric tube robots: The state of the art and future directions. In Int Symp Robot Res 2013 Dec.

Enabling Helical Needle Trajectories with Minimal Actuation: A Screw-Based Approach to Concentric Tube Needle Deployment

E. B. Pitt, P. J. Swaney, H. B. Gilbert, Y. Chen, R. J. Webster III, E. J. Barth

Department of Mechanical Engineering, Vanderbilt University, USA

bryn.pitt@vanderbilt.edu

INTRODUCTION

The clinical need for needle-based therapies capable of accessing tissues unreachable by conventional needles has motivated substantial research into steerable needles (see [1] and [2] for a review of these technologies). In particular, it has been observed that curved paths can be useful in percutaneous procedures [3]. Gilbert, *et al.*, showed that helically pre-curved concentric tube nitinol needles can be deployed in a follow-the-leader (FTL) fashion, such that the needle shaft follows the path traced out by the tip [4]. Further information on concentric tube robots and the mechanics-based models that govern their motion can be found in [5] and [6].

The motivating application for helical needles in [4] was minimally invasive treatment of epilepsy—a neurological disorder that causes debilitating seizures. We have been developing a needle-based procedure for this application that involves delivering thermal energy to the hippocampus with both guidance and thermometry from magnetic resonance imaging (MRI) [4][7][8]. Figure 1 illustrates this application, in which a helical concentric tube needle is used to deliver therapy to the curved structure of the hippocampus through an occipital burr hole in the skull.

A principal challenge to executing FTL deployment of a helical concentric tube needle in soft tissue is the requirement for precise coordination of needle rotation and translation necessary to achieve a smooth "corkscrew-like" motion. To address this, Comber, *et al.*, developed an MRI-compatible needle-driving robot for the aforementioned epilepsy application [7], and Pitt, *et al.*, demonstrated the same robot's ability to accurately achieve FTL deployment of a helical needle [8].

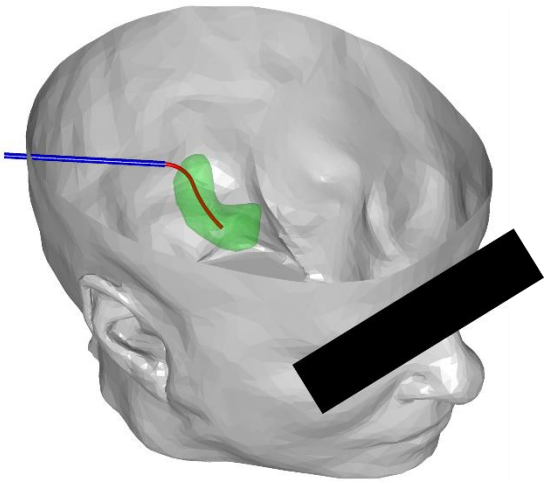

Fig 1. Minimally invasive, helical needle-based treatment of epilepsy. A helical needle (red) deployed from an outer cannula (blue) delivers therapy to the hippocampus (green).

The motivation for our current paper comes from the observation that FTL deployment requires the two actuation degrees of freedom to move at a fixed rate relative to one another, meaning that deployment is actually a single degree-of-freedom operation. Thus, in this paper we mechanically couple the two traditional actuation degrees of freedom through a screw mechanism. The benefit of this approach is that one actuator can be eliminated from the robotic system, making it simpler and less expensive. A further benefit of the approach is that manual insertion of a helical concentric tube robot becomes straightforward, allowing a human operator to deploy the needle in a FTL path by pushing linearly on the back of the screw mechanism. This paper is the first to demonstrate FTL deployment of a helical concentric tube needle by manual actuation.

MATERIALS AND METHODS

Figure 2 shows the screw mechanism and helical needle, assembled in the experimental setup. The prototype screw was manufactured by fused deposition modeling of acrylonitrile butadiene styrene (ABS) using a Stratasys Dimension 768SST. The process of shape setting the helical needle is described in [9].

The superelastic nitinol helical needle is grasped at its base by a collet in the tip of the screw mechanism. The needle is deployed through a fixed, straight, rigid outer cannula. When retracted within the cannula, the needle straightens; however, as the needle deploys from the end of the cannula, the deployed portion of the needle returns to its pre-curved helical shape due to the superelastic properties of nitinol. Achieving FTL deployment requires that the base of the needle be rotated (simultaneously with translation) at a rate equal to the

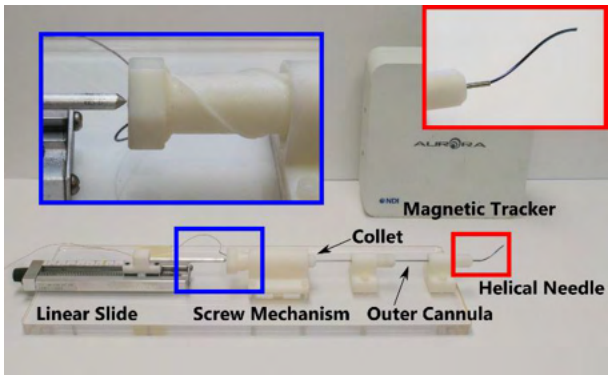

Fig 2. Experimental setup for characterizing deployment of a helical needle using a screw mechanism

needle's pre-curved torsion [4]. A simple screw mechanism is ideally suited to maintain the required constant relationship between translation and rotation. For the system presented here, the helical needle had radius 4.84 mm and pitch 62.38 mm, and the screw mechanism had pitch 69.39 mm.

To assess the quality of the FTL trajectory during insertion and retraction, the path of the needle tip through 3D space was compared to the helical pre-curved shape of the needle. A total of 20 experiments (10 insertions and 10 retractions) were performed in free space. Needle behavior in soft brain tissue should not be expected to differ significantly from behavior in free space, given the high relative stiffness of the needle compared to brain tissue. In all experiments, actuation of the screw mechanism was performed manually. Needle tip position was measured with a Northern Digital, Inc. Aurora magnetic tracking system; insertion distance (deployed arc length) was measured using digital calipers and an aluminium probe mounted to a linear slide (see Fig. 2). During each experiment, needle tip position was measured at 5 mm increments of deployed arc length. To determine the position and orientation of the needle's known (i.e. pre-shaped) helical curve in the robot's base frame, a point based registration was carried out between all measured data points and the points at corresponding arc length locations on the needle curve.

RESULTS

Figure 3 shows the results of one insertion experiment and one retraction experiment. In an ideal FTL deployment, the position of the needle tip would lie exactly on the curve at all times. For a given arc length, the distance between the measured tip position and the point on the curve at the same arc length is a measure of FTL error. Figure 4 shows the FTL error as a function of arc length.

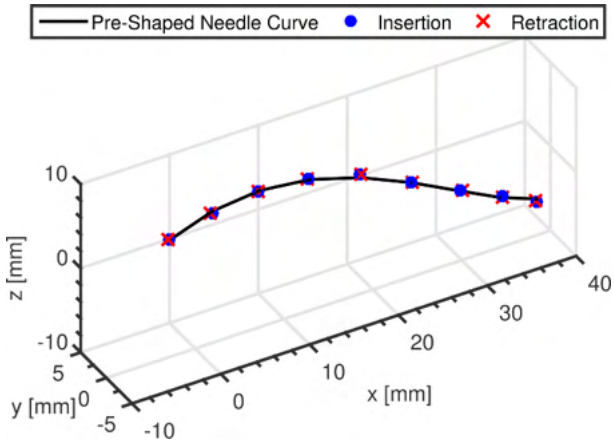

Fig. 3 Point-based registration between measured needle tip positions and the pre-shaped needle curve.

DISCUSSION

The results presented here demonstrate that follow the leader deployment of a helical concentric tube robot can be achieved manually using a screw mechanism to mechanically couple the translational and rotational degrees of freedom. These results provide for the first time a straightforward method to manually insert helical concentric tube needles through a FTL trajectory. Additionally, these results enable a reduction in the cost and complexity of a robot designed to achieve FTL deployment of a helical concentric tube needle by eliminating one actuator.

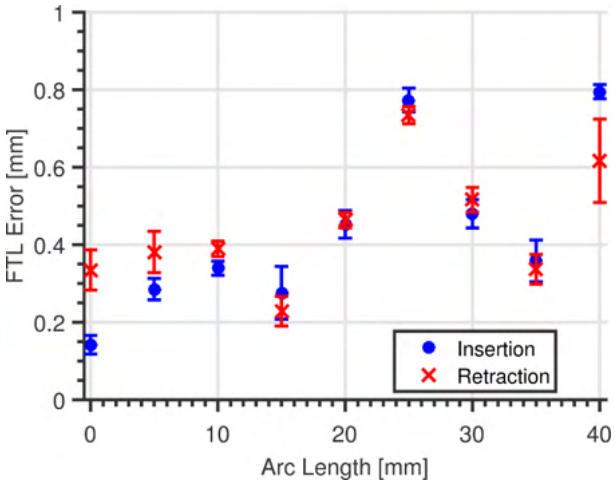

Fig. 4 FTL error versus arc length for insertion and retraction. Reported values represent mean FTL error for all experiments. Error bars represent average absolute deviation from the mean for all experiments.

ACKNOWLEDGEMENTS

This work was supported in part by NSF Grant No. EEC-0540834 and NIH Grant No. 1R21NS091735-01.

REFERENCES

[1] Abolhassani N, Patel R, Moallem M. Needle insertion into soft tissue: A survey. Med. Eng. Phys. 2007;29(4):413–431.

[2] Reed KB, Majewicz A, Kallem V, et al. Robot-assisted needle steering. IEEE Rob Autom Mag. 2011;18(4):35-46.

[3] Sze DY. Use of curved needles to perform biopsies and drainages of inaccessible targets. J Vasc Interv Radiol. 2001;12(12):1441-44.

[4] Gilbert HB, Neimat J, and Webster RJ III. Concentric tube robots as steerable needles: Achieving follow-the-leader deployment. IEEE Trans Robot. 2015;31(2):246-58.

[5] Rucker DC, Jones BA, Webster RJ III. A geometrically exact model for externally loaded concentric-tube continuum robots. IEEE Trans. Robot. 2010;26(5):769–80.

[6] Dupont PE, Lock J, Itkowitz B, Butler E. Design and control of concentric-tube robots. IEEE Trans Robot. 2010;26(2):209–25.

[7] Comber DB, Slightam JE, Neimat JS, et al. Design, additive manufacture, and control of a pneumatic, MR-compatible needle driver. IEEE Trans Robot. 2016;32(1):138-49.

[8] Pitt EB, Comber DB, Chen Y, et al. Follow-the-leader deployment of steerable needles using a magnetic resonance-compatible robot with stepper actuators. ASME J Med Device. In Press.

[9] Gilbert HB, Webster RJ III. Rapid, reliable shape setting of superelastic nitinol for prototyping robots. IEEE Robot Autom Let. 2016;1(1):98-105.

Integration of a Snake-like Dexterous Manipulator for Head and Neck Surgery with the da Vinci Research Kit

S. Coemert[1, 2], F. Alambeigi[2], A. Deguet[2], J. P. Carey[3], M. Armand[2], T. C. Lueth[1], R. H. Taylor[2]

[1]*Institute of Micro Technology and Medical Device Technology (MIMED), Technical University of Munich, Germany*

[2]*Laboratory for Computational Sensing and Robotics, Johns Hopkins University, USA*

[3]*Department of Otolaryngology – Head and Neck Surgery, Johns Hopkins University School of Medicine, USA*

suat.coemert@tum.de

INTRODUCTION

Minimally invasive surgery (MIS) offers significant benefits to patients, including faster healing and less pain. However, MIS also presents significant challenges to the surgeon, including restricted access to the surgical site, reduced dexterity, and reduced visualization. Consequently, robotic systems such as the da Vinci (Intuitive Surgical, Sunnyvale, Ca.) are finding increasing acceptance in MIS applications in urologic, gynecologic, and general surgery. Currently, the DaVinci is the only FDA approved robotic system used in Otolaryngology, where it has been applied in head and neck cancer surgery and thyroid surgery. However, da Vinci applications in skull base surgery are challenging, since surgical tools of this system were not designed to fit into the natural orifices used in transnasal/transotic approaches.

We are developing a snake-like dexterous manipulator (SDM) to assist surgeons with treating petrous apex lesions in the skull base using infralabyrinthine approach [1]. In this approach, the temporal bone is drilled via the mastoid to create an access channel to the petrous apex. The surgeon then removes cystic lesions. However it is usually not possible to reach all regions within the petrous apex without using a steerable tool. The SDM helps surgeon to guide and steer flexible instruments such as curettes, forceps, irrigators, aspirators within the cyst cavity with increased dexterity [2].

MATERIALS AND METHODS

To insert the SDM through the small channel surrounded by vital structures such as cavernous sinus, carotid artery, ocular motor nerves and trigeminal nerve; the outer diameter of it was limited to 3.3 mm. Therefore using a nitinol rod and wire electrical discharge machining (WEDM) process, we designed and fabricated the SDM which has a 3.3 mm outer diameter (OD), a 1.8 mm instrument channel and a 0.7 mm endoscope channel. The overall length of the SDM is 50 mm with 40 mm steerable working length. It provides C-shaped and S-shaped planar bends in two directions and can be rotated around its longitudinal axis. Fig. 1 demonstrates the fabricated SDM.

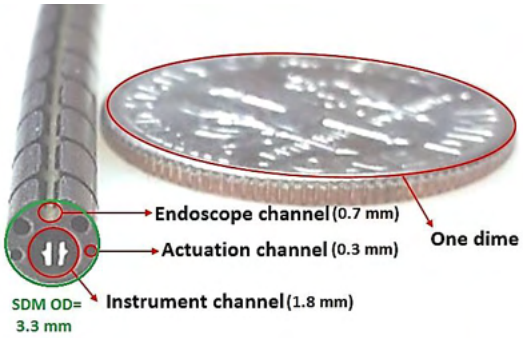

Fig. 1 The fabricated SDM

The flexibility of the SDM is realized by the flexure hinges (Fig. 2a) and the actuation occurs via pull-wires. End loaded cantilever beam model constitutes the foundation of the flexure hinge designs [3]. Eq. (1) describes the relation between the deflection angle and the hinge dimensions. The kinematics of the SDM was modeled based on the constant curvature assumption [4]. The model uses the change in the actuation cable length as an input parameter and predicts the manipulator shape based on this information. In this model, we calculated the homogeneous transformation matrix for each flexure hinge. Fig. 2b shows how the transformation was implemented for a single hinge.

$$\theta = \frac{6\,F\,l^2}{E\,b\,h^3} \tag{1}$$

In Fig. 2, F is the force acting on the tip of the beam; l is the beam length; b is the beam width; h is the beam thickness and E is the corresponding materials' modulus of elasticity; l_t is the actuation cable length; l_θ is the distance between the two ends of the flexure hinge; r is the radius of curvature; and θ is the angle of deflection where d is the distance between the actuation cable channel and the neutral axis of the flexure hinge. The position of the tip of the hinge relative to its base can be expressed by the following transformation matrix:

$${}^{1}T_{4=} = \begin{pmatrix} \cos\theta & 0 & \sin\theta & l_{(\theta)}\,\sin\left(\frac{\theta}{2}\right) \\ 0 & 1 & 0 & 0 \\ -\sin\theta & 0 & \cos\theta & l_{(\theta)}\,\cos\left(\frac{\theta}{2}\right) \\ 0 & 0 & 0 & 1 \end{pmatrix} \tag{2}$$

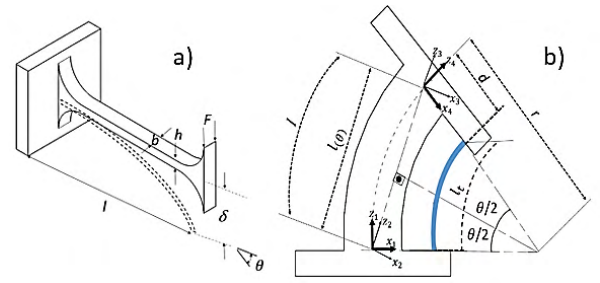

Fig. 2 a) End loaded cantilever beam model **b)** Schematics of constant curvature modeling for a single flexure hinge.

The transformation matrix in eq. (2) has two unknown paremeters: θ and $l_{(\theta)}$. With the help of the geometrical relationship in Fig. 2b, the cable length l_t which is the essentially needed input parameter, can be obtained with the following transformations:

$$\theta = \frac{l - l_t}{d} \tag{3}$$

$$l_{(\theta)} = 2\,\frac{l}{\theta}\sin\left(\frac{\theta}{2}\right) = \frac{2\,d\,l}{l - l_t}\sin\left(\frac{l - l_t}{2\,d}\right) \tag{4}$$

In eq. (3) and (4), l and d are the known parameters from the construction. Therefore we can predict the position and orientation of the distal end of a single hinge based on single unknown parameter which is the change in the actuation cable length. Multiplication of consecutive transformation matrices of each flexure hinge will give the tip position and orientation of the SDM.

In our previous work, we presented how to utilize and modify the da Vinci actuation box as a handheld actuation unit for the designed SDM [1]. A worm-gear mechanism was integrated to the actuation unit which enables the SDM to maintain its position without applying an additional force thanks to its self-locking feature. Fig. 3 shows the use of this manual actuation mechanism in providing C-shaped and S-shaped bends.

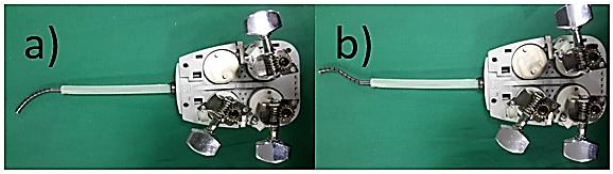

Fig. 3 Handheld actuation concept: a) C-shaped b) S-shaped.

DVRK is a telerobotic research platform that combines the mechanical components obtained from retired first-generation da Vinci Surgical System with the open-source electronics and software developed by researchers at Johns Hopkins University [5]. By taking advantage of the enhanced control architecture of the DVRK system, we integrated the SDM actuation box with the Patient Side Manipulator (PSM) and actuated it by the provided software. An overview of the DVRK system may be found in Fig. 4.

RESULTS

After engaging the SDM and the da Vinci actuation box with the PSM of the DVRK, the actuation was performed at arbitrary incremental rotation angles. Different bending modes as well as roll motion of the SDM were observed at different angles. Fig. 5 shows different configurations of the SDM.

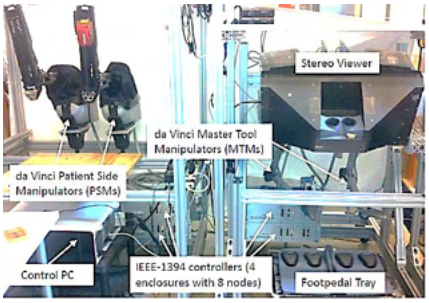

Fig. 4 Overview of the DVRK system [6].

DISCUSSION

We have presented a developing SDM for the treatment of skull base lesions using infralabyrinthine approach. Apart from a handheld actuation concept, we have investigated the feasibility of integrating the SDM with the DVRK for the simultaneous actuation and manipulation of the SDM and the PSM. The future work will include kinematics and dynamics modeling of the SDM to incorporate it in combined control of DVRK and the SDM. Furthermore, experiments will be carried out to investigate the applicability of this model to control the SDM actuation in an accurate manner.

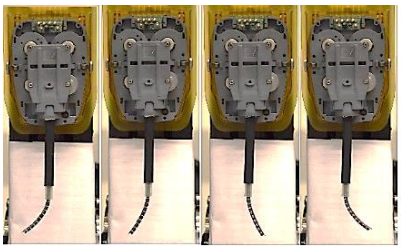

Fig. 5 Several actuation modes of the SDM attached to DVRK.

ACKNOWLEDGEMENTS

This work is partially supported by the BERTI Programme. BERTI is funded by the European Commission under Grant Agreement Number 605162.

REFERENCES

[1] Coemert, S., et al. Development of a Snake-like Dexterous Manipulator for Skull Base Surgery. In EMBC 2016 (accepted for publication).

[2] F. Alambeigi, et al, Design and characterization of a debriding tool in robot-assisted treatment of osteolysis, in IEEE ICRA 2016, to be published.

[3] J. Gere and B. Goodno, Mechanics of materials. Mason, OH: Cengage Learning, 2009.

[4] R. Webster and B. Jones, "Design and Kinematic Modeling of Constant Curvature Continuum Robots: A Review", The International Journal of Robotics Research, vol. 29, no. 13, pp. 1661-1683, 2010.

[5] Kazanzides, P., Chen, Z., Deguet, A., Fischer, G. S., Taylor, R. H., & DiMaio, S. P. (2014, May). An open-source research kit for the da Vinci® Surgical System. In IEEE ICRA 2014, pp. 6434-6439.

Deformation Detection and Tracking on Continuous and Deformable Medical Tools

F. Visentin[1,2], M. Capiluppi[1], K, Suzuki[2], P. Fiorini[1]

[1]*Department of Computer Science, University of Verona, Italy*

[2]*Department of Intelligent Interaction Technologies, University of Tsukuba, Japan*
francesco.visentin@univr.it

INTRODUCTION

Soft robotics is an already established research field within the bio-inspired robotic community. It considers robots that exhibit more natural movements, and are made by *soft* material, such as silicon rubbers [1]. The use of this material has the potentials to lead to machines that are more adaptable, capable, and safer than the existing ones. However, considering soft mechanics introduces design and control issues that differ completely from the rigid ones.

Application domains where soft robots can be advantageous are multiple. Among them, one that seems very promising is related to Minimal Invasive Surgery (MIS) [2]. This opens a new path for the development of novel medical devices that act as a continuous by fully exploiting the material properties, and that are capable to adapt their shape according to the needs. In order to make the novelty in this direction, it is fundamental to provide sensing ability to such devices. This will provide the surgeon with information about the environment with which the tool interacts – e.g. collision with other tools or organs – and the current shape and position of the device without the need of external imaging machine.

In this paper we present a novel method to measure deformations that occur over a continuum deformable device. Solutions have already been presented, but most of them need to embed the sensors in accurately pre-defined positions. Our approach, on the contrary, does not require stiff components embedded directly into the device. Instead, it uses a stretchable smart skin, and bases its sensing capabilities on a tomographic imaging technique that allows having a distributed sensing independent from the underlying design. The method is still in its initial stage, but the results prove its feasibility and open new opportunities in this research field.

MATERIALS AND METHODS

Electrical Impedance Tomography (EIT) is a well-established technique [3,4] that is used to infer the internal structure of the studied domain by estimating its conductivity distribution. Since its initial development, the technique has been used in different application fields spanning from geophysical analysis to patient ventilation monitoring.

In a typical EIT application, electrical current is injected into the studied body, and voltage potentials are measured at its boundaries. The acquired values are then processed to reconstruct a resistivity map of the studied domain. Given an initial homogeneous map, it is possible to detect changes in the domain conductivity due to local variation (Figure 1).

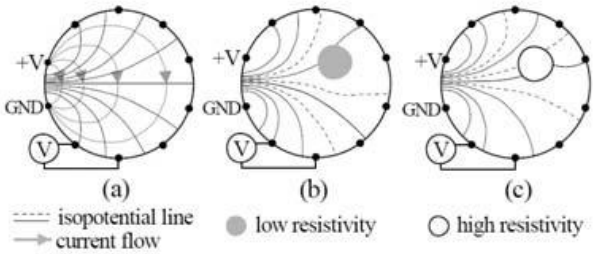

Fig. 1 Electrical Impedance Tomography changes due to local variation. (a) Reference measurements with isopotential lines due to the current injection. (b) and (c) Changes in the isopotential lines and measured voltage potential due to a change in resistivity.

SYSTEM DESCRIPTION

The system that we propose is a simplify version of a standard EIT device. We decided to develop our in-house system in order to be able to fully control its parameters both in the current injection phase, and in the possibility to choose the most appropriate measurement patterns. It consists of three main components: i) a current generator, ii) channel selection, iii) and a computer used to perform the inverse problem solving. The channel selection circuit is designed to allow the control of which electrode acts as a current source, current sink (connected to ground), or none of the two (high impedance stage). An ATmega2560 microcontroller interfaced with Matlab controls the independent switches and is also used as data acquisition system. A customised version of EIDORS [5] is used to perform the inverse solving.

EXPERIMENTAL SETUP

In order to test the feasibility of the system, we tested our device over a continuous, deformable body made of foam. For the initial studies we do not consider significant the size of the device, since the system can be adapted to different situations. A highly conductive stretchable textile is placed over the cylinder, and then attached by electrodes to the EIT system. Figure 2 shows the deformable body used in the measurements.

We both tested the capability of the system to detect multiple touching points over the surface, and

deformation detection. In this last test we evaluated the system only over a single bending point due to material stiffness that limits local deformations, and due to limitations of the size of the material used for the measurements.

Fig. 2 Experimental deformable body. A foam cylinder (green) is used to have the shape of a medical tool. EIT measures are taken over a highly conductive textile (black) that is placed over the cylinder.

RESULTS

A series of simulations have been performed before carrying out the measurements. These were used to correctly select the optimal parameters to be used in the different phases of the data acquisition.

Figure 3 shows the interactions over the conductive surface and the consequent changes in the conductivity due to the textile deformation. As the results suggest, the system is able to identify multiple events (red areas) that occur over the surface of the material. The minimal spatial resolution needed to discriminate between two events is around 10% of the domain width.

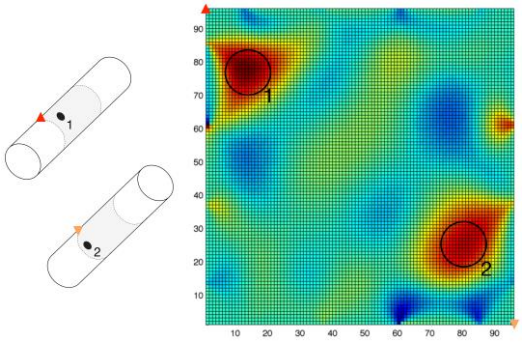

Fig. 3 Simultaneous multi-touch detection. Left: contact points over the conductive textile. Right: reconstructed conductivity map according to the changes produced by the direct contact over the surface.

We also performed manual bending on different locations; the most significant is represented in Figure 4. Similarly to the previous results, the red area indicates the location of a conductivity change. The main difference between the two results is in the size of the deformed area. In this case the area is wider than in the former one.

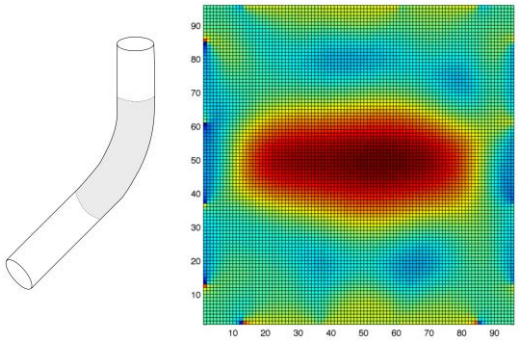

Fig. 4 Deformation identification. The red area indicates where the stretching of the textile occurred. During the experiments almost the whole area covered by the skin was subjected to the bending.

DISCUSSION

We presented a novel method to detect touching and deformation over continuous deformable devices. The method used is based on a tomographic technique known as Electrical Impedance Tomography that estimates the conductivity map of the studied domain. As the results suggest, the method is able to detect both local changes due to direct pressure, and locations where other types of deformation occur (e.g. bending). One of the most important features of the method is that sensing capabilities are continuous in space, without the need to place stiff sensors in the device.

Future works include the full characterization of the deformation according to the sensor readings, and the discrimination between different events. Further studies on other deformable devices and miniaturisation are also part of this workflow, to allow application in MIS.

REFERENCES

[1] F. Iida and C. Laschi, “Soft robotics: Challenges and perspectives,” Procedia Computer Science, vol. 7, no. 0, pp. 99 – 102, 2011.

[2] I. De Falco, M. Cianchetti, A. Menciassi “STIFF-FLOP surgical manipulator: design and preliminary motion evalua-tion” 4th Joint WorkShop on Computer/Robot Assisted Surgery (CRAS), October 14-16, 2014. Genoa, Italy.

[3] R. P. Henderson and J. G. Webster. An Impedance Camera for Spatially Specific Measurements of the Thorax. *IEEE Transactions on Biomedical Engineering*, vol. BME-25, no. 3, pp. 250-254, May 1978.

[4] Lytle, R. and Dines, K. An impedance camera: A system for determining the spatial variation of electrical conductivity. Technical report, Lawrence Livermore Laboratory, University of California, Livermore California. Report UCRL-52413.

[5] Adler A, Lionheart WR. Uses and abuses of EIDORS: an extensible software base for EIT. Physiol Meas. 2006 May, 27(5) S25-42.

A Smart Skin Based Measurement System for Abnormality Identification in Soft Tissue Palpation

F. Visentin[1,2], R. Muradore[1], M. Capiluppi[1], K, Suzuki[2], P. Fiorini[1]

[1]*Department of Computer Science, University of Verona, Italy*

[2]*Department of Intelligent Interaction Technologies, University of Tsukuba, Japan*
francesco.visentin@univr.it

INTRODUCTION

Recent advancements in robotic-assisted surgery have revolutionised the medical field by providing tools that can be used to simplify operations, and recovery of the patients. However, the main drawback remains in the lack of haptic feedback that these tools can provide.

Hence, the use of such systems is limited in many surgical operations since the surgeon can only rely on visual information to evaluate tool-tissue interaction forces during surgery. In this paper we will focus on the palpation task to detect abnormalities. By using robotic systems, surgeons can no longer use long established techniques, such as manual tissue palpation, to identify and locate tissue abnormalities and hidden pathological lesions such as tumours. Although the problem has already been investigated in literature [1], the main objective of this paper is to attempt to tackle it from a different perspective with respect to the solutions available in literature. We propose a system that is a combination of a tomographic imaging technique and of a mechanical stimulation performed by a probe that applies a constant amount of force over the surface of a soft tissue. The measured values can be interpreted as an estimation of the stiffness of the underlying structure, thus giving us information about the presence of abnormalities.

The experiments carried out using a simulated soft tissue show that the system can be used to detect the presence of inhomogeneity within a deformable structure by applying a constant pressure to the domain under investigation.

MATERIALS AND METHODS

The underlying measurement system is based on an established tomographic imaging technique known as Electrical Impedance Tomography (EIT) [2, 3]. This technique is used to infer the internal structure of the studied domain – either 2D or 3D – by estimating its conductivity distribution as a result of applied electrical current and measured voltage potentials. Since its initial development, the technique has been used in different application fields, but it finds its main application in patient ventilation monitoring system.

In order to measure the internal conductivity of the studied domain, an array of electrodes is placed around it. The array is connected to a current source, and to a multiplexing system that allows to select which of the electrodes is used as current source, current sink, or none of the two (high impedance state). According to the selected stimulation pattern, at every measurement step, one electrode is used to inject current, one as ground, while all the remaining are used to measure voltage potentials at the boundaries. Injection and measurement patterns can differ, but usually follow the same scheme. Among the common patterns, the *adjacent* pattern is the most used, where electrodes close to each other is selected both to inject the current and to measure the voltage potentials. The sequences of injection and measurement are then repeated until all the possible combinations of electrodes considered in the selected pattern are evaluated. Figure 1 shows the first two steps of the adjacent pattern.

Once a full cycle of measurements has been acquired, the voltage data are then processed by an inverse solver algorithm that provides the conductivity map that can be exported and analysed using image processing methods.

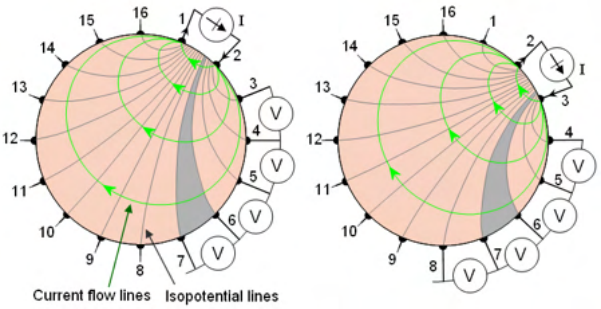

Fig. 1 First two steps of adjacent pattern. Left: Electrode 1 and 2 are used to inject the current, while measurements are taken on the others. Right: Both injection and measurements electrodes are shifted to continue in the data acquisition until a complete cycle of measurements has been completed.

SYSTEM DESCRIPTION

In order to fully control the parameters selection, we developed an in-house low cost EIT system (Figure 2). It consists of three main components: i) a current generator, ii) a channel selector (de-multiplexer and single channel switches), and iii) a computer used for the inverse processing. At the current stage of the development, the system has 8 channels, but it has been designed for further expansions. An ATmega2560 microcontroller interfaced with Matlab controls both the injection and measurement patterns. It is also used to acquire the voltage potentials and transfer them to a computer for data processing. A customised version of EIDORS [4] is used to perform the inverse solving.

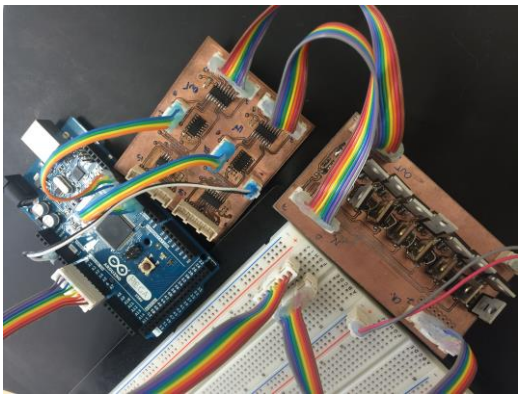

Fig. 2 Developed Electrical Impedance Tomography system. It consists of independent parts that can be easily extended in case more channels are needed.

EXPERIMENTAL SETUP

Differently from the usual EIT systems, our prototype allows to measure changes over a conductive textile that can be used as a smart skin to cover the tissue under examination. The working principle remains unchanged, but what it is produced from the data processing is a map that indicates changes in resistivity due to the textile deformation as a result of stiffness dissimilarities in the underlying material. Following this principle, it is possible to design an experimental setup to test the feasibility of the system in detecting abnormalities in a synthetic tissue.

Our experimental setup (Figure 3) consists of two layers of foam (10x10x1.5cm) within which a more rigid material – a medium-size marble – has been placed to simulate the presence of a tumour. The top layer has then been covered with a highly conductive textile (10x10cm) connected to the EIT system. To provide a homogenous pressure over the whole domain, an additional rigid layer (9x9x0.3cm) and a weight that applies a constant force of 2N has been placed over the experimental setup.

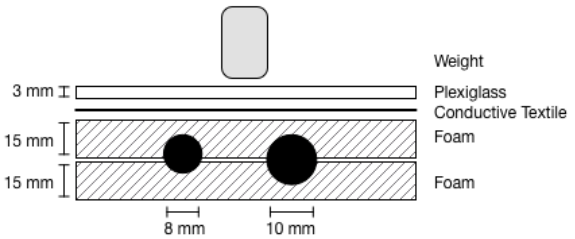

Fig. 3 A schematic representation of the experimental setup. Two rigid bodies were placed within the soft phantom to simulate the presence of tumours.

RESULTS

Before attempting direct measurements over the experimental setup, various simulations have been performed in order to select the optimal parameters to be used in the different phases of the data acquisition process.

Figure 4 shows the result of the measurements performed over the experimental setup. Our technique allows to clearly identify the presence and location of the abnormalities – i.e. harder regions – within the artificial soft tissue.

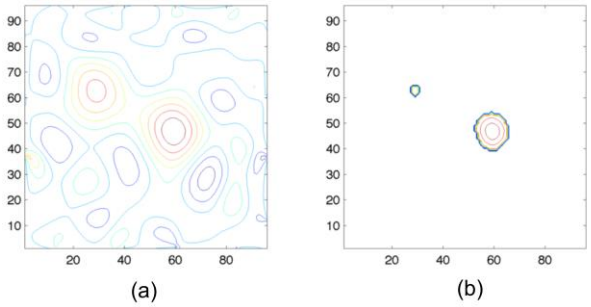

Fig. 4 Results of the proposed method presented as contour map. (a) Reconstructed image. (b) Region having intensity value more than 75% of the maximum value detected. These regions represent the tumour inside the studied media.

DISCUSSION

In this paper we presented a different method to perform abnormality identification in soft tissue palpation. The method uses as working principle a tomographic technique known as EIT to measure differences in conductivity within the studied tissue. As the experimental results suggest, the technique is suitable for abnormality identification within soft tissue of one or multiple abnormalities at the same time. One of the main drawbacks of the method lays in its low spatial resolution that prevents to discriminate objects that are lower in size than 10% of the considered domain. This limitation can be easily overcome with the adoption of a measurement system smaller in size (i.e. electrodes and considered domain) or with a larger number of electrodes.

Future work will mainly focus on increasing the performance of the current experimental setup by (1) removing the noise due to the electronic circuit, and (2) reducing the sensitivity to the material used for the measurements. Other developments are: extension of the method to non-flat surfaces and its possible application as surgical tool in MIS.

REFERENCES

[1] D. Zbyszewski, P. Polygerinos, L.D Seneviratne, and K. Althoefer, A Novel MRI Compatible air-cushion tactile sensor for Minimally Invasive Surgery, ”IEEE/RJS Int. conf. on intelligent Robots and Systems” 2009, pp.. 2647-52

[2] R. P. Henderson and J. G. Webster. An Impedance Camera for Spatially Specific Measurements of the Thorax. *IEEE Transactions on Biomedical Engineering*, vol. BME-25, no. 3, pp. 250-254, May 1978.

[3] Lytle, R. and Dines, K. An impedance camera: A system for determining the spatial variation of electrical conductivity. Technical report, Lawrence Livermore Laboratory, University of California, Livermore California. Report UCRL-52413.

[4] Adler A, Lionheart WR. Uses and abuses of EIDORS: an extensible software base for EIT. Physiol Meas. 2006 May, 27(5) S25-42.

Feasibility of Tissue Classification via da Vinci EndoWrist Surgical Tool

R. L. Dockter[1], J. J. O'Neill[1], T. K. Stephens[1], T. M. Kowalewski[1]

[1]Department of Mechanical Engineering, University of Minnesota

dockt036@umn.edu

INTRODUCTION

Robot-assisted minimally invasive surgery has gained popularity over the past few decades. With the introduction of robotic equipment in the operating room comes a wealth of sensory data inherent to the robot. Yet much of this rich data remains underutilized. One potential application is found in creating tissue-aware surgical robots. Sie et al. have shown that tissue-aware surgical robots are possible via tissue identification in real-time during tissue grasping [1]. This would enable tissue-aware robots to avoid surgical errors such as tissue crush injury [2].

The objective of this study is to determine whether existing data streams for a popular tool like the da Vinci® EndoWrist® can be used to identify grasped tissue. We employ cadaveric human tissues.

MATERIALS AND METHODS

A custom mechatronic setup with a da Vinci® EndoWrist® surgical grasper was utilized for all cadaveric tissue data collection (Fig. 1). The mechatronic device measures both force and position throughout the grasp using load cells and potentiometers, respectively. These measurements are taken at the spindles on the proximal end of the tool as to not disturb the distal grasping end and provide a surrogate for the torque (motor current) and position (encoder counts) already present in the da Vinci® control loop. The mechanical hardware is described in [3]. The electrical hardware was upgraded to include a 24-bit analog-to-digital converter (ADC) for the load cell data, and a 12-bit ADC on a 32-bit microcontroller for the potentiometer data.

Two different cadaveric tissues were grasped along with their surrounding adipose tissue; this resulted in a total of four distinct data sets: kidney, pancreas, kidney adipose, and pancreatic adipose. The tissues were refrigerated and stored at 2°C in 0.09% saline for the pancreas (Fisher Scientific) and KPS-1 for the kidney (Organ Recovery Systems) and all tissues were tested within one week post-mortem. The tissues were removed from refrigeration and data collection immediately began in a room temperature environment. The outside of each organ was grasped repeatedly with the mechatronic device. Data collection on each tissue type occurred with da Vinci® EndoWrist® Maryland Bipolar Forceps.

Position and force data were collected at 1kHz with each grasp lasting approximately 400ms. In total 32 kidney, 12 pancreas, 22 kidney adipose, and 10 pancreatic adipose grasps were collected.

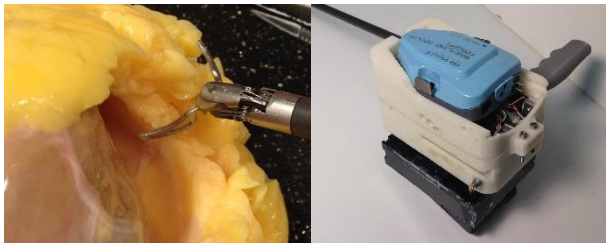

Fig. 1 Experimental setup, showing kidney with surrounding adipose tissue on the left and the mechatronic setup on the right.

Tissue discrimination was achieved using a least squares approach for model training and an error ratio method for online classification. The tissue model used was originally proposed by Yu et al. [4]:

$$u = M\ddot{p} + D\dot{p} + \alpha(e^{\beta p} - 1) \quad (1)$$

Here u represents the grasper force and p is the grasper angle. In order to utilize this model in a least squares method, the nonlinear term $(\alpha(e^{\beta p} - 1))$ is expanded into a second order polynomial $(k_1\epsilon + k_2\epsilon^2)$. Force (u) and angle (p) are expressed in terms of tissue stress (σ) and strain (ϵ) with constants (m and d) changed to reflect appropriate units.

$$\sigma = m\ddot{\epsilon} + d\dot{\epsilon} + k_1\epsilon + k_2\epsilon^2 \quad (2)$$

With this model, the training data is then used to compute least squares parameter sets for each tissue type:

$$\Phi_i = [m, d, k_1, k_2] \quad (3)$$

With these parameter sets computed for each class, online classification is achieved by computing the model error between the current data (σ) and the i[th] linear model:

$$E_i(t) = \|\sigma(t) - X(t)\Phi_i\| \quad (4)$$

Where X is the sample data at a given time step:

$$X(t) = [\ddot{\epsilon}(t), \dot{\epsilon}(t), \epsilon(t), \epsilon(t)^2] \quad (5)$$

Given the model errors for each tissue type, the online tissue is classified by finding the tissue with the lowest cumulative model error at a given time step.

A leave-one-out classification scheme was used for each grasp segment of eash tissue type resulting in 66 total online grasps. This classification followed a binary pairwise approach.

The data were filtered with a 4[th] order Butterworth filter using a 4Hz cutoff frequency. Since we measured position but the independent variable in our tissue model is strain (Eq. 2) we estimated strain by calculating change in position (p), where the position was re-zeroed at the first touch of the grasp. We found the position of first

touch in post-processing by determining the center of the range of force data, and then moving forwards and backwards in time to the limits.
We estimated stress by measuring force and assuming a constant area of the grasper teeth between grasps and allowed the linear model to absorb the constant area.

RESULTS

The table of classification results for each tissue type is included in Table 1. This classification was taken at 176ms which corresponds to the average time a grasp takes to reach the force threshold corresponding to the center of the force range used in segmentations. Classification for a given grasp was considered correct if the minimum cumulative model error corresponded to the true class at the 176ms time.

	Actual			
vs	Kidney	Pancreas	Kidney Adipose	Pancreatic Adipose
Kidney	-	100%	95%	100%
Pancreas	100%	-	86%	60%
Kidney Adipose	78%	100%	-	100%
Pancreatic Adipose	94%	45%	82%	-

Tab. 1 Ordinal classification accuracies using the leave-one-out, one vs. one scheme

The seperation between grasp data for pancreas and kidney tissue is shown in Figure 2. The separation suggests significant discriminating information for strain and its derivative.
The relative contribution of each term in Equation 2 is represented in Figure 3 as a stack plot.

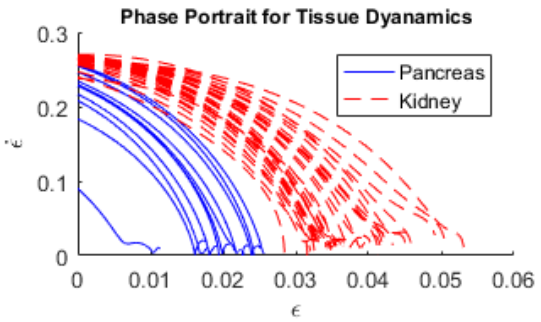

Fig. 2 Phase portrait of ϵ vs. $\dot{\epsilon}$ for pancreas and kidney tissue

DISCUSSION

The results indicate that tissue classification is possible with existing da Vinci® surgical graspers on cadaveric tissue. Previous work was limited to tissue classification using highly-customized surgical graspers [1] and on porcine tissue [3]. This work extends the previous work to classification of two different human cadaveric tissues and corresponding adipose tissue using a more common

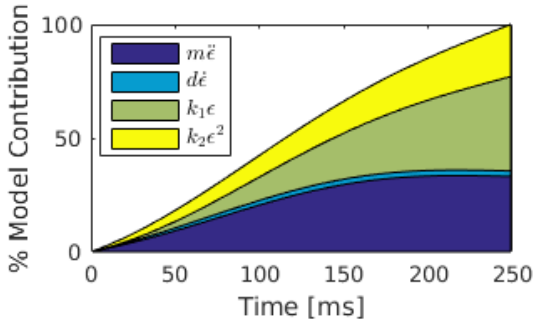

Fig. 3 Representitive stack plot showing the relative contribution for each term in the tissue model.

da Vinci® tool. For both kidney and pancreas, classification accuracies were 100%. Classification was achieved within 170ms of the start of the grasp which is below typical visual reaction time. Figure 3 indicates that dynamic and nonlinear terms have non-negligible contributions to the tissue model. Since all data were collected from sensors on the proximal end of the tool, this work can, in principle, readily integrate to a clinical setting. Placing sensors on the distal grasping end would have resulted in cleaner data, but it would be difficult to incorporate in a clinical setting due to sterilization issues, increased cost, and FDA approval requirements. Further work includes extending classification to more diverse tissue samples and testing a real-time version of the classification algorithm on the embedded hardware. Real-time application of this tissue classification in a surgical setting could help limit accidental tissue crushing and give direct information to the surgeon of the tissue being manipulated.

ACKNOWLEDGEMENTS

Research was sponsored by the Army Research Laboratory and was accomplished under Cooperative Agreement Number W911NF-14-2-0035. The views and conclusions contained in this document are those of the authors and should not be interpreted as representing the official policies, either expressed or implied, of the Army Research Laboratory or the U.S. Government. The U.S. Government is authorized to reproduce and distribute reprints for Government purposes notwithstanding any copyright notation herein.

REFERENCES

[1] A. Sie, M. Winek, and T. M. Kowalewski, “Online identification of abdominal tissues in vivo for tissue-aware and injury-avoiding surgical robots,” in IEEE/RSJ Intell. Robot. Syst. (IROS 2014), 2014, pp. 2036–2042.
[2] S. De, J. Rosen, A. Dagan, B. Hannaford, P. Swanson, and M. Sinanan, “Assessment of tissue damage due to mechanical stresses,” International Journal of Robotics Research, vol. 26, no. 11-12, pp. 1159–1171, 2007.
[3] Stephens, T. K., Meier, Z. C., Sweet, R. M., and Kowalewski, T. M., 2015. “Tissue identification through back end sensing on da vinci endowrist surgical tool”. Journal of Medical Devices, 9(3), p. 030939.
[4] X. Yu, H. J. Chizeck, and B. Hannaford, “Comparison of transient performance in the control of soft tissue grasping,” in IEEE/RSJ Intelligent Robots and Systems, 2007, pp. 1809–1814.

Simultaneous Registration and Stiffness Mapping of a Flexible Environment using Stiffness and Geometric Prior

R. A. Srivatsan[1], L. Wang[2], E. Ayvali[1], N. Simaan[2], H. Choset[1]

[1]*Robotics Institute, Carnegie Mellon University, USA*

[2]*Mechanical Engineering, Vanderbilt University, USA*

rarunsrivatsan@cmu.edu

INTRODUCTION

In minimally invasive surgeries (MIS), surgeons have limited situational awareness of the surgical environment, making navigation a challenging task. Registration of preoperative images to intra-operative anatomy can help improve the situational awareness of the surgeon and validate if the surgery is going as per the preoperative plan. In this work, we use prior information about stiffness and geometry of the organ to develop an implementation for simultaneous registration and stiffness mapping.

While several imaging-based techniques [1], [2] and palpation-based techniques [3] have been used for registration, these methods tend to perform poorly when the organ geometry is rotationally symmetric, as in the case of liver, heart, etc. A rotationally symmetric object has multiple solutions for rotation and/or translation, resulting in an ambiguity in registration [4]. In other applications, this ambiguity is usually resolved by introducing an additional dimension such as surface texture [5], surface reflectance [6], etc.In order to develop a formulation for registration that works reliably for any organ geometry, we extend the formulation of [3] by using a stiffness prior in addition to the geometric prior for resolving the ambiguity in registration. A prior stiffness map can be generated using elastography, physics based simulations or other complementary methods. Through experiments on a flat silicone organ with embedded stiff inclusions, we show that our method accurately estimates the registration as well as the stiffness map and outperforms the state of the art.

MATERIALS AND METHODS

To evaluate our algorithm we have used a custom designed Cartesian robot with an open architecture controller (see Fig. 1(a)). The robot end-effector is equipped with an ATI Nano43 F/T sensor. The end-effector is controlled using a hybrid motion/force controller implemented as in [7].

For the experiment, we used a silicone phantom organ with embedded stiff inclusions as shown in Fig. 1(b). A region of interest was chosen on the surface of the organ and several points in that region were probed. The phantom organ was lubricated to reduce the effect of friction during probing.

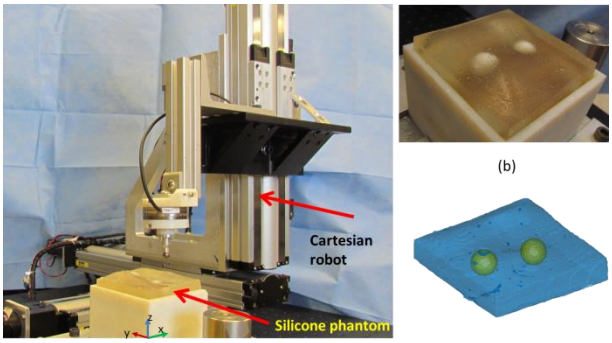

Fig. 1. (a) Cartesian robot setup for experiments. (b) Top view of the silicone phantom organ with embedded stiff inclusions. (c) CAD model of the organ and the stiff inclusions.

The robot was commanded to probe the organ up to a set depth along the normal direction and the applied force was recorded. The force and position measurements, along with the CAD model of the organ and the prior stiffness map, were used to estimate the registation and the stiffness map of the organ.

Steps involved

Our formulation takes the following steps:

0. *Prior information gathering*: In this work the geometric prior is obtained by generating the CAD model of the organ and the inclusions from CT scans (see Fig. 1(c)). We generate the prior stiffness using a physics based simulation that assumes a linear stiffness model. The stiffness values are normalized and classified into two discrete levels, high and low stiffness, using Otsu method [8].
1. *Collection*: In the collection step, we collect sets of position-force measurements which correspond to probing of the same undeformed point on the surface of the organ. For example, $\left(\boldsymbol{p}_j^R, f_j\right)_i$ is a set of m measurements collected for the i^{th} probed point where $j = 1, \dots, m$ and $i = 1, \dots, n$. $\boldsymbol{p}_j^R, f_j$ are the position and force-magnitude measurements.
2. *Stiffness estimation*: We estimate the local stiffness by assuming a linear stiffness model and computing the slope of the best line that describes the variation of depth with the applied force.
3. *Correspondence*: The correspondence step involves finding points on the CAD model that map to the location of each of the undeformed points as estimated from the sensor measurements. In order

to ensure that a point corresponding to a high stiffness region on the model-frame is mapped to a point with high stiffness in the robot's frame, we normalize and classify the estimated stiffness map using [8] (Fig. 2(c) was generated from Fig. 2(a)). We choose the point on the CAD model that is closest and also has the same discrete stiffness level in the prior stiffness map.

4. *Minimization*: The optimal registration $\boldsymbol{T} \in SE(3)$ can be obtained from the following:

$$\boldsymbol{T} = argmin_{\boldsymbol{T}} \sum_{i=1}^{n} \left\| \boldsymbol{p}_i^C - \frac{\boldsymbol{n}_i^C (f_j)_i}{c_i} - \boldsymbol{T}\left(\boldsymbol{p}_j^R\right)_i \right\|^2 , (1)$$

Where $\boldsymbol{n}_i^C$ and $\boldsymbol{p}_i^C$ are the normal vector and the position of the probed point in the model's reference frame and c_i is the estimated stiffness. In this work, Eq. 1 is minimized using a least squares solver [4].

5. We loop between Step 3 and Step 4 until convergence or up to a fixed number of iterations.

RESULTS

The stiffness map estimated by our approach is shown in Fig. 2(a). Note that the two stiff inclusions are clearly visible in the stiffness map. In Fig. 2(d), black-diamond markers show the 180 points that were probed in the region of interest. Green-square markers show the initial guess for the location of the probed points. In Fig. 2(e), blue-star markers show the position as estimated by CMU [3]. Red-circular markers show the position estimated by our approach.

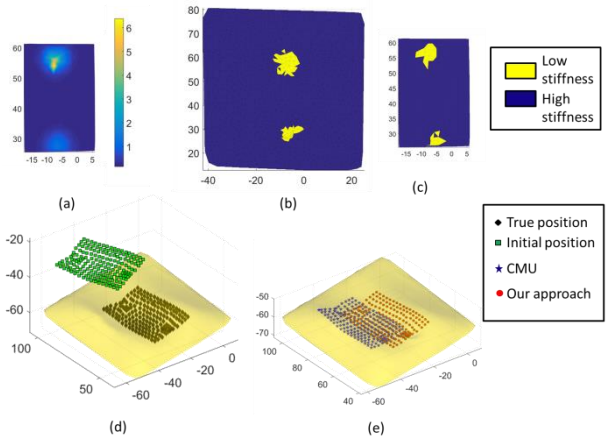

Fig. 2. (a) Estimated stiffness map (stiffness in N/mm). (b) and (c) Prior stiffness map and estimated stiffness map respectively, normalized and stiffness values classified to high and low stiffnesss levels. (d) Initial and true location of probed points. (e) Estimated location probed points.

Table 1: Comparison of registration results

	x (mm)	y (mm)	z (mm)	θ_x (deg)	θ_y (deg)	θ_z (deg)	RMS (mm)
Initial	0	0	0	0	0	0	-
Actual	-20	15	-10	11.46	-8.59	5.73	-
Our approach	-21	16.73	-9.1	11.28	-8.6	5.23	2.19
CMU [3]	-16.4	19.9	-14.8	15.45	5.84	8.16	7.74
ICP[1]	-18.9	20.5	-15.4	16.21	7.35	6.5	7.77

The estimated registration parameters are compared with ICP [1] and CMU [3]. Table 1 shows the RMS error for each of these methods for a representative example. Our approach estimates the registration parameters very accurately and the RMS error is within clinical requirements [9].

DISCUSSION

In this work, we developed a new implementation for simultaneous registration and stiffness mapping of an organ. In contrast to prior work, we have demonstrated successful registration in cases where the organ geometry is rotationally symmetric.

We use a stiffness prior in addition to a geometric prior for finding correspondences with the model frame and hence resolve the ambiguity in registration. By performing experiments on a silicone phantom organ we have shown that our approach can successfully register while estimating the stiffness map and outperform state of the art methods.

While we have used a simple experimental setup and phantom organ, as part of future work we plan to demonstrate the method on the da Vinci surgical robot probing *ex vivo* organs.

ACKNOWLEDGEMENT

This work has been funded through the National Robotics Initiative grants IIS-1426655 and IIS-1327566.

REFERENCES

[1] P. J. Besl and N. D. McKay, "A method for registration of 3-D shapes," IEEE Transactions on Pattern Analysis and Machine Intelligence, vol. 14, pp. 239–256, 1992.

[2] M. V. Wyawahare, P. M. Patil, H. K. Abhyankar, et al., "Image registration techniques: an overview," IJSIP, vol. 2, no. 3, pp. 11–28, 2009.

[3] R. A. Srivatsan, E. Ayvali, L.Wang, R. Roy, N. Simaan, and H. Choset, "Complementary Model Update: A Method for Simultaneous Registration and Stiffness Mapping in Flexible Environments," In Proceedings of ICRA 2016.

[4] K. Arun, T. Huang, and S. Bolstein, "Least-Squares fitting of Two 3-D Point Sets," IEEE Transactions on Pattern Analysis and Machine Intelligence, vol. 9, no. 5, pp. 698–700, 1987.

[5] A. E. Johnson and S. B. Kang, "Registration and integration of textured 3D data," Image and vision computing, 17(2), pp. 135-147, 1999.

[6] L. Cerman, A. Sugimoto, and I. Shimizu. "3D shape registration with estimating illumination and photometric properties of a convex object," In Proceedings of Computer Vision Winter Workshop, 76–81, 2007.

[7] O. Khatib, "A unified approach for motion and force control of robot manipulators: The operational space formulation," IEEE Journal of Robotics and Automation, vol. 3, no. 1, pp. 43–53, 1987.

[8] N. Otsu. "A Threshold Selection Method from Gray-Level Histograms." Automatica 11 (1975): 285-296.

[9] C. A. Linte, J. Moore, and T. M. Peters, "How accurate is accurate enough? A brief overview on accuracy considerations in image-guided cardiac interventions," in Annual International Conference of the Engineering in Medicine and Biology Society, pp. 2313–2316, 2010.

A Robotic Implant for Enterogenesis

K. Price[1], Z. Machaidze[1], T. Jaksic[1], R. Jennings[1], P. E. Dupont[1]

[1]*Boston Children's Hospital, Harvard Medical School, Boston, USA*

karl.price@childrens.harvard.edu

INTRODUCTION

Short bowel syndrome (SBS) is a condition caused by surgical resection or disease of the small intestine [1]. SBS affects 24.4 out of 100 000 live births, and the mortality rate of the condition is high [2]. Of those that SBS affects, it is a highly lethal condition, with mortality reported to exceed 30% [3]. A minimum of 15-25 cm of bowel is required for survival [1]. Treatment options begin with paraenteral nutrition (PN) which is administered through a central venous catheter [2]. This method is effective at maintaining patient health but has many complications such as infection and PN-associated liver disease. Treatments attempt to lengthen the bowel to increase intestinal absorption, an important step toward self-sufficiency. Some surgical approaches to increase the effective length of bowel include: *Longitudinal lengthening* by dividing and connecting a piece of bowel longitudinally, creating two narrow sections of bowel and *serial transverse enteroplasty* which involves stapling the bowel on alternating sides, creating a zig-zag channel through the intestine. Both of these surgical options are limited in that they can only be applied to dilated bowel segments, which may be dysfunctional to begin with, as well as restricting the amount and location of extra length that can be created. Damage to the mesenteric blood supply and enteric leakage can also occur as a result of complex anastomosis [3].

Mechanotransduction has been successfully applied to bowel in in vivo animal experiments. Existing devices are placed inside the bowel and restrict bowel patency [3]. We have shown that axial force can be applied to tubular organs nonobstructively [4]. Although mechanotransduction is known to stimulate bowel growth, surgeons and scientists disagree on how much force should be applied to the organ. This paper presents a small robotic implant which has been developed for enterogenesis while maintaining bowel patency and motility. No bowel resection is required to implant the device. The device is both a research tool to collect strain and tensile force data as well as a prototype for clinical bowel growth. The technique of robotic, in vivo tissue engineering has the potential to substantially improve outcomes in the treatment of SBS.

MATERIALS AND METHODS

The robotic implant (Figure 1) consists of three pairs of bowel attachment rings arranged radially about the robot. This arrangement applies traction to three segments of bowel simultaneously and so triples the length of induced bowel lengthening. An opening is made in each ring to allow the bowel to pass through the ring during attachment as well as to avoid interrupting the blood supply at the point of attachment. The rings are removable, and are attached to the device body using snapping fasteners after being sutured to the bowel. Patient-specific rings of different sizes are manufactured, and interchangeable to find the right fit for the bowel during surgery. The rings translate along a lead screw to stretch an initial 20 mm length to 70 mm, a total displacement of 50 mm. A linear potentiometer (Spectra Symbol) monitors ring position. A force sensor (Honeywell Inc.) measures the tensile force being applied to the bowel. The implant is encased in medical grade silicone (Bentec Medical). The robot controller is implemented on a Sparkfun Orangutan microcontroller, which communicates wirelessly to a laptop by Bluetooth virtual serial port (BlueSmirf, Sparkfun). The control box fits in the pocket of a vest worn by the patient and is battery powered, allowing the patient freedom of movement. A graphical user interface (MATLAB 2014b) is used to control the position of the robot and set a force limit. As the robot stretches the bowel, if the force limit is reached, it will stop movement. Real-time position and force data are plotted on a laptop screen, allowing a physician to monitor the traction forces being applied to the bowel during adjustment.

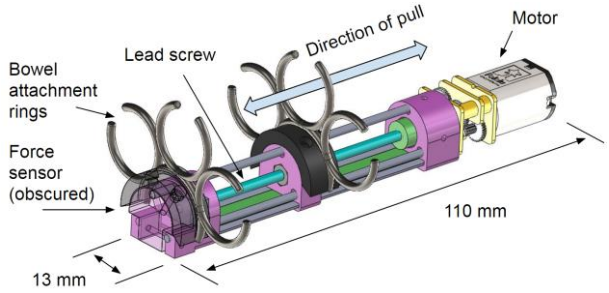

Fig. 1 - Implant schematic. The medical-grade silicone casing and control cable are not shown.

To determine the actuator torque needed for in vivo trials, an experiment with ex vivo sheep bowel was performed. Three segments of small intestine were sutured to the rings using six sutures per lumen on each ring as shown in Figure 2. The distance between the rings was initially 23 mm. This distance was incremented in steps of 0.5 mm until tissue or suture failure. Force data was recorded during the experiment.

To determine the appropriate pig size for in vivo trials and the best position of the implant in the intestinal cavity, positioning was evaluated inside the carcasses of two pigs (Yorkshire Swine, 5 kg, 45 kg). The rings were attached to the small intestine (Figure 4). The size of the implant and implant placement were assessed for feasibility in an in vivo model.

Fig. 2 – Ex vivo test on sheep bowel. Three segments of small intestine are sutured to the rings with six sutures each.

RESULTS

The starting diameter of the sheep bowel was 9 mm, and the ring diameter was 12 mm. Figure 3 presents the force versus elongation distance of bowel. As the bowel was stretched, the diameter of the lumen dilated gradually to match the diameter of the rings (both diameters equal at 2.8 N). Bowel segments failed at 9, 10 and 14 mm of elongation (suture tear out). Force sensor saturation is 9.3 N force. All failures occurred at higher than 9.3 N force, therefore failure forces were not recorded. No flexing of the implant was observed during the tensile test.

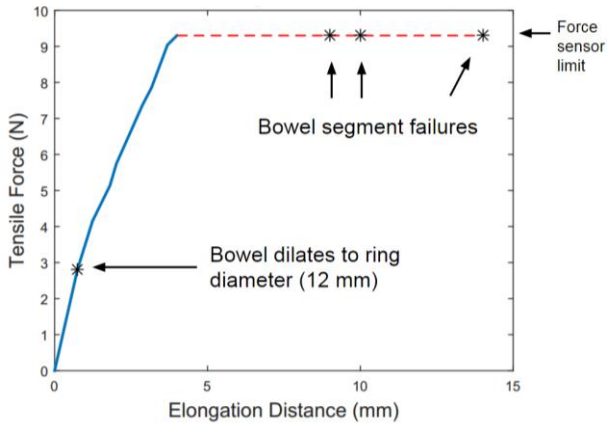

Fig. 3 – Tensile test results of ex vivo sheep small intestine.

The implant fit easily in both carcasses. Three segments of bowel were selected such that they could be positioned parallel to each other in the rings, without causing a kink due to bending of the bowel. Implant position along the left abdominal wall of the 5 kg pig carcass is shown in Figure 4, and no impingement of bowel was noticed. The three-ring arrangement fit easily to the three segments of small intestine. The opening in the rings allowed the bowel to be attached to the device while preserving the mesenteric blood supply.

DISCUSSION

Ex vivo testing indicates that the displacement, force range and size of the current prototype are appropriate to proceed to in vivo testing. Three segments of bowel can be stretched a maximum of 5 cm which will create a potential for 15 cm of growth. This amount of growth could be sufficient to wean a child from PN and so return to normal life.

As the bowel was stretched, it was noticed that the bowel diameter dilated to match the larger diameter of the rings. This suggests the use of oversized rings to avoid constriction of the lumen, maintaining bowel patency throughout the procedure. Bowel absorption can be monitored during treatment and an informed decision will be made when enough extra bowel has grown before the implant is removed.

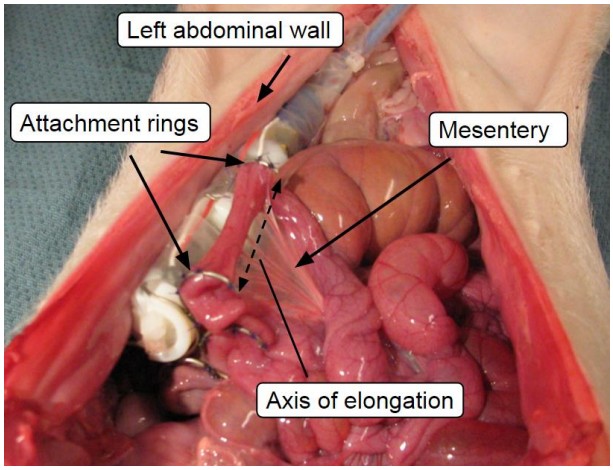

Fig. 4 – Implant inside a fresh dead 5 kg pig. Transverse view showing three implant rings sutured to small intestine, mesentery preserved.

While the device fits inside the abdominal cavity of the 5 kg pig (equivalent to a 6 month old child), the top of the device approaches the bottom of the kidney. To reduce risk, initial in vivo testing will be performed using 15 kg pigs, which possess a longer abdominal cavity. Pig size will be reduced in future experiments.

An animal protocol has been developed and approved by IACUC (Institutional Animal Care and Use Committee) for in vivo, ten day survival studies in a swine model. The device will be surgically implanted and each day following the surgery, the implant will be commanded to stretch the bowel, without applying excessive force. We will investigate the use of the D-xylose and Schilling tests to assess improved intestinal absorption [1]. On day 10, the stretched bowel will be harvested from the animal, its length measured, and compared to the initial measured bowel. Histological analysis will be used to assess muscle cell proliferation and inflammatory response. Results will be compared to a control pig.

REFERENCES

[1] Bonnard A, Staub G, Segura JF, Malbezin S, Dorgeret S, Aigrain Y, de Lagausie P. (2005). Evaluation of intestinal absorption after longitudinal intestinal lengthening for short bowel syndrome. *J Pediatr Surg, 40*(10), 1587-1591.

[2] Wales PW, de Silva N, Kim J, Lecce L, To T, Moore A. (2004). Neonatal short bowel syndrome: population-based estimates of incidence and mortality rates. *J Pediatr Surg*, *39*(5), 690-695.

[3] Spencer AU, Sun X, El-Sawaf M, Haxhija EQ, Brei D, Luntz J, Teitelbaum DH (2006). Enterogenesis in a clinically feasible model of mechanical small-bowel lengthening. *Surgery*, *140*(2), 212-220

[4] Damian DD, Arabagi S, Fabozzo A, Ngo P, Jennings R, Manfredi M, Dupont PE (2014). Robotic implant to apply tissue traction forces in the treatment of esophageal atresia. In *Robotics and Automation (ICRA), 2014 IEEE Int Conf* (pp. 786-792).

Can Coffee Improve Surgical Robot Accuracy?

P. S. Wellborn, P. T. Russell, R. J. Webster III

Vanderbilt Institute in Surgery and Engineering (VISE),
Departments of Mechanical Engineering and Otolaryngology, Vanderbilt University

patrick.s.wellborn@vanderbilt.edu

INTRODUCTION

Transnasal skull base and sinus surgery is often assisted via image guidance systems (e.g. the Brainlab Kolibri [1] – Fig. 1) which show the real-time locations of surgical instruments with respect to the 3D map provided by preoperative volumetric medical images. Image guidance systems often employ optical tracking to measure in real time the locations of both surgical instruments and the patient's head. The accuracy of these systems relies on the rigid coupling between optical tracking markers and the patient. However, the markers are often attached to the patient using an elastic headband that can shift if bumped during use [2].

In this paper, we propose the use of both layer jamming and granular jamming to improve the accuracy of image guided robotic transnasal sinus and skull base surgery. Granular jamming involves drawing a vacuum on a bag filled with granules (e.g. coffee grounds) [3]. Layer jamming involves drawing a vacuum on a bag filled with thin layers of material, to increase the normal force between them and thus prevent them from sliding over one another [4]. We use these technologies to securely and non-invasively attach optical tracking markers to the patient, which enables accurate registration of preoperative medical images to guide surgical robotic systems, or even manually operated instruments. The prototype described in this paper extends our prior work in which granular jamming alone was used with a plastic frame [2]. Here, we use layer jamming in conjunction with granular jamming to create a headband that conforms to the patient's head, becoming rigid when a vacuum is drawn.

An example of where this would be useful is in robot-assisted drilling. Drilling is often required as a first step in transnasal skull base and sinus surgeries to access the surgical site. It has been previously shown that collaborative human-robot systems (in which both the surgeon and the robot hold the drill simultaneously) can assist the surgeon [5] by enforcing virtual fixtures (see [6] for a review) around sensitive anatomy. Another example where registered images and virtual boundaries can be useful is in pituitary surgery, where they have been proposed as a means to prevent damage to the optic nerves and carotid arteries in manual [7] and robotic [8] surgical approaches.

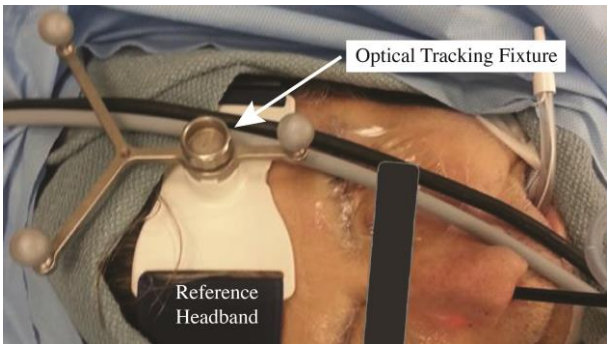

Fig. 1 The Brainlab Kolibri reference headband with an optical tracking fixture attached is shown positioned on a patient during an image-guided transnasal surgery.

MATERIALS AND METHODS

The use of granular jamming and layer jamming in concert enables our headband to both locally and globally conform to the patient's head and then solidify. This enables the headband to non-invasively, yet rigidly, affix optical tracking markers to the patient (see Fig. 2). The granular jamming pads enable local conformation to the contours of the patient's head and layer jamming creates a structure to connect the pads to one another that can similarly stiffen when a vacuum is drawn. The layer jamming band consists of a 0.25 inch stack of 20lb bond paper sealed within an airtight plastic sleeve (Uline, WI, USA), and the granular jamming pad consists of a latex membrane filled with ground coffee. The sleeve was sealed around the paper using a heat sealing machine. To facilitate optical tracking a fixture containing fiducial markers was screwed to the layer jamming band.

To mount the device to a patient, the elastic band surrounding the layer jamming band is first cinched tight, and then a vacuum is drawn on both the granular and layer jamming components to solidify them. A felt tip was used on the ends of the vacuum tubing to ensure that coffee was not suctioned into the tube.

The granular jamming pads are positioned on the temples and at the back of the head as shown in Fig. 2 to position them over areas of the skull with significant variation in

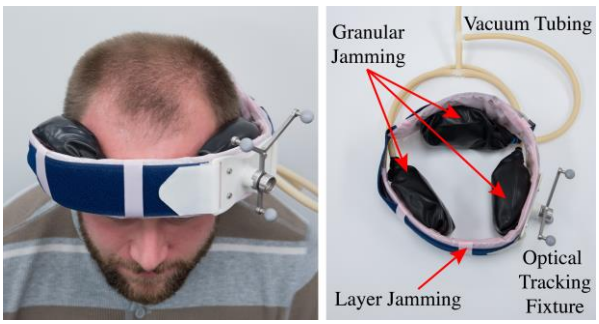

Fig. 2 Our new fixation device features three granular jamming pads, which conform to the patient's skull, and are mounted to a layer jamming band that can solidify to hold them in place relative to one another when a vacuum is drawn.

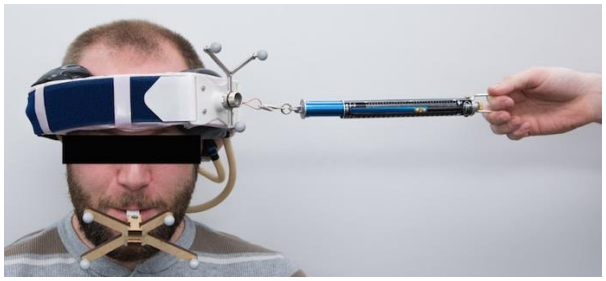

Fig. 3 The test setup for our experiments applying perturbations to the granular/layer jamming headband. A spring scale was used to pull on the headband in four different directions. The movement of the headband markers with respect to bite block markers was measured using an optical tracker as force was applied by hand using the spring scale.

local curvature. After the pads conform to these areas, the layer jamming band holds them in place relative to one another. The elastic band that surrounds the layer jamming band serves to apply an inward force on all components so that the granular jamming pads do not pull away from the patient as they solidify.

In our experiments, we followed the typical clinical positioning of the optical tracking fixture over the patient's left temple – this positioning keeps it out of the surgeon's way and aims it towards the typical tracker mounting location. To test the performance of our device against the standard Brainlab headband, we performed a series of force perturbations (9.81 Newtons) in four directions (up, down, left, and right in the plane tangent to the patient's head under the optical tracking fixture, with "up" being toward the crown of the patient's head). We then optically tracked the position of both the fiducials on the headband, and a second set of fiducials on a bite block in the patient's teeth (see Fig. 3). Note that these forces were applied by hand with a spring scale, and that while every attempt was made to increase the force linearly with respect to time, since the pulls were applied by hand this was not controlled precisely. Tracking was accomplished using the Polaris Spectra (Northern Digital Inc.).

RESULTS

We recorded the movement of the headband markers relative to the bite block markers for both the Brainlab headband and our new granular/layer jamming headband due to the force perturbation, with results shown in Fig. 4. These tests were used to compare the ability of the two headbands to fix the optical tracking markers to the head. Compared to the Brainlab headband, the granular/layer jamming headband reduced the maximum error by 15.1 mm, 7.8 mm, 6.1 mm, and 12.5 mm in the down, up, left, and right directions, respectively.

DISCUSSION AND CONCLUSION

The granular/layer jamming headband presented here provides superior rigidity compared to the standard Brainlab headband. It appears to us that the main source of error with the Brainlab headband is skin mobility over the surface of the skull. The granular jamming pads mitigate this mobility by conforming to areas of

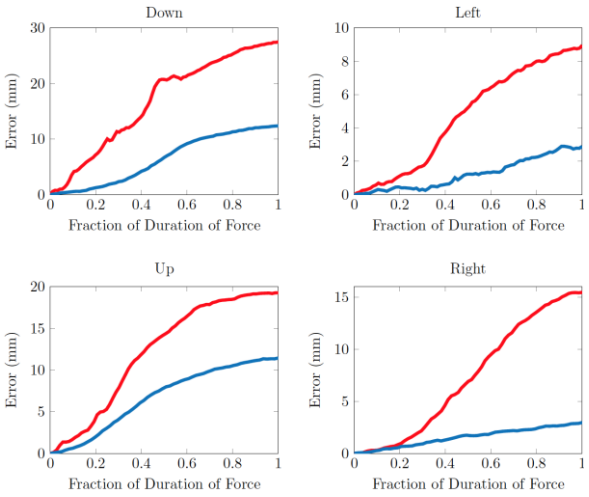

Fig. 4 The error (i.e. movement) of the Brainlab headband (red) vs. the granular/layer jamming headband (blue) as a force of 9.81 N was applied by hand using a spring scale.

curvature variation in the skull. In a real-world operating room we expect a wide variety of perturbation conditions, both constant and intermittent, including those caused by impact, constant loads such as those applied by the wires shown in Fig. 1, etc. We leave it to future work to study the effects of more complex loading conditions, but note that we studied pull and release loads using granular jamming alone in [2]. It is also worth noting that rigidly affixing objects to the patient using our technique has implications beyond image-guidance. It may be useful to attach robots directly to the skull in the future, especially in the context of eye surgery where skull motion relative to the robot can lead to damage to sensitive intraocular structures.

REFERENCES

[1] Lorenz KJ, Frühwald S, Maier H. The use of the BrainLAB Kolibri navigation system in endoscopic paranasal sinus surgery under local anaesthesia. An analysis of 35 cases. HNO. 2006;54(11):851–860.

[2] Wirz R, Lathrop RA, et al. Can coffee improve image guidance? SPIE Medical Imaging, 2015.

[3] Brown E, Rodenberg N, et al. Universal robotic gripper based on the jamming of granular material. Proc. Nat. Acad. Sci. 2010;107(44):18809-18814.

[4] Kim YJ, Cheng S, Kim S, Iagnemma K. A novel layer jamming mechanism with tunable stiffness capability for minimally invasive surgery. IEEE Transactions on Robotics 2013;29(4):1031-1042.

[5] Xia T, Baird C, Jallo G, Hayes K, Nakajima N, Hata N, Kazanzides P. An integrated system for planning, navigation and robotic assistance for skull base surgery. Int. J. Med. Robot. 2008;4(4):321-330.

[6] Bowyer SA, Davies BL, Rodriguez y Baena F. Active constraints/virtual fixtures: a survey. IEEE Transactions on Robotics 2014;30(1):138-157.

[7] Leonard S, Reiter A, Sinha A, Ishii M, et. al. Image-based navigation for functional endoscopic sinus surgery using structure from motion. SPIE Medical Imaging, 2016.

[8] Travaglini TA, Swaney PJ, et al. Initial experiments with the leap motion as a user interface in robotic endonasal surgery. IFToMM Int. Symp. Rob. Mech. 2016:171-179.

From Microrockets to Nanobullets: Towards Realizing the 'Fantastic Voyage'

J. Wang

University of California San Diego, USA

josephwang@ucsd.edu

INTRODUCTION

Over the past decade, several labs - including ours - have developed advanced multi-functional nanomachines based on powerful nanomotors for diverse biomedical applications [1-3]. These research efforts have led to the introduction of new propulsion mechanisms and nanomotor designs and materials, biocompatible fuels, advanced nanoscale motion control, built-in' diagnostics, imaging and cargo-towing therapeutic capabilities, adaptive and responsive operations, and unique collective and swarming behaviors. The new capabilities and functionalities of these microrobots have led to exciting biomedical applications, ranging from the isolation of cancer cells, deep tissue penetration, or intracellular miRNA detection. After a decade of basic research on the synthesis and characterization of synthetic micromotors in test-tube settings, the field has recently reached a new milestone where the performance of these motors was evaluated in live bodies. Our lab demonstrated recently the first applications of synthetic nanomachines within cells [4] and in living animals [5]. As future micro/nanomachines become more powerful and functional, these tiny devices are expected to perform more demanding biomedical tasks.

MATERIALS AND METHODS

The acid-powered microrockets have an open tubular bilayer design, consisting of an outer polymeric layer and inner zinc layer [5]. These microrockets are prepared by a membrane-template electrodeposition approach. The ultrasound-activated microcannons are also prepared by template electrosysthesis. These open tubes are loaded with their therapeutic payloads along with a perfluorocarbon fluid. An ultrasound pulse leads to a rapid evaporation of the latter, resulting in spontaneous 'firing' of the nanobullet payloads from the microcannons [5]. Such firing is 'triggered' by exposure to a focused ultrasound pulse.

RESULTS

In this presentation, we will use two examples to illustrate the powerful capabilities and biomedical prospects of recently developed microrobots, as next-generation efficient nanoscale delivery devices capable of delivering their payloads efficiently into an identified target. We will start with acid-powered microrockets that self propel efficiently in the stomach gastric fluid [5]. Such efficient movement in the gastric fluid reflects the thrust of hydrogen microbubbles generated on the inner zinc surface and leads to a greatly enhanced penetration and retention of the motors and of their payload on the stomach wall. These acid-powered bubble-propelled micromotors possess several distinct functions for potential biomedical use. These include a remarkably high loading capacity, combinatorial delivery of a multitude of cargoes, autonomous release of encapsulated payloads, biocompatibility, and self-destruction. 'On-the-fly' dissolution of the zinc body thus leads to an autonomous release of the encapsulated cargoes and eventual splitting apart of the motors and their complete self destruction and disappearance, leaving nothing toxic behind.. Our *in-vivo* results have demonstrated that the self-propulsion of the micromotors leads to a dramatically improved retention of their payloads in the stomach lining compared to the common passive diffusion and dispersion of orally administrated payloads.

Our second example will focus on acoustic microcannons capable of versatile loading and effective firing of nanobullets [6]. These acoustic microcannons and nanobullets are extremely effective tools for advancing microscale tissue penetration of therapeutic payloads. The electrochemically-synthesized hollow microcannons have been fully loaded with a gel matrix containing the nanobullets and a perfluorocarbon emulsion. Application of a focused ultrasound pulse leads to the spontaneous vaporization of the perfluorocarbon emulsion within the microcannon into a rapidly expanding microbubble, and results in the rapid ejection of the nanobullets in a remarkably high speed and power. These nanobullets could thus be used to drive drugs directly deep into diseased tissues or to deliver genetic material into cell nuclei for gene therapy. The new acoustic-microcannon approach paves the way towards advanced microscale ballistic tools, capable of efficient loading and firing of multiple cargoes, and offer improved accessibility to target locations and enhanced tissue penetration properties towards the realization of the 'magic bullet' vision.

DISCUSSION

Recent advances have created powerful synthetic nanoscale machines that mimic the function of natural nanomotors. Such multi-functional ultrasound-driven nanomotors or catalytic nanomotors possess numerous attractive properties and capabilities that offer considerable promise for variety of biomedical applications ranging from drug delivery to target

isolation. Such *in vivo* biomedical applications have been realized by eliminating the requirements for external fuels. Additional in vivo characterizations are warranted to further evaluate the performance and functionalities of various man-made micromotors in living organisms. The new capabilities of modern microrobots can be readily expanded to simultaneous encapsulation of a wide variety of payloads, possessing different biomedical functions such as therapy, diagnostics, and imaging, hence opening up biomedical opportunities. The resulting nanomachine platforms thus holds considerable promise for the prevention and treatment of diseases. These studies pave the way for creating next-generation efficient nanoscale delivery devices capable of delivering their payloads into an identified target, towards the realization of the 'Fantastic Voyage' and 'magic bullets' visions.

REFERENCES

[1] J. Wang, "Nanomachines: Fundamentals and Applications", Wiley, 2013.

[2] K.E. Peyer, L. Zhang, B.J. Nelson, Bio-inspired magnetic swimming microrobots for biomedical applications *Nanoscale*, 2013**, 5,** 1259.

[3] J. Wang and W. Gao, Nano/Microscale Motors: Biomedical Opportunities and Challenges, *ACS Nano*, 2012, **6,** 5745.

[4] B. Esteban-Fernandez de Avila, A. Martin, F. Soto, M. A. Lopez-Ramirez, S. Campuzano, G. M. Vasquez-Machado, W. Gao, L. Zhang, J. Wang, Single Cell Real-Time miRNA Sensing based on Nanomotors, *ACS Nano*, 2015, **9**, 6756.

[5] W. Gao, R. Dong, S. Thamphiwatana, J. Li, W. Gao, Weiwei, L. Zhang, J. Wang, Artificial Micromotors in the Mouses Stomach: A Step toward in Vivo Use of Synthetic Motors, *ACS Nano*, 2015, **9**, 115.

[6] F. Soto, A. Martin, S. Ibsen, M. Vaidyanathan, V. G. Gradilla, Y. Levin, A. Escarpa, S. C. Esener, J. Wang, Acoustic Microcannons: Towards Advanced Microballistics, *ACS Nano*, 2016, **10,**1522.

Microsurgical Manipulator using a LINAPOD Parallel Mechanism

D. Koo, C. Song

Department of Robotics Engineering, DGIST, Daegu, Korea

csong@dgist.ac.kr

INTRODUCTION

Robot-assisted microsurgical technique has been developed to overcome physiological limitations such as surgeon's hand tremor. Physiological hand tremor has 6~12 Hz frequency and 100 μm amplitude to unregular direction [1]. During microsurgery, the unintended hand tremor may damage to normal tissues unpredictably.

The hands-on cooperatively-controlled robots and handheld robots capable of compensating the tremor have been developed [2]. For example, the steady hand robot, one of the cooperative control robots, can be applied to vitreoretinal surgery, where both the surgeon and the robot hold the surgical tool. The robustness of this robot enhances the surgical stability to reduce the tremor. The other is a handheld robotic approach as well known for Micron and SMART [3, 4]. Micron has 6 degree of freedom (DOF) motions by introducing the Gough-Stewart platform. The hand tremor can be filtered out by multiple modulated sources (LEDs) on the instrument and additional optical tracking system. SMART employs optical coherence tomography as a precise distance sensor to detect a height between the end-effector and the surgical tissue for active tremor compensation. It can reduce one dimensional hand tremor.

LINAPOD, a kind of 6 DOF parallel mechanism, was developed for industrial purpose in University of Stuttgart [5]. This mechanism employs 6-drive modules to have more stiffness than Stewart platform. Each of the drive modules is connected by a linear actuator and a link. It has been consistently studied and used but, to the best of our knowledge, the miniature LINAPOD manipulator has not yet been reported.

In this study, a microsurgical manipulator which contains the miniaturized multi-DOF parallel mechanism, LINAPOD, is presented for microsurgery.

MATERIALS AND METHODS

A. Inverse Kinematics

Fig.1 shows kinematic configuration of the LINAPOD mechanism. The position and orientation of the end-effector in LINAPOD mechanism are dependent on the shaft length of 6 motors. Determination of each shaft length is very important in general 6-PUS parallel mechanism [6]. In the LINAPOD, the vector $\boldsymbol{M_i}$ representing the shaft length of each motor is calculated by the inverse kinematics. The vector $\boldsymbol{M_i}$ can be separated to vector $\boldsymbol{OD_i}$ and $\boldsymbol{OB_i}$ in equation (1), where the point O represents the origin position of base plate (fixed frame), the point B_i shows the end position

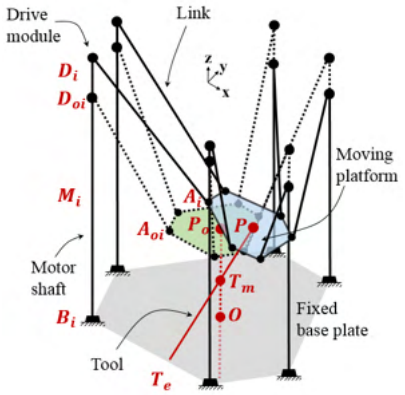

Fig. 1 Kinematic configuration of the LINAPOD mechanism.

of i th shaft on the base plate, and the point D_i depicts the position of i th drive module. The center position of moving platform is a point P and the end position of i th link is point A_i on the particular pose. From these parameters, the equation (1) can be substituted into the equation (2)

$$\boldsymbol{M_i} = \boldsymbol{OD_i} - \boldsymbol{OB_i} \quad (1)$$

$$= \boldsymbol{OP} + \boldsymbol{PA_i} + \boldsymbol{A_iD_i} - \boldsymbol{OB_i} \quad (2)$$

To know the unit vector $\boldsymbol{u_t}$ corresponding to the position and orientation of the tool, the end position and middle position of the tool are denoted by a point T_e and a point T_m, respectively. The subscript o indicates the initial pose of the manipulator and Δd represents relative displacements. Δd_{rcm} represents a setting point of the remote center of motion. l_t is a length of the tool.

$$\boldsymbol{P_oT_e} = \begin{bmatrix} \Delta d_{ex} & \Delta d_{ey} & \Delta d_{ez} + l_t \end{bmatrix}^T \quad (3)$$

$$\boldsymbol{P_oT_m} = \begin{bmatrix} \Delta d_{mx} & \Delta d_{my} & \Delta d_{rcm} \end{bmatrix}^T \quad (4)$$

The vector $\boldsymbol{u_t}$ is defined by two vectors, $\boldsymbol{P_oT_e}$ and $\boldsymbol{P_oT_m}$.

$$\boldsymbol{u_t} = \frac{\boldsymbol{P_oT_e} - \boldsymbol{P_oT_m}}{\left| \boldsymbol{P_oT_e} - \boldsymbol{P_oT_m} \right|} = \begin{bmatrix} u_{tx} & u_{ty} & u_{tz} \end{bmatrix}^T \quad (5)$$

The origin point of the moving plate, P, at a particular pose can be expressed by a vector $\boldsymbol{OP_o}$, a vector $\boldsymbol{P_oT_e}$, and the vector $\boldsymbol{u_t}$.

$$\boldsymbol{OP} = \boldsymbol{OP_o} + \boldsymbol{P_oT_e} - l_t\boldsymbol{u_t} \quad (6)$$

The rotation of the moving plate is represented by the axis rotation n_{rot} and rotation angle θ_{rot}. The axis rotation is obtained by calculating cross product of vector $\boldsymbol{u_{int}}$ corresponding to initial pose of tool and vector $\boldsymbol{u_t}$ corresponding to particular pose. The rotation angle is related to the angle between vector $\boldsymbol{u_{int}}$ and vector $\boldsymbol{u_t}$.

$$n_{rot} = \frac{u_{init} \times u_t}{\left| u_{init} \times u_t \right|} \quad (7)$$

$$\theta_{rot} = \cos^{-1}(u_{init}^T u_t) \quad (8)$$

The rotation matrix of the moving plate can be derived by the Rodrigues' rotation formula.

$$R^{3\times3} = \cos\theta_{rot} I^{3\times3} + \sin\theta_{rot} n_{rot} \times I^{3\times3} + (1-\cos\theta_{rot}) n_{rot}^T n_{rot} \quad (9)$$

The homogeneous transform matrix in equation (10) can be defined by equation (6) and equation (9)

$$\begin{bmatrix} OA_i^{3\times1} \\ 1 \end{bmatrix} = \begin{bmatrix} R^{3\times3} & OP^{3\times3} \\ 0^{3\times3} & 1 \end{bmatrix} \begin{bmatrix} P_o A_{oi}^{3\times1} \\ 1 \end{bmatrix} \quad (10)$$

The desired length of each shaft is obtained by the vector M_i in equation (1) where the length of the vector A_iD_i is constant.

B. System Design

Fig.2 shows 3D design of a miniaturized LINAPOD micromanipulator. It employs 6 SQUIGGLE piezoelectric linear motors (SQL-RV-1.8, New Scale Technologies, Inc., USA). This piezoelectric motor has small size (2.8 mm x 2.8 mm x 6 mm) and generates large force (> 0.3 N at 3.3V).

The shaft of the SQUIGGLE motor has a thread. The motor can make coupled motion such as the combination of translational motion and rotational motion. The drive module including a small bearing (681h, Dynaroll Corp., USA; 1.0 mm thickness x 3.0 mm diameter) is introduced to separate the translational motion from the coupled motion.

For high dexterity and stable maneuver of handheld micromanipulation, the design specifications consider as follows: a transverse diameter and weight are less than 30 mm and 100 g, respectively.

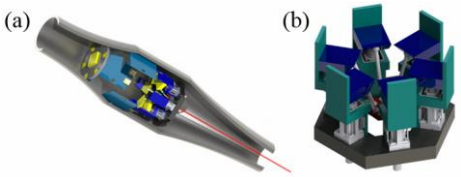

Fig. 2 3D modeling. (a) a handheld micromanipulator, (b) a magnified view of miniature 6-DOF LINAPOD.

C. System Architecture

Fig.3 shows a system architecture of the miniaturized LINAPOD micromanipulator. After detecting the position error, a difference between current position and goal position, the length of six linear actuators is changed to follow the goal position. Each length of the actuator shafts can be calculated by the inverse kinematics. In Fig.3, the hand tremor can be regarded as an external disturbance, and the sensor can detect the hand tremor and the motor driver compensate it as shown in feedback control box.

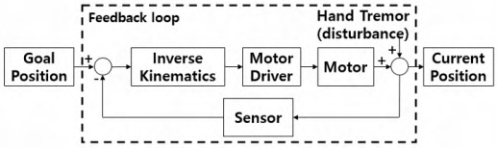

Fig. 3 System architecture of the microsurgical handheld robot.

RESULTS

Fig.4 shows a rapid prototype of the benchtop miniature LINAPOD manipulator composing of 6 SQUIGGLE motors and drive modules. The diameter of LINAPOD mechanism is 25 mm. A pure longitudinal actuation is achieved by the equivalent linear motions of 6 motors.

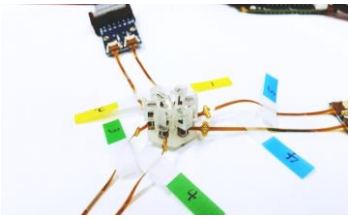

Fig. 4 A benchtop manipulator of the miniature LINAPOD.

CONCLUSION

In this study, the LINAPOD based robot-assisted handheld manipulator is presented for microsurgery. This LINAPOD micromanipulator utilizes 6 piezoelectric linear motors. The exact length of the motor shaft can be derived by inverse kinematics for a particular pose. The current proof-of-concept implementation shows the potential to achieve multi-DOF precise motions which improve microsurgical capabilities and efficiency.

REFERENCES

[1] C. N. Riviere, J. Gangloff, and M. de Mathelin, Robotic compensation of biological motion to enhance surgical accuracy, Proc. IEEE 94(9), 1705–1716 (2006).

[2] Payne, C. J., and G.-Z. Yang. Hand-held medical robots. Ann. Biomed. Eng. 42:1594–1605, 2014.

[3] Yang, S., R. A. MacLachlan, and C. N. Riviere. Manipulator design and operation of a six-degree-of-freedom handheld tremor-canceling microsurgical instrument. IEEE/ASME Trans. Mechatron. 1–12, 2014

[4] Song, C., D. Y. Park, P. L. Gehlbach, S. J. Park, and J. U. Kang. Fiber-optic OCT sensor guided "SMART" micro-forceps for microsurgery. Biomed. Optics. Exp. 4:1045–1050, 2013

[5] K. H. Wurst, C. R. Boer, L. Molinari-Tosatti, and K. S. Smith, LINAPOD-machine tools as parallel link systems based on a modular design, Parallel Kinematic Machines: Theoretical Aspects and Industrial Requirements, pp. 377-394, 1999, Springer-Verlag

[6] J.-P. Merlet, Parallel Robots, 2006, Springer-Verlag

ACKNOWLEDGMENT

This work was supported by the Ministry of Health & Welfare through the Korea Health Industry Development Institute (KHIDI)(HT15C0001) and National Research Foundation of Korea (NRF) grant funded by the Korea government (MSIP) (No.2015R1C1A1A01052915)

Intra-operative Simultaneous Catheter and Environment Modelling for Endovascular Navigation Based on Intravascular Ultrasound, Electromagnetic Tracking and Pre-operative Data

L. Zhao, S. Giannarou, S.-L. Lee, R. Merrifield, G.Z. Yang

The Hamlyn Centre for Robotic Surgery, IGHI, Imperial College London, UK
liang.zhao@imperial.ac.uk

INTRODUCTION

Cardiovascular diseases (CVD) form the single most common cause of death. Catheter procedures are among the most common surgical interventions used to treat CVD. Due to their minimal access trauma, these procedures extend the range of patients able to receive interventional CVD treatment to age groups dominated by co-morbidity and unacceptable risks for open surgery [1]. The downside associated with minimising access incisions lies at the increased complexity and difficult manipulation of the instruments and anatomical targets, which is mainly caused by the loss of direct access to the anatomy and the poor visualisation of the surgical site. The current clinical approaches to endovascular procedures mainly rely on 2D guidance based on X-ray fluoroscopy, which uses ionising radiation and dangerous contrast agents [2].

In this paper, a Simultaneous Catheter and Environment Modelling (SCEM) method is presented for endovascular navigation based on intravascular ultrasound (IVUS) imaging, electromagnetic (EM) sensing as well as the vessel structure information provided from the pre-operative CT/MR imaging (see Fig. 1). Thus, radiation dose and contrast agents are avoided. The proposed SCEM intra-operatively recovers the 3D structure of the vasculature together with the pose of the catheter tip, which the knowledge of the interaction between the catheter and its surroundings can be provided. The corresponding uncertainties of both vessel reconstruction and catheter pose can also be computed which is necessary for autonomous robotic catheter navigation. Experimental results using three different phantoms, with different catheter motions and cardiac motions simulated by using a periodic pump demonstrated the accuracy of the vessel reconstruction and the potential clinical value of the proposed SCEM method.

MATERIALS AND METHODS

The system setup of the proposed SCEM method can be seen in Fig 1. First, for each IVUS image frame, contour extraction was performed with a radial scan [3] to identify high intensity ultrasound reflections, which provides the intersection of the inner vessel wall and the IVUS plane. Suppose I is the contour extracted from the IVUS image, E is the 6DoF pose reported from the EM sensor on the catheter tip, then the proposed SCEM algorithm can be mathematically formulated as a nonlinear optimisation problem which minimises the

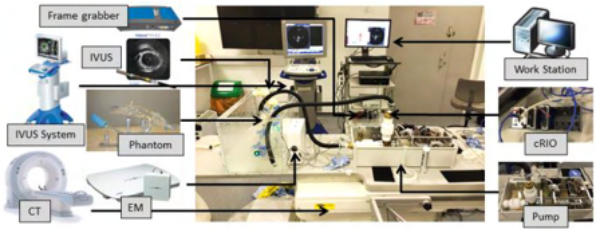

Fig. 1 The experimental setup.

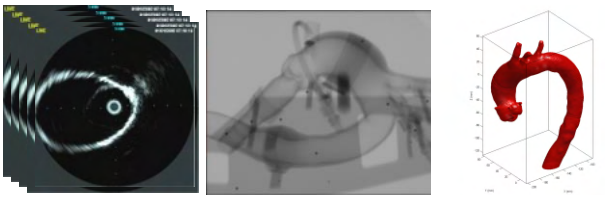

(a) IVUS Images (b) CT Scan (c) 3D Model

Fig. 2 The IVUS images, the pre-operative CT scan and the aortic model segmented in ITK-SNAP.

following objective function:

$$\text{minimise} \quad F(\mathbf{P}) = \|\mathcal{D}(f(I,\mathbf{P}))\|^2_{\Sigma_I^{-1}} + \|E-\mathbf{P}\|^2_{\Sigma_E^{-1}}$$

where, the state vector $\mathbf{P}$ is the catheter pose, function $f(\cdot)$ transforms the IVUS contour I to the global coordinate frame by using $\mathbf{P}$ and $\mathcal{D}(\cdot)$ is the signed distance function pre-computed from the pre-operative data (see Fig. 2), which presents the shortest distances from all the points on contour $f(I,\mathbf{P})$ to the CT model of the vessel in the pre-operative data, with positive inside the model and negative outside the model. Here, both the IVUS contour I and EM pose E are considered as observations with uncertainties (covariance matrices) Σ_I and Σ_E [4]. And the optimisation problem tries to minimise the distances between the contour $f(I,\mathbf{P})$ computed from IVUS and the pre-operative model, weighted by the inverse of uncertainty of IVUS contour Σ_I^{-1}, and minimise the difference between the catheter pose $\mathbf{P}$ in the state vector and the pose E reported from the EM sensor, weighted by the inverse of uncertainty of EM sensor Σ_E^{-1}. We assume there is no common feature between different IVUS contours, with known EM-CT registration, optimisation using a single frame is equivalent to batch/incremental optimisation using a sequence of IVUS images and EM poses.

The proposed nonlinear optimisation can be solved using the Gauss-Newton method by linearising the first term in the objective function via Taylor Series, and the state vector $\mathbf{P}$ is initialised by the EM pose E.

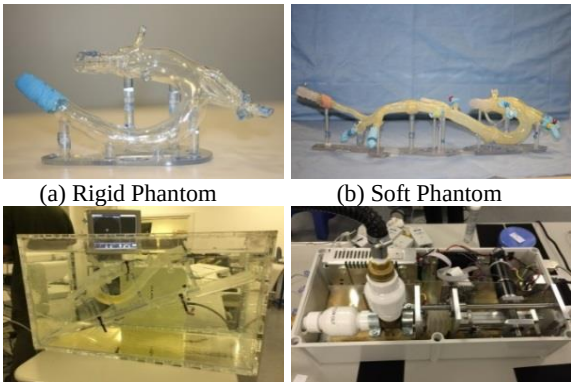

(a) Rigid Phantom (b) Soft Phantom

(c) Silicone Phantom (d) Periodic Pump

Fig. 3 Aortic phantoms used in the experiments: Rigid phantom made of Plexiglas material (a), Soft phantom made of HeartPrint® material (b) and phantom made by silicone (c) which is compatible with the pump (d) to simulate the periodic cardiac motion.

After an optimal solution of the catheter pose is obtained, the 3D vessel can be reconstructed by using it to transform the IVUS contour I to the global coordinate frame by $f(\cdot)$. The corresponding uncertainty of the catheter pose can be obtained as the inverse of the normal equation matrix evaluated at the optimal solution from the optimisation, and the uncertainty of the vessel reconstruction can be computed by using the nonlinear transformation of multivariate Gaussian distributions [5]:

$$\Sigma_P^{-1} = \frac{\partial f}{\partial \mathbf{P}}^T \frac{\partial \mathcal{D}}{\partial f}^T \Sigma_I^{-1} \frac{\partial \mathcal{D}}{\partial f} \frac{\partial f}{\partial \mathbf{P}} + \Sigma_E^{-1}, \quad \Sigma_V = \frac{\partial f}{\partial I} \Sigma_I \frac{\partial f}{\partial I}^T + \frac{\partial f}{\partial \mathbf{P}} \Sigma_P \frac{\partial f}{\partial \mathbf{P}}^T .$$

RESULTS

In the experiments, three aortic phantoms created by Materialise (Leuven, Belgium) were used (see Fig. 3), which are made of Plexiglas (Rigid), their signature HeartPrint® Flex material (Soft) and silicone (Silicone) respectively. Segmented CT scans of the phantoms provided the triangular surface meshes of the models (see Fig. 2). An Aurora 6 DoF EM sensor (NDI, Waterloo, Canada) was attached to the tip of an IVUS catheter (Volcano, San Diego, USA) to provide its position and orientation.

Insertions and/or pullbacks within the Rigid, Soft and Silicone phantoms were performed to validate the proposed SCEM method. Sudden motions were also performed with the Soft and Silicone phantoms to validate the robustness of the abrupt catheter motions. To simulate the cardiac motion, pump with periodic motions was connect to the pump compatible Silicone phantom, and the aortic phantom was deformed periodically by controlling the frequency and volume per stroke of the pump. The pump signal was then used as the ECG signal to gate the IVUS images in the proposed SCEM method.

For each situation, 5 experiments were performed, and the result of one experiment using the Soft phantom is shown in Fig 4. The quantitative evaluation of the 3D vessel reconstruction for all the experiments is shown in Fig 5.

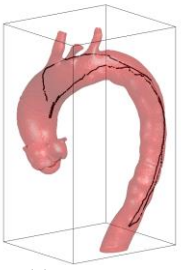

(a) Reconstruction (b) Uncertainty (c) Trajectory

Fig. 4 Results using the soft phantom: 3D reconstruction (a), uncertainty (log) map (b) and the trajectory of the catheter (c).

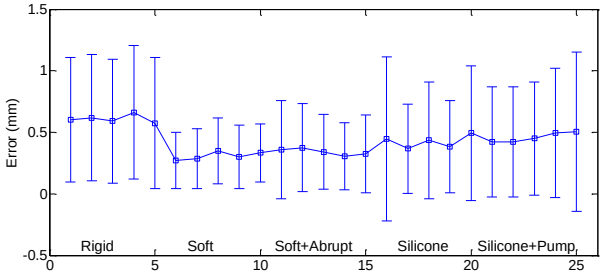

Fig. 5 Vessel reconstruction error of different aortic phantoms and with abrupt catheter motion and cardiac motion simulated by the pump. (The higher error in the Rigid phantom is caused by lower quality IVUS imaging.)

The proposed SCEM method runs in real-time as 800 frames per second on an Intel® Xeon(R) E5-2620 CPU @ 2.0 GHz, and the accuracy of the vessel reconstruction was approximately 0.6mm for the Rigid phantom, 0.3mm for the Soft phantom and 0.4mm for the Silicone phantom.

ACKNOWLEDGEMENT

This work was part of the FP7-ICT Project "Cognitive AutonomouS CAtheter operating in Dynamic Environments (CASCADE)" supported by the Commissions 7th Framework Programme under grant agreement No.601021.

REFERENCES

[1] Mirabel, M., Iung, B., Baron, G., et al. What are the characteristics of patients with severe, symptomatic, mitral regurgitation who are denied surgery? *European Heart Journal* 2007; 28(11):1358-1365.

[2] Wahle A., Prause G.P.M., DeJong S.C., Sonka M. Geometrically correct 3-D reconstruction of intravascular ultrasound images by fusion with bi-plane angiography-methods and validation. *IEEE Transactions on Medical Imaging* 1999;18(8):686-699.

[3] Shi C., Giannarou S., Lee S.-L., Yang, G.Z. Simultaneous catheter and environment modeling for Trans-catheter Aortic Valve Implantation. In: *Proc. IEEE/RSJ IROS*, 2014:2024-2029.

[4] Zhao, L., Giannarou, S., Lee, S.-L., Yang, G.Z. SCEM+: Real-time robust simultaneous catheter and environment modeling for endovascular navigation. *IEEE Robotics and Automation Letters* 2016;1(2):961-968.

[5] Julier, S.J., Uhlmann, J.K. A general method for approximating nonlinear transformations of probability distributions. *Technical report*, Robotics Research Group, Department of Engineering Science, University of Oxford 1996.

Stent Graft Shape Instantiation for Fenestrated Endovascular Aortic Repair

X.-Y. Zhou[1], C. Riga[2], G.-Z. Yang[1], S.-L. Lee[1]

[1]*The Hamlyn Centre for Robotic Surgery, IGHI, Imperial College London, UK*

[2]*Academic Division of Surgery, Imperial College London, UK*
xiaoyun.zhou14@imperial.ac.uk

INTRODUCTION

Abdominal Aortic Aneurysms (AAA) cause a large number of deaths worldwide every year. Current treatment includes Endovascular Aortic Repair (EVAR), when a compressed stent graft is inserted and deployed at the aneurysm to avoid placing the arterial wall under further pressure, under the guidance of X-ray fluoroscopy. However, customised stent grafts with fenestrations or scallops are essential for those AAA patients with complex anatomies, making up 45% of the total number of AAA patients [1]. Aligning fenestrations or scallops with renal arteries when stent grafts are compressed during this Fenestrated Endovascular Aortic Repair (FEVAR) is challenging under 2D X-ray fluoroscopy guidance, usually requires repositioning after deployment, and can cause possible massive haemorrhaging.

Improving EVAR has been researched for years. Demirci et al. recovered stent graft shapes from one X-ray image by registering 3D stent graft shapes onto an X-ray fluoroscopy image [2]. Volpi et al. detected and tracked the stent graft deployment device on 2D X-ray images by Robust Principal Component Analysis [3]. However, these cannot indicate the orientation of fenestrations or scallops and cannot predict the deployed stent graft shape from its compressed state.

In FEVAR, stent grafts are almost invisible under X-ray fluoroscopy due to the influence of tissue. They are also compressed into a deployment device with maximum diameter $10mm$. Stent rings (Fig. 2b) experience twist during manual compression and then untwist themselves during the deployment. In this paper, markers are sewn onto stent rings. Deployed stent graft shapes (Fig. 1b) are predicted from one fluoroscopic image (Fig. 1a) of its compressed state, through shape instantiation, by solving a RPnP (Robust Perspective-n-Point) problem of placed markers that determines the pose of a camera from n correspondences between 3D reference points and their 2D projections. The twisting is recovered by selecting an untwisting reference based on experience.

MATERIALS AND METHODS

A stent graft was modelled as vertices on a circle $[R * cos\theta, R * sin\theta, H]$ at different heights; R is the radius, H is the height, and $\theta \in (0°, 360°)$ is the angle of each vertex. Triangles were generated regularly to connect these vertices (Fig. 2a). The compressed and deployed states of a stent graft were defined by modifying R. Vertices within fenestrations or scallops were removed. The twisting of each circle was controlled by θ [4].

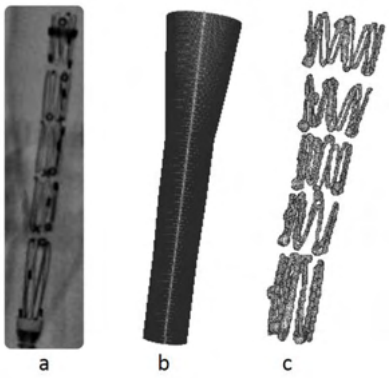

Fig. 1 Shape instantiation from one slice of the compressed stent graft fluoroscopic image: a. X-ray fluoroscopy of a compressed stent graft, b. shape instantiation result, c. the real deployed shape.

With known preoperative 3D marker positions, the Z axis was firstly chosen to divide RPnP into $(n-2)$ RP3P problems with equation systems:

$$f_i(x) = a_i x^4 + b_i x^3 + c_i x^2 + d_i x + e_i = 0$$
$$i \in (1, n-2)$$

Here

$$a_i = A_6^2 - A_1 A_5^2$$
$$b_i = 2(A_3 A_6 - A_1 A_4 A_5)$$
$$c_i = A_3^2 + 2A_6 A_7 - A_1 A_4^2 - A_2 A_5^2$$
$$d_i = 2(A_3 A_7 - A_2 A_4 A_5)$$
$$e_i = A_7^2 - A_2 A_4^2$$

All the possible selections of Z axis were tested and the one with least error was chosen. The depth of each vertex was determined by perspective similar triangles after solving for x. The relationship between 3D positions and 2D projections can be written as:

$$\lambda_i \begin{bmatrix} u_i \\ v_i \\ 1 \end{bmatrix} = \begin{bmatrix} r_1 & r_4 & r_7 \\ r_2 & r_5 & r_8 \\ r_3 & r_6 & r_9 \end{bmatrix} \begin{bmatrix} c & -s & 0 \\ s & c & 0 \\ 0 & 0 & 1 \end{bmatrix} \begin{bmatrix} X_i \\ Y_i \\ Z_i \end{bmatrix} + \begin{bmatrix} t_x \\ t_y \\ t_z \end{bmatrix}$$

The pose is solved by:

$$[A_{2n\times 1}\ B_{2n\times 1}\ C_{2n\times 4}][c\ s\ t_x\ t_y\ t_z\ 1]^T = 0$$

c and s are cos and sin of the rotation angle along the Z axis while $[t_x, t_y, t_z]$ indicate the translation. Normalization was applied on the transformation matrix of the intraoperative pose. Details of each parameter, the solution and normalization were stated in [5].

Five markers with different shapes were printed in a Mlab Cusing R machine (ConceptLaser, Lichtenfels, Germany) with SS316L stainless steel powder and were

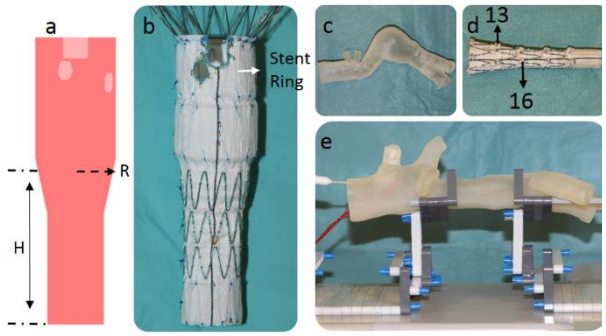

Fig. 2 Modelling and setup: a. modelling of a customised stent graft, b. the real customised stent graft, c. the printed AAA patient phantom, d. the customised stent graft used in validation with markers sewn on, e. experimental setup.

sewn on each stent ring to observe the twisting and untwisting during compression and deployment. Two phantoms (Fig. 2c) segmented from contrast-enhanced Computed Tomography (CT) data of AAA patients were printed on a Stratasys Objet500 (MN, USA). A customised stent graft (20mm diameter, 90mm height, Cook Medical, IN, USA) (Fig. 2d) was used for validation with a deployment device (Medtronic, 8mm diameter, MN, USA). The setup of the experiment is shown in Fig. 2e.

Two locations within the phantoms were selected for setup considering size and curvature fitting between phantoms and the stent graft. X-ray images were taken at 13 view angles from $[-90°, 90°]$ with $15°$ intervals.

X-ray images and CT scans were collected using a GE Innova 4100 (GE Healthcare, Bucks, UK). 3D Slicer [6] was applied for segmenting and identifying 2D marker coordinates with $0.4mm$ resolution. The C-arm, setup and X-ray fluoroscopy coordinate systems were registered together. The position drift caused by the C-arm was corrected by aligning box centres. The angles of markers were approximated by the angles of their nearest vertices on the model.

RESULTS

The untwisting should be along the reference ring that fixates against the artery wall. As we have observed in customised stent graft deployment, this reference ring was usually the first one. However, during our validation, the stent graft was not customised for the phantom. The average angle untwisting of each marker in the two setups is shown in Fig. 3. Due to the mismatch between the stent graft and the phantom, the middle stent rings untwisted less than those towards the ends of the graft. In later shape instantiation, the 13^{th} (setup 1) and the 16^{th} markers (setup 2) (Fig. 2d) were chosen as the reference for untwisting.

The average angle errors of shape instantiation for the two setups are shown in Fig. 4. We can see that the average angle error is approximately $10^{\circ} - 20^{\circ}$ and the performance is not influenced by the view angle.

It takes less than $0.02s$ to instantiate a customised stent graft with five stent rings on an Intel(R) Core(TM) i7-4790 CPU@3.60GHz computer. This running time is linear to the number of marker sets used.

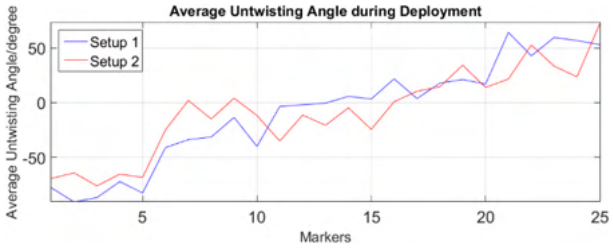

Fig. 3 The average untwisting angle of each marker in the two setups.

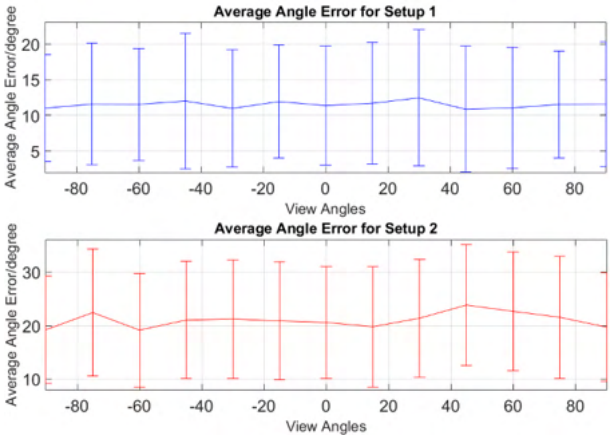

Fig. 4 The average angle error of shape instantiation in setup 1 (top) and setup 2 (bottom) for 13 view angles.

DISCUSSION

The shape instantiation predicts a deployed customised stent graft shape based on one fluoroscopic image of its compressed state with a low angle error. This work improves visualisation of fenestrations or scallops for physicians to align them with renal arteries and hence increase the success rate of FEVAR. Future work includes shape instantiation with bending and improved determination of the reference ring to recover untwisting.

REFERENCES

[1] Arko, F. R., Filis, K. A., et al. "How many patients with infrarenal aneurysms are candidates for endovascular repair? The Northern California experience." Journal of Endovascular Therapy 11.1 (2004): 33-40.

[2] Demirci, S., Bigdelou, A., et al. "3D stent recovery from one X-ray projection." Medical Image Computing and Computer-Assisted Intervention–MICCAI 2011. Springer Berlin Heidelberg, 2011. 178-185.

[3] Volpi, D., Sarhan, M. H., et al. "Online tracking of interventional devices for endovascular aortic repair." International journal of computer assisted radiology and surgery 10.6 (2015): 773-781.

[4] Kho, Y., Garland, M. "Sketching mesh deformations." Acm siggraph 2007 courses. ACM, 2007.

[5] Li, S., Xu, C., et al. "A robust O (n) solution to the perspective-n-point problem." Pattern Analysis and Machine Intelligence, IEEE Transactions on 34.7 (2012): 1444-1450.

[6] Pieper, S., Halle, M., et al. "3D Slicer." Biomedical Imaging: Nano to Macro, 2004. IEEE International Symposium on. IEEE, 2004.

Kinematic-Model-Free Positional Control for Robot-Assisted Cardiac Catheterization

C. L. Cheung[1], K.-H. Lee[1], Z. Guo[1], Z. Dong[1], M. C.W. Leong[1], Y. Chen[1], A. P.W. Lee[2], K.-W. Kwok[1]

[1]*Department of Mechanical Engineering, The University of Hong Kong, Hong Kong*

[2]*Division of Cardiology, Prince of Wales Hospital, The Chinese University of Hong Kong, Hong Kong*

zardchim@hku.hk

INTRODUCTION

Cardiac electrophysiology (EP) [1] is a typical example of catheter interventions for cardiovascular diseases, in which a catheter is delivered from the femoral vein to perform ablation in the heart chamber. It requires precise targeting of the catheter tip at a small region for radio-frequency (RF) ablation of tissues in order to isolate the abnormal electrophysiological signals causing the arrhythmia. This procedure is considered as an effective treatment for heart rhythm disorder (arrhythmia). However, maneuvering of such a long and flexible catheter inside the cardiac chamber is still a challenging task even for the latest advances in the robotic-assisted platforms. The continuum structure of catheter, as well as the rapid cardiac motion, make it very difficult to predict the catheter motion during an intervention.

Previous research attempts [2] aim to control the catheter motion by deriving its explicit kinematic model; however, a number of assumptions, such as that the catheter shape bends as a series of connected arcs without torsion [3], are required. In the real practice, the number and length of these arcs can be changed rapidly due to numerous contacts along the vascular tissue.

To avoid dependency on model based kinematic control for catheter navigation, we developed a model-free control interface capable of providing effective teleoperated control of a clinically used catheter, with the incorporation of visual-motor alignment. A sequential sampling method, particle filtering [4], is used to update the mapping from actuation input to our proposed virtual camera coordinate smoothly in order to realign the visual-motor coordinates time-by-time. It aims to provide the operator with a consistent motion reference to maneuver the catheter tip aiming at the desired target in unknown or unstructured constrained environments. Subject tests have been conducted to demonstrate how the proposed approach enhances the navigation effectiveness.

MATERIALS AND METHODS

As shown in **Fig. 1**, a 2D virtual camera view is defined and attached at the catheter tip, of which the *z*-axis is aligned along the tip normal. The standard catheter is driven by 3 DoFs, namely advancement, rolling and steering $[l, q_r, q_s]$. The incremental tip displacement $\Delta \boldsymbol{x} = \left[x_C(k+1) - x_C(k) \quad y_C(k+1) - y_C(k) \right]^T$ is modelled as a linear function of the incremental change of the latter two DoFs $\Delta \boldsymbol{q}_C = [q_r(k+1) - q_r(k) \quad q_s(k+1) - q_s(k)]^T$ such that:

$$\Delta \boldsymbol{x} = \boldsymbol{J} \Delta \boldsymbol{q}_C \tag{1}$$

where $\boldsymbol{J} \in \mathbb{R}^{2 \times 2}$ is the Jacobian matrix **(Fig. 2)**.

A sequential sampling method, Particle Filtering [5], is implemented to update the Jacobian matrix $\boldsymbol{J}$ online from the measurement of $\Delta \boldsymbol{x}$ and $\Delta \boldsymbol{q}_C$.

The operator teleoperates the catheter with a motion input device specifying the desired change of tip position $\Delta \boldsymbol{x}^* = \left[x_C^*(k+1) - x_C(k) \quad y_C^*(k+1) - y_C(k) \right]^T$ in the virtual camera coordinate. The control input

$$\Delta \boldsymbol{q}_C = \boldsymbol{J}^{-1} \Delta \boldsymbol{x}^* \tag{2}$$

accomplishes the visual-motor alignment where the catheter moves with the desired change $\Delta \boldsymbol{x}^*$ in the virtual camera coordinate.

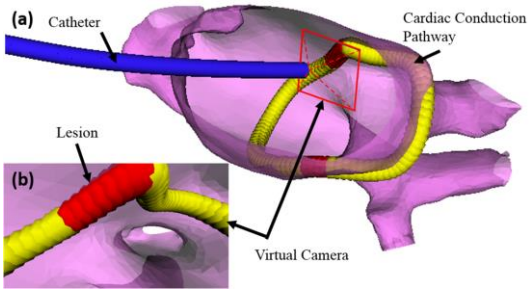

Fig. 1(a) 3-D cardiac roadmap (purple) with lesion targets (yellow) indicated on the pulmonary vein ostium. The targets in red depict the completion of RF ablation. **(b)** Virtual camera view is augmented from the catheter tip's point of view.

RESULTS

To evaluate the proposed catheter control approach, a teleoperated 3-DOF catheter robotic platform has been developed to perform simulated EP procedures on an atrium phantom. The catheter robot (**Fig. 3**(a)) is actuated by 3 stepper motors. Novint Falcon® Haptics

Controller is used for reading motion input command. An electromagnetic tracking system (NDI Aurora) keeps track of the position of catheter tip in the world coordinate. An atrium phantom model (**Fig. 3**(b)) has been fabricated based on a 3D model obtained from patient MR image. Such 3D printed phantom model aims to mimic the constraints characteristics in a clinical scenario.

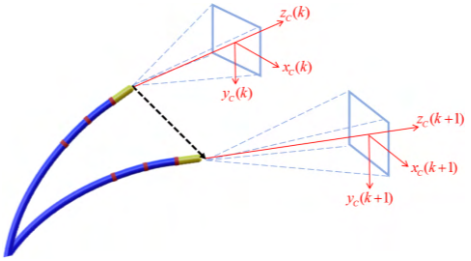

Fig. 2. Illustration of virual camera coordinates aligned with catheter tip.

Subject tests (N=10, age ranging from 20-35) were carried out for evaluation, where the pulmonary vein isolation ablation tasks were simulated using the robotic experimental setup. Each subject performed the same task under two different conditions: 1) Only the fly-through view (**Fig. 1a)** was provided without the proposed control approach. 2) Fly-through view and the virtual camera view (**Fig. 1b**) were provided, where the proposed visual-motor alignment was employed. Each had to perform RF ablation on pre-defined lesions within 5 minutes. The RF ablation at the catheter tipwas activated by a foot pedal.

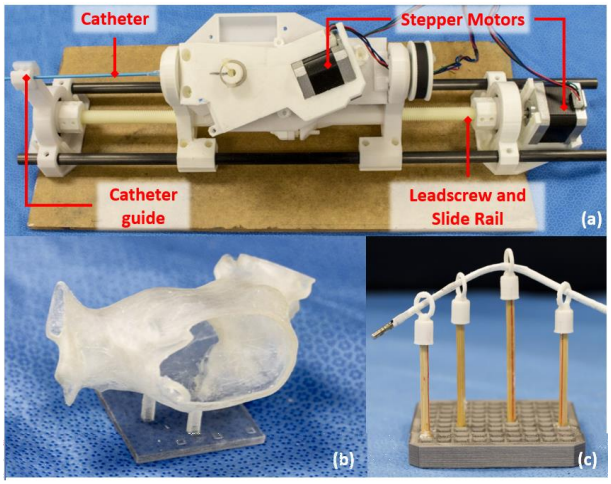

Fig. 3. (a) Tele-operative robotic catheter platform actuated by stepper motors. (b) An atrial phantom model. (c) The catheter is telemanipulated to pass through a series of ring checkpoints.

The performance in terms of: 1) Task accuracy, and 2) Task efficiency are shown in Table I. The total distance traveled and the ablation missed percentage were both measured and evaluated as task efficiency. A maximum of 41% improvement in missed target reduction could be found among the subjects and the average travel distance was reduced by 27%. For task efficiency, subjects were observed that they could successfully ablate a certain target with less attempts using our proposed control method which offers better awareness of distance between the catheter tip and lesion target.

TABLE I. PERFORMANCE INDICES AVERAGED ACROSS THE 10 SUBJECTS IN PERFORMING THE SIMULATED ROBOTIC CATHETERIZATION

	Without alignment		With alignment		Improvement.
Task Efficiency	Mean	SD	Mean	SD	% *p-val.
Aver. Trav. Dist. (mm)	207	30.9	167	35.4	28.8% *0.13
No. of missed target (%)	80.0	1.7	76	6.4	9.3% *0.28
Task Accuracy	Mean	SD	Mean	SD	% *p-val.
No. of times ablation has turn on	12	7.9	8.8	5.0	9.5% *0.54
Average ablation time (sec)	3.41	0.37	3.64	1.26	-6% *0.72
Average tip to lesion target distance (mm)	3.98	0.36	2.48	0.2	37.7% *0.009

DISCUSSION

To avoid dependency on analytical kinematics model, we propose a model-free kinematics control framework for cardiac catheterization, by means of a time series forecasting method called Particle Filtering. To the best of our knowledge, it is the first successful attempt to exploit such time-series forecasting concept in surgical catheterization applications. Promising improvements in both effectiveness and accuracy were found in subject tests, where the proposed method achieved a more accurate control of the catheter in reaching the target ablation point and shorter time for repositioning the catheter tip than without the visual-motor alignment provided. The future work will focus on the extension of the proposed method into dynamic environments, such as navigation under the rapid deformation of cardiovascular tissues due to cardiac motion.

ACKNOWLEDGMENT

This work is supported in parts by the Croucher Foundation and the Research Grants Council (RGC) of Hong Kong. We sincerely thank to the team in the Division of Cardiology, the Prince of Wales Hospital, The Chinese University of Hong Kong (CUHK) for the access to their equipment.

REFERENCE

[1] Z.-J. Zheng, J. B. Croft, W. H. Giles, and G. A. Mensah, "Sudden cardiac death in the United States, 1989 to 1998," *Circulation*, vol. 104, pp. 2158-2163, 2001.
[2] Q. Peng, L. Chuang, Z. Linan, W. Shuxin, L. Hak-Keung, and K. Althoefer, "Fuzzy logic control of a continuum manipulator for surgical applications," in *IEEE ROBIO 2014*, pp. 413-418.
[3] Y. Ganj and F. Janabi-Sharifi, "Catheter Kinematics for Intracardiac Navigation," *IEEE Trans. on Biomedical Engineering*, vol. 56, pp. 621-632, March 2009.
[4] J. Ma and Q. Zhao, "Robot Visual Servo with Fuzzy Particle Filter," *Journal of Computers*, 7:842-845, 2012.
[5] Z. Qingjie, Z. Liqun, and C. Yunjiao, "Online estimation technique for Jacobian matrix in robot visual servo systems," in *ICIEA 2008*, pp. 1270-1275.

Steerable Cannula Robot with Additional Torque Coil Driven Wrist for Arthroscopic Capsular Release

J. Kim[1], K. Kim[2], S. Kang[2], K.-J. Cho[1]

[1]*The School of Mechanical and Aerospace Engineering, Seoul National University, Korea*

[2]*Robot and Media Research Institute, KIST, Korea*

kimjongwoo1988@gmail.com

INTRODUCTION

Capsular release involves removing inflamed and swollen tissue to restore a joint to full range of motion and to reduce pain. The conventional arthroscopic instrument for performing this procedure is stiff and straight, and its distal tip is difficult to maneuver into the correct position in curved joints. [1, 2, 3, 4] Many attempts have been made to perform minimally invasive surgery of curved joints by following the tortuous passages of natural orifices and blood vessels. The concentric tube robot has suggested a novel way to control the distal tip of arthroscopic surgery instruments via relative the transitional and rotational movement of super-elastic nitinol tubes. [5, 6] Patterning the nitinol tubes of the robot enables more stability and permits higher curvature of the tube. [7]

We evaluated the ability of a robotic system, a three-revolute (3R) joint steerable cannula, to perform arthroscopic capsular release on a frozen shoulder joint. The robot consists of four telescoping metal tubes (Figs. 1 and 2) with a 3mm outer diameter. To add an extra degree of freedom for precise and stable control, we added a torque coil–driven wrist at the distal end of the robot. The wrist allows the fourth tube, from which the end-effector emerges, to be independently rotated, which overcomes the general problem with concentric tube robots (also called active cannulas), namely that they interfere with sequential deployment of the tubes. In other words, thanks to the torque coil–driven mechanism, the wrist is able to steer the orientation of the end-effector without changing the configuration of the other tubes.

The steerable cannula robot is suitable for arthroscopic surgery of the curved ball-socket joints of the shoulder, wrist, and hip and potentially also for microjoints such as the temporomandibular joint. The additional control made possible by its unique wrist can help surgeons avoid damage to nerves and other joint tissues. Its hollow structure is capable of equipping a range of endoscopic surgical instruments, such as electrocautery and laser ablation tools. We conducted experiments on a shoulder joint model and a porcine shoulder joint using the prototype version of the robot.

MATERIALS AND METHODS

The steerable cannula robot mainly consists of four hollow metal tubes of progressively smaller diameter (Fig. 1). The first tube is a straight stainless steel tube with a diameter of 3.0mm. The second tube is a pre-curved patterned nitinol tube with a diameter of 2.6mm. The third tube is a pre-curved nitinol tube with a diameter of 2.3mm that does not have any patterning.

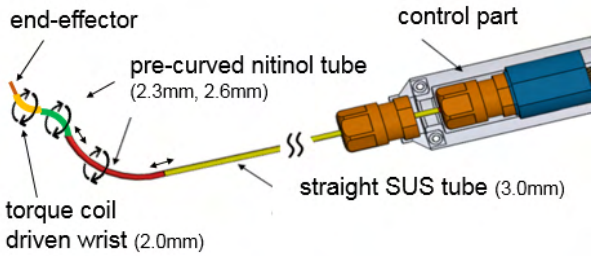

Fig. 1 The components of the steerable cannula. Four metal tubes control the robot's configuration and the position of the distal end. The end-effector passes through the hollow tubes.

A pattern of slits was applied to the second tube to give it stability and a higher curvature. The patterning was engraved by laser machining. The slits increase not only the flexibility of the tube but also the ratio of the tube's torsional rigidity to its bending rigidity, for stability. [7] The straight tube only provides transitional movement, but the second and third tubes provide both rotational and transitional movement to control the distal tip.

The fourth tube has two parts: a pre-curved stainless steel tube of 2.0mm diameter and a torque coil. The proximal end of the stainless steel tube is welded to the torque coil as shown in Fig. 2. The overlapped part between 3rd and 4th tube is not stainless steel but torque coil. The torque coil is characterized by a high torsional force transmission rate, and it bends flexibly so that the fourth tube can deploy through the first, second, and third tubes. The stainless steel tube portion of the fourth tube is immediately adjacent to the distal end of the third tube. The fourth tube can rotate without changing the configuration of the other tubes, allowing the operator to steer the orientation of the distal end of the robot in a low-profile and low-cost manner.

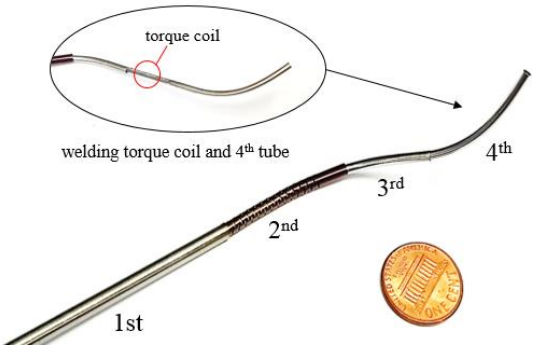

Fig. 2 Detail view of the fourth tube showing the position of the torque coil.

Surgical instruments can pass through the hollow tubes, whose inner diameter is about 1.8mm. In the case of arthroscopic surgery, an electrocautery is used to ablate tissues to accomplish capsular release. The novel 3R joint mechanism allows an easier approach to the inferior glenoid, which is conventionally approached through anterior or posterior portals of the shoulder, using the mean glenoid size of adults as a reference.

RESULTS

We demonstrated that the steerable cannula is feasible instrument for arthroscopic capsular release. A team of surgeons at Seoul Asan Hospital used a simplified version of the robot (i.e., a version with only three tubes) to reach the inferior glenoid and perform capsular release on a frozen porcine shoulder. The inferior glenoid cannot be reached by conventional surgical instruments, but the steerable cannula successfully reached it and allowed the removal of swollen, inflamed tissue near the ball-socket joint. The wrist, driven by the torque coil independently from the other tubes' configuration, helped the end-effector to move more freely, which shortened the surgical procedure. The surgeons were able to use the instrument without any training in its use because controlling the robot is intuitive and easy. The high curvature structure of the robot gives it a high potential for easily accessing the internal structures of microjoints such as the wrist, finger, and temporomandibular joint.

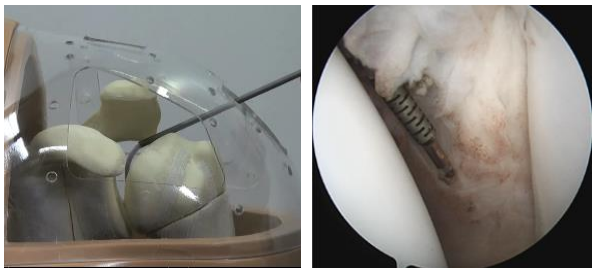

Fig. 3 Left, Feasibility test for performing arthroscopic capsular release on a human shoulder model (left). Right, Endoscopic camera view of clinical test on a frozen porcine shoulder using a simplified version of the robot.

DISCUSSION

In minimally invasive surgery, the orientation of the distal end of an instrument is as important as the position of its distal end. The orientation should head toward the operative target. If the instrument reaches the target position but is headed the wrong way, the surgery cannot be completed. The torque coil–driven wrist adds an additional degree of freedom to the fourth tube of the steerable cannula so that it can steer the orientation of the end-effector at its distal end. In contrast, the typical concentric tube robot must change its whole configuration to alter the orientation of the end effector. In our design, a torque coil–driven wrist rotates independently from interference by the other tubes, and so it allows the operator to steer the orientation of the end-effector without requiring a change in the configuration of the other tubes. Thus the wrist mechanism allows the end-effector to move more freely and the robot to maintain a stable configuration. The robot's 3R joint mechanism enables its distal tip to be moved into areas that are usually unreachable. The pre-curved nitinol tubes fit well with tortuous trajectories. The robot has potential applications for orthopedic surgery on the shoulder, wrist, and hip ball-socket joints and for endonasal surgery. Its trajectories make it easy for a surgeon to avoid the axillary nerve during shoulder surgery, which prevents neurologic damage. [8]

A workspace analysis of the robot shows that its distal end can reach the exact same point in many ways with different orientations of the end-effector thanks to the torque coil– driven wrist. Before the robot can be used in humans, control of the position and orientation of the end-effector need further study. Studies are underway to develop an algorithm to determine the position and orientation of the end-effector. To enhance the system, future work should explore using the robot with instruments other than an electrocautery, optimization of the tube patterning , and testing the torque coil transmission for precise control of the wrist. Ultimately, we expect that this robot will expand the scope of minimally invasive surgery on a wide variety of joints.

ACKNOWLEDGEMENT

This research was supported by the KIST Institutional Program (2E25680) and NRF Korea (2013034695).

REFERENCES

[1] F. A. Simmonds, "Shoulder Pain, With Particular Reference to the Frozen Shoulder", The Journal of Bone and Joint Surgery, 1949, Vol.31 B, No.3, pp.426-432.

[2] Pollock, Roger G. MD, Duralde, Xavier A. MD, Flatow, Evan L. MD, Bigliani, Louis U. MD, "The Use of Arthroscopy in the Treatment of Resistant Frozen Shoulder." The Journal of Clinical Orthopaedics and Related Research, Vol. 304, 1994.

[3] Stephen R. Thompson, M.D., M.Ed., F.R.C.S.C., and Marie-Eve LeBel, M.D., F.R.C.S.C, "Use of a Hip Arthroscopy Flexible Radiofrequency Device for Capsular Release in Frozen Shoulder," Arthroscopy Techniques, Vol.1, No.1, September, 2012 : pp e75-e78

[4] Pearsall IV, A. W., Holovacs, T. F., Speer, K. P., "The low anterior five-o'clock portal during arthroscopic shoulder surgery performed in the beach-chair position", American Journal of Sports Medicine, Vol. 27, Issue 5, 1999, pp. 571-574

[5] H. B. Gilbert, D. C. Rucker, and R. J. Webster III, "Concentric Tube Robots: The State of the Art and Future Directions," 16th International symposium of Robotics Research, 2013.

[6] P. E. Sears and P. E. Dupont, "A steerable needle technology using curved concentric tubes," in IEEE/RJS International Conference on Intelligent Robots and Systems, 2006, pp. 2850-2856.

[7] D. Lee, J. Kim, J. Kim, C. Baek, G. Noh, D. Kim, K. Kim, S. Kang, and K. Cho, "Anisotropic Patterning to Reduce Instability of Concentric-Tube Robots", IEEE Transactions on Robotics, 2015, vol. 31, No. 6, pp. 1311-1323.

[8] W. Z. Burkhead, Jr., MD, R. R. Scheinberg, MD, and G. Box, MD, "Surgical anatomy of the axillary nerve", Journal of Shoulder and Elbow Surgery Vol. 1, Issue. 1, 1992, pp.31-36.

A Soft Pop-Up Proprioceptive Actuator for Minimally Invasive Surgery

S. Russo, T. Ranzani, C. Walsh, R. Wood

Harvard John A. Paulson School of Engineering and Applied Sciences, USA

Wyss Institute for Biologically Inspired Engineering, USA

srusso@seas.harvard.edu

INTRODUCTION

Surgical robots and miniaturized smart instruments have been developed to overcome limitations of current tools and further reduce invasiveness of surgical procedures [1][2]. This miniaturization effort, as well as the development of more flexible instruments that can navigate the body following complex anatomical paths toward the surgical target, often leads to the loss of sensory feedback and dexterity and increases design complexity. Developing mm-scale robots combining distal dexterity and sensor feedback at the surgical site would increase reliability and controllability, especially in flexible endoscopy, where the procedures are primarily based on visual feedback. However, this introduces several technical challenges because of the lack in viable manufacturing technologies at this scale: current approaches mainly rely on fiber optic based sensing systems [3]-[6]. Recently, a pop-up book inspired manufacturing technique has been utilized to fabricate surgical tools with embedded actuation and sensing [6]-[8]. Furthermore, soft materials and soft fluidic micro actuators have been introduced in this paradigm to fabricate soft pop-up mm-scale sensors and actuators for minimally invasive surgery (MIS) [8]. Advantages of this approach include low cost manufacturing, scalability, and flexibility in material selection. Furthermore, the use of soft material provides a safer interface with biological tissue. In this paper, we exploit the soft pop-up fabrication technique to develop a mm-scale bending actuator with proprioceptive capabilities based on capacitive sensing (Fig. 1).

MATERIALS AND METHODS

The soft fluidic micro actuator (SFMA) is fabricated using soft lithography and is composed of two soft layers bonded together via oxygen plasma treatment. The bottom layer is fabricated by spin coating MED-6033, a biocompatible silicone elastomer (NuSil, CA, USA), on a silicon wafer at 350 rpm for 100 s (resulting in a 500 µm thick membrane). The upper layer is fabricated by spin coating MED4-4220, another biocompatible silicone elastomer at 450 rpm for 100 s (400 µm thick membrane). Due to the different shore hardness of the two materials (50A and 17A respectively), the upper layer will expand when pressurized. The SFMA is integrated in the center of the system (Fig. 2) and bonded irreversibly to the rigid-flex

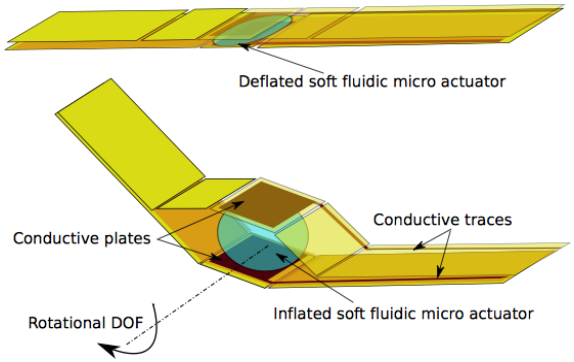

Fig. 1 Soft pop-up proprioceptive bending actuator with embedded capacitive sensing: top, flat configuration (actuator not inflated) and bottom, bent configuration (actuator inflated).

laminate using a chemical surface modification process including oxygen plasma treatment and silanization using (3-Aminopropyl) triethoxysilane (APTES, Sigma-Aldrich Corp., MO, USA). The rest of the laminate is composed of glass-reinforced epoxy laminate sheets (254 µm thick) as rigid material, 9877 (3M, MN, USA) as a biocompatible adhesive (254 µm thick), and DuPont Pyralux copper/polyimide (18 µm copper and 25 µm polyimide) as a flexible layer with conductive electrodes, for a total laminate thickness of 1.83 mm (Fig. 2, left). A secondary conductive trace runs along the main trace to shield possible interference due to capacitance coupling (Fig. 2, right). The laminate is bonded together applying pressure and then laser machined to release the final mechanism. Tubes with an internal diameter of 254 µm (Micro-Renathane Catheter Tubing, Braintree Scientific, Inc., MA, USA) are inserted and sealed (Poxy Pak, Loctite, USA). The SFMA is pressurized with deionized (DI) water and its expansion causes the bending of the soft pop-up mechanism (Fig. 3a and b). The soft pop-up proprioceptive actuator is characterized using an experimental setup consisting of a programmable syringe pump (11 Elite, Harvard Apparatus, MA, USA), a pressure sensor (BSP B010-EV002-A00A0B-S4, Balluff, USA) connected to a NI USB-6002 board (National Instruments, Austin, TX, USA), and a capacitance-to-digital converter (AD7746 Analog Devices, MA, USA).

RESULTS

The experiment consisted of pressurizing the actuator by increasing the volume of DI water (0.012 ml for each step) at a flow rate of 0.01 ml/s, measuring the

corresponding capacitance variation and resolving the relative bending angle visually. Images are taken by placing a camera on a tripod parallel to the system and analyzed in Matlab (Mathworks Inc., Natick, MA, USA). The capacitance measured during actuation is reported in Fig. 3c. Prior to actuation, the soft pop-up proprioceptive actuator is pre-bent of an angle of 17 °. This is due to intentional compression in the laminate to pretension the mechanism. The max pressure reached during testing is 200 kPa, corresponding to a maximum reached bending angle of 78°. Pressures in the same range have already been tested in devices for MIS safely [9]. The system response is compared with a linear fit and the results are reported in Fig. 3c.

DISCUSSION

In this paper, we integrate SFMA into rigid-flex laminates to achieve a soft/folded proprioceptive actuator based on capacitive sensing. Capacitance variation with relative bending angle is characterized showing a linear trend for a bending range from 17 ° to 78 °. According to [8], soft pop-up actuators are able to generate forces in the newton range and can withstand up to 500 cycles before failure. This soft pop-up proprioceptive actuator can be applied as a building block (i.e., a rotational joint) for developing novel mm-scale endoscopic robotic platforms or it can be combined with current flexible instrumentation, e.g., to steer a gripping tool during endoluminal tissue manipulation. The prototype is fabricated entirely with biocompatible components: all materials have been previously applied in disposable medical devices. The maximum measured speed that the actuator is able to achieve is 8.7 °/s with a flow rate of 0.12 ml/s. Future work will include analytical modeling of the capacitance response, plus the possibility of combining capacitance data with volume and pressure information in order to improve the motion accuracy. Furthermore, scalability of the system along with the possibility of integrating electronics on-board will be evaluated.

ACKNOWLEDGMENT

The authors would like to acknowledge the Wyss Institute for Biologically-Inspired Engineering for their support of this work. The authors would also like to acknowledge DARPA (grant FA8650-15-C-7548).

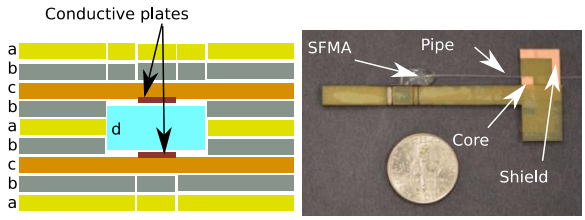

Fig. 2 Left: cross-section of the soft pop-up proprioceptive bending actuator laminate consisting of nine layers: a, b, c, and d the represent rigid, adhesive, flexible materials, and soft fluidic micro actuator respectively. Right: fabricated prototype after lamination and release cuts.

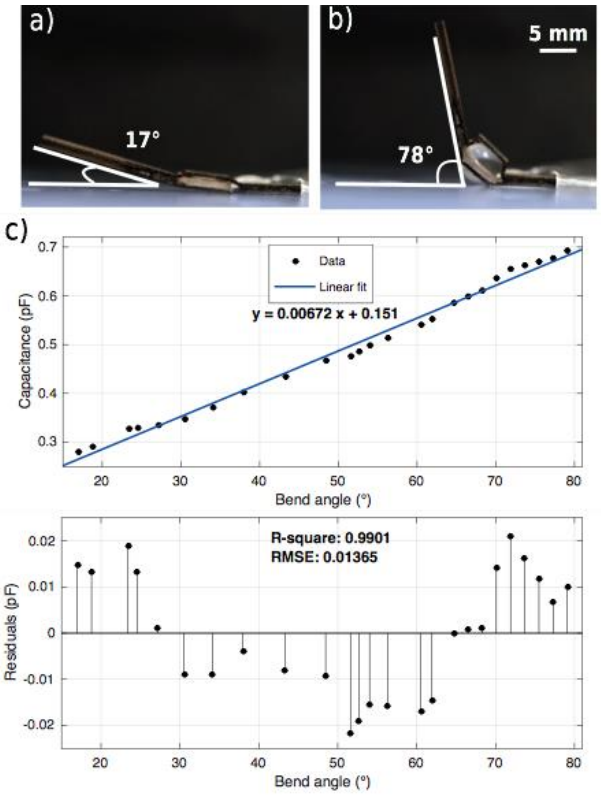

Fig. 3 Soft pop-up proprioceptive actuator characterization. a) Actuator in non-pressurized state. b) Actuator reaching the maximum bending angle. c) Capacitance variation versus bending degrees with linear fit and corresponding residual errors.

REFERENCES

[1] C. Bergeles and G.-Z. Yang, From passive tool holders to microsurgeons: safer, smaller, smarter surgical robots, IEEE Trans Biomed Eng. 2014; 61(5): 1565–1576.

[2] V. Vitiello, S.-L. Lee, T. P. Cundy, and G.-Z. Yang, Emerging robotic platforms for minimally invasive surgery, IEEE Rev Biomed Eng. 2013; (6): 111–126.

[3] S. C. Ryu and P. E. Dupont. Fbg-based shape sensing tubes for continuum robots, IEEE Int Conf Robot Autom. 2014; 3531–3537.

[4] S. Russo, P. Dario, and A. Menciassi, A novel robotic platform for laser-assisted transurethral surgery of the prostate, IEEE Trans Biomed Eng., 2015; 62(2): 489–500.

[5] S. Sareh, et al, A 7.5mm Steiner chain fibre-optic system for multi-segment flex sensing, IEEE Int Conf Intel Rob Sys. 2015; 2336-2341.

[6] J. Gafford, R. Wood, and C. Walsh, Self-assembling, low-cost, and modular mm-scale force sensor, IEEE Sensors Journal. 2016, 16(1): 69–76.

[7] J. Gafford, et al, Snap-On Robotic Wrist Module for Enhanced Dexterity in Endoscopic Surgery, IEEE Int Conf Robot Autom. 2016.

[8] S. Russo, et al, Soft pop-up mechanisms for micro surgical tools: design and characterization of compliant millimeter-scale articulates structures, IEEE Int Conf Robot Autom. 2016.

[9] A. Moers, M. De Volder, and D. Reynaerts, Integrated high pressure microhydraulic actuation and control for surgical instruments, Biomed Microdevices. 2012; 114(4): 699708.

A New Antagonistically Actuated Endoscope: Towards an Inherently Safe Minimally Invasive Examination

A. Stilli[1], A. Cremoni[1], H. A. Wurdemann[2], K. Althoefer[3]

[1]*Department of Informatics, King's College London, UK*

[2]*Department of Mechanical Engineering, University College London, UK*

[3]*School of Electronic Engineering & Computer Science, Queen Mary University of London, UK*

agostino.stilli@kcl.ac.uk

INTRODUCTION

The use of flexible endoscopes (or flexible scopes), introduced into the human body through natural orifices, such as mouth, urethra, or anus, or through small incisions in the skin, allow obtaining and examining visual images of internal soft tissue. In today's medical interventions, these instruments are made of a sequence of rigid and/or semi-flexible links and joints [1], [2]. The operating handle includes either a manual or robotic tendon-based control system to steer and manoeuvre the endoscope tip around organs and, at the same time, to keep a safe distance between the scope and the internal anatomy. These robotic tools typically are made to exhibit a certain flexibility (adapting the endoscopes shape to the anatomy to a certain extent), but also have sufficient stiffness (to be pushed forward through narrow openings towards a desired target without bending excessively) – the stiffness of standard endoscopes cannot be controlled.

A different solution is proposed by Ginsberg et al. in [3], where the flexibility of the probe gradually varies throughout its length due to the changing in the material of the outer tube. In this case the level of compliance of the device can be regulated by means of compressing and extending a specific coil attached to the tip of the probe. Another approach is described in [4], where a flexible laparoscopic camera is able to switch between being rigid and compliant using vacuum pressure.

In this paper, we present our work towards the realisation of an inherently safe, soft, tendon-driven inflatable endoscope. The proposed design has been inspired by our previous work on soft inflatable devices described in [5], [6]. A tendon-based driven actuation was chosen because it minimises the encumbrance of the actuation means, and allowing to place the actuators outside the articulated structure and, in turn, considerably. Hence, this type of actuation ensures miniaturisation of the whole system, decreasing the structure's diameter to a minimum which makes our proposed device suitable for minimally invasive interventions. The proposed system is able to intrinsically vary its structural stiffness level allowing to have a high compliancy during insertion and investigation procedures and a firm pose when a stable camera image at the site of interest is needed. The presented prototype has a diameter at the tip of 11.8 mm, hence, it is suitable to be inserted through a 12 mm trocar port.

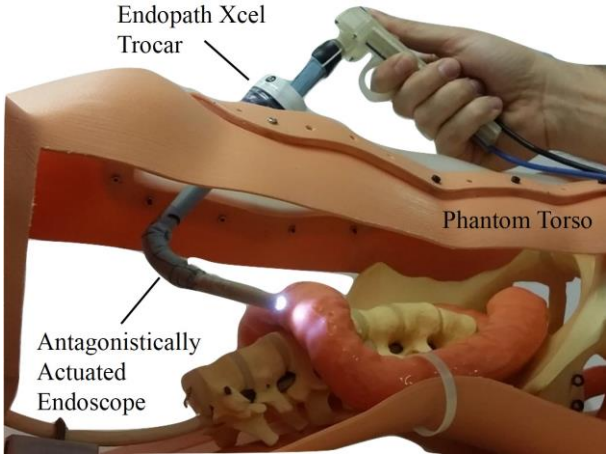

Fig. 1 The new antagonistically actuated endoscope accessing a 1:1 scale phantom of the abdominal cavity through a standard trocar port (12 mm diameter).

MATERIALS AND METHODS

We have created a concept design for a novel inexpensive flexible and steerable soft endoscope (see Fig. 1). The design is inspired and based on our previous work presented in [4] [5]: The soft endoscope actuation principle is based on a combination of pneumatic and tendon-driven actuation. Pneumatic air pressure is used to inflate an air-tight extensible bladder which is fitted inside a non-stretchable fabric sleeve. The outer sleeve limits the inflation of the inner bladder allowing stiffness adjustment by the means of pressure regulation. A number of tendons are fixed to the scope's tip and guided along the length of the manipulator. This actuation means provides steering capability to the system exerting a longitudinal pulling force. When all tendons are pulled simultaneously and the pressure inside the bladder set, both actuation principle are working antagonistically and, hence, the stiffness of the endoscope is increased.

The prototype of the flexible endoscope in Fig. 2(c) is composed of five main elements:

1. A customized sleeve machine-sewn in the shape of a cylinder with a length of 250 mm and a diameter of 18 mm, composed of two layers of polyester fabric;
2. An air-tight bladder made of flexible material (latex) fitted inside the sleeve and pressurised through a 4 mm diameter pressure pipe;
3. Four nylon tendons, 90° spaced apart along the perimeter of the sleeve and attached on one side to the base of the housing structure of the camera and on the other side with four individual sliders. The tendons have been embedded between the two layers of the fabric that composes the outer sleeve;
4. A commercially available endoscopic USB camera with a diameter of 8.5 mm and a length of 45 mm (Flylinktech® USB Endoscope);
5. A 3D printed ergonomic handle to hold the endoscope with a manual control system of four tendon sliders.

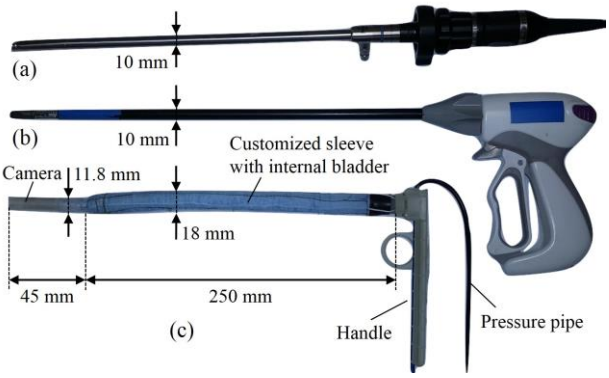

Fig. 2 Comparison of surgical instruments: (a) standard rigid endoscopic camera, (b) laparoscopic instrument, and (c) our new antagonistically actuated endoscope.

RESULTS

The inflatable endoscope proposed in this paper is composed of a single air chamber and a set of four tendons connected to the base of the camera integrated at the tip of the endoscope. Since the four tendons are arranged in the periphery of the central axis of our manipulator with a radial displacement of 90°, the movements of the scope are decoupled along the axis of the Cartesian space allowing intuitive manoeuvring. Figure 3 shows a number of experimental results demonstrating different bending angles: These sequences of body poses were achieved pulling a single tendon successively in two opposing directions keeping the pressure constant at 0.2 bar. The behaviour of the manipulator depends on the constraint posed by the trocar port that is rigid.

DISCUSSION

In this paper, a novel design for a flexible and steerable endoscope was presented and explored. The capability of the system to adjust its compliance by means of an antagonistic actuation principle (tendon-based and pressure actuation) leads to inherently safe contact with delicate soft tissue inside the human body. The novel flexible endoscope is able to elongate, bend around objects and increase stiffness to provide a stable camera view to the user. The squeezability of the manipulator body allows the scope to be easily inserted through narrow openings that are smaller than the actual diameter of the pressurised manipulator. In this manner, the novel flexible endoscope can be inserted through standard trocar ports without limiting its dexterity.

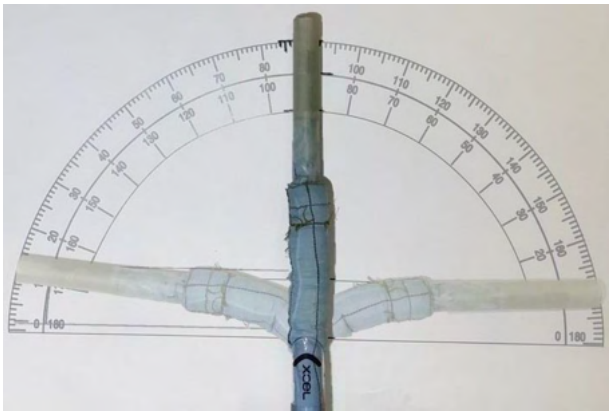

Fig. 3 Bending behaviour of the flexible endoscope in one plane actuated by a single tendon after the insertion through a 12 mm diameter trocar port.

In future works, we will replace the current USB camera with a smaller endoscopic camera with a length. Further, we will explore how to enhance the manual control system for this endoscope combining tendon and pressure actuation.

REFERENCES

[1] P. J. Schuler, M. Scheithauer, N. Rotter, J. Veit, U. Duvvuri, and T. K. Hoffmann, "A single-port operator-controlled flexible endoscope system for endoscopic skull base surgery," HNO, vol. 63, no. 3, pp. 189–194, 2015.

[2] A. Degani, H. Choset, A. Wolf, and M. A. Zenati, "Highly articulated robotic probe for minimally invasive surgery," Proc. - IEEE Int. Conf. Robot. Autom. vol. 2006, pp. 4167–4172, 2006.

[3] G.G. Ginsberg, "Colonoscopy with the variable stiffness colonoscope", Endoscopy, vol. 58, no. 4, pp. 545–552, 2003.

[4] A. Jiang, K. Althoefer, P. Dasgupta, and T. Nanayakkara, "The Core Snake, the variable stiffness laparoscopic camera," in The Hamlyn Symposium on Medical Robotics, London, United Kingdom, 2013.

[5] A. Stilli, H. A. Wurdemann, and K. Althoefer, "Shrinkable, stiffness-controllable soft manipulator based on a bio-inspired antagonistic actuation principle," in IEEE International Conference on Intelligent Robots and Systems, pp. 2476–2481, 2014.

[6] F. Maghooa, A. Stilli, Y. Noh, K. Althoefer, and H. A. Wurdemann, "Tendon and pressure actuation for a bio-inspired manipulator based on an antagonistic principle," Robotics and Automation, IEEE International Conference on. pp. 2556–2561, 2015.

Design and Control of a Soft Robotic Endoscope for Surgical Interventions utilizing Hydraulic Actuation

L. Lindenroth[1], K. Althoefer[1], K. Rhode[2], H. Liu[1]

[1]*Centre for Robotics Research, King's College London, UK*

[2]*Biomedical Engineering Department, King's College London, UK*

Lukas.Lindenroth@kcl.ac.uk

INTRODUCTION

Soft robots show promising applicability in medical interventions due to their inherent compliance, minimizing the risk of injury and providing a flexible tools for dexterous interventions. Existing soft robots designed for medical applications are either driven by tendons or through pneumatics actuation [1]. While the first can easily be miniaturized, it requires undesired rigid structures in the soft material. The latter allows the construction of entirely soft robots, however, it often demands complex setups comprising compressors and pressure regulators. Hydraulic actuation has shown good applicability in rigid body robotic systems. For a soft robotics design, hydraulics show various initial advantages. Actuators can be miniaturized depending on the application constraint. The liquid flow acts as natural damper to avoid rapid pressure changes which could damage the surrounding tissue or silicone structure itself, resulting in leakages. Hydrostatic pressure feedback could be utilized to determine forces applied to the soft structure as it has been shown for rigid-linked robots [2] and liquid-based compliant sensors [3], eliminating the necessity for external force sensors. As an initial step in developing a multi-segment soft robotics endoscope as displayed in figure 1, we demonstrate a cost-efficient and effective actuator system, with promising capabilities for a possible miniaturization. In this paper, we introduce the results of a single segment study, which is driven by a liquid flow induced by the developed linear actuators. We demonstrate that the system is, despite being compliant, capable of accurate, repeatable steering and control it in an open-loop approach based on a Timoshenko beam model.

MATERIALS AND METHODS

For the given work a cylindrical, silicone rubber-based segment is utilized [4]. It comprises three inflatable chambers which are aligned equidistantly in a circular fashion around its central axis, with each chamber being constrained by a thread embedded in the silicone to counteract lateral expansion. To generate a liquid flow into the chambers, linear actuators are designed utilizing hydraulic syringes, stepper motors and bracket elements. A sketch of the actuator is presented in figure 2. The syringes are filled with hydraulic liquid (distilled water) and equipped with diaphragm-based pressure sensors for hydrostatic pressure feedback. The stepper motors are controlled through pulse-width modulated command signals generated by an Arduino Mega 2560 microcontroller. To monitor position and orientation of the segment's tip a stereo camera setup with optical markers is employed. A marker detection and labelling algorithm is run on a separate Linux PC. The single segment with attached optical markers, as utilized in this work is depicted in figure 2.

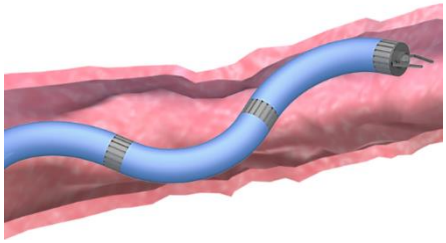

Fig. 1 Multi-segment soft robotic endoscope.

Stability and repeatability

The dynamic behavior of the system is experimentally validated based on its overshoot and position accuracy in a repeated motion. The first is tested with two constant velocities of the linear actuator ($1.6\,\frac{ml}{s}$ and $3.2\,\frac{ml}{s}$) approaching intermediate points with rapid stops on a 30mm uniaxial extension trajectory while for the second property a goal position (7mm displacement) is repeatedly approached inflating all chambers simultaneously. For both tests the tip position is observed.

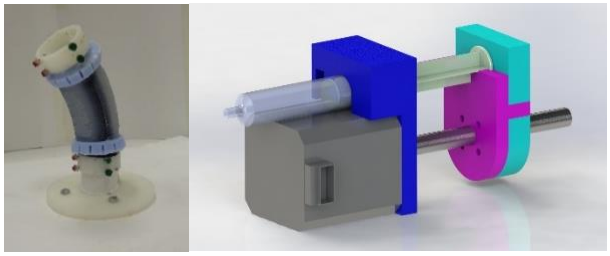

Fig. 2 Soft robotics segment with optical markers (left) and stepper motor-driven hydraulic syringe (right).

Forward kinematics model

For steering purposes, the endoscope segment is modelled as a single, static Timoshenko beam element, according to [5], which is then applied in an open-loop control and monitored with a stereo camera setup. The internal hydrostatic pressures are acting normal to the tip plane segment, resulting in local bending moments in the tip frame about its x- and y-axis respectively. The magnitudes of the latter with respect to the generated pressures are derived geometrically. The tip position in

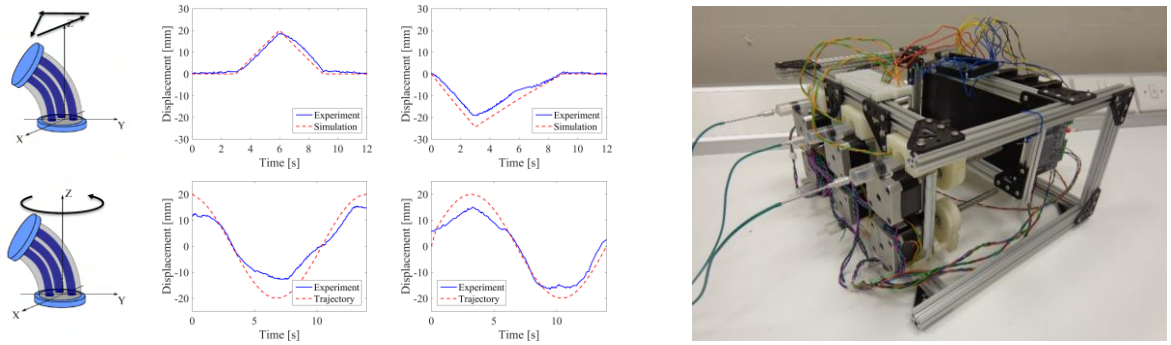

Fig. 4 Trajectories and corresponding data for forward (left, top row) and inverse kinematics (left, bottom row) in x- (centre) and y-axis (centre right) and integrated actuation system comprising multiple automated syringes (right).

x- and y-coordinates can be described as a function of the bending moments as

$$\delta_{x,y} = c_{x,y} \cdot M_{x,y} = \frac{L^3(\Phi + 4)}{12EI} \cdot M_{x,y}$$

Where L corresponds to the initial length of the beam, δ to its deflection and M to the acting bending moment. The Young's modulus E is found experimentally and the moment of inertia I determined geometrically. The factor Φ is defined in [4], characterizing the occurring shear effects. For a normal force F_z applied to the beam tip, the longitudinal extension can be described as

$$\delta_z = c_z \cdot F_z = \frac{L}{EA} \cdot F_z$$

The linear equation set can then be aligned as

$$\begin{bmatrix}\delta_x \\ \delta_y \\ \delta_z\end{bmatrix} = \boldsymbol{C} \cdot \begin{bmatrix}M_x \\ M_y \\ F_z\end{bmatrix} = \begin{bmatrix}c_x & 0 & 0 \\ 0 & c_y & 0 \\ 0 & 0 & c_z\end{bmatrix} \cdot \begin{bmatrix}M_x \\ M_y \\ F_z\end{bmatrix}$$

To determine the tip displacement in x-, y- and z-axis with C being the compliance matrix of the beam. The displacement in z is projected in the bending direction, which is also determined according to the generated bending moments [5].

Inverse kinematics model

For the inverse kinematics description of the segment, the geometric calculations of the local bending moments and the beam compliance are combined as

$$\begin{bmatrix}P_1 \\ P_2 \\ P_3\end{bmatrix} = (\boldsymbol{C} \cdot \boldsymbol{U})^{-1} \cdot \begin{bmatrix}\delta_x \\ \delta_y \\ \delta_z\end{bmatrix}$$

To generate the required pressures a goal deflection, where $\boldsymbol{U}$ relates the pressure vectors to resulting moments and forces.

RESULTS

The results of the dynamic evaluation are presented in figure 3. It can be seen that, for both velocities, there is no overshoot occurring in the tested displacements. The repeatability evaluation shows promising behavior over a number of 20 repetitions, with an average error of 1.25mm and a maximum error of 2.5mm in the tip position. The results of the open-loop control experiment are presented in figure 4. The forward kinematics model is validated with a trajectory following a triangular path of the tip. It can be seen that the model predicts the position with a maximum error of approximately 4mm with minor non-linear behavior in the linearly predicted slopes. The inverse kinematics model is applied in a circular motion of the tip showing, with a maximum error of 10mm, less accurate results in both x- and y-axis.

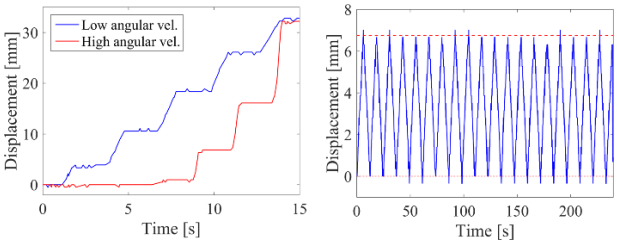

Fig. 3 Results of overshoot (left) and repeatability (right) experiment.

DISCUSSION

In this work we presented an efficient hydraulic actuation system for inflatable soft robots. The actuator system with its repeatable motion and minimal overshoot indicates good applicability to endoscopic interventions. In the future this setup will be extended for multiple segments to increase steering capabilities of the desired endoscope and position feedback will be utilized to apply the derived kinematics algorithms in closed loop approaches to compensate for occurring errors which have been identified in the open loop positioning.

REFERENCES

[1] Rus, Daniela, Tolley, M. T. Design, fabrication and control of soft robots. Nature 2015 521.7553: 467-475.

[2] Sol, E., King, R., Scott, R., & Ferre, M. (2014). "External Force Estimation for Teleoperation Based on Proprioceptive Sensors", International Journal of Advanced Robotic Systems 2014, 1–12.

[3] Russo Stefania, Ranzani Tommaso, Liu Hongbin, Nefti-Meziani Samia, Althoefer Kaspar, and Menciassi Arianna. Soft Robotics. December 2015, 2(4): 146-154. doi:10.1089/soro.2015.0011.

[4] Fras, J., Czarnowski, J., Macias, M., Glowka, J., Cianchetti, M., Menciassi, A. New STIFF-FLOP module construction idea for improved actuation and sensing. IEEE International Conference on Robotics and Automation, 2015 Seattle

[5] Przemieniecki, J. S. Theory of matrix structural analysis. Courier Corporation, 1985.

Modeling and Validation of a Low-Cost Soft-Tethered Endoscopic Platform

I.R. Dawson[1], F. Campisano[2], F. Gramuglia[2], K.L. Obstein[2], E.E.G. Hekman[1], J. Sikorski[1], S. Misra[1,3], P. Valdastri[2]

[1]*Surgical Robotics Lab, University of Twente, The Netherlands*

[2]*STORM Lab, Vanderbilt University, USA*

[3]*Dept. of Biomedical Engineering, University Medical Center Groningen, The Netherlands*

pietro.valdastri@vanderbilt.edu

INTRODUCTION

Nearly 70% of gastric and esophageal cancer cases occur in Low- and middle-income countries (LMICs) and account for 10% of the incident cases worldwide [1]. Screening programs have been shown to be effective in reducing the mortality rate through early detection; however, the resource intensive nature of these programs limits their widespread implementation [2]. In an attempt to overcome these issues, the HydroJet is being developed as a low-cost ($2 to $5 per procedure) endoscopic platform (Fig. 1). The platform was firstly introduced in [3]. The objective of the HydroJet is to serve as a primary screening modality. The system was designed to be portable and disposable—obviating the need for specialized reprocessing/cleaning so that it can be taken to rural and remote locations in LMICs where access to healthcare may not be available. As a primary screening modality, if a suspicious lesion is found, the patient can be triaged to a healthcare institution for further investigation/therapy.

The HydroJet platform consists of a disposable flexible tether with an attached capsule containing a camera for stomach visualization. Actuation of the system is performed using three water jets built into the capsule. Each of the jets can be controlled separately to aim the camera at screening landmarks within the stomach. The tether of the platform has been upgraded with respect to [3] to achieve a lower bending stiffness and a more symmetric workspace. It consists of three Tygon tubes held together using rubber O-rings at regular intervals.

The objective of this study is to investigate kinematic modeling of the HydroJet tether—as an accurate model of its behavior can (a) be utilized for closed loop system control and (b) predict tether behavior for optimization of platform design. As the primary goal of the platform is to orient the camera within the workspace of a human stomach, an error of up to 10 mm is acceptable.

MATERIALS AND METHODS

A. Modeling

The forward kinematics are obtained using a rigid link model, as it is both computationally efficient and capable of modeling manipulators with non-constant curvature [4]. The manipulator is modeled as a chain of n interconnected rigid links with $n+1$ stiff joints connecting each link. The model combines the forward kinematics described by [5] (Fig. 2, top) and the statics described by [4] (Fig. 2, bottom).

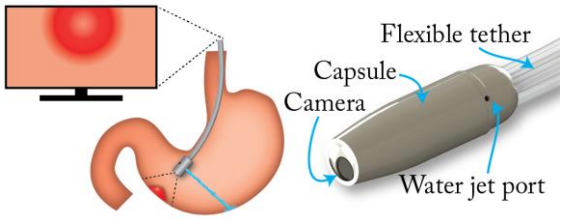

Fig. 1 Left: the HydroJet platform while visualizing part of the stomach. Right: a close-up of the capsule.

In contrast to [4, 5], this model does not assume constant length for each rigid link. This approach enables modeling of manipulators tracked with position or orientation sensors placed at arbitrary locations and enables selective refinement of the model for parts of the manipulator with large curvature. Additionally, the bending stiffness of each joint can be set separately in order to account for stiffer parts of the manipulator, like the HydroJet capsule. Following the derivation in [4], the stiffness of the joints is given by:

$$k_i = \begin{cases} \left(\frac{l_i}{2E_iI_i} + \frac{l_{i+1}}{2E_{i-1}I_{i-1}}\right)^{-1} & i \neq 1, n+1 \\ 2E_1I_1/l_1 & i = 1 \\ 2E_nI_n/l_n & i = n+1 \end{cases} \quad (1)$$

where k_i is the stiffness of joint i, E_iI_i is the bending stiffness of link i, and l_i is the link length.

Actuation of the HydroJet is modeled as a force acting on the tip of the rigid link model. The jet force for each possible valve opening is measured beforehand. The gravity acting on the HydroJet is considered to be uniformly distributed along its length. Lastly, the bending stiffness of the capsule has been included in the model to take the rigid tip into account.

B. Calibration and validation

A calibration procedure is performed to determine both the tether bending stiffness and the jet orientation, as these parameters are initially unknown. During calibration, inputs for three independent sweeps (Fig. 3) –one for each jet–are fed to the system and the resulting static equilibrium tip positions are measured for a tether length of 58 mm. Each sweep is split into 31 steps. Next, these measurements are compared to model estimations for the same inputs and the minimum least squares error method is used to find the bending stiffness and jet angle that minimize the error in tip position and orientation.

During validation, the inputs for three independent sweeps and three paths were fed to the system. This time sweeps were performed at a tether length of 58 mm (31

steps), one path was performed at 58 mm (25 steps) and the other two paths were performed at 68 mm (25 and 31 steps). The accuracy of the calibrated model was determined by comparing the validation set, containing tip position and orientation, to the model estimations.
For both calibration and validation, the Aurora electromagnetic tracking system (Northern Digital, Inc.) was utilized to track deflection with two 6-dof sensors, placed at the base of the tether and inside of the capsule.

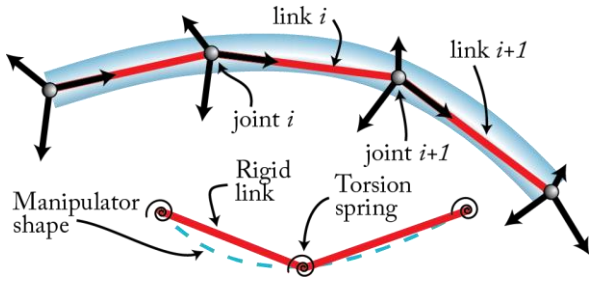

Fig. 2 The manipulator modeled as a chain of interconnected rigid links (top). Each rigid link approximates a constant curvature arc and manipulator stiffness is modeled using torsion springs at the joints (bottom).

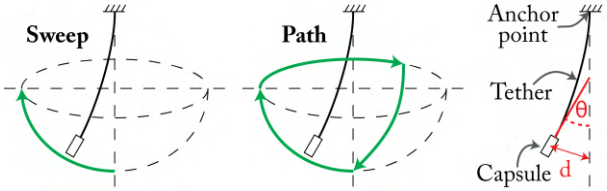

Fig. 3 The HydroJet can perform a sweep (one jet) or track a path (multiple jets). For a 68 mm long tether, the maximum capsule displacement d is 65 mm during a sweep.

RESULTS

The results for all experiments are summarized in Table 1. A visual comparison between the estimated and measured positions of three sweeps is shown in Fig. 4. The results show that each position and orientation can be estimated with a relative error of 17.6% (SD: 14.1%) and 13.5% (SD: 9.3%) respectively. The errors for the sweeps are lower than the errors for the paths.

Tab. 1 The results of the validation. The absolute errors are determined by directly comparing the measurements and estimations. The relative errors take the deviation from the reference configuration into account.

	Error type	Sweep	Path	Total
Position	Mean abs. error [mm]	6.0	8.1	6.9
	SD of abs. error [mm]	4.8	6.3	5.7
	Mean rel. error [%]	14.4	20.6	17.6
	SD of rel. error [%]	6.1	18.3	14.1
Orientation	Mean abs. error [°]	3.7	5.7	4.6
	SD of abs. error [°]	2.1	4.0	3.3
	Mean rel. error [%]	10.1	16.6	13.5
	SD of rel. error [%]	4.4	11.4	9.3

DISCUSSION

This study describes and validates kinematic modeling of the HydroJet platform. These initial results demonstrate that the presented model is accurate for estimating both tip position and orientation. Additionally, estimation of tip behavior is more accurate for sweeps than for paths.

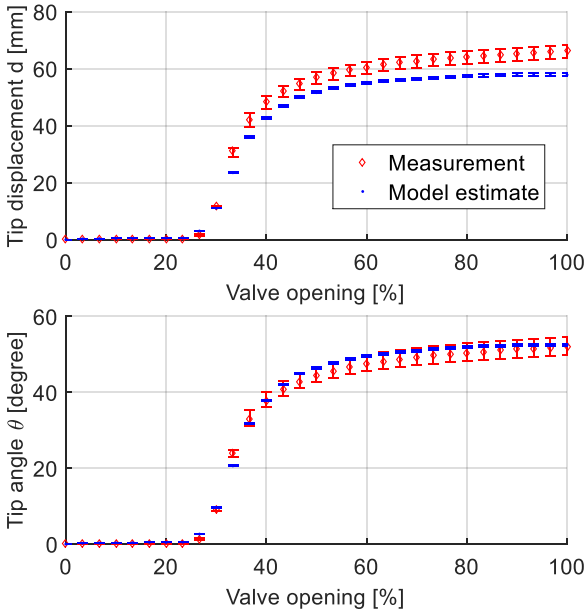

Fig. 4 Measured and estimated tip position and orientation for three separate sweeps. The error bars indicate the ranges for the three sweeps.

The work described in this paper combines two available models and expands them by including variable link lengths and variable manipulator stiffness. The resulting model can also be applied to other areas, e.g. for catheters with variable bending stiffness along their length.
The HydroJet platform is currently under open-loop control. By implementing the model described above, it might be possible to implement closed-loop control that would vastly enhance system usability/intuitive use.
In this study, the position of the base of the tether was known; however, in the clinical setting, this may not be the case. Therefore, research investigating online estimation of tether length and base position is underway.

REFERENCES

[1] American Cancer Society, Cancer Facts & Figures, 2005.
[2] Adami *et al.*, "Primary and secondary prevention in the reduction of cancer morbidity and mortality," *European Journal of Cancer*, vol. 37, Supp. 8, pp. 118-127, 2001.
[3] Caprara *et al.*, "A platform for gastric cancer screening in low-And middle-income countries," *IEEE Transactions on Biomedical Engineering*, 62:1324-1332, 2015.
[4] R.J. Roesthuis and S. Misra, "Steering of multi-segment continuum manipulators using rigid-link modeling and FBG-based shape sensing," *IEEE Transactions on Robotics*, vol. 32, pp. 372-382, 2016.
[5] T. Greigarn and M.C. Çavuşoğlu, "Pseudo-rigid-body model and kinematic analysis of MRI-actuated catheters," in *IEEE Int. Conf. Robot. Autom.*, pp. 2236-2243, 2015.

Research reported in this publication was supported in part by the National Institute of Biomedical Imaging And Bioengineering of the National Institutes of Health under Award Number R01EB018992, in part by the National Science Foundation under grant number IIS-1453129 and CNS-1239355, and in part by the European Research Council (ERC) under the European Union's Horizon 2020 Research and Innovation programme (Grant Agreement #638428 - project ROBOTAR). Any opinions, findings and conclusions or recommendations expressed in this material are those of the authors and do not necessarily reflect the views of the NIH, the NSF or the ERC.

Soft Tactile Array Sensor for Tactile Sensing during Minimally Invasive Surgery

J. Back[1], Y. Noh[1], J. Li[2], S. Wang[2], K. Althoefer[1], H. Liu[1]

[1]*Centre for Robotics Research, King's College London, UK*

[2]*School of Mechanical Engineering, Tianjin University, China*

Junghwan.back@kcl.ac.uk

INTRODUCTION

The absence of the sense of touch is a well-known drawback of robotic minimally invasive surgery (MIS) [1]. In order to provide the sense of touch to MIS tools, numerous methods have been reported such as PVDF, MEMS base method, multiple-beam structure with multiple strain gauge, and optical fiber [1-3]. However, these sensing mechanisms have the common difficulties including miniaturizing the size, increasing spatial resolution of tactile elements, adapting sensor to non-planar tool shape, fabrication complexity, enduring the sterilization procedure and reducing the cost [4]. To overcome above challenges, we propose a novel tactile array sensor consisting of soft material channels. The sensor body is fabricated using 3D printing and silicone rubber casting. Each soft channel measures contract force by light intensity variation using optical fiber. Thus, the proposed sensor has the following advantages: 1) making use of 3D printing and soft material casting, it is suitable to design high density of tactile elements; 2) it easily applies to an arbitrary shape to fit various MIS applications; 3) compared to other light-intensity based tactile sensor, it is easy to fabricate and miniaturize; it avoids the complexity of attaching reflectors to individual sensing elements; 4) it is immune to electromagnetic interference. In this paper, a prototype which has 3×3 tactile elements in an area of 9.5 × 11 mm^2 was developed and tested for feasibility study.

INTERNAL STRUCTURE OF THE SOFT TACTILE ARRAY

The soft array tactile sensor is consisted of the soft tactile array pad and multiple soft channels as shown Fig. 2. The sensor body including the soft channel were manufactured using 3D printing and silicone rubber casting. The soft channel is divided by three parts; the hemisphere to receive contact force, the soft channel in the sensor body to transmit contact force and end of the soft channel to reflect emitted light. When the hemisphere (the part of the channel that extends outwards) is compressed by contact force, the end of the channel is axially protruded as shown in Fig. 1. Thus, a key assumption is the soft material has low compressibility to be protruded, and the key of the sensor principle is a variation of reflected light intensity depending on a displacement of the axial protrusion as shown in Fig. 1.

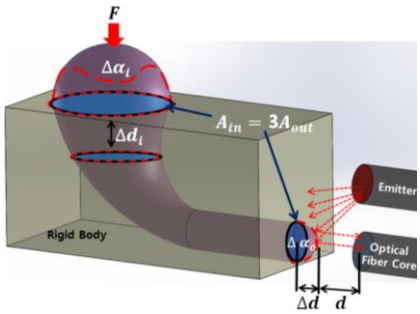

Fig. 1 Diagram of soft material channel, and diagram of light reflection.

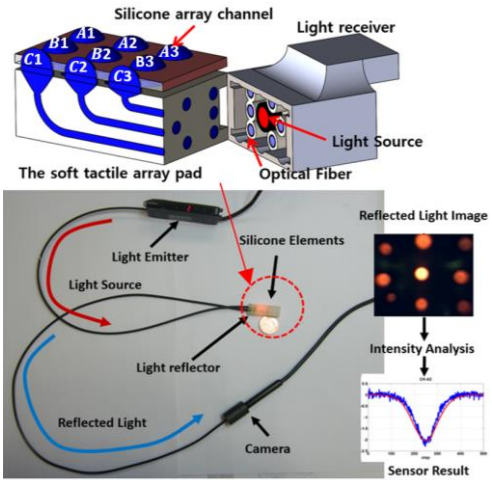

Fig. 2 The first prototype soft tactile array sensor system structure.

The reflected light intensity I depending on the distance d between receiver and the end of the channel can be represented using the inverse-square law,

$$I \propto \frac{r}{d^2} \qquad (1)$$

where r is a constant value denoting the radiation of light at initial distance. Thus, when d is reduced by the soft material's axial protrusion displacement (Δd), the light intensity is increased as shown in Fig. 1. Moreover, the Δd depending on contact force can be amplified by increasing ratio between the protrusion area A_{out} and contact area A_{in}. To observe the light intensity reflection patterns from the multiple channels, a multi-core fibre bundle is used to transmit the light patterns to a camera. The acquired light intensity patterns are then converted into images by the camera and the individual force values can be interpreted as indicated in Fig. 2.

FIRST PROTOTYPE

The first prototype was developed to study feasibility of the soft tactile array sensor as Fig. 2. The soft array pad includes nine independent soft tactile channels, and the light receiver includes an optical bundle which has nine optical fibers and one light emitter. The nine soft material channels cover the first prototype sensor area of 9.5 × 11 mm^2. Each soft material channel was first casted using a silicone rubber (Eco-Flex 50). In the first prototype, to amplify light intensity variation, the radius of protrusion area A_{out} and contact area A_{in} are designed as 1 mm and 3 mm respectively.

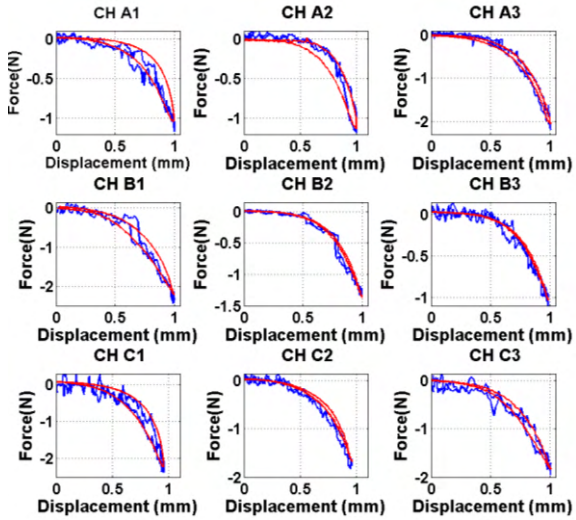

Fig. 3 The blue lines are the measured forces; the red lines are the reference force values (from the Nano17 force sensor). Channel labels are in Fig. 2.

CALIBRATION AND SIGNAL PROCESSING

To verify the sensor's performance in terms of resolution, hysteresis and crosstalk-to-signal ratio, a calibration experiment set-up using a motorized linear guide and a 6-axis force/torque sensor (Nano-17). Each silicone channel was calibrated individually. The received raw image from the camera is divides into nine sub-regions. The average pixel intensity on the red-channel of a sub-region is extracted. Each pixel intensity signal of the soft channel was calibrated using signal scale optimization and defining linear stage. However, due to the use of a USB camera for image capture, the extracted average pixel intensity is noisy. Thus, the noisy signal was processed by a differential filter. Fully detail of the signal processing is available in [4]. The processed signals from the nine elements are as shown Fig. 3. The validation tests on a 3×3 tactile array prototype showed that each of the sensing nodules has average measureable force range from 0 to 1.622 N, with an average accuracy of 97%, average crosstalk-to-signal ratio of 1.8%, and no signal drifting. Through the verification results, we believe that the proposed soft tactile array sensor is suitable for various MIS tool integrations.

FUTURE WORK

We are in a process to develop a flexible surgical palpation probe by integrating the proposed sensor design to a flexible instruments, Fig. 4. The probe is intended to be used for localising tumours inside solid or glandular organs such as liver, kidney and pancreas during MIS. The flexible design of the shaft will provide the dexterity for orienting the tactile array to obtain good contact condition on the soft tissue during palpation. An initial prototype of the ellipse palpation head ($9mm \times 8mm \times 11mm$) was fabricated with 16 soft channels as shown Fig. 4. To enhance the sensor specifications, we will explore light intensity variation depending on type of soft material and the area ratio. Therefore, the sensing mechanism will be further optimized to be workable for MIS palpation.

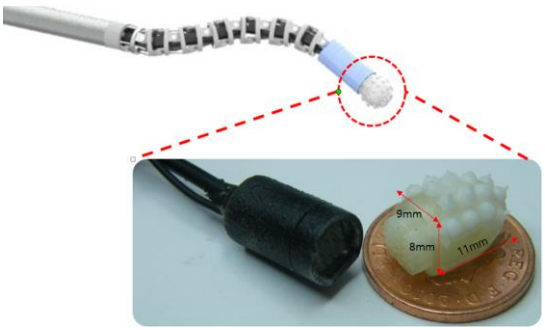

Fig. 4 The design of the flexible palpation probe with soft tactile array sensor integrated.

ACKNOWLEDGEMENT

This research has received support from NSFC Major International (Regional) Joint Research Project "Flexible Tactile-Sensing Surgical Instrument Perception Mechanism and Design Methodology", Grant No: 51520105006.

REFERENCES

[1] P. Puangmali, K Althoefer, LD. Seneviratne, D. Murphy, and P. Dasgupta, "State-of-the-Art in Force and Tactile Sensing for Minimally Invasive Surgery", IEEE Sensors Journal, vol. 8 (4):371- 381 ,2008.

[2] K. Kuwana, A. Nakai, K. Masamune, and T. Dohi, "A Grasping Forceps with a triaxial MEMS tactile sensor for quantification of stresses on organs", IEEE International Conference of IEEE Engineering in Medicine and Biology Society, pp. 4490-4493, 2013

[3] H Liu, J Li, X Song, LD Seneviratne, K Althoefer, "Rolling Indentation Probe for Tissue Abnormality Identification during Minimally Invasive Surgery", IEEE Transactions on Robotics, vol.27, issue.3, 450 – 460, 2011.

[4] J. Back, P. Dasgupta, L. Seneviratne, K. Althoefer, and H. Liu, Feasibility Study – Novel Optical Soft Tactile Array Sensing for Minimally Invasive Surgery, IEEE International Conference on Intelligent Robots and Systems(IROS), pp. 1528-1533, 2015

The Effect of Gripper Scaling on Grip Force Adjustment in Robot-Assisted Surgery – a Preliminary Study

A. Milstein[1], Y. Mintz[2], I. Nisky[1]

[1]*Department of Biomedical Engineering, Ben-Gurion University, Be'er Sheva, Israel*

[2]*Department of Surgery, Hadassah-Hebrew University Medical Center, Jerusalem, Israel*

amitmil@post.bgu.ac.il

INTRODUCTION

In robot-assisted minimally-invasive surgery (RAMIS) the surgeon teleoperates surgical instruments using robotic manipulators. Many RAMIS instruments have a gripper for grasping tissue and surgical equipment. When manipulating an object with a precision grip, we apply a grip force that is slightly larger than needed to not drop the object, and its magnitude is (predictively) adjusted to the load force of the object [1]. Incorrect grip force in surgery may cause excessive fatigue, and may cause iatrogenic injuries to the patients when applying too much grip force, or slippage of tissue from the grasp when not applying sufficient grip force [2].

State of the art RAMIS systems do not present the surgeon with force feedback, and do not provide grip force information from the grasped objects, except from passive pseudo-grip force feedback from two physical springs in the gripper of the master manipulator [3]. Hence, the surgeons must rely on visual cues from the environment to decide how much grip force to apply.

To provide surgeons with force feedback it is important to acquire the force information from the surgical enviornment [4], and present it reliably to the surgeon. Here we bypass the former problem by using image processing to compute a virtual load force, and focus on the latter. We studied the effect of the scaling between manipulator and instrument gripper angles on grip force-load force adjustment in RAMIS. We hypothesized that although not necessary for holding the load, a larger gripper scaling will cause larger grip forces for similiar load forces.

MATERIALS AND METHODS

In Fig. 1a our experimental platform is depicted: a RAVEN II surgical research platform [5] teleoperated by a Sigma7 haptic device. We acquired a video with two Flea3.0 cameras, and presented a 3D view of the experimental scene via a head-mounted device (HMD).

The desired Cartesian position, P_R, of the right instrument was controlled according to:

$$(1)\quad P_R = s_{pos} \cdot \left(P_S - P_{S^*}\right) + P_{R^*}$$

where P_S is the position of the master, and P_{R^*} and P_{S^*} are reference positions to align the local and remote workspaces after instrument clutching, and s_{pos}=0.4.

The desired angle of the RAVEN gripper, g_R, was scaled with respect to the angle of the master, g_S, according to:

$$(2)\quad g_R = s_{grip} \cdot \left(g_S - g_{S_{closed}}\right)$$

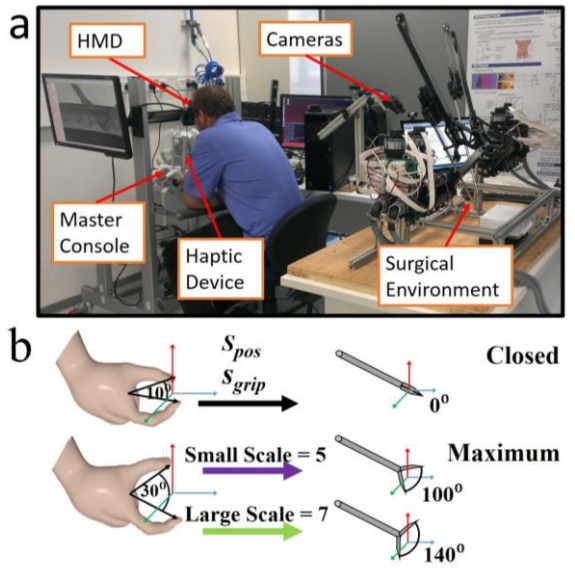

Fig. 1 Experimental setup: a) overview of the system, left side is the surgeon console, and right side is the patient site; b) gripper scaling.

where $g_{Sclosed}$=10 degrees is the aperture of the master in which the RAVEN gripper is fully closed (Fig. 1b). For g_S<10 a grip-force was applied by the closed RAVEN instrument. In this study we used s_{grip}= 5 or 7.

Our implementation of grip-force feedback, f_{gf} to the user is local, and it depended on g_S:

$$(3)\quad f_{gf} = \begin{cases} \left(g_{S_{\max}} - g_S\right) \cdot k_{g,soft} & g_S > g_{S_{closed}} \\ \left(g_{S_{\max}} - g_S\right) \cdot k_{g,hard} + \left(g_{S_{closed}} - g_S\right) \cdot k_{g,hard} & g_S < g_{S_{closed}} \end{cases}$$

where, g_{Smax}=30^0 is the maximum grip angle, $k_{g,soft}$=10[N/rad] and $k_{g,hard}$=1350[N/rad]. In the steady state, f_{gf} was equal to the grip force that the user applied.

Participants interacted with three cylindrical objects, differing in diameter (8mm, 10mm, 12mm), as depicted in Fig. 2a. We assigned a virtual load force to them (1N, 2N, or 3N, respectively). We used real-time video processing using OpenCV to detect lifting and releasing of the objects. The appropriate load force was applied via the master manipulator when the object was lifted.

Five participants performed the experiment. In each trial, they lifted one of the three objects, held it in the air for half a second and released it, and repeated this five times. In each block, each object was presented 10 times, randomly ordered, total of 30 trials and 150 lifts. Each participant performed a block with a small scaling (s_{grip}=5) and a block with a large scaling (s_{grip}=7). Three participants did the small scaling first (*small first*), and

two did the large scaling first (*large first*). Due to the small sample size in this preliminary study, we do not perform statistical hypothesis testing.

We recorded the motion and grip angle, grip force, and load force from the haptic device, as well as motion and grip angle from the RAVEN at 1KHz, downsampled to 200 Hz and lowpass-filtered at 10Hz.

RESULTS

Grip force was calculated at the steady state of the lift, when the object was held stationary in the air. In Fig. 2b, an example of grip force, load force, and position trajectories from 2 lifts in a single trial is depicted. The grip force increases to grasp the object and in anticipation of the load force, and remains roughly constant during the lift. An example of the mean grip force, load force and trajectory for one subject is depicted in Fig. 2c for the small and large scaling. The trajectories are similar, but for this participant, the grip force is larger in the smaller scaling. In Fig. 2d the mean trajectories are depicted for two different objects. As expected, the participant applied larger grip force when lifting the heavier load.

We calculated the mean grip force over different conditions by averaging over the last lift of each trial of all subjects. Fig. 3 depicts that the mean grip force was adjusted to the load force (Fig 3a), and interestingly, it was lower in the *large first* group (Fig. 3b). In general, the mean grip force was lower in the small scaling (Fig. 3a), but this is because the *large first* group reduced their grip force when moving to the small scaling (Fig. 3c). This reduction was much weaker in the *small first* group when they moved to the large scaling.

We analyzed the grip force that was applied on the master side, but for tissue damage, the grip force on the object is important. We could not measure this force, but we calculated a proxy for it based on the desired angle g_R and the width of the held object. Fig. 3d shows that larger scaling led to larger proxy values, and would likely lead to stronger forces on the object.

DISCUSSION

We found that the grip force-load force relation was similar to natural object manipulation, suggesting that load force feedback can assist surgeons to interact naturally with the surgical environment. Our hypothesis about the effect of scaling was right, but the participants learned and reduced their grip forces in their second block, especially in the *large first* group. A study with more participants and several additional control experiments is needed to test our initial hypothesis and investigate grip force adjustment learning.

In this study, participants received pseudo grip force feedback that did not inform them about the grip forces that were applied on the object, likely resulting in larger forces on the objects in the large scaling. This highlights the importance of providing veridical information about the grip force on the grasped objects.

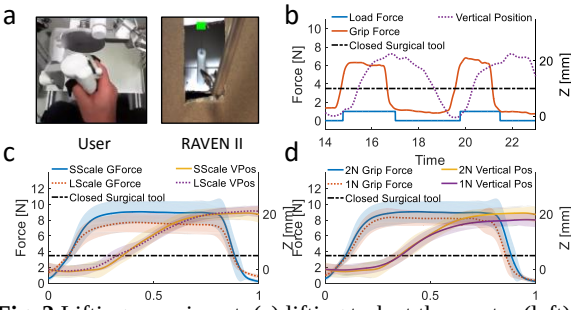

Fig. 2 Lifting experiment. (a) lifting task at the master (left) and patient (right) sites; (b) Example grip force, load force, and vertical position trajectories from a single trial of 1N load force; (c,d) Mean lift trajectories (grip force and vertical position) as a function of normalized time of a single participant from the small first group. (c) for small and large scaling; (d) for objects of 1N and 2N load force. Shaded areas are the standard deviation over all lifts.

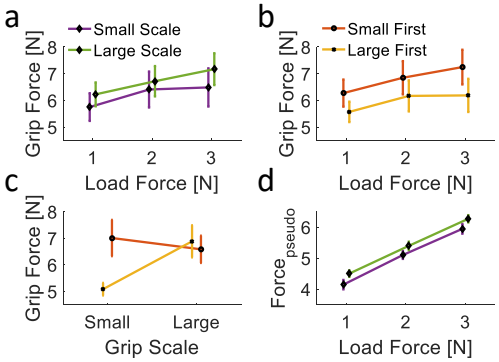

Fig. 3 Mean steady-state grip force with 95% confidence intervals: a) mean grip force of all participants as a function of load force in each scale; b) mean grip force of participants in each group as a function of load force; c) same as (b) but as function of scale; d) mean estimated pseudo force applied to each object in each scale.

ACKNOWLDEGMENTS

We thank Eli Peretz, Doron Haichal and Lidor Bahar for their help with building and maintaining the experimental setup.

This study is supported by the Helmsley Charitable Trust through the ABC Robotics Initiative of Ben-Gurion University of the Negev, and by the Israeli Science Foundation (grant number 823/15).

REFERENCES

[1] G. Westling and R. Johansson, "'Factors influencing the force control during precision grip," *Experimental Brain Research*, vol. 53, no. 2, pp. 277-284, 1984.

[2] A. Szold, R. Bergamaschi, I. Broeders, J. Dankelman, A. Forgione, T. Langø, A. Melzer, Y. Mintz, S. Morales-Conde and M. Rhodes, "'European association of endoscopic surgeons (EAES) consensus statement on the use of robotics in general surgery," *Surg.Endosc.*, vol. 29, no. 2, pp. 253-288, 2015.

[3] T.L. Gibo, D.R. Deo, Z.F. Quek and A.M. Okamura, "'Effect of load force feedback on grip force control during teleoperation: A preliminary study,", Haptics Symposium (HAPTICS), 2014 IEEE , pp. 379-383, 2014.

[4] U. Kim, D. Lee, W.J. Yoon, B. Hannaford and H.R. Choi, "'Force Sensor Integrated Surgical Forceps for Minimally Invasive Robotic Surgery," *Robotics, IEEE Transactions on*, vol. 31, no. 5, pp. 1214-1224, 2015.

[5] B. Hannaford, et al. "'Raven-II: an open platform for surgical robotics research," *Biomedical Engineering, IEEE Transactions on*, vol. 60, no. 4, pp. 954-959, 2013.

Instrument Tip Angular Kinematics in Teleoperated Needle-Driving

Y. Sharon[1], T. S. Lendvay[2], I. Nisky[1]

[1]*Department of Biomedical Engineering, Ben-Gurion University of the Negev*

[2]*Department of Urology, University of Washington*

shayar@post.bgu.ac.il

INTRODUCTION

The technical skill of a surgeon directly impacts patient outcomes [1]. The current state of surgical skills assessment is still performed by direct or video observation by expert surgeons, yielding potentially subjective appraisals. With the advent of robotic-assisted laparoscopic surgery technology, surgical skills can now be deconstructed, quantified, and synthesized using instruments position, velocity, and orientation. The validated objective performance metrics currently used are time to complete task, path length, speed, and curvature [2].

We hypothesize that in certain surgical tasks, the range and the rate of change of instrument orientation are also important. For example, to successfully drive a needle through a tissue, the instrument has to be rotated along the arc of the needle. Except from a few studies of angular speed [3], angular motion was largely overlooked in skill assessment.

In this study, we analyzed teleoperated needle-driving from a previously reported study [4]. We present a new metric: normalized angular displacement of the instruments, and show that it allows for a good distinction between experienced robotic surgeons and novice users when classical metrics fail.

METHODS

Full details of the experimental setup and procedures are reported in [4]. Sixteen subjects participated in the experiment: six experienced surgeons, and ten novices without surgical experience. One novice participant had extensive experience with the experimental setup and hence was removed from the analysis. The participants performed teleoperated needle-driving using a da Vinci Research Kit and open needle-driving. Here, we focus on their teleoperated movements.

The participants sat in front of the master console (Fig. 1.A), and the task board – foam with four marked targets (Fig. 1.B): start (*s*), insertion (*i*), exit (*e*), and finish (*f*) – was placed on the patient-side table. A single needle driving trial consisted of: (I) transport – reaching with needle head from *s* to *i*, (II) insertion – driving the needle through the tissue until its tip exits at *e*, (III) catching – opening the gripper and catching the tip of the needle, and (IV) extraction –pulling the needle and reaching to *f* with its tail (Fig. 1B, 2A). Each participant performed 80 trials with breaks every 10 trials.

The Cartesian position, velocity, and orientation of the needle driver, and its opening angle were recorded at approximately 2kHz. We interpolated and downsampled

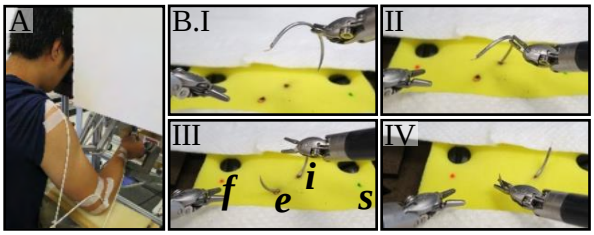

Fig. 1 Teleoperated needle driving with the da Vinci Research Kit. (A) A participant seated at the master console. (B) The task board and task segments: (I) transport, (II) insertion, (III) catching, (IV) extraction.

all data to 100Hz. We used spherical linear interpolation (SLERP) to interpolate the orientation [5], and piecewise cubic Hermite interpolating polynomial (PCHIP) for the rest of the data. We filtered the Cartesian position offline at 6 Hz with a 2nd order zero lag Butterworth filter. We automatically segmented the needle driving movement into its four compenents.

For each trial and each segment, we calculated two metrics: (1) *path length* – a classical measure for surgical skill, and (2) *normalized angular displacement* – accumulated change in instrument orientation normalized by path length. To calculate these two metrics, we found the transformation $\Delta T_{i,i+1}$ (translation $\Delta d_{i,i+1}$ and rotation $\Delta R_{i,i+1}$) between consecutive sampled reference frames T_i and T_{i+1} that were attached to the tip of the inbstrument (Fig. 2B inset), as: $\Delta T_{i,i+1} = T_{i+1} T_i^{-1}$. We calculated the *path length* as $P = \sum_{i=1}^{n-1} \Delta d_{i,i+1}$, where n is the number of samples. We used the *axis-angle* to represent the angle $\Delta\theta_{i,i+1}$ of the rotation $\Delta R_{i,i+1}$, and calculated the *normalized angular displacement* as $A = \frac{1}{P}\sum_{i=1}^{n-1}\left|\Delta\theta_{i,i+1}\right|$.

Preliminary analysis suggested that segment II (insertion) was the most informative, and hence, we focus the statistical analysis on this segment. We log-

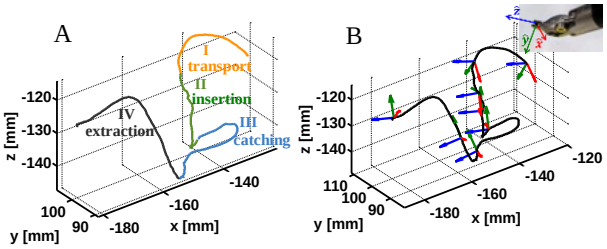

Fig. 2 Path and orientation from a single trial. (A) Right PSM (patient side manipulator) needle driver path. The numbers and the different colors indicate the four segments of the movement. (B) Right PSM's orientations at several samples along the path. The orientation is represented by a frame that was attached to the needle driver as shown in the inset.

transformed the *path length* metric for statistical analysis. We calculated the averages of the first and last 10 trials of each participant, and built a 2-way mixed model ANOVA. The independent variables were: stage (early/late, within subject), experience (novice/expert, between subject), and their interaction. We used the Bonferroni correction for post-hoc comparisons.

RESULTS

Fig. 3 depicts the path length and normalized angular displacement in all four segments (A) and the averages of the first and the last 10 trials (B). The performance of experts was better than of novices – shorter path length and larger angular displacement ($F_{1,13}$=19.37, p<0.001, and $F_{1,13}$=19.47, p<0.001, respectively).

For the path length, there was a statistically significant improvement between early and late trials ($F_{1,13}$=17.21, p=0.001), and a statistically significant interaction between experience and stage ($F_{1,13}$=6.60, p=0.02). In the early trials, the paths of experts were shorter than of novices (p<0.001). The improvement (shortening of the path) of novices was statistically significant, but the improvement of the experts was not (p<0.001, and p=0.33, respectively). As a result, the difference in path length between novices and experts was not statistically significant in the late trials (p=0.07). These results are consistent with our previously reported analysis [4], and the lack of difference between expert surgeons and novice users after only 80 trials suggests that this metric is insufficient for quantifying surgical skill.

For the normalized angular displacement, the stage factor was not statistically significant ($F_{1,13}$=0.42, p=0.56), but the interaction between experience and stage was ($F_{1,13}$=9.14, p=0.01). A post hoc analysis revealed that in early trials, experts were better – they had statistically significant larger angular displacement than novices (p<0.001), and that the novices improved and increased their angular displacement (p=0.01). The difference in the angular displacement of experts between early and late trials was not statistically significant (p=0.15). Importantly, in the late trials the angular displacement of experts was statistically significantly larger than of novices (p=0.02).

DISCUSSION

We present a new promising metric for robot-assisted surgical skill – the normalized angular displacement. This metric captures technical aspects that are taught during surgeons' training, such as rotating their wrists as far back as possible so that the needle addresses the tissue at a right angle and pierces the tissue planes with the least amount of force. We showed that our new metric correlates with experience, and in contrast to the classic metric of path length, showed differences between novices and experts at the end of the short training. Therefore, we suggest that it can add value to skill assessment by combining with additional metrics. Future studies are needed to test this metric on a larger cohort of surgeons and examine whether it may facilitate more efficient training.

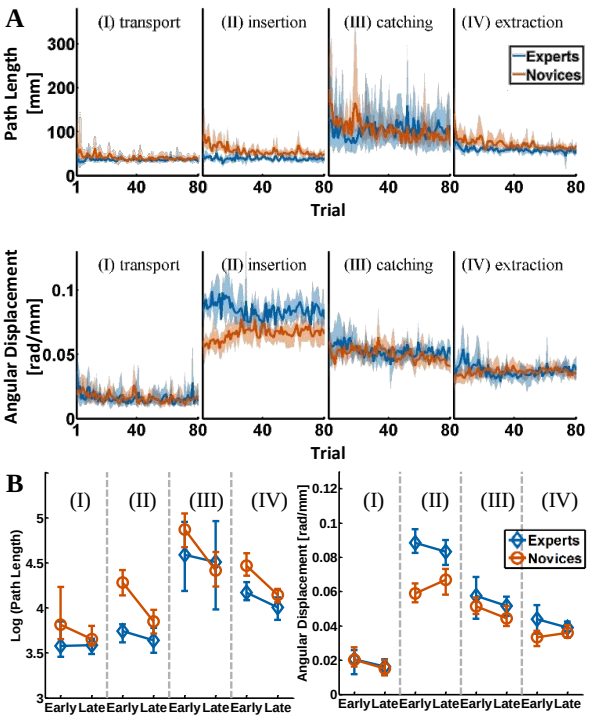

Fig. 3 (A) Path length (upper) and normalized angular displacement (lower) as a function of trial number. Lines are means, shaded areas are 95% bootstrap confidence intervals. (B) Log-transformed average path length (left) and average normalized angular displacement (right) in the first 10 (early) and last 10 (late) trials. Markers are means, error bars are 95% bootstrap confidence intervals.

ACKNOWLEDGEMENTS

We thank Allison Okamura, Michael Hsieh, Zhan Fan Quek and Yuhang Che for their help in obtaining the experimental data. The study was supported by the Helmsley Charitable Trust through the ABC Robotics Initiative, and the ISF grant number 823/15. YS was supported by the Moshal Scholarship Program.

REFERENCES

[1] J. D. Birkmeyer, J. F. Finks, A. O'Reilly, M. Oerline, A. M. Carlin, A. R. Nunn, J. Dimick, M. Banerjee and N. J. Birkmeyer. Surgical skill and complication rates after bariatric surgery. *N. Engl. J. Med. 369(15)*, pp. 1434-1442. 2013.

[2] T. N. Judkins, D. Oleynikov and N. Stergiou. Objective evaluation of expert and novice performance during robotic surgical training tasks. *Surg. Endosc. 23(3)*, pp. 590-597. 2009.

[3] L. Vemer, D. Oleynikov, S. Holtmann, H. Haider and L. Zhukov. Measurements of the level of surgical expertise using flight path analysis from da vinci™ robotic surgical system. *Medicine Meets Virtual Reality 11* pp. 373. 2003.

[4] I. Nisky, Y. Che, Z. F. Quek, M. Weber, M. H. Hsieh and A. M. Okamura. Teleoperated versus open needle driving: Kinematic analysis of experienced surgeons and novice users. IEEE Intern. Conf. on Robotics and Automation. 2015.

[5] P. I. Corke. *Robotics, Vision & Control: Fundamental Algorithms in Matlab* 2011.

Establishing Imaging Protocol for Evaluation of Breast Cancer Margins using High-Speed Confocal Endomicroscopy and Methylene Blue

K. Vyas, M. Hughes G.-Z. Yang

The Hamlyn Centre for Robotic Surgery, IGHI, Imperial College London, UK

k.vyas13@imperial.ac.uk

INTRODUCTION

Breast cancer is one of the leading causes of cancer related deaths worldwide, accounting for about 14% of all cancer related female deaths. The first line of treatment is surgical excision of malignant lesions either by removing the whole breast (mastectomy) or by removing the cancerous lump and a margin of healthy tissue around it (lumpectomy or breast conserving surgery, BCS). BCS is often the treatment of choice for patients with early-stage breast cancer, as it allows for complete tumour excision while still maintaining acceptable cosmesis. However 20-30% of BCS patients require one or more re-operative interventions to obtain oncologically clear resection margins [1].

Endomicroscopic imaging of breast cancer margins

Imaging systems such as fiber-bundle endomicroscopes, which are capable of performing *in vivo* and real-time optical biopsy, could play a critical role in allowing postive margins to be identified intraoperatively. Preliminary studies into the morphological assessment of breast cancer tissues have been carried out using probe-based confocal laser endomicromicrosocpy (pCLE) at a wavelength of 488 nm. This allows imaging of fluorescent dyes such as fluoroscein (intravenous), acriflavine (topical) and proflavine (topical) [2]. Acriflavine allows staining of cell nuclei (unlike fluorescein), but a potential risk of mutagencity has been identified. For successful clinical translation to *in vivo* cellular imaging it is important to identify fluoroscent dyes that are safe for in-human use.

In this work, we develop an in-house high-speed line scan confocal endomicrocopy system to operate at 660 nm wavelength. At this wavelength we can obtain fluorescence images of freshly-excised human breast tissue stained with methylene blue, an FDA approved dye which is already used clinically for intra-operative sentinal lymph node mapping in breast cancer surgery.

MATERIALS AND METHODS

Imaging system

For this study we have converted a high-speed virtual-slit line-scanning confocal endomicroscopy system [3] to operate at 660 nm wavelength (Fig. 1(a)). It uses a cylindrical lens to focus 660 nm light emitted from a laser-diode into a line, which is scanned over the tissue via a flexible fiber-bundle based probe. Returning fluorescence is imaged onto a monochrome rolling shutter CMOS camera (Flea3 FL3-U3-13S2M-CS). The rolling shutter acts as a virtual detector slit, rejecting most of the out-of-focus fluorescence, leading to optical sectioning at frame rates of up to 120 Hz [3].

Patient Data

The study comprised 8 non-neoplastic human breast tissue specimens freshly excised from 2 patients who underwent breast surgery in the months of March and April 2016. Written informed consent was obtained from the patients using the Imperial College tissue bank ethical protocol (R-12047). For this preliminary study, tissue slices that contained non-neoplastic adipose tissue and stroma (as examined by histology) were selected.

The specimen cut-outs (~10x10mm) were first immersed in methylene blue solution at four different concentrations of 0.1%, 0.2%, 0.5% and 1%. The fluorescent agent was left to stain the tissue for 30 s. Following immersement, the cut-outs were gently rinsed with water to wash off excess fluorescent agent for 1 minute and imaged immediately. A representative tissue specimen is shown in Fig. 1(b).

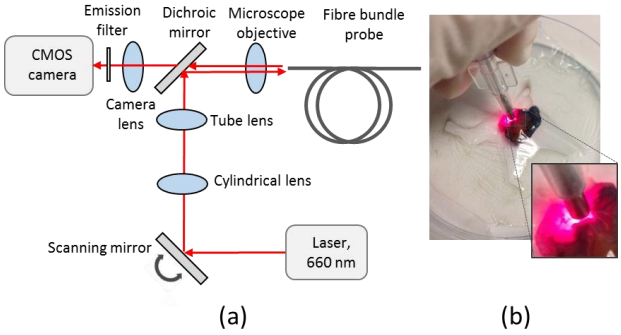

Fig 1. Experimental set-up showing (a) Schematics of the optical system and (b) image of the fiber-bundle probe examining methylene blue stained breast tissue.

Image acquisition and processing

The tip of the endomicroscope probe (Cellvizio Coloflex UHD probe, Mauna Kea Technologies), which contains a 30,000-core Fujikura fiber bundle (FIGH-30-650S), was gently pressed onto the tissue surface. Images were obtained in real-time and stored digitally in a prospectively maintained database of images and corresponding histology. At the end of the imaging session, excess fluorescent dye was gently wiped off the surface of the tissue and the tissue was returned to histology for routine analysis. A pre-processing step for removing the pixelation artefacts produced by the fiber cores, using Delaunay triangulation, and a post-processing step for video mosaicking to create larger field of view images, using a two-way fast normalized cross-correlation (NCC) algorithm, were implemented.

Image quality assessment

Morphological features were identified following the taxonomy of pathologies for normal and neoplastic breast tissue that was developed in our previous study [2] and the image quality was assessed from the visibility of those features in the reconstructed mosaics. The mosaics were scored '1', '2' or '3' based on the clarity with which the tissue structure was visualized (where '1'- almost invisible structure, '2'- partly visible and '3'– clear classification of tissue morphology). The rationale for this categorization was that, if the tissue is stained non-specifically, different tissue structures such as fat cells, nuclei and connecting fibers would all be stained uniformly, thus making it difficult to identify and distinguish them. This would be reflected by an overall reduction in mean image contrast of that image.

RESULTS

The main types of normal breast tissue features present in all the 8 specimens analyzed were adipose tissue and collagen fibers in the stroma. All the specimens were histologically confirmed non-neoplastic. On average 3 imaging tests were performed on each sample and a total of 240 image mosaics were generated. Endomicroscopy images of specimens at different staining concentrations are shown in Fig.2.

In fluorescence endomicroscopy images, the adipose tissue appeared as well-defined and uniform black non-fluorescent oval or polygon shapes with hyper-fluorescent borders and sparsely populated nuclei as bright spots along the borders. The fibrous connective tissue appeared as well-defined hyper-fluorescent bundles of elastic wavy fibers with sparse oval bright spots corresponding to fibroblast nuclei in the stroma.

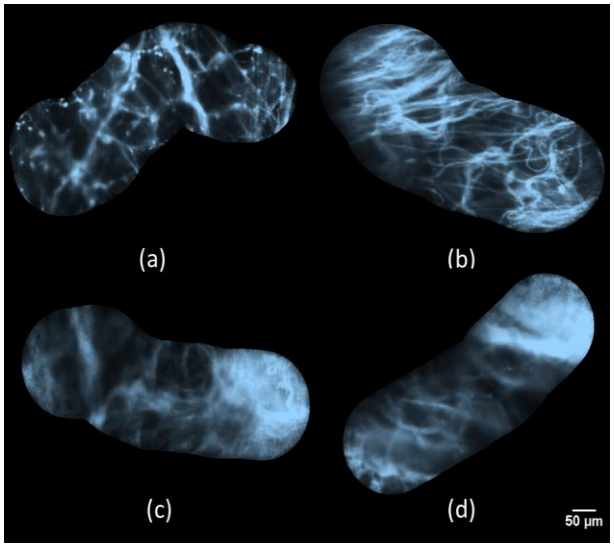

Fig. 2 Representative endomicroscopy mosaics of breast tissue stained with methylene blue at (a) 0.1%, (b) 0.2%, (c) 0.5% and (d) 1.0% concentration. The elastic fibers and nuclei are clearly visible in (a) and (b).

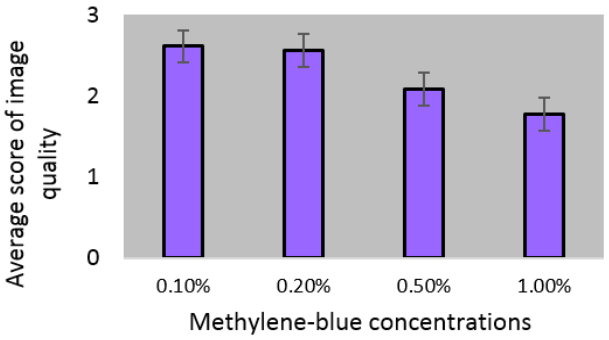

Fig. 3 Effect of methylene blue concentration on endomicroscopy image quality.

Fig. 3 shows the overall scores from the assessment of tissue structure visibility in endomicroscopy mosaics stained at different methylene-blue concentrations. For 0.1% and 0.2% of methylene blue, tissue structure is clearly visible and nuclei are visible as bright spots. For higher concentrations of 0.5% and 1%, even though adipose tissue was partially visible, the hyper-fluorescent, thread-like connective fibers were not identified and the stoma appeared uniformly bright making it difficult to distinguish nuclei.

DISCUSSION

This work shows the potential use of high-speed line scan confocal endomicroscopy operating at 660 nm to evaluate radial margins during BCS in real-time. Clinical trials have demonstrated the suitability of methylene blue for endomicroscopy imaging of human airways using point-scanning pCLE, typically having frame rates on the order of 12 fps (Mauna Kea Technologies). With our system, we can achieve frame rates up to 120 fps, an order of magnitude improvement which helps enable large-area imaging by mosaicking while maintaining high resolution.

Existing literature on endomicroscopy imaging of lung nodules suggests a methylene blue concentration of 0.1%. Our preliminary study indicates that concentrations of 0.1% and 0.2% give optimal results for freshly excised normal breast tissue specimens. Work is on-going to examine the tissue morphology of benign and neo-plastic breast tissue using these different methylene blue concentrations, and obtaining objective assessment by trained pathologists. This work will inform potential future studies using 660 nm confocal endomicroscopy directly in the breast cavity.

REFERENCES

[1] P. Ananthakrishnan et al., "Optimizing surgical margins in breast conservation. International Journal of Surgical Oncology, 2012, Article ID 585670."

[2] Chang, Tou Pin, et al. "Imaging breast cancer morphology using probe-based confocal laser endomicroscopy: towards a real-time intraoperative imaging tool for cavity scanning." Breast cancer research and treatment 153.2 (2015): 299-310.

[3] Hughes, M. et. al. "Line-scanning fiber bundle endomicroscopy with a virtual detector slit." Biomedical Optics Express 7.6 (2016): 2257-68.

Macro- and *Micro-Scale* 3D Gaze Tracking in the Operating Theatre

A. A. Kogkas, M. H. Sodergren, A. Darzi, G. P. Mylonas

Department of Surgery and Cancer, Imperial College London, UK

a.kogkas15@imperial.ac.uk

INTRODUCTION

By approaching the eyes as the only visible part of the brain, we can consider them not just in the conventional sense as receptors of visual stimuli, but also as perception- and cognition-rich actors within the operating theatre. Using eye-tracking, several concepts have been developed for harnessing the power of the human visual system [1], for assessment of expertise [2], for objective measurement of surgical skills and for training [3].

In robotic [4] and laparoscopic [5] surgical settings, screen-based **collaborative eye-tracking** of multiple collaborators was shown to significantly improve verbal and non-verbal communication, task cooperation and efficiency, by allowing to share gaze information between the collaborators. However, **screen-based** eye-trackers restrict the surgeon's head to a fixed position and can only provide 2D gaze information on a screen (*micro-scale*). On the other hand, **wearable** eye-trackers can provide unrestricted theatre-wide (*macro-scale*) 2D gaze information on the head frame-of-reference (Fig. 1). Simultaneous use of both modalities is mutually exclusive due to IR interference of the eye cameras. Moreover, 3D world coordinates would be desirable and beneficial.

We propose a novel framework that can provide unrestricted and simultaneous 3D eye-tracking on both the *macro-* and *micro-scales*, by using **just** a wearable eye-tracker. Preliminary investigations are carried out to assess the feasibility of the proposed framework.

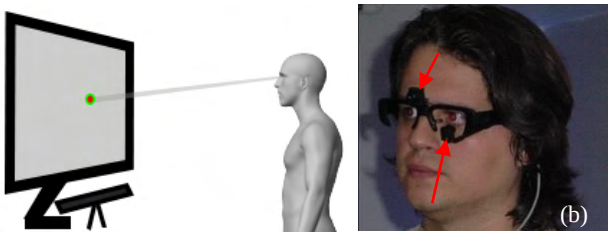

Fig. 1 (a) Screen based eye-tracker. (b) Wearable eye-trackers provide 2D gaze coordinates on the scene camera frame-of-reference, which is equivalent to the head frame-of-reference.

MATERIALS AND METHODS

The proposed framework combines the use of a wearable eye-tracker and its respective RGB/scene camera, RGB-D cameras for real-time 3D reconstruction of the environment and the Parallel Tracking and Mapping (PTAM) methodology [6]. The objective is to estimate the head pose within the 3D reconstructed operating theatre and use this information to map the 2D fixations reported by the eye-tracker to *macro-scale* 3D fixations in the world frame-of-reference.

Based on a monocular camera, PTAM first generates an initial 3D keyframe scaled map of an unknown environment using the five-point stereo algorithm [7]. Then it builds/updates the keyframe map and tracks the camera pose relative to it, in parallel. For the *macro-scale* requirements, we use PTAM to estimate the eye-tracker's RGB/scene camera pose (equivalent to the head pose) in the world frame-of-reference. This information and the 2D fixation point reported by the eye-tracker provide the gaze vector. In a final step, the sparse 3D point cloud generated by PTAM is triangulated and the 3D fixation is estimated by the intersection of the gaze vector with a triangular facet (Fig. 2). For the *micro-scale* requirements, the 3D model of the laparoscope screen is detected and tracked. Gazing on the screen is automatically detected and provided as 3D fixations on the screen model. As a final step, the screen plane position can be refined using perspective transformation in order to obtain more accurate *micro-scale* fixations.

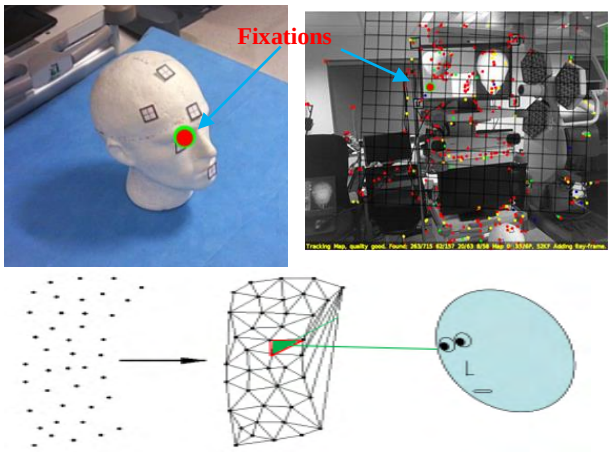

Fig. 2 (Top) Views from the eye-tracker's scene camera, showing the 2D fixations (red dot), the reprojected 3D fixations (green circle), as well as the PTAM generated 3D map and point cloud. (Bottom) The 3D fixation estimation.

Capturing more accurate real world coordinates and dynamic environment updates would require co-registration of a dense 3D point cloud from an RGB-D camera with the corresponding sparse 3D features provided by PTAM. Due to the dissimilarity of the corresponding geometric features, this is not implemented in the current off-line implementation. Instead, a static 3D map was generated once by PTAM, explicitly scaled to real world coordinates, pre-allocated during an initialization step and used thereafter. Also, at the moment, the 3D model of the laparoscope screen is detected and tracked with the assistance of fiducial markers at its four corners. For eye-tracking, the SMI (SensoMotoric Instruments GmbH) glasses are used, with a stated accuracy of 0.5° of visual angle and an RGB/scene camera with a resolution of 1280x960 pixels.

EXPERIMENTAL SETUP

For the experimental setup, an image with ten explicitly positioned and numbered markers is displayed on the monitor. Similarly, ten markers are placed on objects on a surgical table (Fig. 3). The task involves gazing in a predefined order at the monitor and table markers by using variable body and head poses. Eight subjects, 5 males and 3 females between the ages of 24 and 27 with normal uncorrected vision, were invited to take part in the study. After informed consent, the subjects were taken through the experimental setup and given time to familiarize themselves with it. Subjects underwent a 3-point eye-tracking calibration by fixating on a printed pattern at 1*m* distance. Each subject was then instructed to fixate at the twenty markers in ascending order and for at least 3 seconds each, from a predefined standing position, allowing free head-pose. After completion of one round, subjects were asked to repeat the process from a different position. 2D fixations in the head frame-of-reference were recorded by the eye-tracker.

Off-line analysis using the proposed framework was undertaken and the recorded 2D fixations were mapped to 3D fixations in the world frame-of-reference (*macro-scale*) and in the monitor frame-of-reference (*micro-scale*) as appropriate.

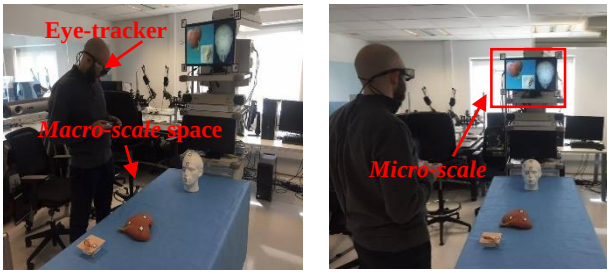

Fig. 3 Illustration of the experimental setup, showing a subject at the two predifined standing positions.

RESULTS

The actual 2D screen and 3D world marker coordinates are compared with those recovered with the proposed framework. The error is calculated as the average Euclidean distance between a marker's actual coordinates and the respective recovered fixation coordinates. One subject was excluded because of corrupted raw eye-tracking data. The results summarized in Table 1 show the error averaged over all subjects. In *micro-scale* mode (screen), the error is reported as a *percentage* of the screen dimensions (51.3x29 cm). In the *macro-scale* mode (world), the error is reported in *cm*. The errors are 1.53% and 8.57 cm respectively.

These values are compounded by the intrinsic error of the eye-tracker due to ocular micro-movements during fixation (drift, microsaccades, physiological nystagmus), the parallax effect [8] and subject-specific cornea irregularities. The intrinsic error is calculated as the Euclidean distance as a *percentage* of the eye-tracker's scene camera frame, between a marker's 2D coordinates and the respective 2D fixation coordinates. A comparison of the intrinsic error with the overall framework error is performed by estimating the framework reprojection error. On the eye-tracker camera frame, the 2D reprojection of a 3D fixation is estimated along with the respected marker's 2D coordinates. Their Euclidean distance as a *percentage* of the camera frame size provides the framework error. The results indicate the framework error at 2.37% and the eye-tracker error at 1.42%. This signifies that 59.92% of the overall framework error is attributed to the eye-tracker.

Table 1. Mean error, standard deviation and maximum error for all subjects.

	Mean	SD	Max
Micro-scale (%) (compounded by eye-tracking error)	1.53	0.98	3.74
Macro-scale (cm) (compounded by eye-tracking error)	8.57	6.85	20.87
Framework reprojection error (%)	2.37	1.89	5.92
Eye-tracker error (%)	1.42	1.03	3.37

DISCUSSION

An early framework that can provide unrestricted theatre-wide and patient-wise 3D eye-tracking was presented. Preliminary evaluation of its accuracy is deemed satisfactory. The study supports our hypothesis that combined *macro-* and *micro-scale* eye-tracking can provide accurate information on the surgeon's fixations both globally and on a laparoscope monitor, which opens the way for a number of practical applications. The proposed framework also promises to solve the parallax problem, which will significantly increase the overall 3D eye-tracking accuracy.

Our immediate plans involve the generation of a real-time and dynamically updated 3D model of the theatre by the use of RGB-D cameras (e.g., Kinect), and implicitly generated and co-registered PTAM maps. This is also expected to improve the head pose estimation.

REFERENCES

[1] G. P. Mylonas, et al. "Gaze-Contingent Motor Channelling, haptic constraints and associated cognitive demand for robotic MIS," *Med. Image Anal.*, vol. 16, no. 3, pp. 612–631, 2012.

[2] T. Tien, P. H. Pucher, M. H. Sodergren, K. Sriskandarajah, G.-Z. Yang, and A. Darzi, "Differences in gaze behaviour of expert and junior surgeons performing open inguinal hernia repair," *Surg. Endosc.*, vol. 29, no. 2, pp. 405–413, 2015.

[3] T. Tien, P. H. Pucher, M. H. Sodergren, K. Sriskandarajah, G.-Z. Yang, and A. Darzi, "Eye tracking for skills assessment and training: a systematic review," *J. Surg. Res.*, vol. 191, no. 1, pp. 169–178, 2014.

[4] K. W. Kwok, L. W. Sun, G. P. Mylonas, D. R. C. James, F. Orihuela-Espina, and G. Z. Yang, "Collaborative gaze channelling for improved cooperation during robotic assisted surgery," *Ann. Biomed. Eng.*, vol. 40, no. 10, pp. 2156–2167, 2012.

[5] A. S. A. Chetwood, K.-W. Kwok, L.-W. Sun, G. P. Mylonas, J. Clark, A. Darzi, and G.-Z. Yang, "Collaborative eye tracking - a potential training tool in laparoscopic surgery," *Surg. Endosc.*, vol. 26, no. 7, pp. 2003–2009, 2012.

[6] G. Klein and D. Murray, "Parallel tracking and mapping for small AR workspaces," *2007 6th IEEE ACM Int. Symp. Mix. Augment. Reality, ISMAR*, 2007.

[7] H. Stewénius, C. Engels, and D. Nistér, "Recent developments on direct relative orientation," *ISPRS J. Photogramm. Remote Sens.*, vol. 60, no. 4, pp. 284–294, 2006.

[8] D. Mardanbegi and D. W. Hansen, "Parallax error in the monocular head-mounted eye trackers," *Proc. 2012 ACM Conf. Ubiquitous Comput. - UbiComp '12*, p. 689, 2012.

Sonopill Pathfinder:
Rapid Prototyping for Ultrasound Capsule Endoscopy

G. Cummins[1], V. Seetohul[2], Y. Qiu[2], K. Wlodarczyk[1], W.A. Lewinger[3], H. Lay[2], B. Cox[4], D. Hand[1], C. Démoré[2], M.Y.P. Desmulliez[1], S. Cochran[2]

[1]School of Engineering and Physical Sciences, Heriot-Watt University, Edinburgh, UK

[2]School of Engineering, University of Glasgow, UK

[3]School of Science and Engineering, University of Dundee, UK

[4]School of Medicine, University of Dundee, UK

G.Cummins@hw.ac.uk

INTRODUCTION

Imaging of the gastrointestinal (GI) tract is vital for the diagnosis of conditions such as colon cancer, haemorrhage or inflammatory bowel disease. Endoscopy is by far the most common approach for diagnosis, though it can induce discomfort in patients. Another disadvantage is that significant regions of the small bowel cannot be easily viewed as standard endoscopic imaging is limited to the upper GI tract and colonoscopy is limited to the terminal ileum and below. Imaging of the small bowel can be achieved by video capsule endoscopy (VCE), which has improved patient acceptance because of the small device size. However, imaging with commercially available endoscopic capsules is limited by the nature of optical imaging to only look at the mucosal surface. Despite this video is the sole imaging method of capsules in development.[1].

The integration of ultrasonic imaging into an endoscopic capsule can be seen as the next extension of VCE as it allows safe, non-ionizing imaging of the GI tract sub-surface[2],[3] with ultrasound imaging already common in upper GI endoscopy. However, engineering challenges such as manufacturability, packaging and increased integration need to be addressed to ensure that ultrasound capsule endoscopy (USCE) can be used as viable diagnostic tool. To investigate these concerns, the Sonopill project [4] is utilising rapid prototyping technology to create "Pathfinder" pills to assess different sensing modalities, including ultrasound for clinical diagnosis [4].This paper presents work conducted on the fabrication of an ultrasound imaging Pathfinder pill.

MATERIALS AND METHODS

The dimensions of any CE device are limited to approximately 1 cm in diameter and 3 cm in length for easy swallowing and travelling through the GI tract. The capsule must also allow ultrasonic waves emitted from the transducer to propagate with little or no reflection at the capsule/transducer or capsule/tissue interfaces. To the authors' knowledge, previous attempts at USCE did not consider the impact of the surrounding capsule casing on ultrasonic transmission [2] or its impact on image quality [3]. Removal of acoustically reflective surfaces by using quarter-wavelength thick material, on the order of 10 μm for the 32 MHz frequency polyvinylidene fluoride (PVDF) focused microultrasound (μUS) transducer is not possible because of manufacturing difficulty and fragility. Lowering the frequency would hinder high quality imaging of the gut wall layers. This problem was addressed for the Pathfinder pill by having the transducer fixed along the central axis of the pill, with the emitted ultrasound reflected off a rotating quartz acoustic mirror embedded in a polydimethylsiloxane (PDMS) dome, shown as A in **Fig. 1**, to give the desired 360^{O} view. PDMS is a biocompatible material with acoustic impedance (1 - 1.9 MRayl) [5], close to that of tissue (1.3 - 1.7 MRayl) [6], minimising impedance mismatch. The μUS transducer as shown by component B in **Fig. 1**, is aligned along the central longitudinal axis of the pill and fixed in place. Previous attempts at USCE rotated the transducer, which may cause excessive stress and strain on any cabling.

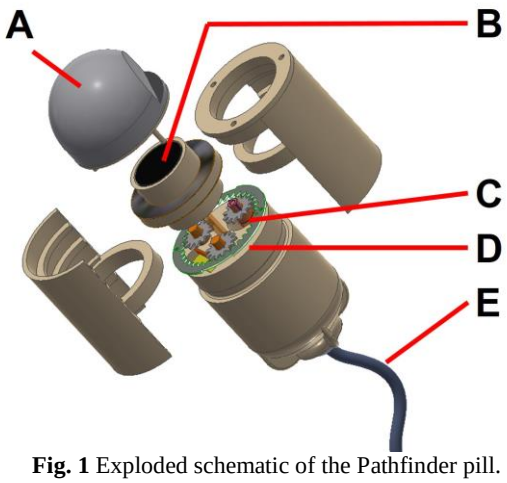

Fig. 1 Exploded schematic of the Pathfinder pill.

Mechanical scanning was used rather than electronic scanning to reduce the need for integration of electronic components. In addition, imaging by mechanical scanning can lead to better image quality because of reduced side lobe interference [2]. The quartz mirror is rotated with a commercial micro-motor of diameter 3.2 mm and length 8.1 mm (103-100. Précis on

Microdrives, London, UK) in conjunction with a laser machined gear assembly, shown as C and D in **Fig. 1**. The gear assembly shown in Fig. 2 comprises an annular gear connected to the midsection of the capsule and three spur gears within it, one driven by the motor. The gear ratio is approximately 2.8:1. Laser micromachining was used as Polyjet and stereolithography additive manufacturing (AM) processes cannot provide the feature resolution needed for the gears. Friction between the rotating section and the static transducer is minimised through the use of PTFE washers (Bokers Inc., MN, USA).

A combined accelerometer and gyroscope (LSM9DS1, STMicroelectronics, Geneva, Switzerland) was included in the capsule to monitor potential rotation and translation of the capsule caused by torqueing of the lower sections have been designed to incorporate fins to stabilise the capsule if this is an issue, though clinical impact must be assessed. The motor, transducer and other components are currently powered via a tether, which is also used to connect external electronics to the transducer. The tether consists of a PTFE tube with an inner diameter of 0.9 mm and outer diameter of 1.1mm, shown as E in Fig. 1. It is intended that the tether will eventually be removed as systems are integrated further into the capsule.

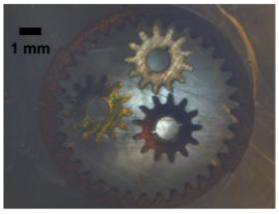

Fig. 2 Magnified view of laser machined gear assembly components.

The majority of the capsule is produced with VeroWhite, a rigid polymer deposited using the Objet Connex 500 AM tool (Stratasys Inc., Rehovot, Israel), shown in beige in Fig. 1. These sections are manually assembled and fixed together using a biocompatible adhesive (4161, Loctite, London, UK) before the entire USCE is coated with a thin film of Parylene C.

RESULTS

Despite the flexibility and ease of production, the design and manufacturing of USCEs with rapid prototyping technologies is complex. As well as the inability to produce the gears with AM processes, the production of the thin rotating outer sections attached to the PDMS dome was problematic due to shell deformation upon removal of the support material. Multiple solutions were implemented to overcome this, such as the interlocking structure shown in Fig. 1 to provide rigidity and increasing the shell thickness, giving the capsule a 10.4 mm outer radius, with the length remaining at 30 mm. These dimensions are closer to those required for clinical use than previous USCEs [2].

Assessment of the diagnostic ability of μUS transducers in the target frequency range was performed using *ex vivo* ethically-sourced, defrosted and rehydrated porcine GI tissue dissected along the long axis and mounted on an agar substrate for mechanically scanning along the short axis. The single-element transducer used for these trials had a 48 MHz centre frequency. The layer distinction within the resultant scans was found to be comparable to histological sections and this distinction was maintained in images, e.g. Fig. 3, simulated at a 25 MHz centre frequency using these scans.

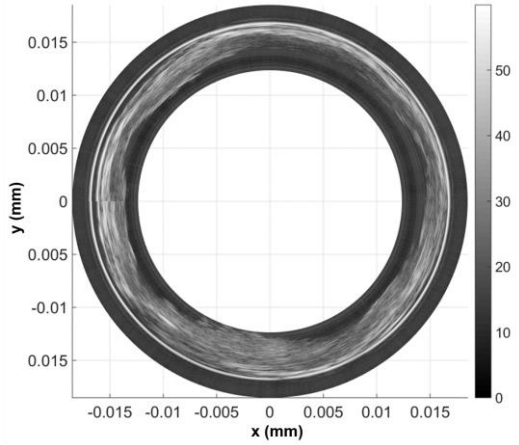

Fig. 3 Reconstructed grey-scale ultrasound image of the full width of dissected pig bowel, digitally processed into a cylinder for use as a virtual phantom. The linear image was stitched together at 9 o'clock to form a continuous loop.

DISCUSSION

Rapid manufacturing techniques such as laser machining and additive manufacturing enable Pathfinder pills to be built quickly to assess different modalities, such as ultrasound imaging and determine solutions to various technical issues. Such devices also provide valuable information that will help to develop USCE as a clinical tool in the future.

REFERENCES

[1] J. L. Toennies, G. Tortora, M. Simi, P. Valdastri, and R. J. Webster, "Swallowable medical devices for diagnosis and surgery: the state of the art," *Proc. Inst. Mech. Eng. Part C J. Mech. Eng. Sci.*, vol. 224, no. 7, pp. 1397–1414, Jan. 2010.

[2] J. H. Lee, G. Traverso, C. M. Schoellhammer, D. Blankschtein, R. Langer, K. E. Thomenius, D. S. Boning, and B. W. Anthony, "Towards wireless capsule endoscopic ultrasound (WCEU)," in *2014 IEEE International Ultrasonics Symposium*, 2014, pp. 734–737.

[3] J. Correia, "Final Report Summary - TROY (Endoscope Capsule using Ultrasound Technology)," 2009.

[4] "Sonopill Website." [Online]. Available: http://sonopill.dundee.ac.uk/.

[5] "Onda Corporation." [Online]. Available: http://www.ondacorp.com/images/Rubbers.pdf. [Accessed: 31-Mar-2016].

[6] T. R. Gururaja, "Piezoelectric transducers for medical ultrasonic imaging," in *ISAF '92: Proceedings of the Eighth IEEE International Symposium on Applications of Ferroelectrics*, 1992, pp. 259–265.

Master Slave Enhanced Endoscopic Optical Coherence Tomography – Prelude to Developing Novel Robot Guided Imaging Tools

A. Bradu[1], S. Rivet[2], M. Hughes[3], G. Gelikonov[4], G.-Z. Yang[3], A. Podoleanu[1]

[1]*Applied Optics Group, School of Physical Sciences, University of Kent, UK*

[2] *Univ. de Bretagne Occidentale, Lab. de Spectrométrie et Optique Laser, France*

[3] *Hamlyn Centre for Robotic Surgery, Imperial College London, UK*

[4]*Institute of Applied Physics RAS, Russia*

a.bradu@kent.ac.uk

INTRODUCTION

One of the key elements in developing a robot-guided tool to allow visualisation of morphological and cellular details is the implementation of a high speed, high resolution imaging device, based on optical coherence tomography (OCT). Probes for endoscopic OCT (EOCT) have been regarded as powerful tools in examining internal organs, various (E)OCT instruments being already devised: common path (where the reference arm of the interferometer is created by placing a partial reflector close to the sample to be imaged), and conventional non common path, (where the arms of the interferometer are independently controlled).

Irrespective of their implementation, to produce images, all conventional OCT instruments are currently based on Fourier transforms (FT) which brings some penalties on image resolution and cost. First, as all EOCT instruments are built using optical fibres, matching their lengths in the arms of the interferometer with micrometric accuracy is challenging. To compensate for the dispersion in the interferometer both hardware, and numerical methods can be implemented. However, these methods are not perfect, leading to an increase in the complexity of the systems or to heavy computation. Second, before FT, data has to be calibrated (re-sampled), process which cannot be perfectly performed and leads to a heavy computational load, which in the end influences the real time operation of the instrument.

We demonstrate here the utilization of the recently introduced Master/Slave (MS) method within an EOCT instrument.

The MS method [1] is based on comparison of shapes of the channelled spectra (CS) at the interferometer output with stored CS shapes. An immediate advantage is that the MS technique can be implemented with raw data, without the need of organizing it in linear frequency slots, as required by the conventional OCT technique. The MS method is also immune to any dispersion left uncompensated within the interferometer [2]. These two properties make the MS method an ideal enhancing tool to be used in EOCT, offering a simple and cost effective way to obtain real-time high resolution images. In [3], real-time production of cross-section MS-OCT images was possible by using GPUs. Here, the production of images is based on a simplified algorithm [4] which allows for real-time display of processed B-scan MS-OCT images without resorting to GPUs or FPGAs [5].

MATERIALS AND METHODS

A schematic diagram of an endoscopic swept source based OCT imaging system assembled for this study is depicted in Fig. 1. As optical source, a swept source was employed. It has a central wavelength of 1300 nm, sweeping range 106 nm and 100 kHz line rate.

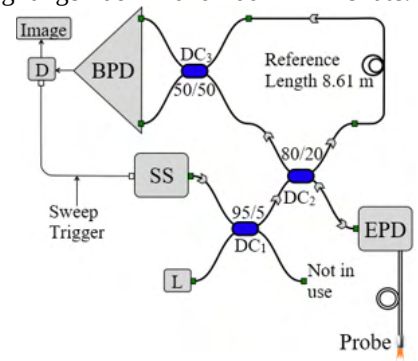

Fig. 1 Schematic diagram of the EOCT instrument.

The configuration uses three single mode directional couplers, $DC_{1\text{-}3}$. DC_1 allows the use of a visible laser diode L for guidance purposes, DC_2 splits the beam of light from SS towards the reference arm and towards the endoscopic probe while DC_3 feeds a balance detection receiver BPD. The signal from the BPD is sent to the input of a fast digitizer D. The OCT probe has a cylindrical form and is composed of stainless steel incorporating copper wires, NdFeB magnets to ensure the lateral scanning and a GRIN lens for focusing the beam of light on the sample, covered by a Teflon tubing. The probe connects to the rest of the inter-ferometer via the electronic probe driver (EPD). The endoscope probe unit (shown in Fig. 2) has a diameter of 2.2mm and a length of the rigid part of 13mm.

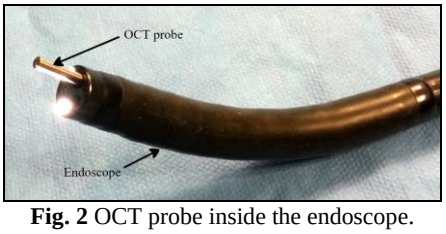

Fig. 2 OCT probe inside the endoscope.

RESULTS

When using MS, to produce a single point in the axial reflectivity profile (A-scan), instead of a FFT, an integral of the product between the raw chirped channelled spectra (CS) and a new kernel function M^* (denoted as a complex mask) is performed for each depth of interest [4]. The accuracy of producing A-scans depends on M^*, which are produced using a few experimental CS only, (complex masks M^* need to be produced once for a given setup). However, when using an EOCT instrument, there are some technical difficulties against MS implementation. These refer to the easiness in collecting experimental CSs from a mirror as they have to be recorded for several optical path differences (OPD) between the arms of the interferometer, which cannot be performed by actuating on the length of the reference arm. This can only be done by axially shifting a mirror in front of the probe, which is accompanied by large changes in the amplitude of the CS modulation. The motivation of the current study is related to the feasibility of using the MS method when restrictions are imposed on the number and the range of axial positions of a mirror where experimental CSs can be recorded from.

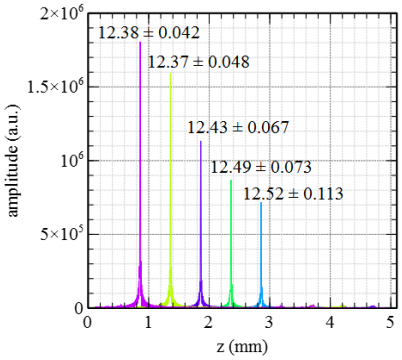

Fig. 3 A-scans corresponding to the 5 positions of the high reflector, the numbers refer to the axial resolutions in microns measured in air (with standard deviation).

To produce M^*, five experimental CSs were measured only using a high reflector as object for five axial positions. The process of recording the five experimental CSs was repeated 10 times. As we observed extremely small variations of M^* from a measurement to the next, it is expected that the accuracy of producing A-scans to be high. This is illustrated in Fig. 3.

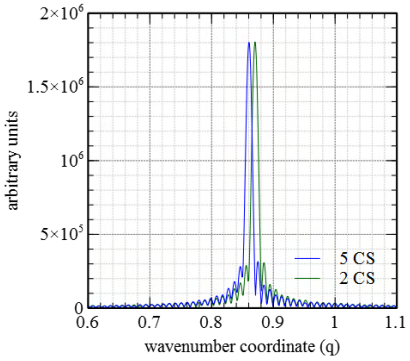

Fig. 4 Reflectivity profiles calculated using 5000 masks generated from 5 and 2 experimental CS respectively.

To add extra simplicity to the process of producing new masks M^*, it would be useful to reduce the number of measurements as much as possible, to a minimum of two. The axial resolution does not change practically at all (Fig. 4), the only drawback being a slight axial shift of the maximum of the sensitivity, which has no effect on the quality of the final cross-sectional image.

DISCUSSION

Following the analysis in the previous section, it is expected to obtain high resolution images by using two experimental CSs only. This is demonstrated in Fig. 5, where high axial resolution *in-vivo* MS-based images of a human thumb are presented. The images, all of them of size 1000 x 300 (lateral x axial) pixels^2 were extracted from a sequence of images produced at 50 Hz. As each of the three images shown were produced by creating a number of 300 masks $\tilde{M}$, the axial separation between two pixels in the image is 5 µm. Despite the small lateral size limited at the moment by the optical/mechanical design of the probe, the helicoidal shape of the sweat glands can still be recognized.

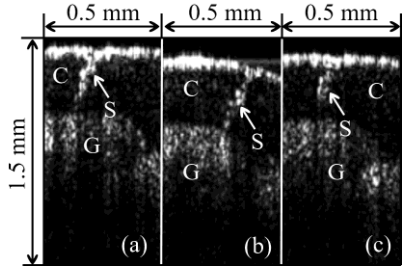

Fig. 5 Three B-scan MS based OCT images of the human thumb showing the stratum corneum (C) and the stratum granulosum (G). In each image a sweat gland (S) is visible.

The use of the MS-OCT method instead of the FT – OCT technique brings several advantages to the EOCT imaging instruments: (i) Simplicity, as demonstrated in this paper to calibrate the system, only two spectra have to be recorded, once for a given setup; (ii) No need for data resampling; (iii) No need to compensate for dispersion; (iv) Real time production of B-scan images. With all these advantages combined, the MS can become the technique of choice to be implemented within any EOCT imaging instrument.

REFERENCES

[1] A. Podoleanu and A. Bradu. Master–slave interferometry for parallel spectral domain interferometry sensing and versatile 3D OCT. Opt. Express 2013 21:19324-38.

[2] A. Bradu, M. Maria, and A. Podoleanu. Demonstration of tolerance to dispersion of Master/Slave Interferometry. Opt. Express 2015 23(11):14148-61.

[3] A. Bradu, K. Kapinchev, F. Barnes, and A. Podoleanu. On the possibility of producing true real-time retinal cross-sectional images using a GPU enhanced master-slave OCT system. J. Biomed. Opt. 2015 20(7):076008.

[4] S. Rivet, M. Maria, A. Bradu, T. Feuchter, L. Leick, and A. Podoleanu. Complex master slave interferometry. Opt. Express 2016 24(3): 2885-904.

[5]. A. Bradu, K. Kapinchev, F. Barnes, and A. Podoleanu. Master slave en-face OCT/SLO. Biomed. Opt. Express 2015 6:3655-69.

Vision Based Distortion Correction of a Deformable Object

B. Huang, Y. Hu, G.-Z. Yang

Hamlyn Centre for Robotic Surgery, IGHI, Imperial College London, UK

b.huang@imperial.ac.uk

INTRODUCTION

Manipulating deformable objects is an important task in daily life and have many applications in medical robotics. The work we present in this paper focuses on detecting and removing unwanted distortions of deformable objects, for example, a stent graft. A stent graft is a tubular structure composed of fabric supported by a metal mesh called a stent sewn on it. It is widely used for a variety of conditions for endovascular intervention. Automatic manufacturing of personalised stent-grafts is a critical unmet clinical demand and robot assisted manufacturing is being pursued. Bimanual manipulation of the stent graft is required during its manufacturing process: two hand to hold the stent graft such that the sewing machine can perform sewing (Figure 1). Extra strain applied to the stent graft will cause surface distortion, making precision sewing difficult. Small distortion of a deformable object is hard to detect by force torque sensors. In this paper, we propose a vision based method to detect the distortions.

Under strains an object can deform in many ways. In computer vision, various visual feature descriptors have been proposed [3,4,6]. These features can be easily tracked and hence allow us to perform qualitative measurement of object deformation. The concepts of shape Jacobean and deformation Jacobean are proposed to map the robot end effector action to the object feature movements [2]. The robot end effector motion is generated to bring the object to a desired shape. However, the planned path does not guarantee to follow the shortest path. In manufacturing tasks, e.g. sewing a stent graft, we need to find a shortest possible path to remove object distortion, in order to avoid further damages. Extra motions of the robot may introduce further distortions, which are not desirable. In this paper, we propose a method to build a distortion classifier of a deformation object and a control strategy to remove undesired distortions. This is a data driven approach that does not require detailed modelling of the object. The method proposed can monitor object deformation and control the robot to react in real time.

MATERIALS AND METHODS

This paper focuses on detecting and correcting the small deformations of the fabric during a stent graft sewing task. During this task, two robot hands hold a stent graft at each end and move it to a desired sewing position (Figure 1). During the movement, the stent graft should not experience extra strain from the robot hands. We call this status as “non-strain status”.

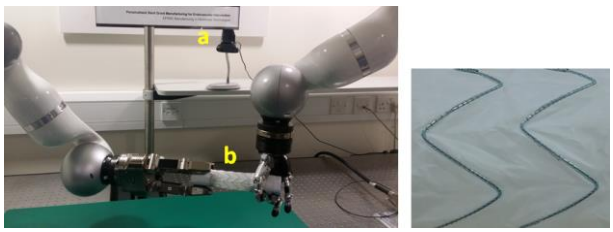

Fig. 1 Bimanual robot system to hold stent graft. Left: (a) camera, (b) stent graft. Right: view of camera.

This bimanual robot system needs to maintain the “non-strain status” during motion. However, distortions may still occur by the imperfection of the robots’ kinematics and of the system’s calibration. Therefore, we need to continuous monitor the status of the stent graft. Once distortion is detected and recognized, we need to generate corresponding commands for the robots to correct the distortion.

According to the elastic theory, the distortion of an object can be classified into four main types: compression/expansion, twist, bending and shearing. Modelling these distortions is difficult; hence we adopt a learning from demonstration approach to classify them. We first generate these distortions manually, by compressing, twisting, bending and shearing the stent graft with one hand, and use a camera to monitor the workspace and focus on the stent graft area.

These distortions are recorded by tracking the Haar-like features on the object surface. The deformation patterns (the current features locations, features moving velocities and displacements with respect to their initial locations) are recorded by camera. Figure 2 shows the snapshots of the four demonstrated distortions.

After recording the deformation patterns, we use the Support Vector Machine (SVM) [1] to build a classifier for the four primitive distortion types. SVM is a kernel based classification method. The kernel function we use in our task is the Radial Basis Function (RBF) kernel and the distance metric between two samples x and x' is defined as:

$$K(x,x') = \exp(-\gamma \|x - x'\|^2)$$

where the parameter γ determines the width of the kernel. The value of γ is determined by a 5-fold cross validation.

After building the distortion classifier by SVM, we use it to recognize the distortion of objects occurring during a task.

After recognizing the type of distortion, the robots are commanded to reduce the distortions. Eight different strategies are designed to correct the distortions (Table 2). The robot will perform these corrections until the

distortion is removed. The distortion is considered to be removed when the sum of the feature displacements is reduced to an experimental threshold.

Table. 1 Training and testing for distortion classifier

Distortion types	Training data	Testing data	Successful classification rate (%)
Compression	1572	300	100
Twist	800	400	89
Bending	900	400	95
Shearing	801	400	89

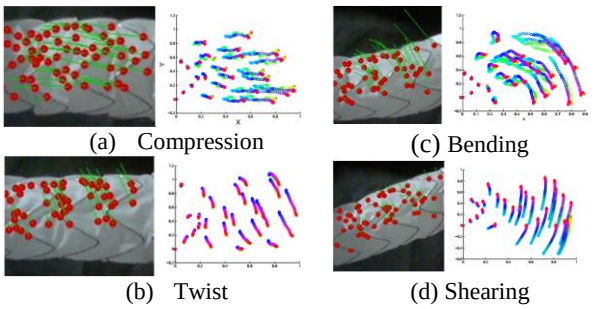

(a) Compression (c) Bending

(b) Twist (d) Shearing

Fig. 2 Four types of primitive distortions. Left figure: demonstrations of different primitive distortion types, red dots represent feature points and green lines represent moving directions. Right figure: feature points motion trajectories.

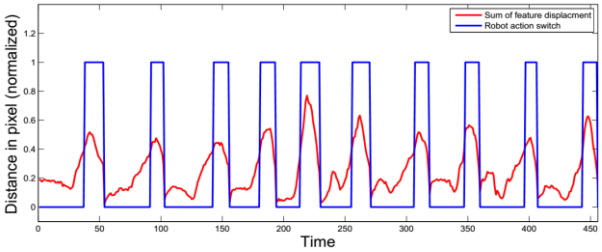

Fig. 3 Ten experiments of robot reacting to detected distortions. Blue line represents robots' status: 0 is the right hand to apply small strain on the stent graft and cause distortion, 1 is the left hand to react to the distortion. Red line represents the sum of features' displacement. Smaller displacement means less distortion. It can be seem that when robot status is 0 the displacement increases, when robot status is 1 the displacement decrease.

RESULTS

We conduct two experiments to verify our approach: one to test the accuracy of the SVM distortion classifier and another to test the robot reaction. Each type of distortion is demonstrated for five times, each time lasts for a second. At each time frame, the feature points' location, velocities and displacements are stored for training. For the testing purpose, we separate part of the data for testing. Here we use the open source library OpenCV to detect and track the features. Figure 2 shows the feature points positions changes for different types of distortion.

The overall number of training data for the distortion classifier is listed in the Table 1. We trained the classifier with the LIBSVM library [1] and with the γ to be 0.01, according to the 5-fold cross validation. We then test this distortion classifier by the testing set. The classification results are listed in the Table 1.

We then implement this distortion classifier on our robot system and use it to reduce distortion. We conduct the experiments by commanding the right robot hand to apply small strains. The vision system monitors the motion of the feature points and once the sum of the motions is larger than a threshold, i.e. distortion occurs, the right hand stops moving. The distortion classifier is used to detect the type of distortion. According to the action table (Table 2), the left hand chooses an action to counteract the detected distortion. It stops moving when the displacement of the feature points is less than the threshold. Figure 3 shows ten trials of continuous occurrence of distortions and corrections. It can be seem that once the left hand is activated, it can react to reduce the stent graft distortions.

Table 2 Object distortion types and corresponding corrections.

Distortion types	Features moving directions	Robot reaction
Compression	+x	Moving to +x
	-x	Moving to -x
Twist	+y	Rotating along -x
	-y	Rotation along +x
Bending	+y	Rotating along –z and moving clockwise around the bending pivot point
	-y	Rotating along +z and moving anti-clockwise around the bending pivot point
Shearing	+y	Moving towards +y
	-y	Moving towards -y

CONCLUSIONS

We present a vision based approach to reduce distortion of deformable object in a bimanual task. The proposed vision system is able to recognize the primitive types of distortion of a stent graft: compression, twisting, bending and shearing. The experimental results have shown that with the proposed approach, the success rate of distortion identification is over 90% and the robot can generate appropriate action to reduce the distortions.

REFERENCES

[1] C.-C. Chang and C.-J. Lin. Libsvm: a library for support vector machines. ACM Transactions on Intelligent Systems and Technology (TIST), 2011.

[2] J. Das. Robotic control of deformable continua and objects therein. PhD thesis, Vanderbilt University, 2010.

[3] S. Hirai, T. Tsuboi, and T. Wada. Robust grasping manipulation of deformable objects. In Proc. IEEE Symp. on Assembly and Task Planning, 411–416, 2001.

[4] D. Navarro-Alarcon, Y.-h. Liu, J. G. Romero, and P. Li. On the visual deformation servoing of compliant objects: Uncalibrated control methods and experiments. The International Journal of Robotics Research, 33(11):1462–1480, 2014.

[5] P. Viola and M. Jones. Rapid object detection using a boosted cascade of simple features. In Proc. CVPR, 1, I–511. IEEE, 2001.

[6] P. Zacharia, N. Aspragathos, I. Mariolis, and E. Dermatas. A robotic system based on fuzzy visual servoing for handling flexible sheets lying on a table. Industrial Robot: An International Journal, 36(5):489–496, 2009.

Author Index

Z

The Hamlyn Symposium on Medical Robotics

25th-28th June, 2016
Imperial College London and
the Royal Geographical Society, London